Unraveling the Complex Vibronic Coupling in Highly Fluorinated Aromatic Systems

Dissertation

zur Erlangung des Doktorgrades

Dr. rer. nat.

der Mathematisch-Naturwissenschaftlichen Fakultät
der Christian-Albrechts-Universität zu Kiel

vorgelegt von
Jonas Andreas Kus

Institut für Physikalische Chemie
Kiel 2022

Erster Gutachter: Prof. Dr. Friedrich Temps
Zweiter Gutachter: Prof. Dr. Jürgen Grotemeyer

Tag der mündlichen Prüfung: 03.02.2022
Zum Druck genehmigt: 03.02.2022

Erklärung

Hiermit erkläre ich an Eides statt, dass die vorliegende Abhandlung – abgesehen von der Beratung durch meinen Betreuer Prof. Dr. Friedrich Temps – nach Inhalt und Form meine eigene Arbeit ist.

Diese Arbeit hat weder in Auszügen noch in ganzer Form einer anderen Stelle im Rahmen eines Prüfungsverfahrens vorgelegen. Sie wurde in ihrer Gesamtheit nicht veröffentlicht und auch nicht zur Veröffentlichung eingereicht.

Teile dieser Arbeit wurden zur Veröffentlichung in einer wissenschaftlichen Fachzeitschrift eingereicht. Dies bezieht sich auf das folgende Kapitel:

UNTERKAPITEL 3.5
JONAS ANDREAS KUS, OLE HÜTER und FRIEDRICH TEMPS, "Real-time observation of multi-mode vibronic coherence in pentafluoropyridine", J. Chem. Phys. **147**, 013938 (2017).

Die Arbeit ist unter Einhaltung der Regeln guter wissenschaftlicher Praxis der Deutschen Forschungsgemeinschaft entstanden.

Mir wurde kein akademischer Grad entzogen.

Kiel, Februar 2022

Jonas Andreas Kus

Abstract

Highly fluorinated aromatic molecules exhibit a rather unique behavior: the fluorination stabilizes $\pi\sigma^*$ states. For pentafluorobenzene (PFB), this so-called perfluoro effect was identified as the major driving force in modulating the dynamics of the S_1 ($\pi\pi^*$) state in the past. Intense vibronic coupling between the directly excited $\pi\pi^*$ (S_1) and higher-lying $\pi\sigma^*$ states, mediated by out-of-plane vibrational modes, yields remarkable oscillations of the time-resolved response signals.

Hitherto, only few fluorinated aromatic molecules were subjected to femtosecond time-resolved experiments. In this Thesis, the influence of the effects of number, position, and nature of substituent as well as the influence of a heteroatom in the aromatic system on the dynamics of the S_1 state were systematically investigated by means of femtosecond time-resolved time-of-flight mass spectrometry and corresponding photoelectron imaging spectroscopy, supported by ab initio calculations. The set of molecules included 1,2,3-trifluorobenzene (1,2,3-TriFB), all three tetrafluorobenzene isomers (TFB), pentafluorotoluene (PFT), pentafluorophenol (PFPh) as well as chloro- and bromopentafluorobenzene (ClPFB, BrPFB), and pentafluoropyridine (PFPy). Nearly all time-resolved parent ion yields showed intense single-frequency oscillations. The photoelectron spectroscopy confirmed vibronic coupling to be the origin of the oscillations, dominated by low-frequency coupling modes. The oscillations became more pronounced the more fluorine atoms were attached to the aromatic rings and the closer they were to each other. In contrast, different substituents damped the oscillations. Astonishingly, a complex multi-mode oscillation was observed for 1,2,3,5-TFB, exhibiting two oscillational frequencies. Thus, the dynamics of 1,2,4,5-TFB (no oscillation), 1,2,3,5-TFB (multi-frequency oscillation), and 1,2,3,4-TFB (single-frequency oscillation) are strikingly different, despite nearly identical electronic structures, highlighting that subtle changes like changing the fluorine position can heavily impact the dynamics. PFPy showed an even more intricate signal pattern. Four oscillational frequencies were observed, of which at least three were attributed to genuine vibrational modes. Hence, the dynamics of PFPy impressively demonstrates that one can actually map the motion of multiple vibrational modes of the coupled wavepacket at once in real time.

Zusammenfassung

Fluorierte aromatische Systeme besitzen die bemerkenswerte Eigenschaft, dass der erste angeregte elektronische Zustand S_1, der $\pi\pi^*$-Charakter aufweist, bei der Bewegung eines kohärenten Vibrationswellenpakets stark mit höherliegenden $\pi\sigma^*$-Zuständen gekoppelt sein kann. Bewegung entlang der Koordinaten der koppelnden Schwingungen führt zu starker Vermischung der elektronischen Charaktere. Zusätzlich wird der tieferliegende, gemischte Zustand energetisch stabilisiert, wodurch die Übergangswahrscheinlichkeit zu ionischen Zuständen deutlich verringert wird. Wie sich die Anzahl und Position der Fluoratome sowie zusätzliche Substituenten und unterschiedliche aromatische Systeme auf die Dynamik des S_1-Zustandes auswirken, wurde in dieser Dissertation mittels femtosekunden-zeitaufgelöster Flugzeit-Massenspektrometrie und Photoelektronen-Geschwindigkeitskartographie untersucht. Insgesamt wurden für die systematische Studie neun Moleküle ausgewählt: 1,2,3-Trifluorbenzol (1,2,3-TriFB), die drei Tetrafluorbenzolisomere (TFBs), Pentafluortoluol (PFT), Pentafluorphenol (PFPh), Chlorpentafluorbenzol (ClPFB), Brompentafluorbenzol (BrPFB) und Pentafluorpyridin (PFPy).

Die TOF-MS Signale nahezu aller Moleküle wiesen starke Intensitätsoszillationen innerhalb der ersten Picosekunden nach Anregung auf, die der schwingungsinduzierten Kopplung und der dadurch bedingten Veränderung der Ionisationswahrscheinlichkeit zugeordnet werden konnten. Die Oszillationen wurden ausgeprägter, je mehr Fluoratome in direkter Nachbarschaft zueinander vorlagen. Zusätzliche Heteroatome oder Gruppen führten zu einer schnelleren Dämpfung und geringeren Amplituden der Oszillationen. Im Gegensatz zu den meisten anderen Molekülen konnte für PFPy eine deutliche Multi-Frequenzoszillation, welche sich aus vier Frequenzen zusammensetzte, beobachtet werden. Drei dieser Frequenzen wurden unterschiedlichen Schwingungsmoden zugeordnet. Somit konnten mehrere Schwingungen des kohärenten Wellenpakets experimentell aufgelöst werden. Ein ähnlich komplexes Verhalten wurde für 1,2,3,5-TFB beobachtet, dessen Signal von zwei Frequenzen moduliert wird. Der Vergleich mit 1,2,4,5-TFB (keine Oszillation) und 1,2,3,4-TFB (bedeutend intensivere Einzelfrequenzoszillation) zeigt, dass bereits die Position der Fluoratome starken Einfluss auf die Kopplung hat.

Contents

1 Introduction

Photo-induced chemical reactions have sparked scientific interest for centuries. Especially in the past four decades, they have evolved into a versatile pillar of chemical synthesis.[1,2] While in the early days, photochemical reactions had to be approached by trial and error, nowadays the community strives to predict the outcomes for increasingly complex molecules.[3–6] The key step in enabling us to do so is to understand the fundamental photochemical and photophysical processes of the respective core building blocks.

One of the most prominent building blocks of organic chemistry is benzene. Thus, considerable effort has been undertaken to understand its electronic structure and dynamics. The readily accessible lower-lying excited electronic states are characterized by electron transfer from occupied π to unoccupied π^* molecular orbitals. Since benzene exhibits D_{6h} symmetry (Mulliken notation[7]) in the planar electronic ground state, the symmetries of the highest occupied molecular orbitals are $(a_{2u})^2(e_{1g})^4$. Transition of one electron from e_{1g} to the unoccupied e_{2u} orbital may give rise to one of three singlet states denoted by their symmetry as $^1B_{2u}$, $^1B_{1u}$, and $^1E_{1u}$ (cf. Ref. [8] and references therein).

The first excited singlet state S_1 ($\pi\pi^*$) is of 1 $^1B_{2u}$ character, exhibiting a highly structured UV absorption band between 280–220 nm. Although the transition is formally symmetry forbidden, the restrictions for electronic transitions are weakened by excitation of e_{2g} out-of-plane vibrational modes (cf. Refs. [8–11] and references therein). The corresponding electronic deactivation pathways are strongly dependent on the excitation wavelength λ_{pump}. The journey of unraveling the deactivation mechanisms upon excitation at wavelengths $\lambda_{pump} \geq 245$ nm has probably best been summarized by C. S. Parmenter.[12] Nearly independent of the environment,[13] excitation between 260–245 nm[14] yields a fluorescence quantum yield of $\Phi_f \approx 0.2$[15,16] and a S_1 lifetime of $\geq$75 ns.[12] The rather small fluorescence quantum yield hints at a major nonradiative deactivation channel for which detection of a lower-lying triplet state in the solid phase suggested a pathway involving intersystem crossing (ISC).[17] Although direct observation of the triplet state in the gas phase failed, sensitization studies on the isomerization of *cis*- and *trans*-2-butene in combination with benzene unveiled that

the nonradiative decay is indeed dominated by ISC to the lower-lying triplet state.[14,18]

In stark contrast, excitation of benzene at $\lambda_{pump} \leq 245$ nm eliminates fluorescence nearly quantitatively. Thus, an additional deactivation pathway was presumed. The nature of this so-called "channel 3", however, remained elusive. Three main hypotheses were discussed: an ultrafast internal conversion (IC) to the ground state (GS), an ultrafast ISC, and structural rearrangement. Since it was deemed improbable that changing the excitation wavelength by a mere few nanometers would lead to an ultrafast IC to the GS, IC was dismissed. Likewise, ISC was ruled out. Thus, relaxation by structural rearrangement, e.g., isomerization, was thought to be the most plausible deactivation pathway.[12] Shortly afterwards, these conclusions were questioned by further wavelength-dependent fluorescence studies hinting towards IC.[19] The advent of improved ab initio calculations eventually enabled researchers to gain new insights into the deactivation mechanism. Work by Sobolewski et al.[20] and Palmer et al.[21] predicted that deactivation follows IC to the GS, but requires a temporary change in molecular structure into a prefulvene.[20,21]

Time-Resolved Ionization

The invention of novel femtosecond time-resolved pump–probe techniques allowed to experimentally monitor energy dissipation proceeding within a few picoseconds. In pump–probe experiments, an electronic state of interest is excited by a femtosecond pump pulse. A second, time-delayed probe pulse promotes the excited molecule to a different vibrational/electronic state. The response to the probe pulse depends strongly on the transition probability between the initially excited target state and the final state. Since temporal evolution of the initially excited state alters the transition probability to higher-lying states by the probe pulse, a sequence of probe snapshots monitors the changes of the excited state.[22–24]

If the sum of the neutral excited-state energy E_x and the probe photon energy $\hbar\omega_{probe}$ exceeds the ionization threshold IE_i, photoelectrons (PE) with a kinetic energy E_{el}

$$E_{el} = E_x + \hbar\omega_{probe} - IE_i \tag{1.1}$$

are emitted. In the most simple picture of a transition between a single neutral and an ionic electronic state, the energy distribution of the electrons is deter-

mined by the vibrational structures in these states, as each excited vibrational mode alters E_x and IE_i and thus may change the resulting E_{el}. In general, the intensity distribution in photo-induced electronic transitions like photoionization is described by the Franck–Condon principle.[25,26] The vibronic wave function of a state $|\psi\rangle$ may be split in an electronic $|\psi_e\rangle$ and a vibrational part $|\psi_v\rangle$

$$|\psi\rangle = |\psi_v\rangle|\psi_e\rangle. \tag{1.2}$$

The intensity of a photo-induced electronic transition between the initial $|\psi''\rangle$ and the final state $|\psi'\rangle$ is thus

$$I(t) \propto |\langle\psi'_v|\langle\psi'_e|\boldsymbol{\mu}|\psi''_e\rangle|\psi''_v\rangle|^2, \tag{1.3}$$

with the electronic transition dipole moment $\boldsymbol{\mu}$. If the Born–Oppenheimer approximation holds true,[27] Equation 1.3 can be further factorized to

$$I(t) \propto |\langle\psi'_e|\boldsymbol{\mu}|\psi''_e\rangle|^2|\langle\psi'_v|\psi''_v\rangle|^2. \tag{1.4}$$

The second factor on the right-hand side is known as the Franck–Condon factor.[28] The dependence of the intensity on the overlap of the vibrational wave functions $|\psi''_v\rangle$ and $|\psi'_v\rangle$

$$\langle\psi'_v|\psi''_v\rangle$$

shows that the intensity of a transition is increased when the vibrational wave functions are similar in both electronic states, i.e., the vibrational excitation of the lower-lying electronic state is vertically transferred to the higher-lying one. Even though excitation of different vibrational modes is not explicitly prohibited, the probabilities of such non-vertical transitions are lower. Ultimately, the Franck–Condon factors determine the distribution of photoexcited vibrational states and consequently the energy distribution of the photoelectrons in an ionizing transition.[28]

The ionization probability also depends strongly on the electronic transition dipole moment, indicated in Equation 1.4. Extending T. Koopmans theorem,[29] connecting the ionization and highest-occupied molecular orbital energies, leads to the assumption that upon photoionization of excited electronic states preferentially the excited electron is emitted, without simultaneous reordering of the remaining valence electrons. Thus, which ionic state will be populated is determined by the structure of the remaining electrons. As a direct consequence,

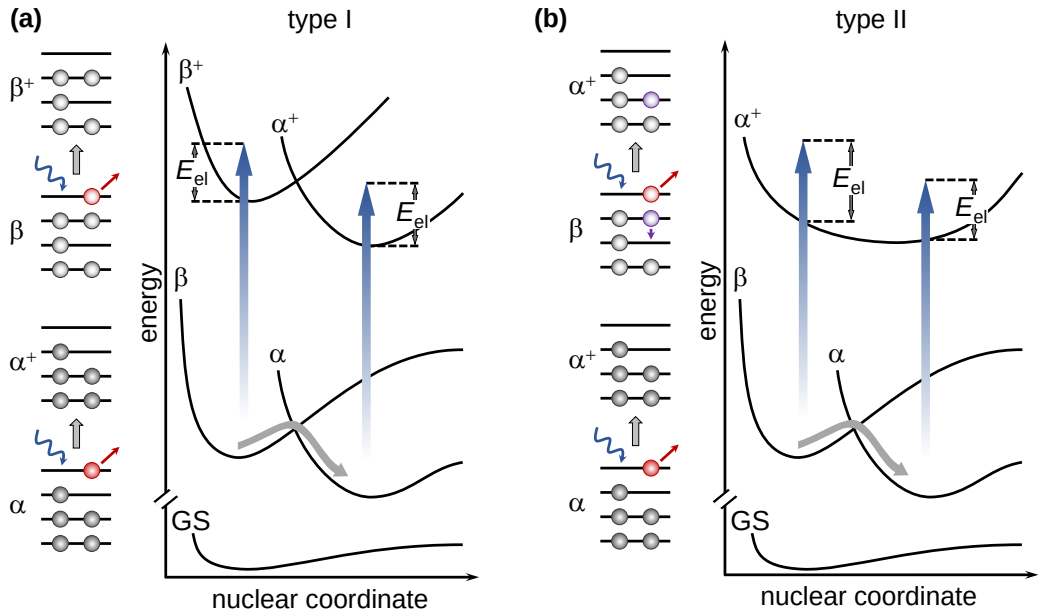

Figure 1.1. **(a)** Schematic depiction of the complementary or type I ionization of two neutral electronic states α and β, that differ in their electron distributions. Absorption of a photon (blue cosine arrows) detaches the excited electron (red circles), leading to two different ionic states α^+ and β^+. **(b)** In the corresponding or type II ionization, the detachment of one photoelectron is accompanied by the simultaneous reordering of the remaining valence electrons (grey circles). Thus, ionization of either α and β leads to the same ionic state α^+. Internal conversion between the neutral excited states may shift the photoelectron energy E_{el} following either ionization mechanism.

ionization from different excited neutral states might lead to different (excited) ionic states, also known as complementary ionization or type I ionization. If ionization leads to the same ionic state by reordering of the remaining electrons, a corresponding type II ionization occurs (cf. Refs. [30–32] and references therein). Both mechanisms are depicted schematically in Figure 1.1.

All in all, E_{el} comprises the information of vibrational and electronic excitation of the states involved in the ionization transition. Furthermore, the excited neutral target state predetermines the final ionic state and resulting changes of E_{el} thus also reflect the character of the neutral excited state. Regardless of the exact ionization mechanism, a transition from the initially excited neutral state to a lower-lying electronic state often induces shifts of the photoelectron kinetic energy distribution. Therefore, time-resolved detection of the kinetic energy, by photoelectron spectroscopy, allows one to follow the evolution of the neutral excited states in real time. Since essentially every electronic state might be ionized, mapping the complete reaction pathway is not hampered by

optically dark states, in contrast to other pump–probe methods that rely on optical electronic transitions.[33–36] Nevertheless, data acquisition is rather time consuming (cf. Chapter 2), contrary to the comparably fast detection of cations in the corresponding time-resolved time-of-flight mass spectra (TOF-MS). Although the ions do not provide direct insight into the underlying processes, the decay of the ion yield monitors the lifetime of the excited electronic state. On the basis of this information, suitable time stamps for PE spectra may be selected. Hence, the complementary information of both methods comprehensively pictures the deactivation pathways in the molecules.

At last, time-resolved PE spectroscopy proved to be most valuable for unraveling the S_1 ($\pi\pi^*$) deactivation mechanism of benzene.[37–43] Distinct characteristic changes in the PE energies confirmed the expected IC to the GS,[37–40,43,44] but most surprisingly, also revealed additional ISC to triplet states.[41,42,45] Ultimately, the electronic deactivation of benzene comprises all initially proposed deactivation pathways, depending on the excitation energy of the molecules.

Modulation of the Decay Signals by Quantum Beating

While already the deactivation mechanisms of benzene are astonishingly complex for such a small molecule, elucidation of the deactivation pathway becomes even more complicated upon substitution of the hydrogen atoms in the molecular framework. A prominent example for an increased complexity of photo-induced deactivation is phenol. Besides a deactivation pathway via O-H bond fission discussed in Section 3.7, a recent investigation by Woo and Kim[46] showed that the exponential decay signal of the S_1 state ($\pi\pi^*$) of phenol may be strongly modulated under certain circumstances: After excitation at ≈268 nm, the parent ion yield exhibited intense oscillations with a frequency of $\nu = (3.302 \pm 0.001)$ cm^{-1} in the picosecond time-resolved TOF-MS experiments. The frequency agreed perfectly with the energy gap between the vibrational modes 1^1 (in Wilson notation,[47] 934.9 cm^{-1}) and $4^1 10b^1$ (938.3 cm^{-1}).[46] In contrast, tuning the excitation wavelength to ≈264 nm yielded $\nu = (1.655 \pm 0.001)$ cm^{-1}, equal to the energy gap of modes 12^2 (1564.1 cm^{-1}) and $8a^1$ (1565.9 cm^{-1}). Therefore, the oscillation was attributed to quantum beating, a fundamental mechanism of quantum dynamics,[22,48–50] between those modes.

Quantum beatings may arise in general, when two different vibrational modes are coherently excited by a laser pulse. The resulting wave function $\Psi(t)$ then

becomes a superposition of the individual vibrational eigenstates $|m(t)\rangle$ and $|n(t)\rangle$,

$$|\Psi(t)\rangle = a_m(t)|m(t)\rangle + a_n(t)|n(t)\rangle, \tag{1.5}$$

weighted by the coefficients $a_m(t)$ and $a_n(t)$. Writing the temporal evolution of the non-stationary vibrational eigenstates $|x(t)\rangle$ as

$$|x(t)\rangle = |\psi_x\rangle e^{-i\omega_x t}, \tag{1.6}$$

with $|\psi_x\rangle$ being the stationary eigenstates at $t = 0$ and ω_x denoting the transition energy, the combined wave function reads

$$|\Psi(t)\rangle = a_m(t)|\psi_m\rangle e^{-i\omega_m t} + a_n(t)|\psi_n\rangle e^{-i\omega_n t}. \tag{1.7}$$

The intensity $I(t)$ of a subsequent forced (e.g., by ionization) or spontaneous transition (e.g., fluorescence) to a different electronic state $|\psi'\rangle$ is proportional to the overlap of the wave functions of the initial and the final state

$$I(t) \propto |\langle\psi'|\boldsymbol{T}|\Psi(t)\rangle|^2, \tag{1.8}$$

with $\boldsymbol{T}$ being the transition (e.g., transition dipole) operator. Thus, the intensity is strongly modulated by the evolution of $|\Psi(t)\rangle$. Based on Equations 1.7 and 1.8, it can be shown that this evolution induces the so-called quantum beating of the signal,[22,48–50]

$$I(t) \propto \cos(\omega_n - \omega_m)t, \tag{1.9}$$

that reflects the oscillating population transfer between two vibrational eigenstates within a single electronic state.

In pump–probe experiments, the beatings can be resolved best, if the probe pulse can only promote one of the beating eigenstates to a higher-lying state. Thus, a signal will arise with increasing population of this specific eigenstate. In case of phenol, Woo and Kim observed pronounced beatings when probing at $\lambda_{\text{probe}} = 309$ nm, since the probe pulse energy was insufficient to populate both vibrational states in the ionic state corresponding to the beating eigenstates in the neutral electronic state. Tuning to higher photon energies allowed for ionization independent of the temporal phase of the beating, strongly decreasing the modulation depth. Contrary, when choosing a suitable ionization wavelength, basically no damping of the beating was detected, modulating the parent ion

yield for several nanoseconds until the electronic deactivation of S_1 ($\pi\pi^*$) was completed. Therefore, the authors concluded that only little internal vibrational redistribution (IVR) took place.[46]

Quantum beatings have also been observed for phenol derivatives. Using femtosecond time-resolved mass spectrometry, Young et al. reported that substitution of either one (guaiacol) or two (syringol) hydrogen atoms in *ortho* positions by methoxy groups enabled even more complex beating patterns.[51] In the case of guaiacol, the decay of the S_1 state ($\pi\pi^*$) was modulated by two frequencies, $\nu = 134$ cm^{-1} and $\nu = 163$ cm^{-1}. The parent ion signal of syringol also showed two frequencies, $\nu = 78$ cm^{-1} and $\nu = 112$ cm^{-1}. Although the simultaneous appearance of two frequencies suggested two separate beatings between three or four different vibrational modes, they actually originated from the excitation of overtones of a single out-of-plane vibrational mode. In contrast, in the same study no beating was observed for phenol. Since the employed broadband femtosecond laser pulses excited multiple vibrational modes at once, prohibiting a clear quantum beating pattern, these observations are not contradictory to Ref. [46]. However, adding a second hydroxy group to phenol in the *ortho* position (catechol) eventually facilitated detection of two beating frequencies, of $\nu = 113$ cm^{-1} and $\nu = 141$ cm^{-1}.[52]

Similar beating patterns have also been reported for fluorinated phenol derivatives. Zhang and coworkers observed femtosecond time-resolved oscillations of the parent ion yields of *o*-fluorophenol and 2,4-difluorophenol after excitation to the S_1 state ($\pi\pi^*$). In the first case, the ion yield was modulated with $\nu = 109$ cm^{-1}, in the second case by up to two frequencies, $\nu = 70$ cm^{-1} and $\nu = 89$ cm^{-1}.[53,54] Varying the pump and probe wavelengths for 2,4-difluorophenol by only a few nanometers allowed the authors to switch between modulating the signal by none, one (either 70 cm^{-1} or 89 cm^{-1}), or both frequencies,[54] emphasizing that selective pump–probe studies are realizable even with broadband femtosecond laser pulses.

Of course, phenol derivatives are not the only molecules exhibiting such quantum beatings. In the past decade, femtosecond time-resolved mass spectrometry and photoelectron spectroscopy were successfully employed for observing similar patterns in CS_2,[55,56] pyrimidine,[57,58] and 2,4-difluoroaniline.[59] Picosecond time-resolved beatings were also observed for fluorotoluene[60] and 2,4-difluorobenzene.[61]

The Perfluoro Effect

Noticeable, several of these systems share fluorine as a common substituent. Compared to hydrogen, fluorine atoms have a much higher electron negativity, which withdraws electron density from the rings. Static photoelectron spectroscopy played a crucial role in elucidating how exactly this affects the electronic structure. Numerous studies used He(I) and He(II) radiation for direct one-photon ionization of the molecules in the electronic ground state to assign the resulting photoelectron (PE) bands to electrons originating from the bound orbitals. Brundle et al. were the first to systematically compare the bands of a variety of aromatic and nonaromatic molecules with their perfluorinated counterparts.[62,63] They observed two clear trends upon substitution of the aromatic hydrogen atoms by fluorine atoms. Firstly, orbitals of σ character, located at the C-F bonds, are stabilized by several eV, and secondly, π orbitals are also lowered in energy, but to an order of magnitude less.

In the following, Hitchcock et al. discussed the effects of fluorination on the antibonding σ^* orbitals.[64] Based on a combination of previous electron attachment[65,66] and electron transmission studies,[67] as well as their own results from electron impact experiments, they concluded that the perfluoro effect also applies to the antibonding orbitals. In agreement with the trends for the bonding orbitals, the energy of the π^* orbitals is virtually unaltered upon fluorination, whereas the σ^* orbitals are significantly stabilized. In the past decades the conclusions concerning both the bonding and the antibonding orbitals were confirmed.[68–71]

As the low-lying excited electronic states of benzene are of $\pi\pi^*$ character, $\sigma^* \leftarrow \pi$ transitions may only be found near the ionization threshold.[8,64] Yet, the stabilization of σ^* but unaltered π orbital energies lead to dramatically lower $\pi\sigma^*$ state transition energies upon fluorination. As the perfluoro effect increases with increasing number of fluorine atoms, the stabilization might hence result in $\pi\sigma^*$ states accessible with UV light for highly fluorinated benzenes. Indeed, electron impact spectra of the three tetrafluorobenzene (TFB) isomers, 1,2,4,5-TFB, 1,2,3,5-TFB, and 1,2,3,4-TFB, as well as of pentafluorobenzene (PFB) and HFB exhibit additional bands not present in the less-fluorinated benzenes.[72] For the TFBs these bands are well above 6 eV (<200 nm). In contrast, for PFB and HFB these bands are located at 5.32–5.85 eV (≈230–210 nm), i.e., between the $\pi\pi^*$ transitions corresponding to the 1 $^1B_{2u}$ (S_1) and 1 $^1B_{1u}$ (S_2) states in benzene. However, the nature of the bands remained elusive, as charge

transfer processes from fluorine to carbon or to the C-F bonds were identified as possible origins too.[72] Philis et al., who studied the UV absorption of various fluorobenzenes, finally confirmed these bands to be associated with $\pi\sigma^*$ states.[73] Furthermore, they observed a significant loss of structure in the shape of the S_1 ($\pi\pi^*$) absorption bands with increasing number of fluorine atoms (cf. Chapter 3), attributed to the vicinity of the $\pi\sigma^*$ states.

Time-resolved measurements of the S_1 dynamics of highly fluorinated benzenes remained scarce. It was shown that the fluorescence lifetime is substantially decreased to less than 10 ns upon fluorination,[74,75] and that PFB and HFB both exhibit two-component fluorescence decays.[76] In 2005 Zgierski et al. validated these reports and strived to unravel the deactivation mechanism.[77] Their time-dependent density-functional theory (TDDFT) calculations indicated even lower-lying, optically dark $\pi\sigma^*$ states, not observed in previous spectroscopic studies. These states were estimated to be only ≈0.3–0.8 eV above the lowest-lying $\pi\pi^*$ states, and for HFB actually below said state. As a consequence of an additional fluorescence red-shift, the energetic ordering of the excited states for PFB and HFB was proposed to be $\pi\sigma^* < \pi\pi^*$. Furthermore, it was concluded that excitation of the $\pi\pi^*$ state is followed by IC to the $\pi\sigma^*$ state. Interestingly, their calculated excited-state molecular structures exhibited intense out-of-plane deformations. It was briefly noted that the deformation in HFB most likely results from pure electronic effects.[78–80] In contrast, vibronic coupling[81–83] (*vide infra*) was assumed to distort the molecular structures of the other fluorobenzenes.[77]

Shortly afterwards, Kovalenko et al. presented time-resolved transient absorption measurements of 1,2,3,4-TFB, PFB, and HFB after excitation to the lowest-lying $\pi\pi^*$ state in solution and revealed the true beauty of highly fluorinated benzenes.[84] They observed pronounced intensity oscillations with frequencies of 80–105 cm^{-1}. Since no oscillations were present in the energy domain, vibrational quantum beating as the underlying mechanism was dismissed. Rather favored was the theory of oscillating electronic transitions between the presumed near-degenerate $\pi\pi^*$ and $\pi\sigma^*$ states. Femtosecond time-resolved TOF-MS of HFB by Studzinski et al. ultimately ruled out vibrational quantum beating, as the oscillational frequencies of the parent ion yield of HFB were virtually wavelength independent.[85] Moreover, an alternative oscillation origin was proposed. Instead of reoccurring $\pi\pi^*/\pi\sigma^*$ transitions, the initial excitation of the $\pi\pi^*$ state was assumed to result in an ultrafast IC to the lower-lying $\pi\sigma^*$ state, promoted by an out-of-plane mode. The subsequent periodic motion of the respective

wavepacket on the $\pi\sigma^*$ state potential energy hypersurface was thought to alter the ionization probability.

Both models were questioned by equation-of-motion coupled-cluster singles and doubles (EOM-CCSD) calculations of Mondal et al.,[86–88] which placed the $\pi\sigma^*$ states consistently above the $\pi\pi^*$ states, in contrast to the ordering obtained at the TDDFT level of theory. Nevertheless, scans along the totally symmetric vibrational modes indicated rather low-lying conical intersections (CI)[20] between the excited $\pi\pi^*$ and the higher-lying $\pi\sigma^*$ states in highly fluorinated benzenes. Hence, in the accompanying dynamics simulations the $\pi\sigma^*$ states were partially populated after excitation of the $\pi\pi^*$ states. However, neither significant population oscillations nor complete depopulation of the $\pi\pi^*$ state were predicted. Yet, their calculations indicated increasingly strong $\pi\pi^*/\pi\sigma^*$ vibronic coupling (*vide infra*) via out-of-plane vibrational modes. The coupling was identified to increase the density of vibrational states in the $\pi\pi^*$ states and to be responsible for the diffuse absorption bands of the highly fluorinated benzene derivatives.

Origin of the Oscillations in Pentafluorobenzene

In 2016, the S_1 ($\pi\pi^*$) dynamics of PFB were investigated by femtosecond time-resolved TOF-MS for the first time. Hüter et al. observed pronounced parent ion yield oscillations, depicted in Figure 1.2.[89] The oscillation exhibited frequencies of 74–78 cm^{-1}, independent of the chosen excitation wavelength. The oscillatory lifetimes, on the other hand, were found to be wavelength dependent and ranged from

$$\tau_{osc}^{PFB} = 6.5 \text{ ps}$$

at $\lambda_{pump} = 265$ nm to

$$\tau_{osc}^{PFB} = 1.7 \text{ ps}$$

at $\lambda_{pump} = 240$ nm. Furthermore, two underlying exponential decay components were determined with

$$\tau_1^{PFB} = 20\text{–}24 \text{ ps}$$

and

$$\tau_2^{PFB} = 540\text{–}870 \text{ ps}$$

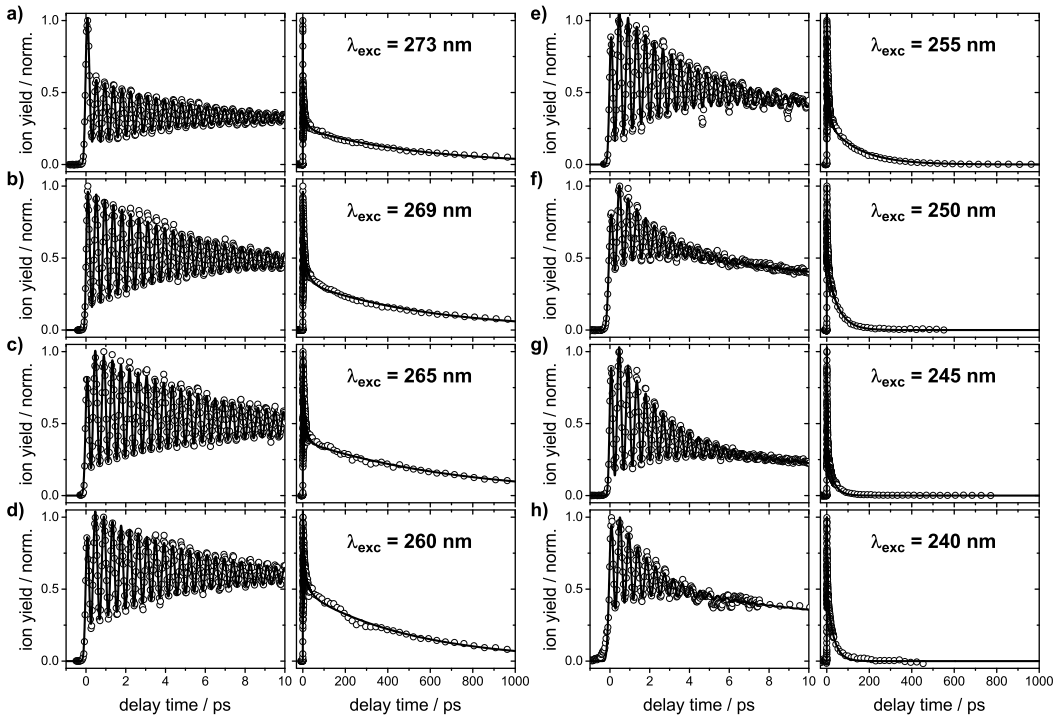

Figure 1.2. Transient parent ion yields (black circles) of PFB after excitation at various wavelengths between $\lambda_{\text{pump}} = 273$–$240$ nm and ionization at $\lambda_{\text{probe}} = 804$ nm. The left-hand column shows the data in the first ten picoseconds, the right-hand column in the first nanosecond after excitation. The black lines represent the employed model fit functions. Reproduced from O. Hüter et al., "Long-lived coherence in pentafluorobenzene as a probe of $\pi\pi^*$ – $\pi\sigma^*$ vibronic coupling", J. Chem. Phys. **145**, 014302 (2016), with the permission of AIP Publishing.

at $\lambda_{\text{pump}} = 273$–$260$ nm. While the latter was assigned to the deactivation to the ground state, the former was attributed to IVR. A substantial decrease of the lifetimes to

$$\tau_1^{\text{PFB}} = 11 \text{ ps}$$

and

$$\tau_2^{\text{PFB}} = 144 \text{ ps}$$

was observed at $\lambda_{\text{pump}} = 255$ nm. It was argued that the shorter excitation wavelength lead to faster deactivation to the ground state by enabling access to a low-lying conical intersection.

In the corresponding photoelectron spectra two main bands emerged, one broad signal α at $E_\alpha = 0.4$ eV and a narrow one β at $E_\beta = 0.8$ eV, initially thought to belong to the $\pi\pi^*$ and the $\pi\sigma^*$ states. As both signals oscillated equally in intensity and phase with respect to the pump–probe delay time and

in agreement with the parent ion yield oscillation, the initial assignment was scrutinized. A careful comparison of the electronic structures of the neutral and ionic states revealed that these two signals actually arise from two different transitions starting at the S_1 state. Signal β was attributed to the $D_0 \leftarrow S_1$ (ionic ground state) and band α to the $D_1 \leftarrow S_1$ (first excited ionic state) transition. Accordingly, the previously suggested mechanisms underlying the oscillations were dismissed and it was concluded that the oscillation originated from dynamics on the S_1 potential energy hypersurface (PEHS).

To elucidate the S_1 dynamics, the potential energy curves (PECs) of several low-lying electronic states were calculated along the normal mode coordinates Q_i of various vibrational modes at the extended multi-configuration quasi-degenerate second-order perturbation theory (XMCQDPT2)[90] level of theory. It was proposed that the molecular configuration of the planar ground state initially is preserved upon photoexcitation onto the S_1 PEHS, in agreement with the Franck–Condon principle. Remarkably, for four out of six b_1 vibrational modes, leaving the Franck–Condon region resulted in stabilization of the potential energy, as the PECs along the normal mode coordinates Q_{20}–Q_{15} of the six b_1 out-of-plane modes in Figure 1.3 show. More precisely, pronounced double-well PECs were calculated for these modes, with the center of symmetry being the quasi-planar structure in the Franck–Condon region. The deformation was assigned to originate from vibronic coupling between the $\pi\pi^*$ and the higher-lying $\pi\sigma^*$ state, i.e., the perturbation of electronic structures mediated by vibrational modes. This phenomenon is also called pseudo-Jahn–Teller effect.[81–83] In contrast to the actual Jahn–Teller effect,[78–80] the vibrations do not lift the degeneracy of a given electronic state, but couple the wave functions of at least two individual electronic states of different symmetry, resulting in the stabilization of the lower-lying and the de-stabilization of the higher-lying state.

The S_1 dynamics were simulated using the multi-configuration time-dependent Hartree method[91,92] with a modified Hamiltonian based on the PECs. Following Köppel et al. and assuming a diabatic basis, i.e., allowing the otherwise forbidden state crossing,[93] the Hamiltonian $\boldsymbol{H}$ in its general form reads

$$\boldsymbol{H} = H_0(\boldsymbol{Q})\mathbf{1} + \boldsymbol{W}(\boldsymbol{Q}) \tag{1.10}$$

with $H_0(\boldsymbol{Q})$ being the ground-state Hamiltonian, depending on the vector $\boldsymbol{Q}$

$$\boldsymbol{Q} = (Q_1, Q_2, \ldots, Q_m) \tag{1.11}$$

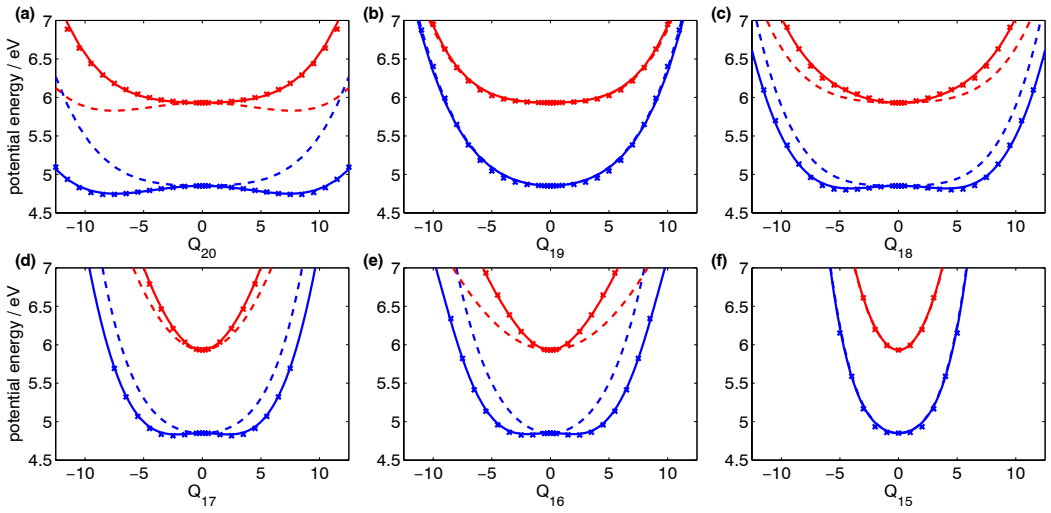

Figure 1.3. **(a–f)** Diabatic (dashed lines) and adiabatic (solid lines) potential energy curves of the S_1 (blue, $\pi\pi^*$, $^1B_2$) and S_2 state (red, $\pi\sigma^*$, $^1A_2$) of PFB along the normal mode coordinates Q_{20}–Q_{15} of the six b_1 out-of-plane vibrational modes. The crosses are single-point energies at XMCQDPT2 level of theory, the lines are the result of the vibronic coupling model (see text for details). Reproduced from O. Hüter et al., "Long-lived coherence in pentafluorobenzene as a probe of $\pi\pi^* - \pi\sigma^*$ vibronic coupling", J. Chem. Phys. **145**, 014302 (2016), with the permission of AIP Publishing.

of the dimensionless vibrational normal mode coordinates Q_x. Moreover, $\mathbf{1}$ and $\boldsymbol{W}(\boldsymbol{Q})$ denote the identity and the potential energy matrix, respectively. The ground-state Hamiltonian may also be expressed by

$$H_0(\boldsymbol{Q}) = \sum_i \frac{\omega_i}{2}\left(\frac{\partial^2}{\partial Q_i^2} + Q_i^2\right). \tag{1.12}$$

Here, ω_i is the frequency of the vibration. The potential energy matrix is a square matrix defined as

$$\boldsymbol{W} = \begin{pmatrix} W_{11} & W_{12} & \cdots & W_{1m} \\ W_{21} & W_{22} & \cdots & W_{2m} \\ \vdots & \vdots & \ddots & \vdots \\ W_{m1} & W_{m2} & \cdots & W_{mm} \end{pmatrix}. \tag{1.13}$$

The diagonal elements are

$$W_{nn}(\boldsymbol{Q}) = E_n + \sum_{i,j>i} \gamma_{ij}^{(n)} Q_i Q_j + \sum_{i,j>i} \sigma_{ij}^{(n)} Q_i^2 Q_j^2, \tag{1.14}$$

and the off-diagonal ones include linear and third-order coupling terms, e.g.,

$$W_{12}(\boldsymbol{Q}) = \sum_i \lambda_i^{(12)} Q_i + \sum_{i,j>i} \eta_{ij}^{(12)} Q_i^2 Q_j. \tag{1.15}$$

E_n is the constant potential energy of a state n at $\boldsymbol{Q} = 0$, the ground-state equilibrium molecular structure. The variables γ_{ij} and σ_{ij} describe *intrastate* coupling constants, whereas λ_i and η_{ij} are *interstate* coupling parameters. The magnitude of these constants determines the extent of the perturbation.[93] Which PECs have to be taken into account is determined by the symmetry of the electronic states and the vibrational modes. As a prerequisite for coupling, the product of the irreducible representations Γ_{Q_i} of the coupling mode and $\Gamma_{n/m}$ of the coupling states must contain the totally symmetric representation Γ_A

$$\Gamma_n \times \Gamma_{Q_i} \times \Gamma_{n/m} \supset \Gamma_A. \tag{1.16}$$

Hence, the intrastate perturbation is mediated only by totally symmetric modes, and interstate coupling between electronic states of different symmetries can involve only non-totally symmetric motion. For the sake of simplicity, just the b_1 modes coupling the $^1B_2$ ($\pi\pi^*$) and $^1A_2$ ($\pi\sigma^*$) states were taken into account, omitting the totally symmetric "tuning modes", which alter the energy difference between the electronic states.[82,93] Two different models were constructed. The so-called 3D model included only the three lowest-frequency b_1 modes, whereas in the 6D model all coupling modes were considered. In both cases the coupling constants were obtained by a least-square fit of the Hamiltonian against the actual calculated energy along the normal mode coordinates.

In the simulation based on the 3D model, population of the $\pi\pi^*$ state by a broadband femtosecond pulse resulted in the excitation of a coherent wavepacket of the three vibrational modes. Shortly after excitation, the wavepacket split in two parts, one leaving the FC region in $+Q$ and one in $-Q$ direction. The departure from the FC region led to a strong coupling of the $\pi\pi^*$ and the $\pi\sigma^*$ states. Therefore, a population flow from the former to the latter was observed, which is identical to a mixing of the $\pi\pi^*/\pi\sigma^*$ characters, depicted in Figure 1.4 (a). The farther the wavepacket was away from the FC region, the higher the $\pi\sigma^*$ fractional contribution. However, the wavepacket motion was found to be highly regular. After leaving the FC region, the wavepacket ultimately hit the outer potential barriers and the motion reversed (cf. Figure 1.4 (b)). Back

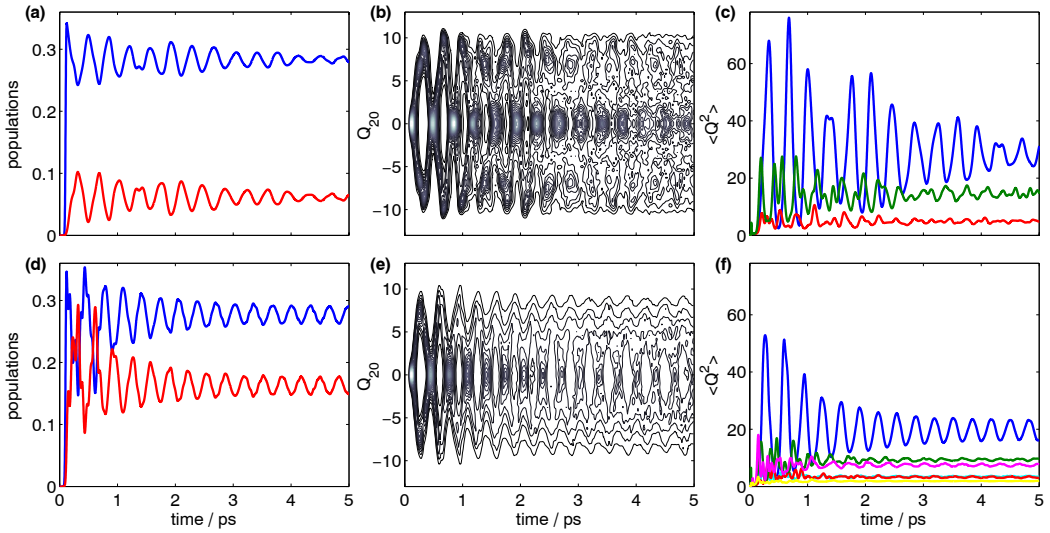

Figure 1.4. Simulated quantum dynamics obtained from the 3D (upper row) and 6D models (lower row) for PFB. **(a), (d)** Populations of the $\pi\pi^*$ (blue) and $\pi\sigma^*$ (red) diabatic electronic states. **(b), (e)** Contour plot of the reduced density of the $\pi\pi^*$ component of the wavepacket along the normal mode coordinate Q_{20}. **(c), (f)** Time-dependent expectation values $\langle Q^2 \rangle$ of the squared position operators of the b_1 modes Q_{20} (blue), Q_{19} (red), Q_{18} (green), Q_{17} (magenta), Q_{16} (cyan), and Q_{15} (yellow). Reproduced from O. Hüter et al., "Long-lived coherence in pentafluorobenzene as a probe of $\pi\pi^* - \pi\sigma^*$ vibronic coupling", J. Chem. Phys. **145**, 014302 (2016), with the permission of AIP Publishing.

in the FC region, the two wavepacket parts recombined and subsequently split again. It was proposed that this periodic motion directly transferred to an oscillation in the electronic character of the S_1 state. Eventually, the wavepacket dephased and so did the population transfer. Although the periodic mixing was found to be dominated by the lowest-frequency b_1 modes (cf. Figure 1.4 (c)), astonishingly the wavepacket motion was stabilized by introducing the remaining three coupling modes in the 6D model, as shown in Figure 1.4 (d–f). Thus, it was concluded that only the coherent excitation of multiple modes allows for a long-lived population oscillation. A full-dimensional model, which will probably describe the population oscillation even better due to the inclusion of all vibrational modes and thus both *intrastate* and *interstate* coupling, is in development.[94]

As the ionic ground state structure of PFB is planar, out-of-plane deformations decrease the Franck–Condon overlap, thereby minimizing the ionization probability. In addition, ionization of the $\pi\pi^*$ and $\pi\sigma^*$ states in PFB is complementary. The electronic structure in the $\pi\pi^*$ state corresponds to both the ionic ground state and the first excited ionic state. An ionic state corresponding to the

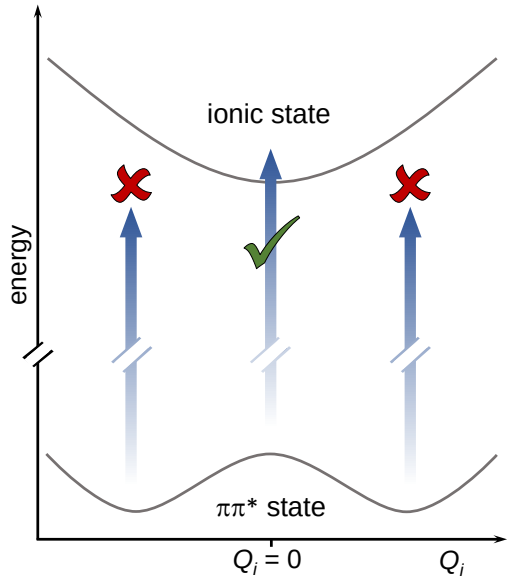

Figure 1.5. Schematic PECs of the $\pi\pi^*$ and an ionic state in PFB with respect to an out-of-plane normal mode coordinate Q_i in the presence of vibronic coupling of the neutral excited states. The coupling induces deformation of the molecular structure that decreases the FC overlap between the formerly pure $\pi\pi^*$ state and the ionic states, lowering the ionization probability. The mixing of the electronic characters decreases the ionization probability further. Ionization by femtosecond laser pulses (arrows) is essentially only possible when the vibronic wavepacket is in the vicinity of the FC region ($Q_i = 0$), resulting in an oscillation of the observable signal.

$\pi\sigma^*$ state, however, was energetically not accessible by the chosen ionization wavelengths. Therefore, the mixing of the electronic character of the states decreases the ionization probability further with rising $\pi\sigma^*$ proportion of the electronic character. Overall, the wavepacket motion periodically changes the ionization probability, as schematically shown in Figure 1.5. Consequently, the regular wavepacket motion was identified to be responsible for the observed signal oscillations. PFB is thus one of the rare molecules in which a wavepacket movement can be directly mapped in the pump–probe signal.

Notwithstanding of the extensive and expensive calculations performed to unravel the origin of the oscillations, optimization of the molecular structure in the S_1 state at RI-SCS-CC2 level of theory also readily gave insights into the coupling mechanism. Rather unsurprisingly, the S_1 equilibrium structure strongly resembles the displacement introduced by the b_1 coupling modes. Mainly the five fluorine atoms are bent out-of-plane. While the fluorine atom positioned at the principle axis of symmetry is bent out-of-plane by 33°, the remaining four fluorine atoms are bent in the opposing direction by 8°, i.e., the motif

of the deformation exhibits b_1 symmetry with respect to the principle axis of symmetry.[89] Calculation of the vibrational frequencies in the S_1 state yielded $\nu = 84$ cm^{-1} for the lowest-energy b_1 mode, fitting well to the observed oscillational frequency of $\nu_{osc} \approx 74$–78 cm^{-1}. Although the RI-SCS-CC2 method approximates harmonic potentials,[95,96] it was confirmed the method is suitable to estimate the order of magnitude ought to be expected for the vibrational frequencies, because the double-well potentials are reasonably harmonic near the minima.[94] Hence, calculations at RI-SCS-CC2 level of theory are the first step in understanding the coupling dynamics.

Scope of this Thesis

In a follow-up study based on their work in the initial publication,[89] Sala and Egorova recently reported on simulated photoelectron spectra.[94] Their simulations indicated oscillations not solely in intensity, but also in photoelectron energy. It was assumed that these oscillations are likely obscured in the experimental results by the underlying multi-photon processes, i.e., population of high-lying intermediate states within the probe pulse duration. Furthermore, they improved the model Hamiltonian and developed an even better model including all vibrational modes for a future publication.

Apart from Ref. [94], it became noticeably quiet in the past years regarding research on the highly fluorinated benzenes. This Thesis is aimed to fill the void. Herein, the well-established tools of time-resolved TOF-MS and corresponding PE spectroscopy were employed to unravel the diverse photodynamics induced by vibronic coupling in highly fluorinated aromatic molecules. Following a short introduction to the experimental setup and calculational methods in Chapter 2, Chapter 3 deals with comparative studies of how the number of fluorine atoms, their positions, and different non-hydrogen substituents in pentafluoro derivatives influence the S_1 dynamics. Moreover, the impact of nitrogen in the aromatic ring on the coupling will be addressed. To this end, results on 1,2,3-trifluorobenzene (1,2,3-TriFB), 1,2,4,5-tetrafluorobenzene (1,2,4,5-TFB), 1,2,3,5-TFB, 1,2,3,4-TFB, pentafluoropyridine (PFPy, published in Ref. [97]), pentafluorotoluene (PFT), pentafluorophenol (PFPh), chloropentafluorobenzene (ClPFB), and bromopentafluorobenzene (BrPFB) are reported and discussed in light of the behavior of PFB.[89] All experimental results are complemented by ab initio calculations of the molecular and electronic structures. In addition, the pump wavelength was varied for the TFB isomers and PFPh to rule out wave-

length dependencies of the observed dynamics. For PFPh, these dependence studies aid the discussion of possible O-H bond fission in Subsection 3.7.4, based on preliminary ab initio estimations. In total, the S_1 ($\pi\pi^*$) dynamics of nine different fluoroaromatic systems were systematically investigated in this work.

References

[1]W. A. Noyes and L. S. Kassel, "A review of photochemistry", Chem. Rev. **3**, 199 (1926).

[2]H. D. Roth, "The beginnings of organic photochemistry", Angew. Chem. Int. Ed. Engl. **28**, 1193 (1989).

[3]H. E. Zimmerman, "Five decades of mechanistic and exploratory organic photochemistry", Pure Appl. Chem. **78**, 2193 (2006).

[4]N. Hoffmann, "Photochemical reactions as key steps in organic synthesis", Chem. Rev. **108**, 1052 (2008).

[5]T. Kumpulainen, B. Lang, A. Rosspeintner, and E. Vauthey, "Ultrafast elementary photochemical processes of organic molecules in liquid solution", Chem. Rev. **117**, 10826 (2017).

[6]Q.-Q. Zhou, Y.-Q. Zou, L.-Q. Lu, and W.-J. Xiao, "Visible-light-induced organic photochemical reactions through energy-transfer pathways", Angew. Chem. Int. Ed. **58**, 1586 (2019).

[7]R. S. Mulliken, "Report on notation for the spectra of polyatomic molecules", J. Chem. Phys. **23**, 1997 (1955).

[8]G. Herzberg, *Electronic Spectra of Polyatomic Molecules* (D. Van Nostrand Inc., 1966), pp. 555–561.

[9]H. Sponer, G. Nordheim, A. L. Sklar, and E. Teller, "Analysis of the near ultraviolet electronic transition of benzene", J. Chem. Phys. **7**, 207 (1939).

[10]F. M. Garforth, C. K. Ingold, and H. G. Poole, "95. Excited states of benzene. Part I. Introductory consideration of some spectral properties of vibrations accompanying electronic transitions of benzene and deuterated benzenes", J. Chem. Soc., 406 (1948).

[11]J. H. Callomom, T. M. Dunn, I. M. Mills, and H. C. Longuet-Higgins, "Rotational analysis of the 2600 Å absorption system of benzene", Phil. Trans. Roy. Soc. (London) **259**, 499 (1966).

[12]C. S. Parmenter, "Radiative and nonradiative processes in benzene", in *Adv. Chem. Phys.* Edited by I. Prigogine and S. A. Rice, 22nd ed. (John Wiley & Sons, Inc., New York, 1972), pp. 365–421.

[13]E. M. Anderson and G. B. Kistiakowsky, "Fluorescence and intersystem crossing of benzene-h_6, -d_6, and -1,4-d_2", J. Chem. Phys. **51**, 182 (1969).

[14]W. A. Noyes and D. A. Harter, "Energy balance in the photochemistry of benzene", J. Chem. Phys. **46**, 674 (1967).

[15]J. A. Poole, "The fluorescence of benzene and benzene-d_6", J. Phys. Chem. **69**, 1343 (1965).

[16]W. A. Noyes, W. A. Mulac, and D. A. Harter, "Some aspects of the photochemistry of benzene", J. Chem. Phys. **44**, 2100 (1966).

[17]H. Shull, "Vibrational analysis of the 3400A triplet-singlet emission of benzene", J. Chem. Phys. **17**, 295 (1949).

[18]R. B. Cundall and T. F. Palmer, "The photosensitized isomerization of butene-2", Trans. Faraday Soc. **56**, 1211 (1960).

[19]J. H. Callomon, J. E. Parkin, and R. Lopez-Delgado, "Non-radiative relaxation of the excited $\widetilde{A}^1B_{2u}$ state of benzene", Chem. Phys. Lett. **13**, 125 (1972).

[20]A. L. Sobolewski, C. Woywod, and W. Domcke, "*Ab initio* investigation of potential-energy surfaces involved in the photophysics of benzene and pyrazine", J. Chem. Phys. **98**, 5627 (1993).

[21]I. J. Palmer, I. N. Ragazos, F. Bernardi, M. Olivucci, and M. A. Robb, "An MC-SCF study of the S_1 and S_2 photochemical reactions of benzene", J. Am. Chem. Soc. **115**, 673 (1993).

[22]A. H. Zewail, "Femtochemistry: Atomic-scale dynamics of the chemical bond using ultrafast lasers (Nobel lecture)", Angew. Chem. Int. Ed. **39**, 2586 (2000).

[23]A. H. Zewail, "Femtochemistry: Atomic-scale dynamics of the chemical bond", J. Phys. Chem. A **104**, 5660 (2000).

[24]J. M. Hollas, *Modern Spectroscopy*, 4th ed. (John Wiley & Sons, Ltd., Chichester, 2004).

[25]J. Franck and E. G. Dymond, "Elementary processes of photochemical reactions", Trans. Faraday Soc. **21**, 536 (1926).

[26]E. U. Condon, "Nuclear motions associated with electron transitions in diatomic molecules", Phys. Rev. **32**, 858 (1928).

[27]M. Born and R. Oppenheimer, "Zur Quantentheorie der Molekeln", Ann. Phys. **389**, 457 (1927).

[28]S. T. Pratt, "Excited-state molecular photoionization dynamics", Rep. Prog. Phys. **58**, 821 (1995).

[29]T. Koopmans, "Über die Zuordnung von Wellenfunktionen und Eigenwerten zu den einzelnen Elektronen eines Atoms", Physica **1**, 104 (1934).

[30]V. Blanchet, S. Lochbrunner, M. Schmitt, J. P. Shaffer, J. J. Larsen, M. Z. Zgierski, T. Seideman, and A. Stolow, "Towards disentangling coupled electronic–vibrational dynamics in ultrafast non-adiabatic processes", Faraday Discuss. **115**, 33 (2000).

[31]V. Blanchet, M. Z. Zgierski, and A. Stolow, "Electronic continua in time-resolved photoelectron spectroscopy. I. Complementary ionization correlations", J. Chem. Phys. **114**, 1194 (2001).

[32]M. Schmitt, S. Lochbrunner, J. P. Shaffer, J. J. Larsen, M. Z. Zgierski, and A. Stolow, "Electronic continua in time-resolved photoelectron spectroscopy. II. Corresponding ionization correlations", J. Chem. Phys. **114**, 1206 (2001).

[33]D. M. Neumark, "Time-resolved photoelectron spectroscopy of molecules and clusters", Annu. Rev. Phys. Chem. **52**, 255 (2001).

[34]D. W. Chandler, A. I. Chichinin, T. S. Einfeld, A. T. J. B. Eppink, K.-H. Gericke, O. Heber, H. Helm, P. L. Houston, T. N. Kitsopoulos, K. T. Lorenz, C. Maul, U. Müller, D. H. Parker, T. P. Rakitzis, J. L. Springfield, D. Strasser, T. Suzuki, E. A. Wade, B. J. Whitaker, S.-M. Wu, and D. Zajfman, *Imaging in Molecular Dynamics: Technology and Applications*, edited by B. J. Whitaker (Cambridge University Press, Cambridge, 2003).

[35]A. Stolow, A. E. Bragg, and D. M. Neumark, "Femtosecond time-resolved photoelectron spectroscopy", Chem. Rev. **104**, 1719 (2004).

[36]T. Suzuki, "Femtosecond time-resolved photoelectron imaging", Annu. Rev. Phys. Chem. **57**, 555 (2006).

[37]J. M. Smith, X. Zhang, and J. L. Knee, "Intramolecular relaxation of S_1 benzene studied with picosecond photoionization and photoelectron spectroscopy", J. Phys. Chem. **99**, 1768 (1995).

[38]W. Radloff, T. Freudenberg, H.-H. Ritze, V. Stert, F. Noack, and I. Hertel, "Lifetime of the benzene dimer in the S_2 electronic state", Chem. Phys. Lett. **261**, 301 (1996).

[39]W. Radloff, V. Stert, T. Freudenberg, I. V. Hertel, C. Jouvet, C. Dedonder-Lardeux, and D. Solgadi, "Internal conversion in highly excited benzene and benzene dimer: femtosecond time-resolved photoelectron spectroscopy", Chem. Phys. Lett. **281**, 20 (1997).

[40]G. A. Worth, R. E. Carley, and H. H. Fielding, "Using photoelectron spectroscopy to unravel the excited-state dynamics of benzene", Chem. Phys. **338**, 220 (2007).

[41]D. S. N. Parker, R. S. Minns, T. J. Penfold, G. A. Worth, and H. H. Fielding, "Ultrafast dynamics of the S_1 excited state of benzene", Chem. Phys. Lett. **469**, 43 (2009).

[42]R. S. Minns, D. S. N. Parker, T. J. Penfold, G. A. Worth, and H. H. Fielding, "Competing ultrafast intersystem crossing and internal conversion in the 'channel 3' region of benzene", Phys. Chem. Chem. Phys. **12**, 15607 (2010).

[43]Y.-I. Suzuki, T. Horio, T. Fuji, and T. Suzuki, "Time-resolved photoelectron imaging of $S_2 \rightarrow S_1$ internal conversion in benzene and toluene", J. Chem. Phys. **134**, 184313 (2011).

[44]G. Féraud, T. Pino, C. Falvo, P. Parneix, T. Combriat, and P. Bréchignac, "Intramolecular processes revealed using UV-laser-induced IR-fluorescence: a new perspective on the 'channel three' of benzene", J. Phys. Chem. Lett. **5**, 1083 (2014).

[45]T. J. Penfold, R. Spesyvtsev, O. M. Kirkby, R. S. Minns, D. S. N. Parker, H. H. Fielding, and G. A. Worth, "Quantum dynamics study of the competing ultrafast intersystem crossing and internal conversion in the 'channel 3' region of benzene", J. Chem. Phys. **137**, 204310 (2012).

[46]K. C. Woo and S. K. Kim, "Real-time observation of fermi resonances in the S_1 state of phenol", J. Phys. Chem. Lett. **11**, 161 (2020).

[47]E. B. Wilson, "The normal modes and frequencies of vibration of the regular plane hexagon model of the benzene molecule", Phys. Rev. **45**, 706 (1934).

[48]S. Haroche, "Quantum beats and time-resolved fluorescence spectroscopy", in *High-Resolution Laser Spectroscopy*, edited by K. Shimoda (Springer Berlin Heidelberg, Berlin, Heidelberg, 1976), pp. 253–313.

[49]E. Hack and J. R. Huber, "Quantum beat spectroscopy of molecules", Int. Rev. Phys. Chem. **10**, 287 (1991).

[50]W. Demtröder, *Laserspektroskopie*, 5th ed. (Springer-Verlag Berlin Heidelberg, Berlin, 2007), pp. 501–506.

[51]J. D. Young, M. Staniforth, J. C. Dean, G. M. Roberts, F. Mazzoni, T. N. Karsili, M. N. Ashfold, T. S. Zwier, and V. G. Stavros, "Towards understanding photodegradation pathways in lignins: the role of intramolecular hydrogen bonding in excited states", J. Phys. Chem. Lett. **5**, 2138 (2014).

[52]J. D. Young, M. Staniforth, M. J. Paterson, and V. G. Stavros, "Torsional motion of the chromophore catechol following the absorption of ultraviolet light", Phys. Rev. Lett. **114**, 233001 (2015).

[53]F. Ling, S. Li, X. Song, Y. Wang, J. Long, and B. Zhang, "Femtosecond time-resolved observation of butterfly vibration in electronically excited *o*-fluorophenol", Sci. Rep. **7**, 15362 (2017).

[54]F. Ling, S. Li, X. Song, Y. Tang, Y. Wang, and B. Zhang, "Visualization of coherent nuclear motion between different geometries in photoexcited 2,4-difluorophenol", Phys. Rev. A **95**, 043421 (2017).

[55]T. Fuji, Y.-I. Suzuki, T. Horio, and T. Suzuki, "Excited-state dynamics of CS_2 studied by photoelectron imaging with a time resolution of 22 fs", Chem. Asian J. **6**, 3028 (2011).

[56]R. Spesyvtsev, T. Horio, Y.-I. Suzuki, and T. Suzuki, "Observation of the wavepacket dynamics on the $^1B_2(^1\Sigma_u^+)$ state of CS_2 by sub-20 fs photoelectron imaging using 159 nm probe pulses", J. Chem. Phys. **142**, 074308 (2015).

[57]S. Li, J. Long, F. Ling, Y. Wang, X. Song, S. Zhang, and B. Zhang, "Real-time visualization of the vibrational wavepacket dynamics in electronically excited pyrimidine via femtosecond time-resolved photoelectron imaging", J. Chem. Phys. **147**, 044309 (2017).

[58]F. Ling, S. Li, Y. Wang, P. Wang, and B. Zhang, "Vibrational coherence in the composition-selected wavepacket of photoexcited pyrimidine", J. Chem. Phys. **150**, 044308 (2019).

[59]F. Ling, Y. Wang, S. Li, J. Wei, Y. Tang, and B. Zhang, "Imaging reversible and irreversible structural evolution in photoexcited 2,4-difluoroaniline", J. Phys. Chem. Lett. **9**, 5468 (2018).

[60]J. A. Davies and K. L. Reid, "Elucidating quantum number-dependent coupling matrix elements using picosecond time-resolved photoelectron spectroscopy", Phys. Rev. Lett. **109**, 193004 (2012).

[61]J. Midgley, J. A. Davies, and K. L. Reid, "Complex and sustained quantum beating patterns in a classic IVR system: the $3^1 5^1$ level in S_1 *p*-difluorobenzene", J. Phys. Chem. Lett. **5**, 2484 (2014).

[62]C. R. Brundle, M. B. Robin, N. A. Kuebler, and H. Basch, "Perfluoro effect in photoelectron spectroscopy. I. Nonaromatic molecules", J. Am. Chem. Soc. **94**, 1451 (1972).

[63]C. R. Brundle, M. B. Robin, and N. A. Kuebler, "Perfluoro effect in photoelectron spectroscopy. II. Aromatic molecules", J. Am. Chem. Soc. **94**, 1466 (1972).

[64]A. P. Hitchcock, P. Fischer, A. Gedanken, and M. B. Robin, "Antibonding σ^* valence MOs in the inner-shell and outer-shell spectra of the fluorobenzenes", J. Phys. Chem., 531.

[65]H.-P. Fenzlaff and E. Illenberger, "Low energy electron impact on benzene and the fluorobenzenes. Formation and dissociation of negative ions", Intern. J. Mass Spectrom. Ion Processes **59**, 185 (1984).

[66]J. Milhaud, "Dissociate electron attachment to monohalogenated benzenes", Chem. Phys. Lett. **118**, 167 (1985).

[67]J. R. Frazier, L. G. Christophorou, J. G. Carter, and H. C. Schweinler, "Low-energy electron interactions with organic molecules: Negative ion states of fluorobenzenes", J. Chem. Phys. **69**, 3807 (1978).

[68]B. C. Trudell and S. J. W. Price, "The ultraviolet photoelectron spectra of C_6F_5X compounds, X = (F, Cl, Br, I, H, CH_3)", Can. J. Chem. **57**, 2256 (1979).

[69]C. Motch, A. Giuliani, J. Delwiche, P. Limão-Vieira, N. J. Mason, S. V. Hoffmann, and M.-J. Hubin-Franskin, "Electronic structure of hexafluorobenzene by high-resolution vacuum ultraviolet photo-absorption and He(I) photoelectron spectroscopy", Chem. Phys. **328**, 183 (2006).

[70]P. Decleva, M. Stener, D. M. P. Holland, A. W. Potts, and L. Karlsson, "Perfluoro effects in the occupied and virtual valence orbitals of hexafluorobenzene", J. Phys. B: At. Mol. Phys. **40**, 2939 (2007).

[71]D. M. Holland, D. A. Shaw, M. Stener, and P. Decleva, "A study of the valence shell electronic structure of hexafluorobenzene using photoabsorption and photoelectron spectroscopy, and TDDFT calculations", J. Phys. B: At. Mol. Phys. **42**, 245201 (2009).

[72]R. P. Frueholz, W. M. Flicker, O. A. Mosher, and A. Kuppermann, "Electronic spectroscopy of benzene and the fluorobenzenes by variable angle electron impact", J. Chem. Phys. **70**, 3057 (1979).

[73]J. Philis, A. Bolovinos, G. Andritsopoulos, E. Pantos, and P. Tsekeris, "A comparison of the absorption spectra of the fluorobenzenes and benzene in the region 4.5-9.5 eV", J. Phys. B: At. Mol. Phys. **14**, 3621 (1981).

[74]G. L. Loper and E. K. C. Lee, "Fluorescence decay and radiative lifetimes of fluorinated aromatic molecules", Chem. Phys. Lett. **13**, 140 (1972).

[75]G. M. Breuer and E. K. C. Lee, "Fluorescence decay times and non-radiative decay rates of the first excited singlet states of methylated and fluorinated benzenes", Chem. Phys. Lett. **14**, 404 (1972).

[76]D. V. O'Connor, M. Sumitani, J. M. Morris, and K. Yoshihara, "Non-exponential picosecond fluorescence decay in isolated pentafluorobenzene and hexafluorobenzene", Chem. Phys. Lett. **93**, 350 (1982).

[77]M. Z. Zgierski, T. Fujiwara, and E. C. Lim, "Photophysics of aromatic molecules with low-lying $\pi\sigma^*$ states: Fluorinated benzenes", J. Chem. Phys. **122**, 144312 (2005).

[78]H. A. Jahn, E. Teller, and F. G. Donnan, "Stability of polyatomic molecules in degenerate electronic states - I—Orbital degeneracy", Proc. R. Soc. London, A **161**, 220 (1937).

[79]T. J. Sears, T. A. Miller, and V. E. Bondybey, "The Jahn–Teller effect in $C_6F_6^+$", J. Chem. Phys. **74**, 3240 (1981).

[80]K. Raghavachari, R. C. Haddon, T. A. Miller, and V. E. Bondybey, "Theoretical study of Jahn–Teller distortions in $C_6H_6^+$ and $C_6F_6^+$", J. Chem. Phys. **79**, 1387 (1983).

[81]G. Fischer, *Vibronic Coupling: The Interaction between the Electronic and Nuclear Motions* (Academic Press, London, 1984).

[82]I. B. Bersuker, "Pseudo-Jahn–Teller effect—A two-state paradigm in formation, deformation, and transformation of molecular systems and solids", Chem. Rev. **113**, 1351 (2013).

[83]M. Sala, *Quantum Dynamics and Laser Control for Photochemistry* (Springer International Publishing Switzerland, Cham, 2016).

[84]S. A. Kovalenko, A. L. Dobryakov, and V. Farztdinov, "Detecting electronic coherence in excited-state electron transfer in fluorinated benzenes", Phys. Rev. Lett. **96**, 068301 (2006).

[85]H. Studzinski, S. Zhang, Y. Wang, and F. Temps, "Ultrafast nonradiative dynamics in electronically excited hexafluorobenzene by femtosecond time-resolved mass spectrometry", J. Chem. Phys. **128**, 164314 (2008).

[86]T. Mondal and S. Mahapatra, "Photophysics of fluorinated benzene. I. Quantum chemistry", J. Chem. Phys. **133**, 084304 (2010).

[87]T. Mondal and S. Mahapatra, "Photophysics of fluorinated benzene. II. Quantum dynamics", J. Chem. Phys. **133**, 084305 (2010).

[88]T. Mondal, S. R. Reddy, and S. Mahapatra, "Photophysics of fluorinated benzene. III. Hexafluorobenzene", J. Chem. Phys. **137**, 054311 (2012).

[89]O. Hüter, M. Sala, H. Neumann, S. Zhang, H. Studzinski, D. Egorova, and F. Temps, "Long-lived coherence in pentafluorobenzene as a probe of $\pi\pi^*$ – $\pi\sigma^*$ vibronic coupling", J. Chem. Phys. **145**, 014302 (2016).

[90]A. A. Granovsky, "Extended multi-configuration quasi-degenerate perturbation theory: The new approach to multi-state multi-reference perturbation theory", J. Chem. Phys. **134**, 214113 (2011).

[91]H.-D. Meyer, U. Manthe, and L. S. Cederbaum, "The multi-configurational time-dependent Hartree approach", Chem. Phys. Lett. **165**, 73 (1990).

[92]M. H. Beck, A. Jäckle, G. A. Worth, and H.-D. Meyer, "The multiconfiguration time-dependent Hartree (MCTDH) method: a highly efficient algorithm for propagating wavepackets", Phys. Rep. **324**, 1 (2000).

[93]H. Köppel, W. Domcke, and L. S. Cederbaum, "Multimode molecular dynamics beyond the Born-Oppenheimer approximation", in *Adv. Chem. Phys.* Edited by I. Prigogine and S. A. Rice, 57th ed. (John Wiley & Sons, Inc., New York), pp. 59–246.

[94]M. Sala and D. Egorova, "Imaging large amplitude out-of-plane motion in photoexcited pentafluorobenzene using time-resolved photoelectron spectroscopy: a computational study", Photochem. Photobiol. Sci. **17**, 1036 (2018).

[95]C. Hättig, "Geometry optimizations with the coupled-cluster model CC2 using the resolution-of-the-identity approximation", J. Chem. Phys. **118**, 7751 (2003).

[96]A. Köhn and C. Hättig, "Analytic gradients for excited states in the coupled-cluster model CC2 employing the resolution-of-the-identity approximation", J. Chem. Phys. **119**, 5021 (2003).

[97]J. A. Kus, O. Hüter, and F. Temps, "Real-time observation of multi-mode vibronic coherence in pentafluoropyridine", J. Chem. Phys. **147**, 013938 (2017).

Methods

2

2.1 Experimental Setup

The principles of femtosecond laser pulse generation have been outlined in depth in the literature,[1–4] as well as in previous Theses written in this group,[5–8] and thus will not be discussed here. Likewise, comprehensive descriptions of the underlying concepts of time-of-flight mass spectrometry and velocity map imaging of electrons can be found in previous Theses[6,9,10] and will be omitted for the sake of brevity.

2.1.1 Pump and Probe Pulse Generation

The experimental setup in the present work employed a regenerative amplified Ti:Sa femtosecond laser system (Coherent Libra-HE) with a repetition rate of 1 kHz. The pulses were centered at 800 nm with a temporal full width at half maximum of 90 fs. For the work described in Section 3.5), the fundamental wavelength was centered at 804 nm. The output of the laser system (3.7 mJ per pulse) was split twice to carry out other experiments simultaneously. The remaining pulse (1.7 mJ per pulse) available for the work in this Thesis was split again for the generation of the pump (0.7 mJ per pulse) and probe pulses (1.0 mJ per pulse). The optical setup is schematically depicted in Figure 2.1.

For the pump pulses, parts of a chirped white-light continuum were mixed with the frequency-doubled fundamental in a non-collinear optical parametric amplifier (NOPA). The NOPA output ranged between 480–560 nm with pulse energies of 7–25 μJ. The pulses were compressed with a prism compressor to a pulse duration of 20–40 fs. After subsequent frequency doubling, the pulses at $\lambda_{\text{pump}} = 240$–$275$ nm (0.3–1.0 μJ per pulse) were focused into the vacuum chamber with a curved mirror of 50 cm focal length. If necessary, the intensity of the pump pulses was attenuated by a neutral density gradient filter after the prism compressor. Pump pulses at wavelengths ≤240 nm (0.1–0.7 μJ per pulse) were generated by sum-frequency mixing of the compressed NOPA pulses

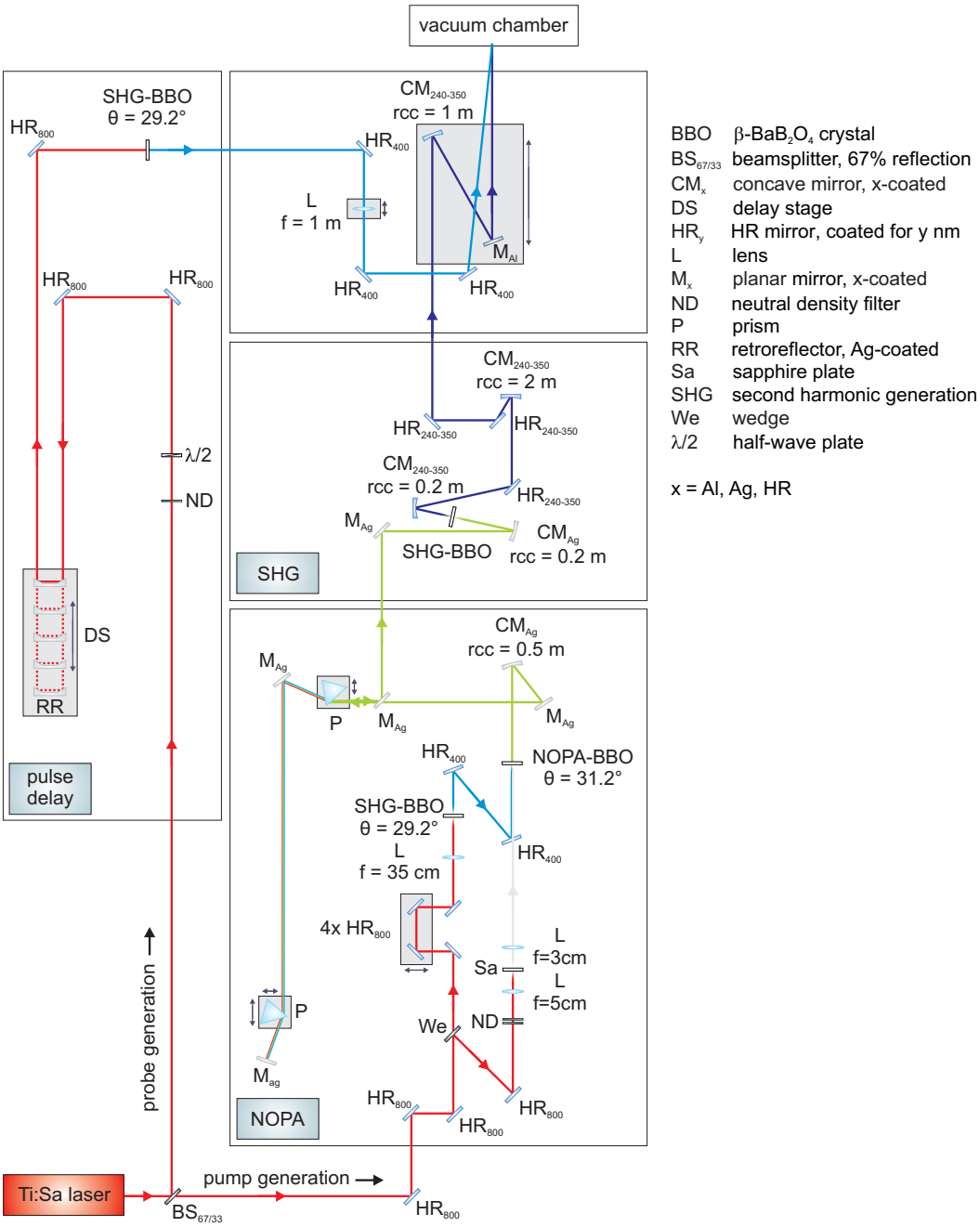

Figure 2.1. Schematic sketch of the optical setup for the pump and probe pulse generation employed in the femtosecond time-resolved mass spectrometry and photoelectron spectroscopy experiments for pump wavelengths >240 nm and probing at 400 nm. For pump wavelengths ≤240 nm, the compressed NOPA output was mixed with the frequency doubled fundamental partitioned off the probe beam. Probing at 800 nm required removal the SHG crystal and replacement of the mirrors.

with the frequency-doubled fundamental. Regardless of the wavelength, the polarization was set to be parallel to the detector surface (||-polarization).

The excited molecules were probed either at the fundamental or its second harmonic wavelength. In both cases, the fundamental was time delayed by using a retroreflector mounted on a computer-controlled linear translation stage (Physik Instrumente M-521.DG). Afterwards, the beam was focused into the vacuum chamber by a lens of 100 cm focal length, or frequency doubling was employed prior to focusing. For the imaging experiments, solely $\lambda_{\text{probe}} = 400$ nm was used as the probe wavelength to reduce excitation of intermediate states. As for the pump pulses, the polarization at either wavelength was set fixed to parallel polarization unless noted otherwise.

2.1.2 Signal Generation and Data Analysis

The setup of the home-built time-of-flight mass spectrometer and photoelectron imaging detection unit was described in H. Studzinski's Thesis.[6] O. Hüter's rather extensive improvements were comprehensively summarized in his Thesis.[10]

Molecular Beam

In short, the molecular samples were kept in a reservoir outside of the two-chambered stainless steel vacuum apparatus. Seeded in helium carrier gas at 2 bar backing pressure, the molecules entered the first chamber through a pulsed valve (100 Hz), generating a supersonic molecular beam. Either a Parker Series 9 pulsed valve, or a Gyger micro valve type SMLD-300G V (0.45 mm orifice diameter) was used. The implementation of the Gyger valve is discussed separately (*vide infra*). In case of pentafluorophenol, the valve and the preceding in-line sample reservoir were heated[9,11] to 40 °C. A Pfeiffer Vacuum TMU 521 turbomolecular pump kept the pressure in the valve chamber below 1×10^{-5} mbar, regardless of the valve employed. The molecular beam entered the second chamber through a conical skimmer (Beam Dynamics Model I, 0.5 mm orifice diameter). In the second chamber, a Pfeiffer Vacuum TMH 261 turbomolecular pump achieved operating pressures of 2×10^{-7} mbar.

The molecular beam was crossed by the co-propagating laser pulses between the repeller and extractor of a Wiley–McLaren electrode assembly,[12] modified as proposed by Eppink and Parker.[13] The generated cations were accelerated towards the detector by applying voltages of 2000 V and 1720 V to the repeller and extractor plates, respectively. The accelerated cations hit a pair of Hamamatsu (F4294-07) multi-channel plates (MCPs) in chevron configuration, joint by an intermediate voltage connector.[6,10] A total voltage of −2000 V was applied to the configuration, of which −1900 V was distributed towards the beam-facing MCP, −1000 V to the connector, and −180 V to the detector facing MCPs. The impingement of the cations on the MCPs created a cascade of electrons, which subsequently stroke a stainless steel anode serving as the actual detector, connected to a Stanford Research SR445 amplifier. The 25 times amplified signal was transferred to an oscilloscope (Rhode & Schwartz RTO 1002, 600 MHz, 10 GSa/s), and digitized in the selected temporal window of the complete time-of-flight mass spectrum. Typically, the signal of 100–500 laser shots was accumulated and averaged before the data was transferred to a LabView routine which controlled the delay steps as well as integrated and stored the signals (see O. Hüter's Thesis for details).[10] For the subsequent analysis, the information of at least 500 individual shots was averaged. The data points (integrated signal intensities) at defined delay steps were fitted by exponential decay functions

$$F_i(t) = A_i \times e^{-t/\tau_i}, \tag{2.1}$$

and/or damped cosine functions

$$C_i(t) = A_i \times \cos(\omega_i t + \phi_i) e^{-t/\tau_i}, \tag{2.2}$$

convoluted with a Gaussian instrument response function

$$G(t) = \frac{1}{\sqrt{2\pi}\sigma_{\mathrm{IRF}}} \exp\left(-\frac{t-t_0}{2\sigma_{\mathrm{IRF}}}\right)^2, \tag{2.3}$$

$$S(t) = G(t) \otimes \left(\sum_i F_i(t) + \sum_j C_j(t)\right), \tag{2.4}$$

using the Levenberg-Marquard algorithm implemented in Wolfram Mathematica 11.[14] Here, τ_i are the respective decay time constants, A_i the corresponding

amplitudes, ω_i the oscillational frequency, ϕ_i the phase, and σ_{IRF} the standard deviation of the Gaussian IRF. For 1,2,4,5-TFB in Section 3.2 an additional rise component

$$R_i(t) = A_i \times (e^{-t/\tau_i} - e^{-t/\tau_{\mathrm{rise}}}) \tag{2.5}$$

needed to be introduced. For the sake of consistency, index i of the decay time components is increases with increasing decay time and was chosen such that all τ_i are in the same order of magnitude, e.g., all ultrashort constants below ≈0.5 ps are labeled by $i = 1$. Thus, for some molecules the numbering of decay constants may not be continuously.

Photoelectron Imaging Spectroscopy

In case of the photoelectrons, the acceleration of the electrons was realized by applying −4000 V/−2930 V to repeller/extractor. To center the photoelectrons on the detector, a voltage of −40 V was applied to a pair of stainless steel plates mounted perpendicular to the electrode assembly.[11] Two different MCP/detector assemblies were used for the detection of the photoelectrons. For the work in Section 3.5, Photonis MCPs (MCP 40/12/10/8 I 60:1 MP, MS), backed by a Burle Electro-Optics (Model 3025FM) detector, were used.[6,10] The detector was a fiber-optical vacuum window coated by a P43 phosphorescence layer, in turn coated by a thin aluminum layer, to which a voltage of 4500 V was applied. The beam-facing MCP was grounded to ensure field-free conditions. At the detector-facing MCP a voltage of 1700 V was applied, gated by a fast transistor switch (Behlke HTS 31-03-GSM) to minimize mapping of stray electrons. Due to degradation of the previous one, for all other experiments except for the work in Section 3.5 a new detector MCP-45-2-40-P43-CF100 (GIDS-GmbH) was used. In contrast to the Burle detector, the P43 phosphor is not attached to the window, hence is replaceable. A lower MCP voltage of 1400 V was employed, whereas 4500 V was kept for the screen.

The position-sensitive phosphorescence induced by the photoelectrons was imaged by a pco.1600 CCD camera (1600×1200 pixel, PCO AG). The PEs of two separate laser shots were accumulated before the data was transferred to the connected computer. In total, at least 50 000 individual images were summarized and stored at each pump–probe delay step. Afterwards these images were centered and symmetrized by another LabView routine written by O. Hüter.[10] The post-processed images were inverted using the pBasex program, yielding

raw photoelectron spectra, i.e., the photoelectron intensity with respect to the detector pixel.[15]

The analysis required an energy calibration of the detector. For this, xenon atoms were ionized above threshold by either four or five probe photons at 400 nm, resulting in two transitions to the $^2P_{2/3}$ ionic ground state and one to the $^2P_{1/2}$ excited ionic state. The positions of the corresponding three signals were fitted to obtain the calibration curve connecting the detector pixels to the photoelectron energy.[10,16] Axis conversion of the raw molecular PE spectra aided by the calibration curve in combination with a Jacobian transform, correcting the intensity,[17] yielded the actual PE spectra. However, this transformation strongly enhances signals near $E_{\mathrm{el}} = 0$ eV, hampering distinction of low-energy signals. If necessary to disentangle specific signals, also the non-Jacobian transformed PES are presented. Finally, the spectra were normalized and referenced to the spectrum at $\Delta t = t_0$, the temporal overlap of the pump and probe pulses.

The least number of photons needed to ionize any molecule in the two-color process are $m = 1$ pump and $n' = 2$ probe photons. Depending on the frequencies ω_{x} of the absorbed photons and the ionization energy IE_{i} of the molecule, this $1+2'$ process yields photoelectrons with a maximum available kinetic energy of

$$E_{\mathrm{avl}}^{m+n'} = \hbar \times (\omega_{\mathrm{pump}} \times m + \omega_{\mathrm{probe}} \times n') - IE_{\mathrm{i}} \tag{2.6}$$

at $\Delta t = t_0$. Electrons with energies above $E_{\mathrm{avl}}^{1+2'}$ indicate the absorption of more photons and will thus be treated as background. In the photoelectron spectra, $E_{\mathrm{avl}}^{1+2'}$ is marked to distinguish the actual signal and background. Furthermore, the transient ion yields are given in a panel on top of the transient PES. Arrows in color of the individual spectra indicate the delay time at which the PES were obtained.

Moreover, for some molecules the ionization energy is low enough to enable ionization by absorption of $m = 2$ pump photons. Absorption of $n' = 4$ probe photons also suffices to ionize any molecule in the ground state. Noteworthy, the single-color (SC) ionization processes require substantially increased pulse intensities compared to the time-resolved $1+2'$ ionization. To avoid background signals, the pulse energies of the pump and probe pulses were kept as low as possible in the time-resolved PES and were vastly increased to obtain the SC PES.

For the sake of brevity, only a selection of photoelectron images are presented in the following Chapter, except for the results of PFPy. The remaining images

can be found in the overview in Chapter C in the appendix. The grey numbers in the lower right corners of the PEI give the total number of generated electrons.

Gyger Valve

In this work the Gyger micro valve type SMLD-300G V was tested as a novel valve. This prototype valve works in principle similar to the Parker Series 9 valve. An electromagnet pulls back a pin for a given time, opening the valve. After switching the holding voltage off, the pin is pushed back by a spring, sealing the valve. However, the sealing concepts of the two valves differ. While the Parker valve uses a soft material at the tip of the pin, the tip of the Gyger pin is made of ruby. This ruby sphere is pushed onto the semi-soft material Torlon.

The valve is controlled by the Gyger VC Mini controller, which allows for operation in three different modes. In the first mode, the trigger, switching the electromagnet on, and the hold time, i.e., the time the electromagnet is switched on, can be solely software-controlled. In the second mode, an external trigger signal may be provided, while the subsequent holding time is again determined by the software settings. In this Thesis, a third option was used. A precisely timed square-wave signal generated in a delay generator (Stanford Research DG645, controlling also all other timings mentioned herein) was forwarded to the VC Mini. The valve was only opened for the duration of the signal, typically between 60–80 μs, identical to the trigger signal for the Parker valve. Thus, the complete trigger-and-hold timings were set fixed externally. Since the delay generator voltage output of 5 V was insufficient to match the input voltage of 12–24 V needed to trigger the VC Mini, the signal was amplified to 20 V by a home-built amplifier.

As shown exemplary in Figure 2.2, the two different valve types yield virtually identical signals. However, in contrast to the Parker valve, the Gyger valve features no maintainable parts, eliminating the delicate adjustments needed for the former. After well over 500 hours of operation yet no wear effects were noticeable. Therefore, the Gyger valve is easier in use, while simultaneously yielding signals of identical quality compared to the Parker valve.

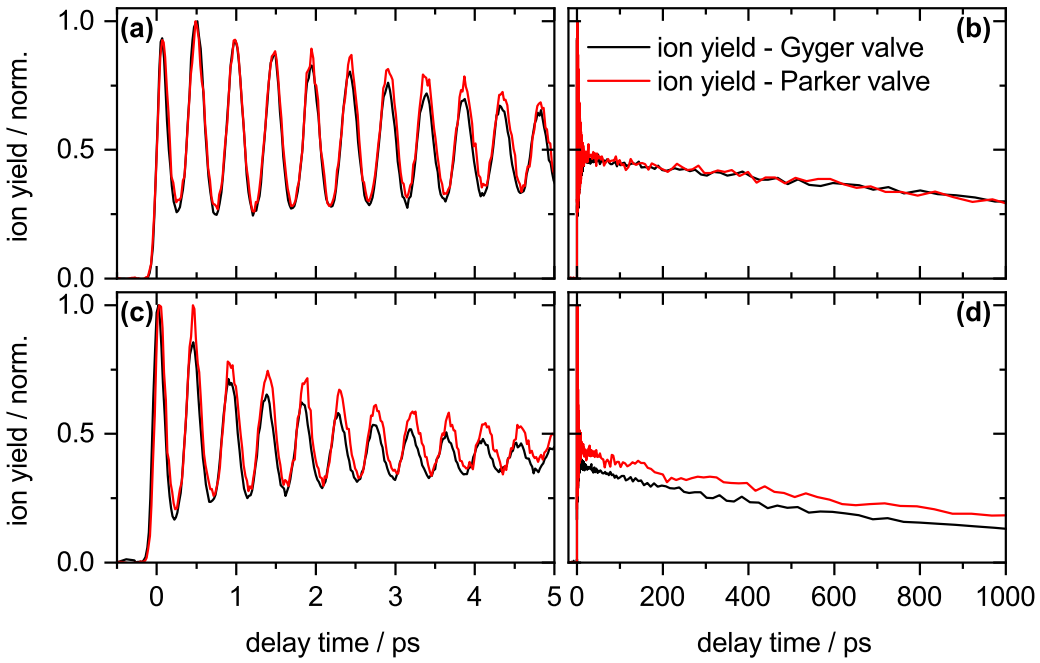

Figure 2.2. Ion yields of **(a–b)** 1,2,3,4-TFB and **(c–d)** PFT after excitation at $\lambda_{pump} = 260$ nm and ionization at $\lambda_{probe} = 400$ nm using the Gyger (black) and the Parker valve (red). The signals are virtually identical and independent of the valve used.

2.2 Calculations

2.2.1 Principles

The ultimate goal of every quantum chemical calculation is to solve the Schrödinger equation

$$\boldsymbol{H}\Psi = E\Psi \tag{2.7}$$

for a molecule as accurate as possible. In the following, only a brief overview of some methods are given. Details can be found in, e.g., Refs. [18, 19].

Hartree–Fock Method

Ab initio methods try to solve the Schrödinger equation without previous knowledge of the wave function Ψ. One of the earliest approaches to obtain a suitable wave function and the overall Energy E is the Hartree–Fock method.[20–22] In a first approximation, it was assumed that the total wave function of a molecule can be described as the product of the individual electron wave functions

$$\Psi = \psi_1(\mathbf{x}_1)\psi_2(\mathbf{x}_2)\dots\psi_N(\mathbf{x}_N). \tag{2.8}$$

Yet, this product does not account for the spin of ½ of the electrons and the thereby required antisymmetric behavior. Thus, so-called Slater determinants[23]

$$\Psi = \Phi(\mathbf{x}_1, \mathbf{x}_2, \dots, \mathbf{x}_N) = \frac{1}{\sqrt{N!}} \begin{vmatrix} \phi_1(\mathbf{x}_1) & \phi_2(\mathbf{x}_1) & \cdots & \phi_N(\mathbf{x}_1) \\ \phi_1(\mathbf{x}_2) & \phi_2(\mathbf{x}_2) & \cdots & \phi_N(\mathbf{x}_2) \\ \vdots & \vdots & \ddots & \vdots \\ \phi_1(\mathbf{x}_N) & \phi_2(\mathbf{x}_N) & \cdots & \phi_N(\mathbf{x}_N) \end{vmatrix} \tag{2.9}$$

are constructed which fulfill these conditions. Here, the determinant elements are denoted as the product of spatial orbitals ψ and the spin function, i.e., spin orbitals ϕ_N, dependent on the electron coordinates $\mathbf{x}_N$.[18,19] In principle, the absolute energy of the studied molecule is determined by

$$E = \langle\Phi|\boldsymbol{H}|\Phi\rangle. \tag{2.10}$$

The energy of a single electron i within the manifold can be approximated by utilizing the Fock operator $\boldsymbol{F}_i$

$$\boldsymbol{F}_i = \boldsymbol{h}_i + \sum_j^{N_{\text{elec}}} (\boldsymbol{J}_j - \boldsymbol{K}_j), \tag{2.11}$$

assuming the the Born–Oppenheimer approximation holds true.[24] The motion of an electron i within the field of the nuclei is addressed by the one-electron operator $\boldsymbol{h}_i$. $\boldsymbol{J}_j$ is called the Coulomb operator and describes the repulsion between electrons, while the exchange operator $\boldsymbol{K}_j$ accounts for the effect when exchanging electrons. In sum, the latter two operators describe the two-electron interaction. If canonical orbitals ϕ'_N are used, for which the Fock matrix becomes diagonal, the energy of the spin orbital is obtained by the pseudo-eigenvalue equation

$$\boldsymbol{F}_i \phi'_i = \varepsilon_i \phi'_i. \tag{2.12}$$

Hence, the energy of a single orbital is

$$\varepsilon_i = \langle \phi'_i | \boldsymbol{F}_i | \phi'_i \rangle = h_i + \sum_j^{N_{\text{elec}}} (J_{ij} - K_{ij}). \tag{2.13}$$

It is worth noting that the absolute energy E is explicitly not the sum of all orbital energies, because the two-electron part of the Fock operator would be counted twice in such a sum. Correcting this error and introducing a constant factor V_{nn} for the nuclei interaction, the absolute energy is given as

$$E = \sum_i^{N_{\text{elec}}} \varepsilon_i - \frac{1}{2} \sum_{ij}^{N_{\text{elec}}} (J_{ij} - K_{ij}) + V_{\text{nn}}. \tag{2.14}$$

Since the Fock operator is actually not associated with the absolute energy, but the variation thereof,[19] the Hartree–Fock equation (2.12) can be utilized to optimize the molecular orbitals in an iterative process, aimed to find a solution with the lowest possible energy. However, the eigenvalues depend on all molecular orbitals owing to the Coulomb and exchange operators. Therefore, the equation can only be solved if all other orbitals are known a priori. Thus, an initial guess of the orbitals as a starting point is required. Each starting orbital

ϕ_i' is constructed by expanding the molecular orbital in terms of M_{basis} atomic orbitals χ_α,

$$\phi_i' = \sum_{\alpha}^{M_{\text{basis}}} c_{\alpha i}\chi_\alpha, \tag{2.15}$$

weighted by expansion coefficients $c_{\alpha i}$. Employing this linear combination of atomic orbitals (LCAO), i.e., of the basis set, the Hartree–Fock equation can be rewritten as

$$\boldsymbol{F}_i \sum_{\alpha}^{M_{\text{basis}}} c_{\alpha i}\chi_\alpha = \varepsilon_i \sum_{\alpha}^{M_{\text{basis}}} c_{\alpha i}\chi_\alpha. \tag{2.16}$$

Multiplication from the left by the complex-conjugated basis function, followed by additional integration gives the Roothaan–Hall equation

$$\boldsymbol{FC} = \boldsymbol{SC}\boldsymbol{\varepsilon}, \tag{2.17}$$

with the Fock matrix $\boldsymbol{F}$, the coefficient matrix $\boldsymbol{C}$, and the eigenvalue matrix $\boldsymbol{\varepsilon}$. The overlap elements between the basis functions are contained within the matrix $\boldsymbol{S}$.[18,19,25,26] In the iterative process, the initial Fock matrix $\boldsymbol{F}$ is diagonalized and the resulting set of coefficients is used to construct a new Fock matrix. These steps are repeated until the coefficients prior to diagonalization and afterwards are essentially identical, which consequently represents a self-consistent field (SCF) solution.

Many-Body Perturbation Theory

As a major drawback of the Hartree–Fock method, the interaction between the electrons is averaged. In this mean-field approximation, the electron correlations are neglected. In addressing these correlations, a variety of methods were developed, one being the many-body perturbation theory in which a perturbation term $\boldsymbol{H}'$ is added to the unperturbed Hamiltonian $\boldsymbol{H}_0$

$$\boldsymbol{H} = \boldsymbol{H}_0 + \lambda\boldsymbol{H}'. \tag{2.18}$$

The coefficient λ describes the extent of the perturbation. Likewise, the wave function and the energy are constructed by

$$\Psi = \lambda^0\Psi_0 + \lambda^1\Psi_1 + \lambda^2\Psi_2 + \cdots + \lambda^N\Psi_N \tag{2.19}$$

and

$$E = \lambda^0 E_0 + \lambda^1 E_1 + \lambda^2 E_2 + \cdots + \lambda^N E_N, \tag{2.20}$$

for zero-, first- second-, and nth-order perturbation. The first-order correction to the wave function can be determined by expanding the wave function in terms of the unperturbed basis of Slater determinants Φ_i

$$\Psi_1 = \sum_i c_i \Phi_i. \tag{2.21}$$

In contrast to the Hartree–Fock method, the overall wave function is thus not constructed of a single determinant. The additional determinants represent excitations of electrons from occupied to unoccupied molecular orbitals. Depending on the number of excited electrons, they are called singly-, doubly-, etc., excited determinants, or Singles (S), Doubles (D), etc. Including all possible excitation is the idea behind another approach, the so-called full Configuration Interaction (CI) method.[18,19] In perturbation theory, the first-order expansion coefficients of the determinants are obtained by

$$c_i = -\frac{\langle \Phi_i | \boldsymbol{H}_1 | \Phi_0 \rangle}{\langle \Phi_i | \boldsymbol{H}_0 - E_0 | \Phi_i \rangle}. \tag{2.22}$$

Moreover, it can be shown that the first-order correction of the energy is a result of

$$E_1 = \langle \Phi_0 | \boldsymbol{H}_1 | \Phi_0 \rangle. \tag{2.23}$$

Analogously, the higher-order perturbation corrections can also be described by the unperturbed basis functions, although it becomes increasingly more complicated.

In the Møller–Plesset perturbation theory approach[27] the unperturbed Hamiltonian is built by the sum of Fock operators

$$\boldsymbol{H}_0 = \sum_{i=1}^{N_{\text{elec}}} \boldsymbol{F}_i = \sum_{i=1}^{N_{\text{elec}}} \left(\boldsymbol{h}_i + \sum_{j=1}^{N_{\text{elec}}} (\boldsymbol{J}_j - \boldsymbol{K}_j) \right). \tag{2.24}$$

The perturbation correction is achieved by

$$\boldsymbol{H}' = \boldsymbol{H} - \boldsymbol{H}_0 = \sum_{i=1}^{N_{\text{elec}}} \sum_{j>i}^{N_{\text{elec}}} \boldsymbol{g}_{ij} - \sum_{i=1}^{N_{\text{elec}}} \sum_{j=1}^{N_{\text{elec}}} \langle \boldsymbol{g}_{ij} \rangle = \boldsymbol{V}_{\text{ee}} - 2\langle \boldsymbol{V}_{\text{ee}} \rangle, \tag{2.25}$$

with

$$g_{ij} = \frac{1}{|\mathbf{r}_i - \mathbf{r}_j|} \tag{2.26}$$

being the repulsion between the electrons i and j, described by their respective coordinates $\mathbf{r}$. $\boldsymbol{V}_{\mathrm{ee}}$ is the potential energy operator of the electron repulsion. The zeroth-order energy is the sum of the molecular orbital energies

$$E_0 = \langle \Phi_0 | \boldsymbol{H}_0 | \Phi_0 \rangle = \sum_{i=1}^{N_{\mathrm{elec}}} \varepsilon_i. \tag{2.27}$$

As discussed for the Hartree–Fock method, the mere sum of the orbital energies counts the electron repulsion twice, so the first-order correction

$$E_1 = \langle \Phi_0 | \boldsymbol{H}' | \Phi_0 \rangle = \langle \boldsymbol{V}_{\mathrm{ee}} \rangle - 2\langle \boldsymbol{V}_{\mathrm{ee}} \rangle = -\langle \boldsymbol{V}_{\mathrm{ee}} \rangle \tag{2.28}$$

in combination with E_0 yields the Hartree–Fock energy. Therefore, the second-order correction is the first actual improvement compared to the Hartree–Fock method. This correction requires doubly excited configurations, since according to Brillouin's theorem the matrix elements between the reference and the singly excited states are zero.[18,19] The second-order correction of the energy is thus

$$E_2 = \sum_{i<j}^{\mathrm{occ}} \sum_{a<b}^{\mathrm{vir}} \frac{\langle \Phi_0 | \boldsymbol{H}' | \Phi_{ij}^{ab} \rangle \langle \Phi_{ij}^{ab} | \boldsymbol{H}' | \Phi_0 \rangle}{E_0 - E_{ij}^{ab}} \tag{2.29}$$

and the total energy

$$E(\mathrm{MP2}) = \sum_{i<j}^{\mathrm{occ}} \sum_{a<b}^{\mathrm{vir}} \frac{(\langle \phi_i \phi_j | \phi_a \phi_b \rangle - \langle \phi_i \phi_j | \phi_b \phi_a \rangle)}{\varepsilon_i + \varepsilon_j - \varepsilon_a - \varepsilon_b}. \tag{2.30}$$

This so-called MP2 method (2 for the order of perturbation) achieves determination of 80–90 % of the correlation energy. Including further orders of perturbation does not necessarily improve the energy substantially, but increases the computational costs.[19]

Coupled Cluster

In coupled cluster (CC) methods an excitation operator $\boldsymbol{T}$

$$\boldsymbol{T} = \boldsymbol{T}_1 + \boldsymbol{T}_2 + \cdots + \boldsymbol{T}_{N_{\mathrm{elec}}} \tag{2.31}$$

is employed, generating new Slater determinants by acting on the reference wave function Φ_0

$$\boldsymbol{T}_1\Phi_0 = \sum_{i}^{\text{occ}}\sum_{a}^{\text{vir}} t_i^a \Phi_i^a, \tag{2.32}$$

$$\boldsymbol{T}_2\Phi_0 = \sum_{i<j}^{\text{occ}}\sum_{a<b}^{\text{vir}} t_{ij}^{ab} \Phi_{ij}^{ab}. \tag{2.33}$$

The total wave function Ψ is obtained via

$$\Psi = e^{\boldsymbol{T}}\Phi_0 \tag{2.34}$$

with

$$e^{\boldsymbol{T}} = \mathbf{1} + \boldsymbol{T} + \frac{1}{2}\boldsymbol{T}^2 + \frac{1}{6}\boldsymbol{T}^3 + \cdots = \sum_{k=0}^{\infty}\frac{1}{k!}\boldsymbol{T}^k. \tag{2.35}$$

Importantly, $e^{\boldsymbol{T}}$ can also be written as

$$e^{\boldsymbol{T}} = 1 + \boldsymbol{T}_1 + (\boldsymbol{T}_2 + \frac{1}{2}\boldsymbol{T}_1^2) + (\boldsymbol{T}_3 + \boldsymbol{T}_2\boldsymbol{T}_1 + \frac{1}{6}\boldsymbol{T}_1^3) + \ldots. \tag{2.36}$$

Applied to the reference wave function, the first term leaves the function unaltered and the second term results in singly excited states. The first parenthesis includes doubly excited states, yet as connected ($\boldsymbol{T}_2$) and disconnected ($\boldsymbol{T}_1^2$) excitation. In the former case, two electrons interact directly and in the latter they do not.[19] Analogously, the second parenthesis describes triply excited determinants and so forth. In general, the energy is obtained by

$$E(\text{CC}) = \langle\Phi_0|e^{-\boldsymbol{T}}\boldsymbol{H}e^{\boldsymbol{T}}|\Phi_0\rangle. \tag{2.37}$$

If all possible elements of $\boldsymbol{T}$ are considered, the resulting wave function is identical to the wave function in the full CI approach. However, customarily the excitation operator is truncated. Since the first element yields simply the Hartree–Fock reference function and according to Brillouin's theorem single excitations result in zeros as solutions, the lowest-level operator is given by

$$\boldsymbol{T} = \boldsymbol{T}_2 \tag{2.38}$$

including the doubly excited states, referred to as Coupled Cluster Doubles (CCD). If singly and doubly excited states are included via

$$\boldsymbol{T} = \boldsymbol{T}_1 + \boldsymbol{T}_2 \tag{2.39}$$

or triply excited states

$$\boldsymbol{T} = \boldsymbol{T}_1 + \boldsymbol{T}_2 + \boldsymbol{T}_3 \tag{2.40}$$

the methods are called CCSD and CCSDT, respectively. Each level improves the overall wave function but also increases the costs.

Reducing these costs while retaining good description of the systems is the aim of the CC2 method,[28] a hybrid between CCSD and MP2 to some extent. While the Singles are introduced as in CCSD, the doubly excited states are constructed based on perturbation theory as in MP2. Thereby, the amplitudes t_2 can be calculated by knowing the amplitudes of the singly excited determinants t_1.[19] Even though the resulting energies are approximately as accurate as in MP2, the CC2 method allows the calculation of, e.g., excitation energies and transition moments, owing to the inclusion of the singles.[28] In essence, these properties are obtained via the response of the system on a time-dependent perturbation.[28]

2.2.2 Employed Calculational Methods

The equilibrium molecular structures in the neutral and ionic ground states where optimized using second-order Møller-Plesset perturbation theory (MP2) under the resolution of the identity (RI) approximation and the spin-component scaling (SCS) modification (RI-SCS-MP2).[29–33] As will be shown, all molecules are planar in the ground states and based on the neutral ground state structures vertical excitation energies (VEEs) and ionization energies (VIE) were calculated using the second-order approximate coupled cluster method in the same variant (RI-SCS-CC2).[28,34–39] For both methods the def2-TZVPPD[40–42] basis set was used. Molecular structures in the first excited neutral state S_1 and the first two excited ionic states D_1 and D_2 were also optimized at RI-SCS-CC2 level of theory. Their single-point energies compared to the single-point energies of the optimized neutral ground state structures yielded adiabatic excitation (AEE) and ionization energies (AIE). Hessian diagonalizations were applied to confirm the nature of the stationary points obtained from the structure optimizations. Since analytical second derivatives are not available at the CC2 level of theory, the derivatives

were calculated as finite differences of the first derivatives. All calculations were carried out using the Turbomole 7.0[43,44] program package.

In Section 3.5, reproduced from Ref. [45], with the permission of AIP Publishing, the VEEs to the neutral excited states of PFPy were also calculated by applying the extended multi-configuration quasi-degenerate second-order perturbation theory (XMCQDPT2) method[46] to the complete active space self-consistent field (CASSCF) wavefunctions with an active space of eight electrons in nine orbitals. These orbitals include the three highest occupied π orbitals, the three lowest unoccupied π^* orbitals, two σ^* orbitals, and the nitrogen n orbital, using the aug-cc-pVDZ basis set[47] and the Firefly QC package[48] which is partially based on the GAMESS (US)[49] code. The π and π^* orbitals are delocalized over the molecular frame, while the σ^* orbitals are located on specific C-F bonds and show substantial 3s Rydberg character. The CASSCF method gave a wrong ordering of the excited states, therefore state-averaging over the twelve lowest CASSCF states was necessary.

References

[1]S. Mukamel, *Principles of Nonlinear Optical Spectroscopy* (Oxford University Press, Inc., New York, 1995).

[2]D. G. McLean, S. Kirkpatrick, and R. L. Sutherland, *Handbook of Nonlinear Optics*, edited by R. L. Sutherland, 2nd ed. (Marcel Dekker, Inc., New York, 2003).

[3]W. Demtröder, *Laserspektroskopie*, 5th ed. (Springer-Verlag Berlin Heidelberg, Berlin, 2007).

[4]T. Amand, V. Blanchet, A. Bonvalet, E. Constant, B. Couillaud, A. Ducasse, B. Girard, C. Hirlimann, M. Joffre, X. Marie, E. Mével, J. Oberlé, C. Rullière, F. Salin, and L. Sarger, *Femtosecond Laser Pulses*, edited by C. Rullière, 2nd ed. (Springer Science+Business Media, Inc., New York, 2005).

[5]M. Foca, "Investigations of ultrafast photoisomerization of photochromic molecular switches by fs-time-resolved transient absorption spectroscopy", Dissertation (Christian-Albrechts-Universität zu Kiel, 2005).

[6]H. Studzinski, "Ultrafast radiationless dynamics of selected electronically excited aromatic molecules by femtosecond time-resolved mass spectrometry and photoelectron imaging", Dissertation (Christian-Albrechts-Universität zu Kiel, 2007).

[7]N. Schwalb, "Ultrafast electronic deactivation dynamics in DNA model systems by femtosecond UV fluorescence spectroscopy", Dissertation (Christian-Albrechts-Universität zu Kiel, 2009).

[8]R. Siewertsen, "Ultrafast photochromic reactions of structurally modified furylfulgides and a bridged azobenzene", Dissertation (Christian-Albrechts-Universität zu Kiel, Kiel, 2011).

[9]H. Nicken, "Laserspektroskopische Untersuchung wasserstoffbrückengebundener Komplexe des Indazols und 5-Aminoindazols im Molekularstrahl", Dissertation (Christian-Albrechts-Universität zu Kiel, Kiel, 2011).

[10]O. Hüter, "Femtochemistry of vibronically coupled excited electronic states of carbonyl compounds and highly fluorinated benzene", Dissertation (Christian-Albrechts-Universität zu Kiel, 2016).

[11]J. A. Kus, "Untersuchung von Zimtsäuremethlyester mittels femtosekunden-zeitauf-gelöster Massenspektrometrie und Photoelektronengeschwindigkeit-skartographie", Master's thesis (Christian-Albrechts-Universität zu Kiel, 2015).

[12]W. C. Wiley and I. H. McLaren, "Time-of-flight mass spectrometer with improved resolution", Rev. Sci. Instrum. **26**, 1150 (1955).

[13]A. T. J. B. Eppink and D. H. Parker, "Velocity map imaging of ions and electrons using electrostatic lenses: application in photoelectron and photofragment ion imaging of molecular oxygen", Rev. Sci. Instrum. **68**, 3477 (1997).

[14]Wolfram Research, Inc., *Mathematica, Version 11.0*, Champaign, IL, 2016.

[15]G. A. Garcia, L. Nahon, and I. Powis, "Two-dimensional charged particle image inversion using a polar basis function expansion", Rev. Sci. Instrum. **75**, 4989 (2004).

[16]O. Hüter and F. Temps, "Note: Energy calibration of a femtosecond photoelectron imaging detector with correction for the ponderomotive shift of atomic ionization energies", Rev. Sci. Instrum. **88**, 046101 (2017).

[17]J. Mooney and P. Kambhampati, "Get the basics right: Jacobian conversion of wavelength and energy scales for quantitative analysis of emission spectra", J. Phys. Chem. Lett. **4**, 3316 (2013).

[18]A. Szabo and N. S. Ostlund, *Modern quantum chemistry: Introduction to advanced electronic structure theory* (Dover Publications, Inc., Mineola, 1996).

[19]F. Jensen, *Introduction to computational chemistry*, 2nd ed. (John Wiley & Sons, Ltd., Chichester, 2007).

[20]D. R. Hartree, "The wave mechanics of an atom with a non-coulomb central field. Part I. Theory and methods.", Math. Proc. Cambridge **24**, 89 (1928).

[21]D. R. Hartree, "The wave mechanics of an atom with a non-coulomb central field. Part II. Some results and discussion.", Math. Proc. Cambridge **24**, 111 (1928).

[22]V. Fock, "Näherungsmethode zur Lösung des quantenmechanischen Mehrkörperproblems", Z. Physik **61**, 126 (1930).

[23]J. C. Slater, "The theory of complex spectra", Phys. Rev. **34**, 1293 (1929).

[24]M. Born and R. Oppenheimer, "Zur Quantentheorie der Molekeln", Ann. Phys. **389**, 457 (1927).

[25]C. C. J. Roothaan, “New developments in molecular orbital theory”, Rev. Mod. Phys. **23**, 69 (1951).

[26]G. G. Hall and J. E. Lennard-Jones, “The molecular orbital theory of chemical valency viii. a method of calculating ionization potentials”, Proc. R. Soc. Lond. A **205**, 541 (1951).

[27]C. Møller and M. S. Plesset, “Note on an approximation treatment for many-electron systems”, Phys. Rev. **46**, 618 (1934).

[28]O. Christiansen, H. Koch, and P. Jørgensen, “The second-order approximate coupled cluster singles and doubles model CC2”, Chem. Phys. Lett. **243**, 409 (1995).

[29]M. Häser and R. Ahlrichs, “Improvements on the Direct SCF Method”, J. Comput. Chem. **10**, 104 (1989).

[30]F. Weigend and M. Häser, “RI-MP2: First derivatives and global consistency”, Theor. Chem. Acc. **97**, 331 (1997).

[31]F. Weigend, M. Häser, H. Patzelt, and R. Ahlrichs, “RI-MP2: Optimized auxiliary basis sets and demonstration of efficiency”, Chem. Phys. Lett. **294**, 143 (1998).

[32]S. Grimme, “Improved second-order Møller-Plesset perturbation theory by separate scaling of parallel- and antiparallel-spin pair correlation energies”, J. Chem. Phys. **118**, 9095 (2003).

[33]C. Hättig, A. Hellweg, and A. Köhn, “Distributed memory parallel implementation of energies and gradients for second-order Møller-Plesset perturbation theory with the resolution-of-the-identity approximation”, Phys. Chem. Chem. Phys. **8**, 1159 (2006).

[34]C. Hättig and F. Weigend, “CC2 excitation energy calculations on large molecules using the resolution of the identity approximation”, J. Chem. Phys. **113**, 5154 (2000).

[35]C. Hättig and A. Köhn, “Transition moments and excited-state first-order properties in the coupled-cluster model CC2 using the resolution-of-the-identity approximation”, J. Chem. Phys. **117**, 6939 (2002).

[36]C. Hättig, “Geometry optimizations with the coupled-cluster model CC2 using the resolution-of-the-identity approximation”, J. Chem. Phys. **118**, 7751 (2003).

[37]A. Köhn and C. Hättig, "Analytic gradients for excited states in the coupled-cluster model CC2 employing the resolution-of-the-identity approximation", J. Chem. Phys. **119**, 5021 (2003).

[38]R. Ahlrichs, "Efficient evaluation of three-center two-electron integrals over Gaussian functions", Phys. Chem. Chem. Phys. **6**, 5119 (2004).

[39]A. Hellweg, S. A. Grün, and C. Hättig, "Benchmarking the performance of spin-component scaled CC2 in ground and electronically excited states", Phys. Chem. Chem. Phys. **10**, 4119 (2008).

[40]A. Schäfer, C. Huber, and R. Ahlrichs, "Fully optimized contracted Gaussian basis sets of triple zeta valence quality for atoms Li to Kr", J. Chem. Phys. **100**, 5829 (1994).

[41]F. Weigend and R. Ahlrichs, "Balanced basis sets of split valence, triple zeta valence and quadruple zeta valence quality for H to Rn: Design and assessment of accuracy", Phys. Chem. Chem. Phys. **7**, 3297 (2005).

[42]D. Rappoport and F. Furche, "Property-optimized Gaussian basis sets for molecular response calculations", J. Chem. Phys. **133**, 134105 (2010).

[43]R. Ahlrichs, M. Bär, M. Häser, H. Horn, and C. Kölmel, "Electronic structure calculations on workstation computers: The program system turbomole", Chem. Phys. Lett. **162**, 165 (1989).

[44]*TURBOMOLE V7.0 2015, a development of University of Karlsruhe and Forschungszentrum Karlsruhe GmbH, 1989-2007, TURBOMOLE GmbH, since 2007; available from http://www.turbomole.com.*

[45]J. A. Kus, O. Hüter, and F. Temps, "Real-time observation of multi-mode vibronic coherence in pentafluoropyridine", J. Chem. Phys. **147**, 013938 (2017).

[46]A. A. Granovsky, "Extended multi-configuration quasi-degenerate perturbation theory: The new approach to multi-state multi-reference perturbation theory", J. Chem. Phys. **134**, 214113 (2011).

[47]R. A. Kendall, T. H. Dunning Jr., and R. J. Harrison, "Electron affinities of the first-row atoms revisited. Systematic basis sets and wave functions", J. Chem. Phys. **96**, 6796 (1992).

[48]A. A. Granovsky, *Firefly version 8*, `http://classic.chem.msu.su/gran/firefly/index.html`.

[49]M. W. Schmidt, K. K. Baldridge, J. A. Boatz, S. T. Elbert, M. S. Gordon, J. H. Jensen, S. Koseki, N. Matsunaga, K. A. Nguyen, S. Su, T. L. Windus, M. Dupuis, and J. A. Montgomery Jr., "General atomic and molecular electronic structure system", J. Comput. Chem. **14**, 1347 (1993).

Results and Discussion

3

The structural formulas of 1,2,3-TriFB, 1,2,4,5-TFB, 1,2,3,5-TFB, 1,2,3,4-TFB, PFPy, PFT, PFPh, ClPFB, and BrPFB are depicted in Figure 3.1. In addition, the structural formulas of PFB and HFB are shown. Previously reported results for the former are instrumental for the discussions herein, whereas the dynamics of HFB are altered by the Jahn–Teller effect,[1–3] affecting the degenerate $\pi\sigma^*$ states. Thus, HFB is only included for the sake of completeness and will not be discussed to great extent. Except for PFT and PFPh, all molecules exhibit at least one C_2 rotational axis. Thereby, most of the molecules belong to the C_{2v} point group in the planar neutral and ionic ground states according to Mulliken's notation.[4] 1,2,4,5-TFB and HFB have more than one rotational axis and belong to the D_{2h} and D_{6h} point group, respectively. Owing to the methyl (PFT) and hydroxy group (PFPh), both PFT and PFPh belong to the C_s point group. Yet, some molecular properties can be explained in terms of irreducible representations of the C_{2v} point groups if these substituents are temporarily neglected, discussed in detail in Section 3.6 for PFT and Section 3.7 for PFPh.

As highlighted in the Introduction, the molecular dynamics of fluorinated aromatic systems tend to be rather complex. Therefore, a separate Section is dedicated for the individual results and discussions of electronic and molecular structure calculations, of the time-resolved mass spectrometry, and of the photoelectron imaging experiments for each molecule. It should be noted that Section 3.5 is a shortened, but otherwise unaltered version of Ref. [5], and thus some notations (e.g., photoelectron peak labels) may slightly differ compared to the ones employed in other Sections. A short summary and broader comparison of all major results is featured in Section 3.10, also including the comparative discussion of all the excited state deactivation dynamics. Cartesian coordinates of the calculated molecular structures and vibrational frequencies are listed in Chapters A and B in the appendix.

As shown in Figure 3.2, virtually no photo-induced dissociation is observed after excitation. As an exception, C-Br bond breaking and ring fragmentation occurs in the case of BrPFB. The additional signal in the TOF-MS of PFPh is also a ring fragmentation product. The attention is focused on the parent ions in the

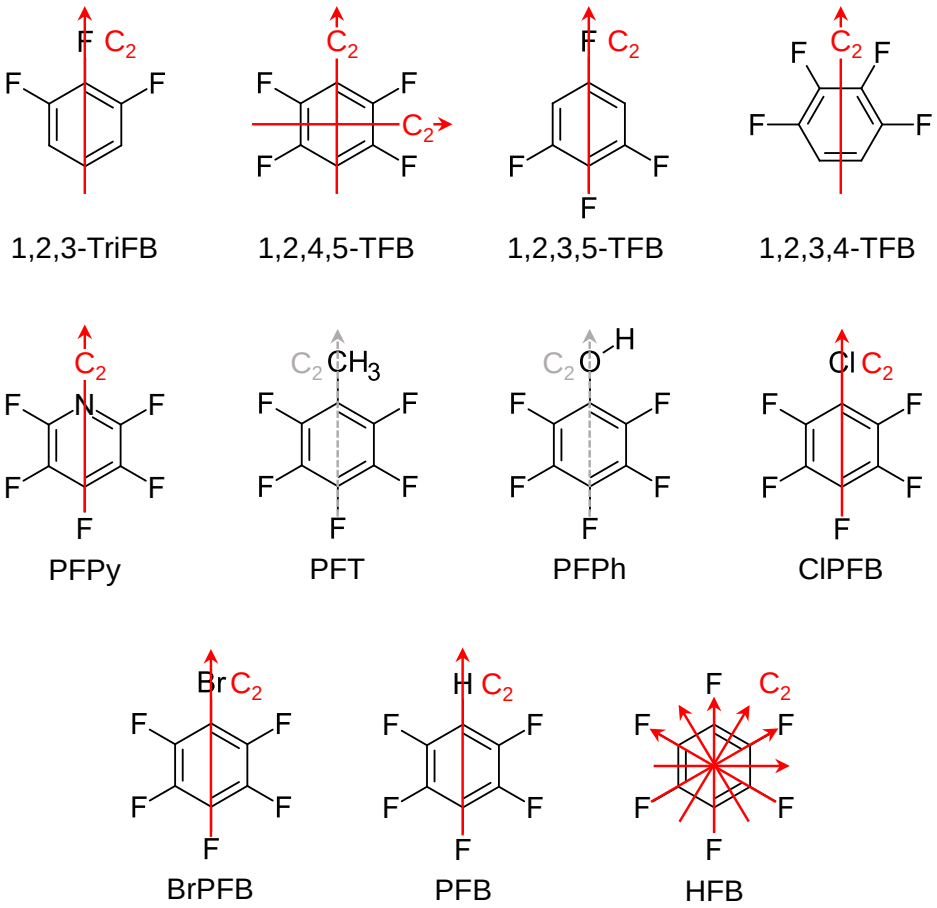

Figure 3.1. Structural formulas of the molecules discussed herein. Actual and hypothetical C_2 rotational axes are depicted as red and grey arrows, respectively.

following, since their femtosecond time-resolved behavior maps the dynamics of the molecules upon photoexcitation to the S_1 states.

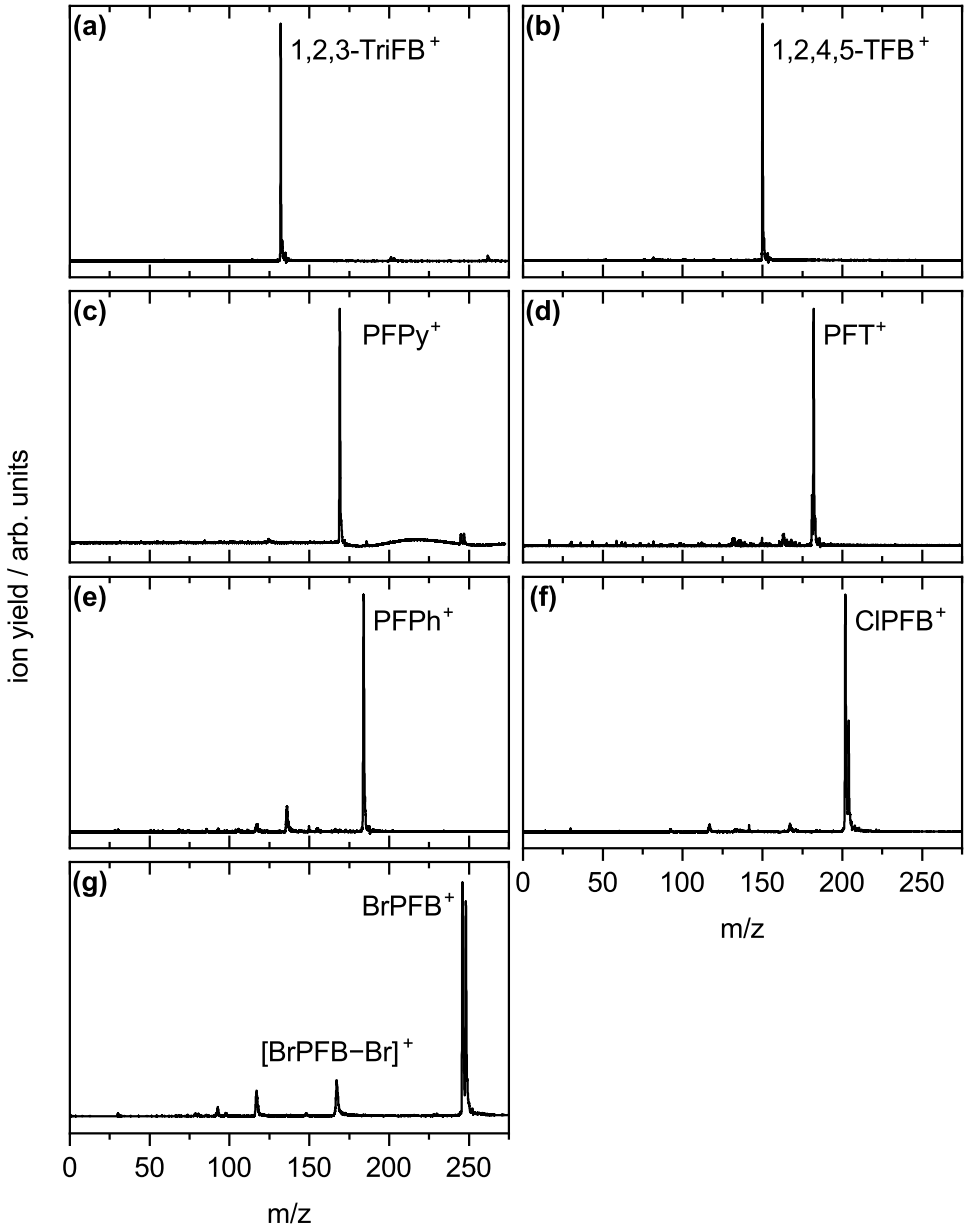

Figure 3.2. TOF mass spectra of **(a)** 1,2,3-TriFB, **(b)** 1,2,4,5-TFB (by way of example for the TOF-MS of the three TFB isomers), **(c)** PFPy, **(d)** PFT, **(e)** PFPh, **(f)** ClPFB, and **(g)** BrPFB at $\Delta t = 0$ ps (t_0) after excitation at $\lambda_{\text{pump}} = 260$ nm (250 nm for 1,2,3-TriFB) and ionization at $\lambda_{\text{probe}} = 400$ nm. For PFPy, single-color ionization at $\lambda_{\text{probe}} = 402$ nm was employed. The most intense signals in the spectra are the respective parent ion peaks.

3.1 1,2,3-Trifluorobenzene

3.1.1 Molecular and Electronic Structure

To choose a suitable pump wavelength to excite the first $\pi\pi^*$ state it is indispensable to know the electronic structure of the molecules beforehand. Thus, first the gas-phase UV absorption spectrum of 1,2,3-TriFB was obtained, displayed in Figure 3.3. Two absorption bands are observed. The first band is centered at 250 nm (4.96 eV) and features a diffuse structure. The first shallow peak of this structure is observed at 265 nm (4.68 eV). A second, more intense absorption band rises at wavelengths <220 nm (>5.64 eV). Limited by the resolution of the spectrometer, the band cannot be fully resolved.

Neutral States

To assign the absorption bands to electronic states, the vertical excitation energies (VEEs) to the first eight excited electronic states were calculated at RI-SCS-CC2 level of theory. The results are shown in Table 3.1. The first neutral excited state S_1 ($1\ ^1B_2$) exhibits $\pi\pi^*$ character and a VEE of 5.11 eV (243 nm). The S_2 state ($2\ ^1A_1$) is also a $\pi\pi^*$ state, with a VEE of 6.41 eV (193 nm). The S_2 state is predicted to be in close vicinity to two $\pi\sigma^*$ states, $1\ ^1B_1$ and $1\ ^1A_2$, at 6.66 eV (186 nm) and 6.81 eV (182 nm), respectively. Although all higher-lying states exhibit transition energies >7 eV, especially the S_7 ($3\ ^1A_1$) and the S_8 state ($2\ ^1B_2$) play a role in the ionization mechanism, as will be discussed.

In these transitions, electrons from the highest-occupied molecular orbitals (HOMO and HOMO−1, π character) are excited to unoccupied molecular orbitals. In the $\pi\pi^*$ states, the electron density is allocated to π^* orbitals, but stays in the conjugated system. On the other hand, in the $\pi\sigma^*$ transitions, the electron density is shifted out of the ring. The involved σ^* orbitals exhibit Rydberg character and density nodes between the carbon and the fluorine atoms, as illustrated in Figure 3.4. The configurations of the electrons in these orbitals in the S_1–S_4 states, but also in the S_7 and S_8 state, are listed in Table 3.2. In general, the molecular orbitals of all studied systems are shaped very similarly and for the sake of brevity only deviations are highlighted in the following Sections.

The VEEs are based on the planar molecular structure in the S_0 ground state, optimized at RI-SCS-MP2 level of theory. In contrast to the S_0 structure, the molecules experience pronounced out-of-plane deformation in the S_1 state, as

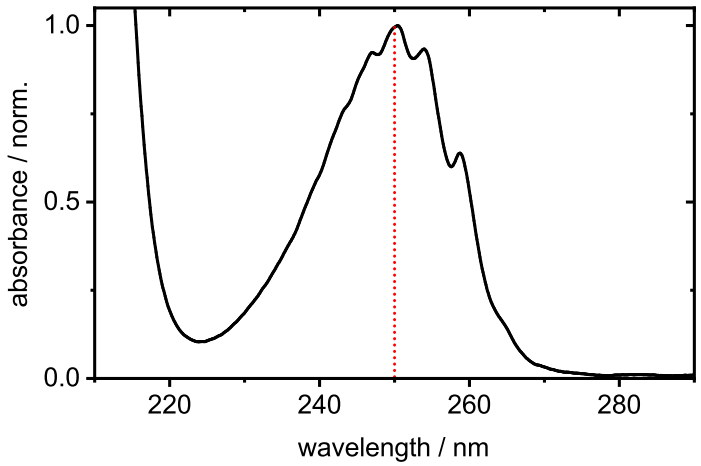

Figure 3.3. Normalized gas-phase UV absorption spectrum of 1,2,3-TriFB. The dotted red line indicates the chosen excitation wavelength of $\lambda_{\text{pump}} = 250$ nm to excite the S_1 state ($\pi\pi^*$).

Table 3.1. Vertical excitation energies (VEE) and oscillator strengths f (in parentheses) of the first eight neutral electronically excited states, the ionic ground state and the first two ionic electronically excited states for 1,2,3-TriFB, calculated at RI-SCS-CC2 level of theory. Where available, the respective adiabatic energy (AEE) is listed. Experimental energies are given if possible.

	symm.	calc. VEE eV	calc. AEE eV	exp. VEE eV	exp. AEE eV
S_1 ($\pi\pi^*$)	$1\,^1B_2$	5.11 (0.0001)	4.91	4.96[†]	
S_2 ($\pi\pi^*$)	$2\,^1A_1$	6.41 (0.0003)			
S_3 ($\pi\sigma^*$)	$1\,^1B_1$	6.66 (0.0031)			
S_4 ($\pi\sigma^*$)	$1\,^1A_2$	6.81 (0.0000)			
S_5 ($\pi\sigma^*$)	$2\,^1B_1$	7.20 (0.0190)			
S_6 ($\pi\sigma^*$)	$2\,^1A_2$	7.21 (0.0000)			
S_7 ($\pi\pi^*$)	$3\,^1A_1$	7.30 (0.6517)		7.2[†]	
S_8 ($\pi\pi^*$)	$2\,^1B_2$	7.35 (0.6971)			
D_0 (π^{-1})	$1\,^2B_1$	9.77	9.53	9.55[‡]	9.4[‡]
D_1 (π^{-1})	$1\,^2A_2$	10.05		9.73[‡]	
D_2 (π^{-1})	$2\,^2B_1$	12.80		12.5[a]	12.1[‡]

[a] Ref. [6] [†] this work [‡] re-evaluated in this work, based on Ref. [6]

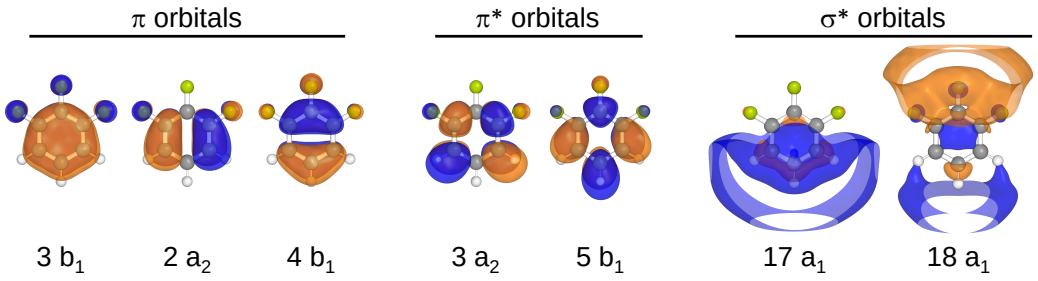

Figure 3.4. Calculated molecular orbitals for the ground state structure for 1,2,3-TriFB with significant contributions to the electronic configurations of the neutral excited states S_1–S_4 (cf. Table 3.2).

Table 3.2. Molecular orbital configuration and their weighted contributions to the S_1–S_4, S_7, and S_8 states and the first three ionic states of 1,2,3-TriFB. Correlations between the neutral and the ionic states according to Koopmans's theorem are given.

neutral state	3 b_1 (π)	2 a_2 (π)	4 b_1 (π)	3 a_2 (π^*)	5 b_1 (π^*)	17 a_1 (σ^*)	18 a_1 (σ^*)	weight (%)	corr. ion. state
S_0 ($^1A_1$)	2	2	2						
S_1 ($^1B_2$, $\pi\pi^*$)	2	2	1	1				47	D_0
	2	1	2		1			47	D_1
S_2 ($^1A_1$, $\pi\pi^*$)	2	2	1		1			49	D_0
	2	1	2	1				45	D_1
S_3 ($^1B_1$, $\pi\sigma^*$)	2	2	1				1	49	D_0
S_4 ($^1A_2$, $\pi\sigma^*$)	2	1	2				1	49	D_1
	2	1	2			1		17	D_1
S_7 ($^1A_1$, $\pi\pi^*$)	2	1	2	1				48	D_1
	2	2	1		1			41	D_0
S_8 ($^1B_2$, $\pi\pi^*$)	2	1	2		1			46	D_1
	2	2	1	1				45	D_0
ionic state									
D_0 ($^2B_1$, π^{-1})	2	2	1						
D_1 ($^2A_2$, π^{-1})	2	1	2					99	
D_2 ($^2B_1$, π^{-1})	1	2	2					80	

the comparison of the calculated equilibrium structures in Figure 3.5 shows. The four carbon atoms 2, 3, 5, and 6 (numbering according to Figure 3.5) span a plane in the S_1 state. The two remaining carbon atoms, located at the principle axis of symmetry, all hydrogen atoms and F-8/12 are nearly in-plane, i.e., their out-of-plane bending angles are less than −5° with respect to said plane. Contrary, F-7 is bent out-of-plane by 24° and thus in the opposed direction compared to the other substituent atoms. Therefore, the molecular structure essentially shows b_1 symmetry. Based on the structures of the S_0 and the S_1 state an adiabatic excitation energy (AEE) of 4.91 eV (253 nm) was calculated. In addition to the molecular structures, depictions of the displacement vectors of the out-of-plane vibrational modes and the respective calculated frequencies in the S_1 state are also given in Figure 3.5, which are instrumental for the following discussions of the molecular dynamics. A comprehensive list of all vibrational frequencies can be found in Table B.1 in the appendix.

Aided by the calculations, the first absorption band is assigned to the S_1 state ($\pi\pi^*$, $1\ ^1B_2$). The calculated (5.11 eV) and the observed VEE (4.96 eV) are in excellent agreement. However, the calculated AEE of 4.91 eV (253 nm) substantially overestimates the AEE, as a first shallow peak of the S_1 band is observed at 4.68 eV (265 nm). Though it should be noted that this peak not necessarily represents the adiabatic $S_1 \leftarrow S_0$ transition, it is a good first estimate, considering no high resolution studies were performed yet. The second absorption band is assigned to the S_2 state ($\pi\pi^*$, $2\ ^1A_1$), since the calculated VEE of 6.41 eV (193 nm) fits well to the band onset at 220 nm.

Ionic States

In the ionization of 1,2,3-TriFB, an electron previously located in the π orbitals is detached from the molecule. If an electron from the HOMO is detached during the ionization, the ionic ground state D_0 (π^{-1}, $1\ ^2B_1$) is reached, as shown in Table 3.2. The calculations at RI-SCS-CC2 level of theory predict a vertical ionization energy (VIE) to the D_0 state of 9.77 eV. The first excited ionic state D_1 (π^{-1}, $1\ ^2A_2$) is characterized by a singly occupied HOMO−1 orbital and a VIE of 10.05 eV. Both states are energetically well separated from the second excited ionic state D_2 (π^{-1}, $2\ ^2B_1$) estimated at 12.80 eV. Only one electron resides in the HOMO−2 π orbital in the D_2 state. As will be shown in the following Sections, the same electron configuration pattern emerges for all fluorobenzenes, except for ClPFB and BrPFB, and will thus not be explicitly mentioned again.

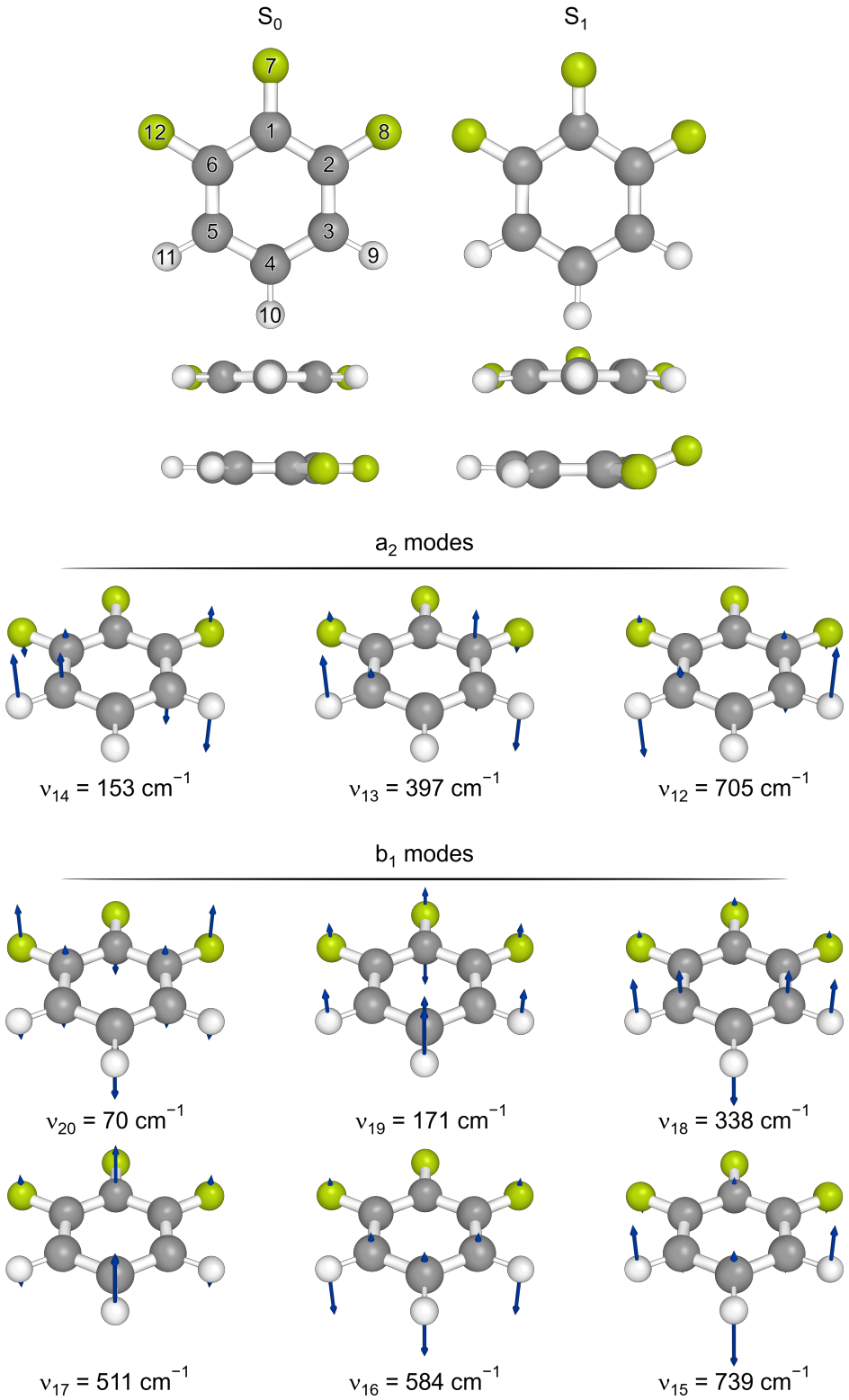

Figure 3.5. Calculated molecular structures of 1,2,3-TriFB in the S_0 and the S_1 state ($\pi\pi^*$), optimized at the RI-SCS-MP2 and RI-SCS-CC2 levels of theory, respectively. The calculated displacement vectors of the out-of-plane modes are illustrated by blue arrows. Their respective frequencies in the S_1 state are listed.

Optimization of the molecular structures only converged for the D_0 state. The calculations suggest a planar configuration (not shown for the sake of brevity), likewise to the S_0 state structure. The adiabatic ionization energy (AIE) between the optimized structures in the D_0 and the S_0 state was calculated to be 9.53 eV.

In contrast to the neutral electronic states, the structure of the ionic states received some attention in the past, both of experimentalists and theoreticians. In 2012, high-level calculations by Faraji and Köppel revealed strong coupling between various ionic states.[7] Furthermore, the authors showed that the D_0 and the D_1 state are only separated by 0.1 eV, approximately, thereby slightly closer than estimated herein. Bieri et al.[6] attributed photoelectrons with kinetic energies between 9.3–10 eV in their He(II) PES to population of both ionic states. The observed PE distribution is determined by a steep intensity increase starting at ≈9.3 eV and peaking at 9.55 eV, closely followed by a second major peak at 9.73 eV. Lacking further experimental and theoretical data at that time, an ionization energy of 9.7 eV was assigned to both the D_0 and the D_1 state. In light of the calculations of Faraji and Köppel, the two major peaks are reassigned to originate from the vertical $D_0 \leftarrow S_0$ and the $D_1 \leftarrow S_0$ transitions, respectively. The PES band corresponding to the D_2 state starts to rise at ≈12 eV, peaking at a VIE of 12.5 eV. While the vertical ionization energies are readily available from the PES, the adiabatic transition energies are rather not. Bondybey et al.,[8] reported an adiabatic energy difference of 2.7 eV between the D_0 and the D_2 state, based on their laser-induced fluorescence spectra of the D_2 state. The difference fits perfectly the energy gap between two shoulders in the rising flanks of the D_0 and D_2 PES bands at 9.4 eV and 12.1 eV, respectively. Therefore, the shoulders are assigned to originate from the adiabatic transitions.

The AIE and VIE calculated in this work at RI-SCS-CC2 level of theory are in good agreement with the reevaluated experimental transition energies to the D_0–D_2 states (cf. Table 3.1).

Overall, the electronic transitions are well described at RI-SCS-CC2 level of theory. Yet, it also becomes apparent that the method consistently overestimates the transition energies. This tendency was already reported for the transition energies of PFB.[9,10] Nevertheless, the method was found to be well suited to describe the trends in the potential energy of the electronic states.[9,10] Hence, at the chosen excitation wavelength $\lambda_{\text{pump}} = 250$ nm the S_1 state ($\pi\pi^*$) is selectively excited, since the higher-lying states are inaccessible by absorption of a single pump photon.

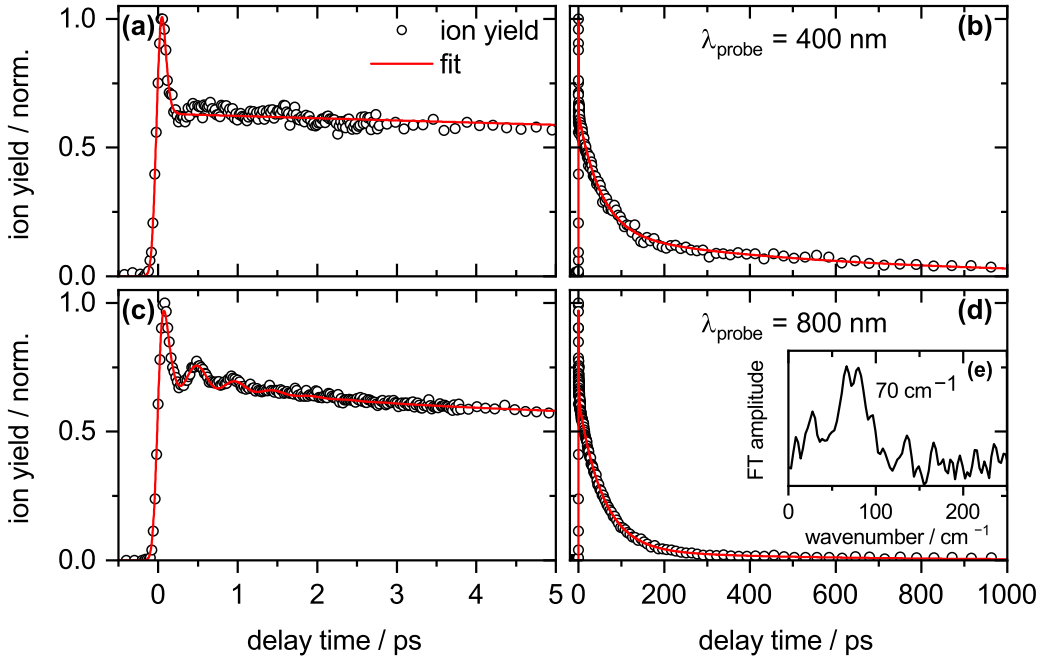

Figure 3.6. Measured transient parent ion yield signals (black circles) and applied fit model functions (red lines) for 1,2,3-TriFB after excitation at $\lambda_{\text{pump}} = 250$ nm and ionization at $\lambda_{\text{probe}} = 400$ nm **(a–b)** resp. $\lambda_{\text{probe}} = 800$ nm **(c–d)**. The left-hand column shows the data in the first five picoseconds, the right-hand column in the first nanosecond after excitation. The fit parameters are listed in Table 3.3. **(e)** Fourier transform of the oscillatory signal component after subtraction of the exponential decay functions.

3.1.2 Time-Resolved Time-of-Flight Mass Spectra

The transient parent ion yields of 1,2,3-TriFB after excitation at $\lambda_{\text{pump}} = 250$ nm and ionization at both $\lambda_{\text{probe}} = 400$ nm and 800 nm are depicted in Figure 3.6. All fit parameters of the applied fit model functions are listed in Table 3.3. A major fraction of the intense signal decays within few femtoseconds after the temporal overlap of the pump and probe pulses ($\Delta t = t_0$). Limited by the time-resolution of $\sigma_{\text{IRF}} = 50$ fs, the ultrafast decay $\tau_1^{\text{1,2,3-TriFB}}$ cannot be resolved further. When choosing 800 nm as the ionization wavelength, the initial decay is followed by a short-lived oscillation with a frequency of $\nu_{\text{osc}}^{\text{1,2,3-TriFB}} = 70$ cm^{-1}. Fourier transform of the oscillatory signal component verified the frequency (cf. Figure 3.6 (e)). The decay time of the oscillation was set fixed to $\tau_{\text{osc}}^{\text{1,2,3-TriFB}} = 0.5$ ps to fit the data. In contrast, at $\lambda_{\text{probe}} = 400$ nm an analogous behavior only manifests itself through a shallow signal dip at $\Delta t = 0.3$ ps. The origin of the oscillation is discussed in Subsection 3.1.4.

Table 3.3. Parameters for the fits of the transient parent ion yields of 1,2,3-TriFB after excitation at $\lambda_{pump} = 250$ nm and ionization at either $\lambda_{probe} = 400$ nm (upper row) or 800 nm (lower row). 2σ fit errors are given in parentheses. If no error is given the value was set fixed.

σ_{IRF}	A_1	τ_1	A_2	τ_2	A_3	τ_3	A_4	τ_4	A_{osc}	τ_{osc}	ν_{osc}	ϕ_{osc}
fs	%	ps	%	ps	%	ps	%	ps	%	ps	cm^{-1}	π
$\lambda_{probe} = 400$ nm												
52(5)	80	$< \sigma_{IRF}$			15(1)	52.9(44)	5(1)	590(150)				
$\lambda_{probe} = 800$ nm												
50	41(4)	$< \sigma_{IRF}$	9(1)	1.19(14)	38(1)	56.1(26)	3(1)	460(260)	9(1)	0.5	70	−0.09

Further marginal probe wavelength-dependent differences are observed for the subsequent exponential signal decays. For ionization at $\lambda_{probe} = 800$ nm, three exponential decay functions with

$$\tau_2^{1,2,3\text{-TriFB}} = 1.2 \text{ ps}$$
$$\tau_3^{1,2,3\text{-TriFB}} = 54 \text{ ps}$$
$$\tau_4^{1,2,3\text{-TriFB}} = 550 \text{ ps}$$

are required to describe the decay well. Contrary, at 400 nm the signal decay is well described by the two long-lived functions, i.e., without $\tau_2^{1,2,3\text{-TriFB}}$. Since the component $\tau_2^{1,2,3\text{-TriFB}}$ exhibits only an a low amplitude of less than 10 %, the overall slightly better signal to noise ratio at $\lambda_{probe} = 800$ nm probably is the reason why the component is not observed at $\lambda_{probe} = 400$ nm. Although the exponential decays of all molecules herein are discussed in Section 3.10, it should be noted that the initial ultrafast decay likely is associated with a rapid leaving of the Franck-Condon (FC) region.

3.1.3 Time-Resolved Photoelectron Images

In Figure 3.7 the photoelectron images of 1,2,3-TriFB and their respective meridional slices through the reconstructed three-dimensional distributions at $\Delta t = 0.06$ ps after excitation at $\lambda_{pump} = 250$ nm and ionization at $\lambda_{probe} = 400$ nm (a), and $\Delta t = 50$ ps (b) are shown. Darker shades equal more particles. At $\Delta t = 0.06$ ps four main features are observed. Starting at the center, a rather broad area is followed by an intense, narrow ring, again followed by two less in-

tense, close-lying signals. However, the latter are only observed at $\Delta t = 0.06$ ps. After just $\Delta t = 0.26$ ps these signals vanish and are not reoccurring, as can be seen in the corresponding PES in Figure 3.8 (a). The PES reveal the broad area comprises photoelectrons with energies between 0–0.5 eV, though the electron yield decreases towards increasing photoelectron energies. Thus, a clear center of the signal cannot be observed, even without applying the Jacobian transformation. The area is labeled α. The following narrow signal β is centered at $E_\beta = 0.89$ eV. Since no oscillations were observed in the parent ion yields at $\lambda_{\text{probe}} = 400$ nm, neither band exhibits intensity oscillations.

While for all other molecules in this Thesis single-color background signals were efficiently avoided, decent transient PE signal intensities for 1,2,3-TriFB were only achieved by allowing considerable background signals. The background PE images at $\lambda_{\text{pump}} = 250$ nm and $\lambda_{\text{probe}} = 400$ nm are shown in Figure 3.7 (c) and (d) and the PES in Figure 3.8 (a) as grey lines. Although at $\Delta t = 50$ ps the intensity of band α is largely determined by the SC background, the decay in intensity from $\Delta t = 0.06$ ps to $\Delta t = 50$ ps highlights that the band is a genuine result of the transient ionization process.

The high-intensity single-color PEI at $\lambda_{\text{pump}} = 250$ nm in Figure 3.7 (e) exhibits two close-lying low-energy signals ζ and η. If the Jacobian transformation is omitted, the signals peak at $E_\zeta \approx 0.14$ eV and $E_\eta \approx 0.30$ eV as depicted in the corresponding PES in Figure 3.8 (c). The SC PEI at $\lambda_{\text{probe}} = 400$ nm (Figure 3.7 (f)) features four distinct rings. Starting at the center, a narrow signal is followed by two adjacent, less intense signals. The highest-energy signal nearly faints in the intense background. The four signals β, γ, δ, and ϵ peak at $E_\beta = 0.89$ eV, $E_\gamma = 1.5$ eV, $E_\delta = 1.7$ eV, and $E_\epsilon = 2.2$ eV (cf. Figure 3.8 (d)). Band β, as well as γ and δ are at identical positions as the three signals observed in the transient PES at $\Delta t = 0.06$ ps. Analogous to the transient PES, the Jacobi transform does not lead to superimposed bands. In the following Sections, the non-Jacobi transformed PES are therefore only shown if they provide meaningful additional information.

Assignment of the PE Signals

After excitation of a neutral electronic state, the PE energy E_{el} depends on the energy of the populated neutral electronic state E_{x}, the number n' and frequency

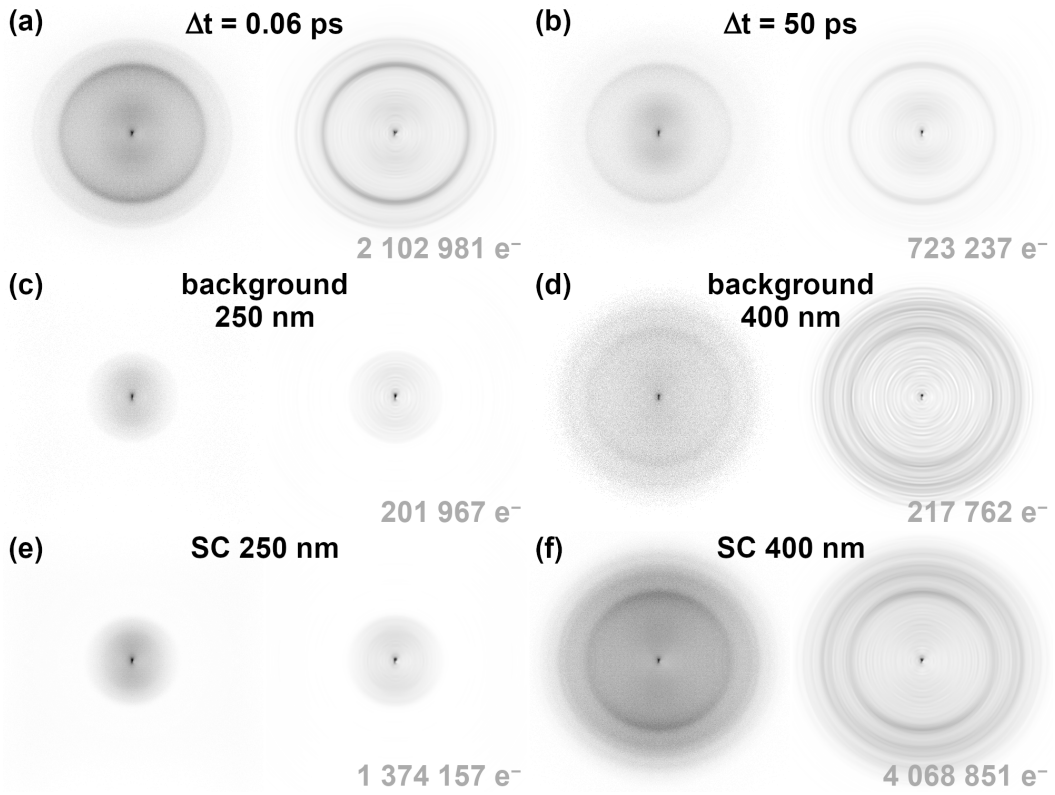

Figure 3.7. Photoelectron images (left) and their corresponding meridional slices through the recovered three-dimensional photoelectron distributions (right) of 1,2,3-TriFB. **(a)** At $\Delta t = 0.06$ ps after excitation at $\lambda_{\text{pump}} = 250$ nm and ionization at $\lambda_{\text{probe}} = 400$ nm and **(b)** at $\Delta t = 50$ ps. **(c–d)** Single-Color background. **(e–f)** High-intensity SC photoelectron images obtained at 250 nm **(e)** and 400 nm **(f)**.

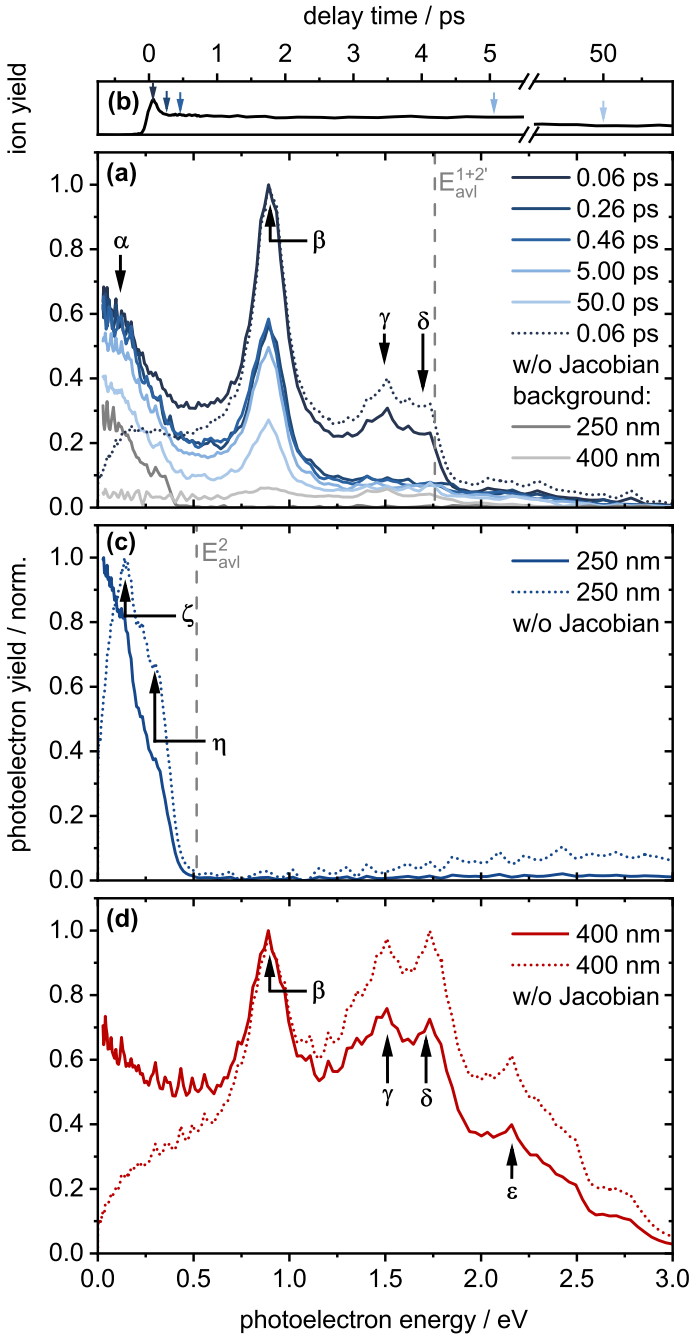

Figure 3.8. **(a)** Transient PE spectra of 1,2,3-TriFB after excitation at $\lambda_{\text{pump}} = 250$ nm and ionization at $\lambda_{\text{probe}} = 400$ nm. The two main photoelectron signals labeled α and β are observed at $E_\alpha < 0.5$ eV and $E_\beta = 0.89$ eV. Two additional signals labeled γ and δ ($E_\gamma = 1.5$ eV and $E_\delta = 1.7$ eV) are present only at $\Delta t = 0.06$ ps. Solid lines (blue transient, grey background) show the PE spectra with Jacobian transformation, dotted lines without. The grey dotted line indicates the maximum available photoelectron energy $E_{\text{avl}}^{1+2'}$ associated with the $D_0 \leftarrow S_0$ transition by $1+2'$ ionization. **(b)** Corresponding transient parent ion yields (cf. Figure 3.6 (a)). Arrows mark the delay time $\Delta t = 0$–50 ps at which the PES were obtained. **(c–d)** Single-color PE spectra taken at higher 250 nm pump **(c)** and 400 nm probe **(d)** intensities. The PE peaks β, γ, and δ are observed. The additional signals ϵ, ζ, and η are located at $E_\epsilon = 2.2$ eV, $E_\zeta \approx 0.14$ eV, and $E_\eta \approx 0.30$ eV. The grey dotted line indicates the maximum available photoelectron energy E_{avl}^{2} generated by two 250 nm photons. At 400 nm the max. available energy $E_{\text{avl}}^{4'}$ is 3.00 eV.

ω_{probe} of the probe photons, and the ionization energy of the molecule IE_{i}, as shown in Equation 3.1.

$$E_{\text{el}} = E_{\text{x}} + \hbar \times \omega_{\text{probe}} \times n' - IE_{\text{i}}. \tag{3.1}$$

Thus, the reason why two major signals are observed in the time-resolved PES might be a varying number of probe photons is absorbed, multiple neutral electronic states are excited, or multiple ionic states are populated. The absorption of more than two probe photons can confidently be ruled out, since such signals should be separated by the energy of a probe photon (3.10 eV), way more than the actual observed difference between α and β ($\Delta E > 0.4$ eV). In the simplest scenario of population of two different neutral electronic states prior to ionization, the energetic spacing between the PE signals would be equal to the energy gap between the two electronic states. Yet, the estimated energy gap of 1.3 eV (cf. Table 3.1) separating the initially excited S_1 state ($\pi\pi^*$, 4.96 eV) and the higher-lying states does not fit to the energy difference of the two observed PE bands. Furthermore, and more importantly, the energy of the pump photons at $\lambda_{\text{pump}} = 250$ nm (4.96 eV) is insufficient to excite any higher lying state. Of course, the excited S_1 state might exhibit a low-lying conical intersection (CI) to another electronic state, as was proposed earlier for PFB[11,12] and HFB.[13,14] Nevertheless, such a conversion should be accompanied by a decay of the PE signal corresponding to the S_1 state and a simultaneous rise of a signal originating from the second state. Since both α and β exhibit equal delay-time dependent behaviors, they must be associated with the same excited state, the initially excited S_1 state. Crucially important, it follows that the oscillation observed in the parent ion yield maps dynamics on the potential energy hypersurface (PEHS) of the S_1 state.

The appearance of two PE signals from a single neutral excited state therefore indicates two different ionic states are populated by photoionization. To which ionic state detachment of an electron will lead is strongly influenced by the electronic configuration of the neutral state excited prior to ionization. The more similar the configurations of the (excited) neutral and the (excited) ionic state are, the more likely this specific ionic state will be populated in the ionization process, known as Koopmans's picture.[15–17] As a consequence, if the configuration of the neutral state shows resemblance to the configurations of multiple ionic states, transitions to all of these might occur. Following the example of Stolow and co-workers,[16,17] the calculated electron configurations can be utilized to

determine which of the ionic states most likely is populated in the ionization processes. For this, the electron configurations of the neutral and ionic states, listed in Table 3.2, are compared. The S_1 state is formed by the excitation of electrons from the highest occupied molecular orbital (HOMO) or from the second highest occupied molecular orbital (HOMO−1) to unoccupied orbitals. Noteworthy, the same applies to the S_7 and S_8 state. Removing one electron from the HOMO correlates to the D_0 state and from HOMO−1 to the D_1 state. Assuming the excited electrons are detached in the photoionization process, transition from the S_1 to both the D_0 and D_1 states seem feasible.

The electron configuration is, however, not the sole parameter determining the final ionic state, since population of different ionic states also requires different excitation energies. The reevaluation of PES spectra in the literature (*vide supra*) revealed that the D_0 and the D_1 state are in close vicinity to each other with VIEs of 9.55 eV and 9.73 eV, respectively. In contrast, transitions to the second excited ionic state D_2 require more than 12.1 eV (cf. Table 3.1). Considering that the molecules were excited at $\lambda_{\text{pump}} = 250$ nm (4.96 eV), followed by the absorption of two probe photons at $\lambda_{\text{probe}} = 400$ nm (3.10 eV) totaling an energy of 11.16 eV, ionization might easily lead to either the D_0 or the D_1 state, yet not to the D_2 state. Therefore, not only are both the D_0 and the D_1 state energetically accessible, but based on the electron configurations transitions to both ionic states is ought to be expected, resulting in two PE signals with an energetic spacing equivalent to the energy gap of the ionic states. The observed energy gaps between the signals α and β ($\Delta E > 0.4$ eV) fit reasonably well to the D_0–D_1 energy gap of ≈0.2 eV, especially considering the broad nature of α and that the ionization energy difference was solely determined by the corresponding vertical transition energies. According to Equation 3.1, transitions to higher-lying states yield signals with lower PE energy, thus α is assigned to originate from the transition to the D_1 state and β to the D_0 state. The assignment is in agreement with the results on PFB, for which also two PE bands were observed and assigned to transitions to two ionic states.[9]

Different vibrational structures of the excited neutral and the (excited) ionic states are the reason for the signal widths of α and β. In the simplest picture the ionization is a transition from a neutral to an ionic electronic state, of which neither is vibrationally excited, i.e., an adiabatic transition. Such a transition yields a very narrow PE signal, since the kinetic energy of the photoelectrons is well defined by the adiabatic energies of the two states. A narrow signal may

also be observed when the vibrational structure and frequencies of the neutral excited and ionic states are nearly identical, so that the vibrational excitation in the neutral state is carried over to the ionic state in an adiabatic-like transition. However, if the degree of vibrational excitation in either electronic state is different, the relative energy gap between the two states changes, thus changing the energy of the PEs. The more severely the vibrational excitations differ, the broader the energy distribution becomes, as more and varying transitions become possible. Hence, it is reasonable to assume adiabatic(-like) transitions lead to β, yet signal α is the result of a vertical transition.

Calculation of Neutral State Transition Energies

The energy of the photoelectrons E_{el} depends on the transition energies of the neutral (E_{x}) and ionic states (IE_{i}) involved in the ionization process, as well as on the number and frequency of the probe photons (cf. Equation 3.1). Conversely, the energy of the neutral state excited prior to ionization can be calculated utilizing Equation 3.2, since signal β indicates an adiabatic transition and the adiabatic ionization energy to the D_0 state is known for 1,2,3-TriFB.

$$E_{\mathrm{x}} = IE_{\mathrm{i}} + E_{\mathrm{el}} - \hbar \times \omega_{\mathrm{probe}} \times n'. \tag{3.2}$$

In theory, the last state populated prior to ionization should be the S_1 state, as was concluded in the case of PFB.[9] After excitation of the S_1 state, Hüter et al.[9] observed a broad band α at $E_\alpha = 0.4$ eV and one narrow band β at $E_\beta = 0.8$ eV, both equally oscillating in intensity with respect to the delay time. Employing Equation 3.2 with an ionization energy of 9.64 eV,[18] a peak energy of $E_\beta = 0.8$ eV, and the energy of two probe photons at $\lambda_{\mathrm{probe}} = 402$ nm (6.18 eV) yielded a S_1 AEE of 4.26 eV (291 nm). Although the proposed AEE is ≈0.16 eV red-shifted to the onset of the UV absorption band, it fitted well to the AEE calculated at CASSCF/XMCQDPT2 level of theory. It was argued that the severe out-of-plane deformation of the molecular structure in the S_1 state considerably alters the transition probabilities from the planar ground state to the S_1 state. As a consequence, the adiabatic transition from the ground state minimum to the S_1 state minimum is essentially not observed in the UV spectrum.[9]

Calculation of the S_1 AEE of 1,2,3-TriFB based on the peak energy $E_\beta = 0.89$ eV of band β, the adiabatic ionization energy of the D_0 state $IE = 9.4$ eV, and the energy of two probe photons at $\lambda_{\mathrm{probe}} = 400$ nm (2×3.10 eV) yields 4.1 eV

(302 nm). This value deviates by 0.8 eV from the AEE estimated at RI-SCS-CC2 level of theory (4.91eV). As already discussed, the calculation greatly overestimates the AEE of 1,2,3-TriFB and thus this deviation comes at no surprise. Yet, the estimate is also located 0.6 eV below the first shallow peak at 4.68 eV (265 nm) in the S_1 absorption band and 0.4 eV red-shifted towards the band onset at ≈275 nm (4.51 eV). In accord with the conclusions drawn for PFB, the deviation may be the result of the deformed molecular structure in the S_1 state. However, while both molecules are planar in the ground state, the molecular structure of PFB in the S_1 state is deformed to considerably greater extent. One of the fluorine atoms is bent out of the plane by 33° and the other four atoms by 8° in the opposed direction.[9] In contrast, the centered fluorine atom of 1,2,3-TriFB is bent out-of-plane by 24°, while the others are nearly in-plane in the S_1 state. Therefore, the shift of the absorption band compared to the adiabatic transition energy between the S_0 and the S_1 state should be minimal for 1,2,3-TriFB. Consequently, the pronounced deviation between the estimated and the reported AEE suggests the S_1 state might not be the last state excited prior to ionization. Since the temporal behavior of the PE signals established no transition to a low-lying excited state happens, the unknown state has to be excited in the ionization process. Indeed, the required absorption of the two probe photons might be a stepwise process within the pulse duration of 90 fs. If molecules already excited by a pump photon absorb a single probe photon, totaling an energy of 8.06 eV, an intermediate high-lying neutral electronic state might be excited. Depending on the energy and the dynamics of the intermediate state, the observed energy E_{el} of the photoelectrons may be primarily determined by the intermediate state.[19,20] If the dynamics include ultrafast relaxation to a lower-lying minimum of the state or to another state within the probe pulse duration, the subsequent ionization by a second probe photon will result in PEs with less energy. The transition energy to such an intermediate state can be calculated by adding again E_β to the ionization energy, but only subtracting the energy of the second probe photon. For 1,2,3-TriFB, this yields 7.2 eV, which fits well to the calculated VEE of ≈7.3 eV of the $\pi\pi^*$ states 3 $^1A_1$ (S_7) or 2 $^1B_2$ (S_8, cf. Table 3.1). The electronic configuration is very similar for both states (cf. Table 3.2) and the states both correlate equally to the ionic states D_0 and D_1, so excitation of either state seems plausible. Though the direct transition from the S_1 state (1 $^1B_2$) to the S_7 state (3 $^1A_1$) is symmetry forbidden, the combined energy of one pump and one probe photon of 8.06 eV exceeds the

transition energy to the S_7 state by >0.8 eV. Thus, an initial population of an even higher-lying state and a subsequent relaxation to the S_7 state might still be a viable excitation route.

Excitation of intermediate states may also play a key role in the pathway leading to band α. The broad energy distribution of the $D_1 \leftarrow S_x$ transition would then indicate latter is of vertical type, i.e., the vibrational structure of the D_1 and the S_x state would show major differences. Owing to the diffuse nature of α and lacking further information for the intermediate and D_1 states, the exact pathway remains elusive. Hence, it is cautiously assumed that the pathways leading to the two PE signals both involve excitation of the same intermediate states, as schematically visualized in Figure 3.9.

Besides signals α and β, two overlapping bands γ at $E_\gamma = 1.5$ eV and δ at $E_\delta = 1.7$ eV are observed in the transient PES. These signals are only present at $\Delta t = 0.06$ ps and both vanish after just $\Delta t = 0.26$ ps. Furthermore, both signals are observed in the SC PES at $\lambda_{\text{probe}} = 400$ nm, too. Albeit it should be noted that the appearance of PE bands with the same energy in the SC and the transient ionization might be purely coincidental, it is more reasonable to assume the same origin. Two routes towards the signals seem feasible. First of all, the initial excitation of the S_1 state by either absorption of one pump or two probe photons might be followed by direct ionization, i.e., without excitation of any intermediate states. Second, and conversely, within the probe pulse duration an intermediate state is excited prior to ionization. The temporal behavior of the two signals hints towards the latter. The vanishing of both bands within $\Delta t = 0.26$ ps after excitation indicates ultrafast relaxation on the S_1 potential energy hypersurface efficiently prohibits the underlying ionization pathway. The rapid initial parent ion yield decay associated with the leaving of the FC region substantiates the proposal of such an ultrafast relaxation. If the relaxed structure would exhibit a potential energy too low to allow direct ionization by absorption of two probe photons, any other ionization pathway involving two probe photons would also be prohibited. The presence of signals α and β at later times shows that this is not the case. On the other hand, a potential intermediate state would be located at 8.0 eV. Since the combined energy of one pump and one probe photon of 8.06 eV barely exceeds 8.0 eV, relaxation may very well stop excitation of the state. Therefore, population of a highly excited intermediate state, followed by ionization to the D_0 state probably is the origin of signal δ. Due to the plethora of possible electronic states with calculated transition

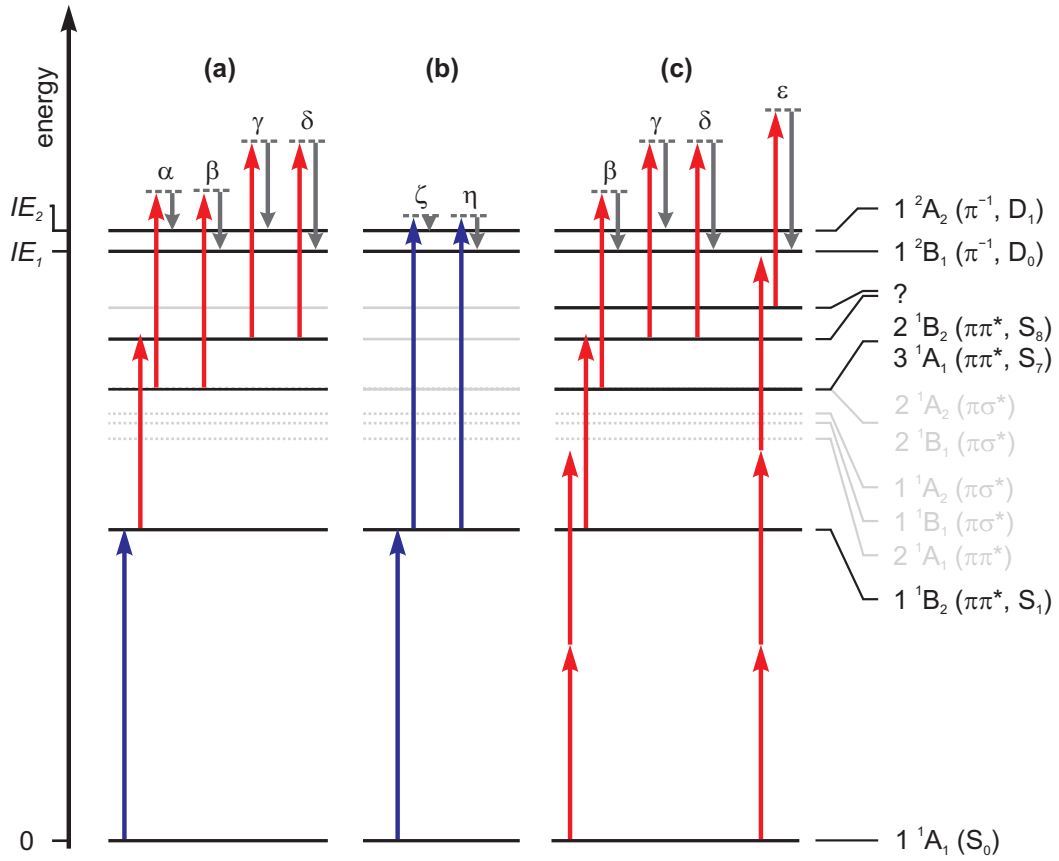

Figure 3.9. Proposed multi-color and single-color ionization schemes for 1,2,3-TriFB. The energies of the photons at $\lambda_{pump} = 250$ nm (blue) and $\lambda_{probe} = 400$ nm (red) and of the photoelectrons (grey) are depicted as vertical arrows. Solid black horizontal lines: experimentally intermediate and final states, solid and dotted (calculated values) grey horizontal lines: non-participating other intermediate states. **(a)** Transient ionization pathways by one-photon absorption to the S_1 state ($1\ ^1B_2$) and subsequent two-photon ionization to the D_0 ($1\ ^2B_1$) and D_1 states ($1\ ^2A_2$) showing the origin of PE peaks α–δ. **(b)** Single-color ionization pathways at $\lambda_{pump} = 250$ nm to the D_0 and D_1 states showing the origin of PE peaks ζ and η. **(c)** Single-color ionization pathways at $\lambda_{probe} = 400$ nm to the D_0 and D_1 states showing the origin of PE peaks β–ϵ.

energies of more than 7.5 eV (not shown for the sake of brevity) no specific state is assigned. The spacing of $\Delta E = 0.2$ eV between signals γ and δ suggests that the former results from the ionization to the D_1 state. Noteworthy, in the single-color case the excess energy of 9.3 eV in a three-photon transition also introduces sufficient energy for a direct population of the intermediate state.

Overall, the time-resolved PE signals enable valuable insight into the dynamics of the initially excited state S_1, the populated ionic states and the ionization mechanism. The data provide conclusive evidence that the S_1 neutral excited state is populated by absorption of a pump photon, and no internal conversion to a different low-lying excited state takes place. Within the probe pulse duration, one probe photon is absorbed, exciting high-lying intermediate state(s). The subsequent absorption of a second probe photon ionizes the molecules, leading to the ionic ground and the first excited ionic state. Determination of the true S_1 AEE via high-resolution spectroscopy will help to unravel whether the proposed mechanism is correct, since it would provide the actual minimum energy in the S_1 state. Regardless of the exact ionization pathways, the intermediate states only determine the shape and position of the PE bands, but not the observed dynamics, as they are only populated within the probe pulse duration. Therefore, it has to be emphasized that the observed oscillations of the parent ion yields must originate from dynamics on the potential energy hypersurface of the initially excited S_1 state.

Single-Color Ionization Pathways

In the case of the SC ionization at $\lambda_{\text{pump}} = 250$ nm, the excess energy introduced by the absorption of two photons (9.92 eV) suffices to populate the D_0 and the D_1 state. Subtracting the signal energies of $E_\zeta \approx 0.14$ eV and $E_\eta \approx 0.30$ eV from the energy of the two pump photons yield 9.78 eV and 9.62 eV, respectively, i.e., the energy remaining in the ions. Given that neither of the SC PES signals ζ and η are well-resolved, these values fit very well to the re-evaluated VIEs of the D_1 state at 9.73 eV and of the D_0 state at 9.55 eV. The lack of photoelectrons with the maximum available energy E^2_{avl} in the two-photon ionization process may hint towards excitation of the S_1 state as an intermediate state, as illustrated in Figure 3.9 (b).

In addition to the signals γ and δ, the SC ionization at $\lambda_{\text{probe}} = 400$ nm yields the band β, also observed in the transient PES, and a signal ϵ at $E_\epsilon = 2.2$ eV. The former shows that both in the transient and the SC ionization either the

3 $^1A_1$ (S_7) or 2 $^1B_2$ (S_8) state are excited in the ionization mechanism. However, two pathways leading to the state(s) are possible. Either the absorption of two photons first excites the S_1 state and subsequent absorption of an additional photon excites the intermediate state(s), or three photons are absorbed at once. Though the excitation of the S_1 state is deemed more likely, both pathways seem plausible. A distinct signal corresponding to α is not observed, probably due to the broad background towards $E_{\mathrm{el}} = 0$ eV. The signal ϵ presumably originates from three-photon excitation of another intermediate state at 8.5 eV. As for signals γ and δ, no specific state is assigned to the transition energy. The direct adiabatic $D_0 \leftarrow S_0$ ionization pathway seems to play a minor role, since only few electrons with the corresponding maximum available energy $E_{\mathrm{avl}}^{4'}$ are observed. The proposed ionization pathways leading to the signals are depicted in Figure 3.9 (c).

3.1.4 Origin of the Oscillations

1,2,3-TriFB is not the first fluorinated aromatic system reported to exhibit intense signal oscillations. Hüter et al.[9] observed a pronounced long-lived (>5 ps), single-frequency oscillation of the PFB parent ion yield, after excitation of the S_1 state ($\pi\pi^*$). Their analogous PES results revealed the transient parent ion yield solely maps the dynamics of the S_1 state. Furthermore, varying the excitation wavelength between 273 nm and 240 nm lead to the conclusion that shorter excitation wavelengths will shorten the oscillatory lifetimes, yet do not alter the frequencies.[9] As extensively outlined in Chapter 1, ab initio calculations at extended multi-configuration quasi-degenerate second-order perturbation theory (XMCQDPT2) level of theory in combination with electronic dynamics simulations unveiled the reason for the oscillation: intense multi-mode vibronic coupling between the $\pi\pi^*$ and the higher-lying $\pi\sigma^*$ state, mediated by out-of-plane vibrational modes.[9] The authors calculated the potential energy of the first $\pi\pi^*$ ($^1B_2$) and the first $\pi\sigma^*$ ($^1A_2$) states along the normal mode coordinates of the potential b_1 coupling modes. For four out of six considered modes, a pronounced double-well character of the S_1 state was proposed. In the well minima, the molecular structure is highly distorted and the electronic character of the state is a mixture of the coupled $\pi\pi^*$ and the $\pi\sigma^*$ states. Accordingly, the equilibrium structure in the S_1 state, optimized at RI-SCS-CC2 level of theory, reflects the distortion introduced by the b_1 out-of-plane modes. The maxima of

the barriers between the double-well minima are located at the FC region, which is quasi planar and corresponds to the molecular structure of the ground state.

In broadband femtosecond experiments a coherent wavepacket of coupling modes is excited in the S_1 state. As soon as the wavepacket leaves the FC region, the coupling takes effect. The coupling changes the vibrational ψ''_v and the electronic part ψ''_e of the wave function. Thus, the transition dipole moment $\boldsymbol{\mu}$ to a different electronic state, e.g., an ionic state, with an vibrational wave function ψ'_v and and electronic wave function ψ'_e, is altered. Consequently, the transition strength S between the states, shown in Equation 3.3

$$S = |\langle\psi'_v|\langle\psi'_e|\boldsymbol{\mu}|\psi''_e\rangle|\psi''_v\rangle|^2, \tag{3.3}$$

changes, i.e., is reduced, leading to decreased ion yields. The wavepacket moves further away from the FC region until it hits the outer energy barriers of the potential energy hypersurface. At this point the movement reverses back to the FC region, increasing the ion yield again. Ultimately, the oscillation of the ion yield is the direct observation of the wavepacket movement. The frequency of the oscillation is primarily determined by the most dominant coupling mode.[9,10]

The PES results of 1,2,3-TriFB show that the dynamics also exclusively take place at the potential energy hypersurface of the initially excited S_1 state ($\pi\pi^*$), in agreement with the dynamics of PFB, strongly indicating the observed intensity oscillations of the respective parent ion yields originates from the vibronic coupling between the $\pi\pi^*$ and a higher-lying $\pi\sigma^*$ state too. Of course, one could argue the oscillations might show quantum beating of certain vibrational modes.[21–31] However, the oscillational frequencies resulting from quantum beating are highly excitation-wavelength dependent. Albeit not performed for 1,2,3-TriFB, results presented for the three TFB isomers in Sections 3.2–3.4, for PFPh in Section 3.7, and for PFB[9] do not indicate any wavelength dependence of the oscillations in the studied systems. Therefore, it is reasonable to assign the oscillation in the transient signals of 1,2,3-TriFB to the vibronic coupling between the initially excited S_1 ($\pi\pi^*$) and a higher-lying $\pi\sigma^*$ state.

1,2,3-TriFB belongs to the C_{2v} point group. The first excited $\pi\pi^*$ and $\pi\sigma^*$ states show B_2 and B_1 symmetry, respectively, and can be coupled by a_2 modes. Yet, the energy gap of only 0.15 eV between the first and second $\pi\sigma^*$ states (cf. Table 3.1) renders coupling between the $\pi\pi^*$ and the second $\pi\sigma^*$ state plausible too. The latter has A_2 symmetry, so vibrational modes of b_1 symmetry might couple the

states. Calculation of the vibrational frequencies in the S_1 state at RI-SCS-CC2 level of theory reveals that the lowest-energy a_2 and b_1 modes exhibit frequencies of $\nu_{14}^{1,2,3\text{-TriFB}} = 153\ \text{cm}^{-1}$ and $\nu_{20}^{1,2,3\text{-TriFB}} = 69\ \text{cm}^{-1}$ (cf. Figure 3.5), respectively. The frequency of the b_1 mode fits substantially better to the observed oscillational frequency of the transient ion yield of $\nu_{\text{osc}}^{1,2,3\text{-TriFB}} = 70\ \text{cm}^{-1}$. Furthermore, it is expected for the optimized molecular structure in the S_1 state of 1,2,3-TriFB to show the same symmetry as the coupling modes, analogous to the results of PFB. As depicted in Figure 3.5 and discussed (*vide supra*), the deformed molecular structure in the S_1 state of 1,2,3-TriFB essentially is of b_1 symmetry. Based on the comparison of the oscillational and vibrational frequencies and the molecular structures, the b_1 modes are assigned to be the coupling modes. Surprisingly, the coupling between the $\pi\pi^*$ and the second, not the first, $\pi\sigma^*$ state seems to dominate the observed dynamics, in contrast to the coupling mechanism of PFB. The comparison of the molecular structures and the vibrational modes hence proves to be a valuable tool to gain further insight into the coupling dynamics.

3.2 1,2,4,5-Tetrafluorobenzene

3.2.1 Molecular and Electronic Structure

In Figure 3.10 the UV absorption spectrum of 1,2,4,5-TFB is depicted. A pronounced and structured absorption band is observed. The band is centered at 265 nm (4.68 eV). The first feature of the structure peaks at 274 nm (4.53 eV), which corresponds to the AEE, confirmed by high-resolution spectroscopy.[32–34] Transitions to the fundamental and to overtones of the totally symmetric ν_4 vibrational mode (cf. Table B.2) shape the structure.[33,35] A second major band begins to rise below 220 nm, yet cannot be further characterized.

Neutral States

To assign the fully resolved absorption band to an electronic state, the VEEs to the first eight neutral electronic states were calculated at RI-SCS-CC2 level of theory. The results are listed in Table 3.4. The first excited state exhibits $\pi\pi^*$ character (S_1, $1\ ^1B_{2u}$) and an estimated VEE of 4.92 eV (252 nm). The S_2 state ($1\ ^1B_{1g}$) is of $\pi\sigma^*$ character, with a calculated VEE of 6.45 eV (192 nm). A second $\pi\pi^*$ state (S_3, $1\ ^1B_{1u}$) is located at 6.46 eV (192 nm), nearly isoenergetic with the S_2 state. The higher-lying states are either of $\pi\pi^*$ or $\pi\sigma^*$ character, exhibiting calculated VEEs of more than 7 eV (<177 nm). Although these states are irrelevant for the assignment of the absorption bands, the photoelectron spectra indicate that the S_8 state ($\pi\pi^*$, $2\ ^1B_{2u}$) at 7.55 eV might be populated as an intermediate state in the multi-color ionization process (*vide infra*).

Based on the calculated VEEs, the first absorption band is assigned to the S_1 state ($\pi\pi^*$). The band arising below 220 nm is attributed to the absorption of the S_3 state ($\pi\pi^*$). These assignments are in line with the assignment in the literature.[36,38] For both states the calculated transition energies overestimate the actual values by ≈0.25 eV. In fact, the calculated VEEs of all states exceed the experimental transition energies (cf. Table 3.4), fitting well to the previously discussed tendency of RI-SCS-CC2 to overestimate the electronic transition energies for fluorobenzenes.[9,10] The discrepancies range from 0.24 eV for the S_1 state to 0.79 eV for the S_5 state. However, higher transition energies do not correspond to bigger energy differences, and no clear trend regarding the discrepancies becomes apparent. Furthermore, it should be noted that a VEE of 5.70 eV (218 nm) to the S_2 state ($\pi\sigma^*$) was reported, based on an unpublished

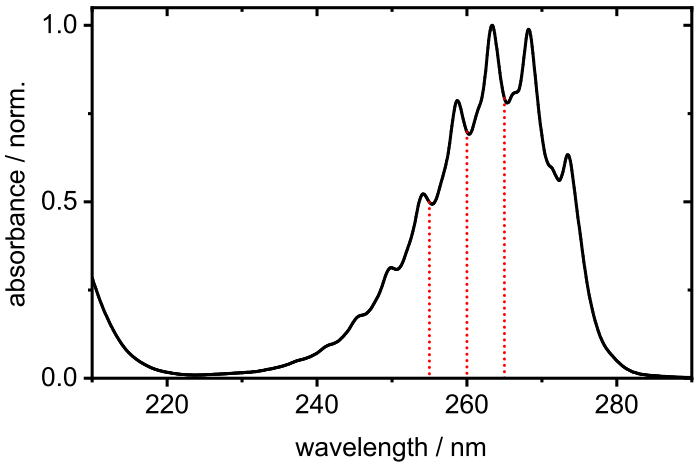

Figure 3.10. Normalized gas-phase UV absorption spectrum of 1,2,4,5-TFB. The dotted red lines indicate the chosen excitation wavelength of $\lambda_{\text{pump}} = 265$–$255$ nm to excite the S_1 state ($\pi\pi^*$).

Table 3.4. Vertical excitation energies (VEE) and oscillator strengths f (in parentheses) of the first eight neutral electronically excited states, the ionic ground state and the first two ionic electronically excited states for 1,2,4,5-TFB, calculated at RI-SCS-CC2 level of theory. Where available, the respective adiabatic energy (AEE) is listed. Experimental energies are given if possible.

	symm.	calc. VEE eV	calc. AEE eV	exp. VEE eV	exp. AEE eV
S_1 ($\pi\pi^*$)	$1\,^1B_{2u}$	4.92 (0.0333)	4.65	4.68[a,†]	4.53[d–f]
S_2 ($\pi\sigma^*$)	$1\,^1B_{1g}$	6.45 (0.0000)		5.70[b]	
S_3 ($\pi\pi^*$)	$1\,^1B_{1u}$	6.46 (0.0016)		6.20[a,c]	
S_4 ($\pi\sigma^*$)	$1\,^1B_{2g}$	7.21 (0.0000)			
S_5 ($\pi\sigma^*$)	$1\,^1B_{3u}$	7.29 (0.0104)		6.50[a,c]	
S_6 ($\pi\pi^*$)	$2\,^1B_{1u}$	7.39 (0.6711)		6.85[c]	
S_7 ($\pi\sigma^*$)	$2\,^1B_{1g}$	7.44 (0.0000)			
S_8 ($\pi\pi^*$)	$2\,^1B_{2u}$	7.55 (0.6455)		7.20[†] / 7.26[a,c]	
D_0 (π^{-1})	$1\,^2B_{1g}$	9.58	9.30		9.38[c,f–k]
D_1 (π^{-1})	$1\,^2B_{2g}$	10.60	10.42		10.04[g]
D_2 (π^{-1})	$1\,^2B_{3u}$	12.85	12.65		12.35[g]

[a] Ref. [36] [b] Ref. [37], based on unpublished absorption spectra. [c] Ref. [38]
[d] Ref. [32] [e] Ref. [33] [f] Ref. [34] [g] Ref. [18] [h] Ref. [39] [i] Ref. [40] [j] Ref. [41]
[k] Ref. [42] [†] this work

absorption spectrum.[37] The absorption spectrum herein does not feature an distinct band for the symmetry-forbidden transition. Therefore, the suggested experimental VEE to the S_2 state cannot be confirmed.

Optimizations of the molecular structure in the neutral ground state yielded a planar structure. Employing Mulliken's notation,[4] 1,2,4,5-TFB hence belongs to the D_{2h} point group. Contrary, the S_1 state structure shows an out-of-plane deformation. As the comparison of the structures in Figure 3.11 shows, only four out of the six carbon atoms (atoms 7, 8, 10 and 11) are in plane in the S_1 state. The angle between said plane and the two remaining carbon atoms 3 and 6 is 3°. Additionally, the two hydrogen atoms are bent out-of-plane by 12° and all four fluorine atoms by −8°. The calculated structure is in good agreement with structures proposed before.[32–34,41,43] Noteworthy, the deformation is less pronounced than for most other fluorobenzenes, e.g., PFB, for which one of the fluorine atoms is bent 33° out of the plane.[9] Based on the optimized structures, a $S_1 \leftarrow S_0$ adiabatic excitation energy of 4.68 eV (265 nm) was calculated, overestimating the experimental AEE of 4.53 eV (274 nm).[32–34] For the sake of consistency, illustrations of the displacement vectors of the out-of-plane vibrational modes and the respective calculated frequencies in the S_1 state are also given Figure 3.11. A comprehensive list of the calculated frequencies of the vibrational modes in the S_0 state, in the S_1 state, and in the ionic states D_0–D_2 of 1,2,4,5-TFB is given in Table B.2 in the appendix.

Ionic States

In addition to the neutral states, the vertical ionization energies to the first three ionic states were calculated. The calculated VIE to the ionic ground state (D_0, 1 $^2B_{1g}$) is 9.58 eV. The first excited ionic state D_1 (1 $^2B_{2g}$) is placed at 10.60 eV. The second excited ionic state D_2 (1 $^2B_{3u}$) is well separated from the first two states by more than 2 eV and exhibits a predicted VIE of 12.85 eV. All ionic states show π^{-1} character.

Likewise to the molecular structure in the neutral ground state, the molecules are planar in all three ionic states (not shown for the sake of brevity). 1,2,4,5-TFB thus is the only molecule in this Thesis for which optimization of the structures in the excited ionic states converged. The calculations yielded an AIE of 9.30 eV for the $D_0 \leftarrow S_0$ transition, underestimating the actual AIE of 9.38 eV,[18,34,38–42] though not by a huge margin. The calculated AIE to the D_1 (10.42 eV) and the

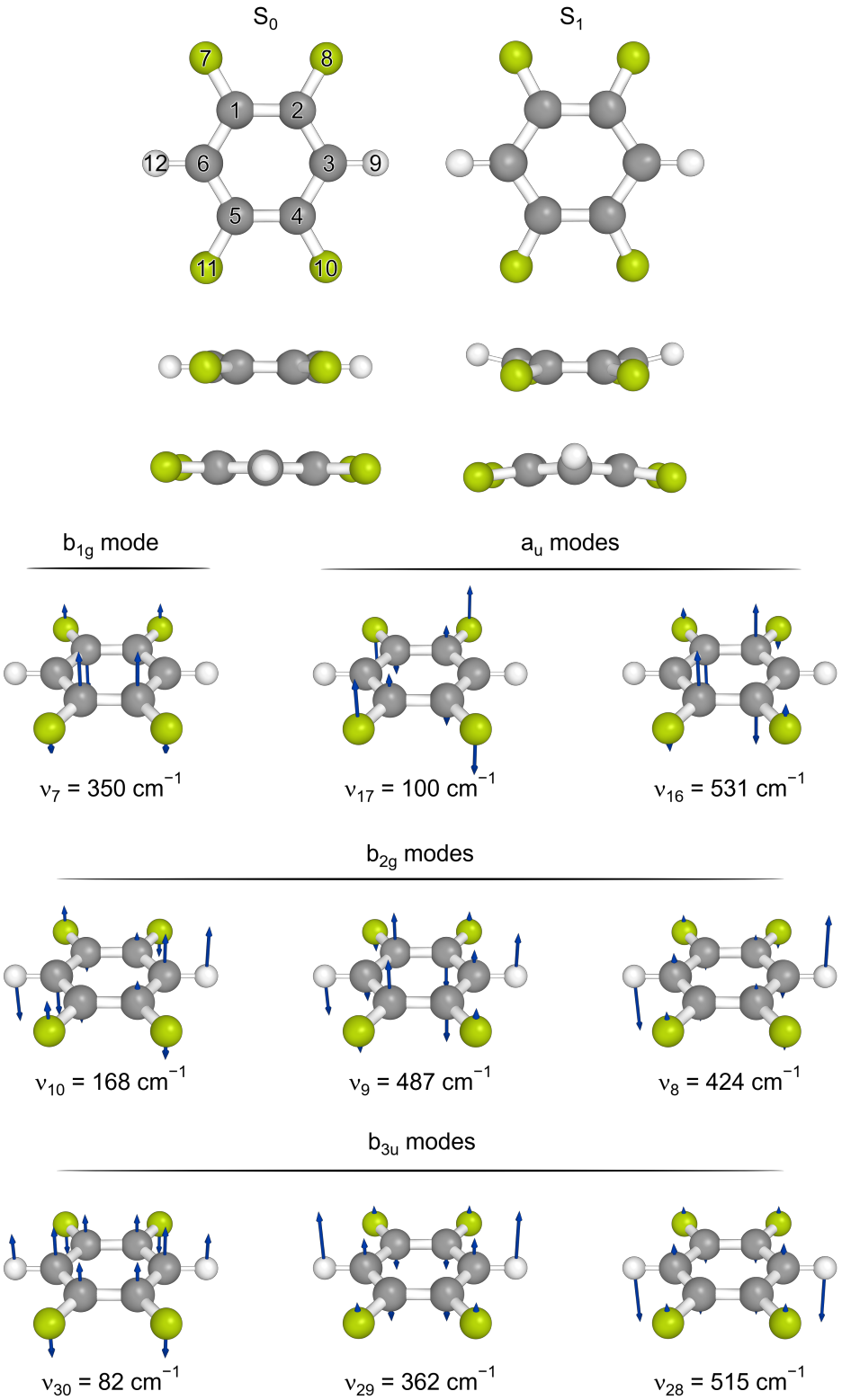

Figure 3.11. Calculated molecular structures of 1,2,4,5-TFB in the S_0 and the S_1 state ($\pi\pi^*$), optimized at the RI-SCS-MP2 and RI-SCS-CC2 levels of theory, respectively. The calculated displacement vectors of the out-of-plane modes are illustrated by blue arrows. Their respective frequencies in the S_1 state are listed.

D_2 state (12.65 eV) exceed the experimentally observed AIEs by ≈0.4 eV (cf. Table 3.4).

3.2.2 Time-Resolved Time-of-Flight Mass Spectra

To unravel the dynamics of the S_1 state, the molecules were excited at $\lambda_{\text{pump}} = 260$ nm and ionized at either $\lambda_{\text{probe}} = 400$ nm or $\lambda_{\text{probe}} = 800$ nm. Furthermore, 1,2,4,5-TFB was also excited at $\lambda_{\text{pump}} = 265$ nm and $\lambda_{\text{pump}} = 255$ nm, followed by ionization at 800 nm. The calculations highlight that for all three chosen excitation wavelengths the S_1 state is selectively excited.

Independent of the ionization wavelength, an ultrafast, but shallow initial signal decay for the transient parent ion yield of 1,2,4,5-TFB is observed after excitation at $\lambda_{\text{pump}} = 260$ nm, shown in Figure 3.12. The applied model fit functions yield decay constants of

$$\tau_1^{\text{1,2,4,5-TFB}} = 0.2\text{–}0.4 \text{ ps}.$$

The complete sets of fit parameters at all different wavelengths are listed in Table 3.5. Subsequent to the initial decay, the signal pattern depends on the ionization wavelength and on the polarization of the probe pulses. When choosing $\lambda_{\text{probe}} = 800$ nm and the default parallel polarization (∥) to the detector surface, a signal rise is observed. The corresponding rise time was determined to be

$$\tau_{\text{rise}}^{\text{1,2,4,5-TFB}}(800 \text{ nm}) = 1 \text{ ps}.$$

In contrast, no delayed rise was observed when rotating the polarization to be perpendicular (⊥) to the detector surface (cf. Figure 3.12 (e–f)) or probing at $\lambda_{\text{probe}} = 400$ nm (polarization parallel to the detector surface). The decay of the parent ion yield following the delayed rise is again independent of the ionization wavelength and the polarization. The signals are well described by two decay constants

$$\tau_2^{\text{1,2,4,5-TFB}} = 2 \text{ ps}$$
$$\tau_4^{\text{1,2,4,5-TFB}} = 2600 \text{ ps}.$$

It should be noted that description of the ion yield decay at $\lambda_{\text{probe}} = 800$ nm($\perp$) does not require the short decay constant $\tau_1^{\text{1,2,4,5-TFB}}$. The reason for this remains elusive.

The transient parent ion yields after excitation at $\lambda_{\text{pump}} = 265$–$255$ nm are shown in Figure 3.13. These slight changes of the excitation wavelengths do not alter the number of decay constants. However, the decay times slightly increase to

$$\tau_1^{\text{1,2,4,5-TFB}}(265\text{ nm}) = 0.65\text{ ps},$$
$$\tau_{\text{rise}}^{\text{1,2,4,5-TFB}}(265\text{ nm}) = 1.24\text{ ps},$$
$$\tau_2^{\text{1,2,4,5-TFB}}(265\text{ nm}) = 2.24\text{ ps},$$

and

$$\tau_4^{\text{1,2,4,5-TFB}}(265\text{ nm}) = 2616\text{ ps}$$

at $\lambda_{\text{pump}} = 265$ nm. In contrast, a decrease to

$$\tau_1^{\text{1,2,4,5-TFB}}(255\text{ nm}) = 0.31\text{ ps},$$
$$\tau_{\text{rise}}^{\text{1,2,4,5-TFB}}(255\text{ nm}) = 0.74\text{ ps},$$
$$\tau_2^{\text{1,2,4,5-TFB}}(255\text{ nm}) = 0.73\text{ ps},$$

and

$$\tau_4^{\text{1,2,4,5-TFB}}(255\text{ nm}) = 1351\text{ ps}$$

is observed at $\lambda_{\text{pump}} = 255$ nm. Hence, the time constants evident the mere change of the excitation wavelength by 5 nm from 260 nm to 255 nm halves the overall $\pi\pi^*$ state lifetime. This trend will be further discussed in Section 3.10.

3.2.3 Origin of the Signal Rise

Shortly summarizing, a delayed rise of the parent ion yield is observed for 1,2,4,5-TFB, independent of the excitation wavelength, but exclusively at $\lambda_{\text{probe}} =$

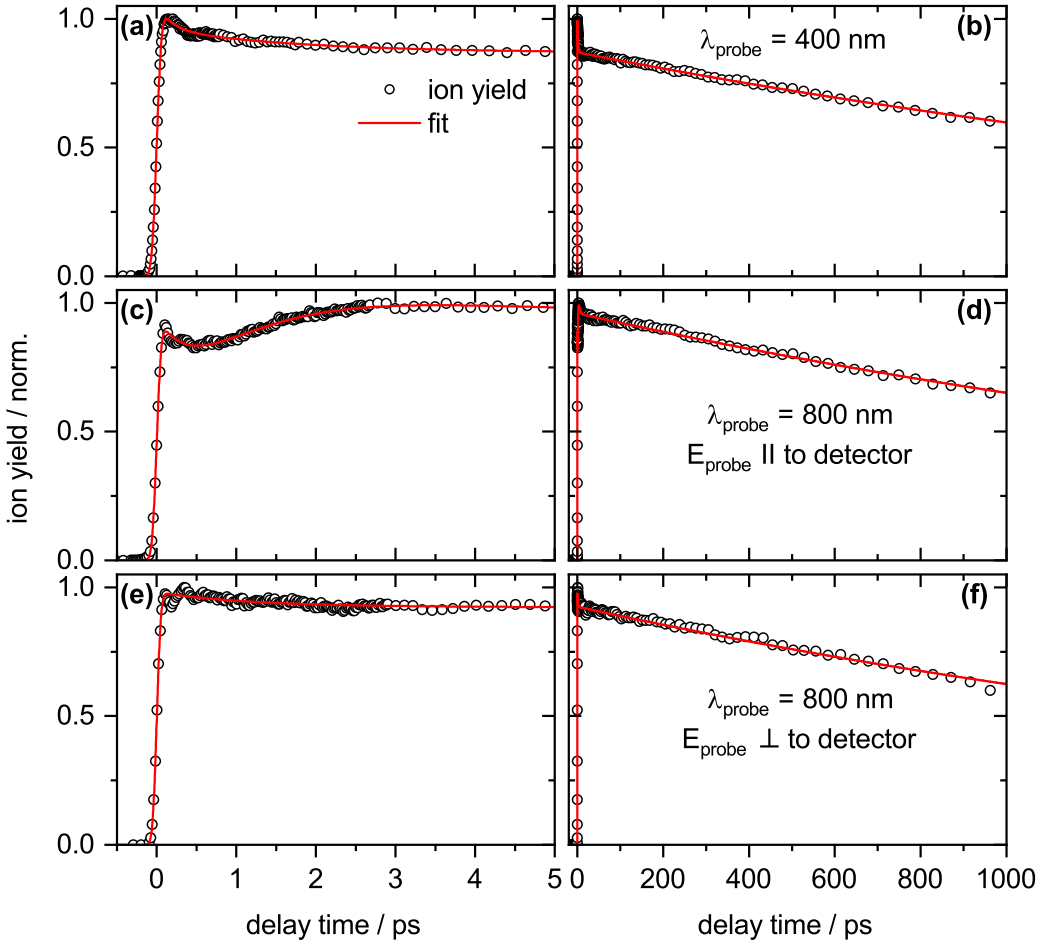

Figure 3.12. Measured transient parent ion yield signals (black circles) and applied fit model functions (red lines) for 1,2,4,5-TFB after excitation at $\lambda_{pump} = 260$ nm and ionization at $\lambda_{probe} = 400$ nm **(a–b)** resp. $\lambda_{probe} = 800$ nm **(c–f)**. The left-hand column shows the data in the first five picoseconds, the right-hand column in the first nanosecond after excitation. The fit parameters are listed in Table 3.5. The probe polarizations at $\lambda_{probe} = 800$ nm were varied from the default $\parallel$ polarization to the detector surface (panels **(c)**, **(d)**) to $\perp$ to the detector surface (panels **(e)**, **(f)**).

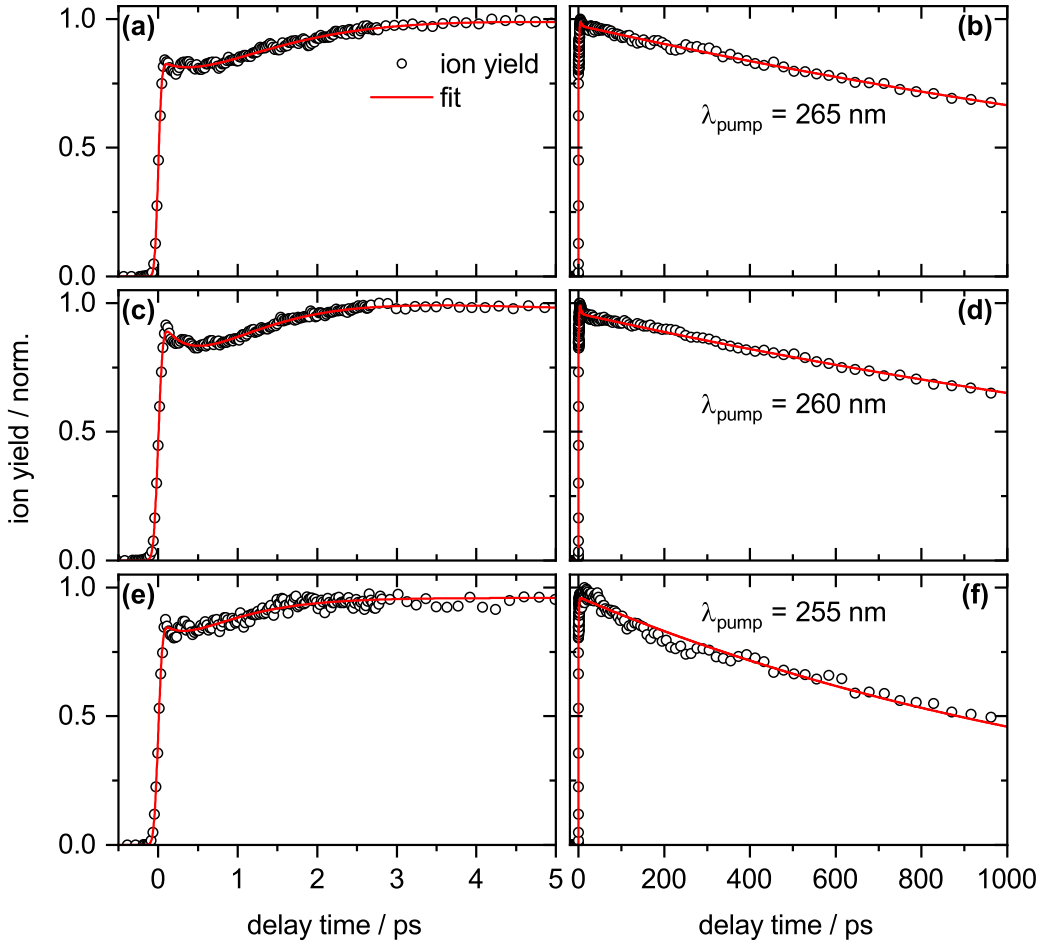

Figure 3.13. Measured transient parent ion yield signals (black circles) and applied fit model functions (red lines) for 1,2,4,5-TFB after excitation at $\lambda_{pump} = 265$ nm **(a–b)**, $\lambda_{pump} = 260$ nm **(c–d)**, and $\lambda_{pump} = 255$ nm **(e–f)** and ionization at $\lambda_{probe} = 800$ nm. The left-hand column shows the data in the first five picoseconds, the right-hand column in the first nanosecond after excitation. The fit parameters are listed in Table 3.5.

Table 3.5. Parameters for the fits of the transient parent ion yields of 1,2,4,5-TFB after excitation at $\lambda_{pump} = 260$ nm and ionization at $\lambda_{probe} = 400$ nm, as well as fit parameters after excitation at $\lambda_{pump} = 265$–255 nm ionization at $\lambda_{probe} = 800$ nm (polarization $\parallel$ and $\perp$ to detector plane). 2σ fit errors are given in parentheses. If no error is given the value was set fixed.

λ_{pump} nm	pr. pol.	σ_{IRF} fs	A_1 %	τ_1 ps	A_2 %	τ_2 ps	A_4 %	τ_4 ps	τ_{rise} ps
$\lambda_{probe} = 400$ nm									
260		48(1)	9(1)	0.17(5)	9(1)	1.76(26)	82(1)	2662(43)	
$\lambda_{probe} = 800$ nm									
265		35(1)	29	0.65(1)	17	2.24(7)	54	2616(59)	1.24
260	$\parallel$	45(1)	34	0.46(19)	16	2.2(18)	50(1)	2575(52)	1.01(86)
	$\perp$	41(2)			6(1)	1.15(24)	94	2547(71)	
255		42(4)	15	0.31(4)	33	0.73(3)	52	1351(44)	0.74

800 nm, if the probe pulse polarization is set parallel to the detector surface. No other molecule in this Thesis shows such a delayed rise or polarization dependence of the ion yield, as will be shown by way of example on 1,2,3,4-TFB in Section 3.4.

The delayed rise must be a result of the ionization process, because the excitation conditions were kept identical when altering the probe pulse polarization. After excitation of the S_1 state, four additional photons at $\lambda_{probe} = 800$ nm are needed to ionize the molecules. If these four photons are not absorbed in a single step, but a (resonant) intermediate state is excited within the probe pulse duration, the subsequent ionization is facilitated, resulting in a higher ion yield.[44–46] Such an intermediate state might be excited via absorption of one, two or three probe photons. Based on the results at $\lambda_{probe} = 400$ nm ($\parallel$ polarization to the detector surface), which did not yield a delayed rise, the absorption of two photons can be ruled out. The energy of one probe photon (1.55 eV) suffices to excite either the S_2 ($\pi\sigma^*$) or the S_3 state ($\pi\pi^*$, cf. Table 3.4). If three photons are absorbed (4.65 eV), the excess energy enables excitation of a plethora of electronic states. Thus, the absorption of one or three photons both allow excitation of potential intermediate states and both possibilities appear feasible. In theory, polarization dependent differences in the photoelectron distributions, mapped via velocity map imaging, might reveal the exact ionization pathways. Unfortunately, the $\perp$-polarized pulses rotate the z-axis of the photoelectron dis-

tribution to be perpendicular to the detector surface, prohibiting reconstruction of the energy distribution.[47–49] As a consequence, the employed experimental conditions do not allow to disentangle the proposed pathways. Changing the ionization wavelength to, e.g., $\lambda_{\text{probe}} = 267$ nm (4.65 eV) in future studies to stop the direct excitation of any low-lying intermediate states may thus be the most promising option to gain further insight into the origin of the delayed rise.

Noteworthy, the polarization dependence suggests an alignment of the molecules in the molecular beam, since an ensemble of randomly aligned molecules should yield polarization independent signals. The intensities of the pump and the probe beam are both insufficient to force such an alignment.[50,51] Nevertheless, the transition probability to an excited state is increased if the transition dipole moment is parallel to the polarization direction of the laser pulse. Therefore, molecules for which the direction of the transition dipole moment coincides with the polarization of the pulses are predominantly excited and the excitation of the S_1 state intrinsically introduces a selection of molecular orientation.[52,53] In the case of 1,2,4,5-TFB, the S_1 state shows B_{2u} symmetry. According to the character table of the D_{2h} point group, the transition dipole moment thus should lay along the y-axis of the molecule, i.e., the axis in between the neighboring fluorine atoms. Hence, the excitation probably is increased if said axis is parallel to the pulse polarization. Moreover, the delay of the signal rise indicates excitation to the intermediate state is not only polarization-, but also time-dependent. Thus, some kind of rearrangement has to happen after excitation of the S_1 state before the intermediate state can subsequently be excited. The structure optimizations predict 1,2,4,5-TFB to be slightly out-of-plane distorted in the S_1 equilibrium structure, in contrast to the planar configuration in the ground state (*vide supra*). The structural deformation is an effect of the weak coupling between the excited S_1 state ($\pi\pi^*$) and the S_2 state ($\pi\sigma^*$), which will be discussed in detail in Section 3.10. It seems plausible that the intermediate state might only be accessible after the molecule is deformed.

In summary, the unique polarization dependent dynamics of 1,2,4,5-TFB are likely the result of the multi-photon nature of the ionization process. Shortly after the initial excitation of the S_1 state by the pump pulse, either one or three additionally absorbed photons at $\lambda_{\text{probe}} = 800$ nm excite an intermediate state. Although the detailed mechanism can only be assumed, rearrangement of the molecular structure in the S_1 state might facilitate population of said intermediate

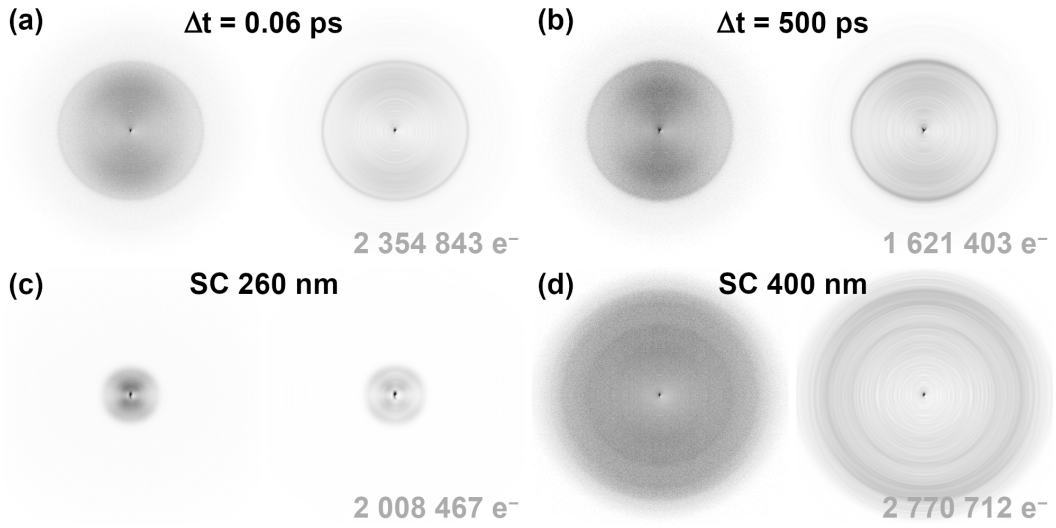

Figure 3.14. Photoelectron images (left) and their corresponding meridional slices through the recovered three-dimensional photoelectron distributions (right) of 1,2,4,5-TFB. **(a)** At $\Delta t = 0.06$ ps after excitation at $\lambda_{\text{pump}} = 260$ nm and ionization at $\lambda_{\text{probe}} = 400$ nm and **(b)** at $\Delta t = 500$ ps. **(c–d)** High-intensity single-color photoelectron images obtained at 260 nm **(c)** and 400 nm **(d)**.

state. However, elucidating the exact ionization pathway is beyond the scope of this Thesis.

3.2.4 Time-Resolved Photoelectron Images

The PE images resulting of the transient pump–probe process at $\lambda_{\text{pump}} = 260$ nm and $\lambda_{\text{probe}} = 400$ nm for 1,2,4,5-TFB, shown in Figure 3.14 at $\Delta t = 0.06$ ps (a) and at $\Delta t = 500$ ps (b), exhibit a strong diffuse signal, followed by a narrow ring. Based on the PES shown in Figure 3.15 (a), these two signals α and β peak at $E_\alpha = 0.5$ eV and $E_\beta = 0.92$ eV, respectively.

The high-intensity single-color PEI at $\lambda_{\text{pump}} = 260$ nm (Figure 3.14 (c)) shows two low-energy signals ζ and η, peaking at $E_\zeta = 0.04$ eV and $E_\eta = 0.13$ eV (cf. Figure 3.15 (c)). The SC ionization at $\lambda_{\text{probe}} = 400$ nm yields a broad background (Figure 3.14 (d)). Only two distinct signals β and γ on top of the background are observed, peaking at $E_\beta = 0.92$ eV and $E_\gamma = 1.7$ eV, as depicted in Figure 3.15 (d).

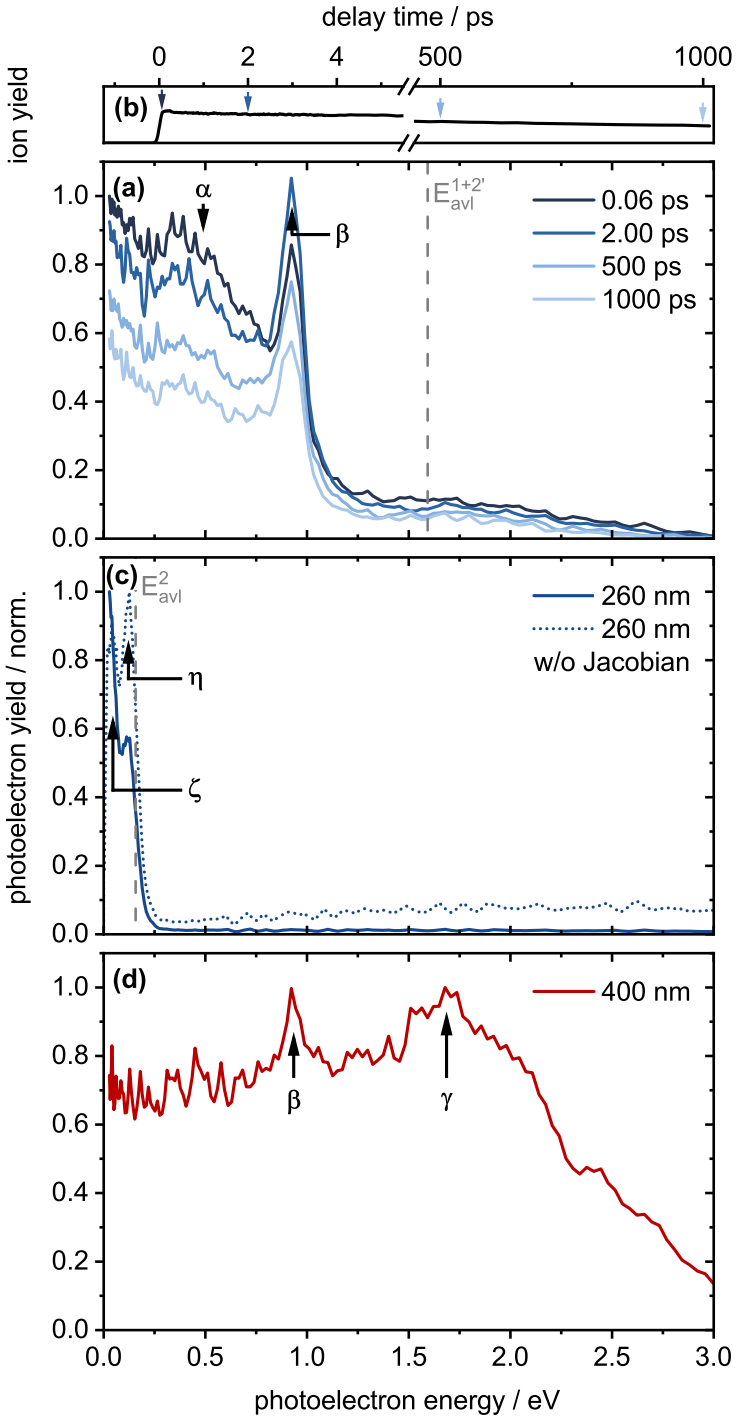

Figure 3.15. **(a)** Transient PE spectra of 1,2,4,5-TFB after excitation at $\lambda_{\text{pump}} = 260$ nm and ionization at $\lambda_{\text{probe}} = 400$ nm. The two main photoelectron signals labeled α and β are observed at $E_\alpha = 0.5$ eV and $E_\beta = 0.92$ eV. The grey dotted line indicates the maximum available photoelectron energy $E_{\text{avl}}^{1+2'}$ associated with the $D_0 \leftarrow S_0$ transition by $1 + 2'$ ionization. **(b)** Corresponding transient parent ion yields adapted from Figure 3.12 (a). Arrows mark the delay time $\Delta t = 0$–1000 ps at which the PES were obtained. **(c–d)** Single-color PE spectra taken at higher 260 nm pump **(c)** and 400 nm probe **(d)** intensities. Solid lines show the PE spectra with Jacobian transformation, dotted lines without. The additional signals γ, ζ, and η are located at $E_\gamma = 1.7$ eV, $E_\zeta = 0.04$ eV, and $E_\eta = 0.13$ eV. The grey dotted line indicates the maximum available photoelectron energies E_{avl} generated by two 260 nm photons (E_{avl}^2). At 400 nm the max. available energy is 3.02 eV.

Multi-Color Ionization Pathways

In agreement with previous assignments (cf. Section 3.1 and Ref. [9]), the narrow band β is attributed to the transition to the D_0 state and the broad band α to the transition to the D_1 state. The energy difference between $E_\alpha = 0.5$ eV and $E_\beta = 0.92$ eV of >0.4 eV fits reasonably well to the energy gap between the ionic states of ≈0.7 eV (cf. Table 3.4). Even though the absence of additional signals rising in at any delay time indicates that the deactivation of the initially excited S_1 state does not involve population of any other excited state, the ionization pathway, on the other hand, might.

To understand the underlying ionization mechanism, the energy of the state excited prior to ionization can be calculated via Equation 3.2 in Section 3.1. Subsequent to the excitation of the S_1 state by the pump pulse, two additional probe photons are needed for the direct $D_0 \leftarrow S_1$ ionization transition. The sum of the AIE to the D_0 state of 9.38 eV[18,34,38–42] and the energy E_β, minus the energy of two probe photons at $\lambda_{probe} = 400$ nm (2×3.10 eV) should yield the AEE of 4.53 eV.[32–34] However, the actual result is 4.10 eV. The energy difference of 0.43 eV essentially rules out the direct ionization mechanism. Subtracting the energy of just one probe photon yields 7.20 eV, which fits near perfectly to the intense VUV absorption maximum of the S_8 state ($\pi\pi^*$, $2\ ^1B_{2u}$) at 7.26 eV.[36,38] Therefore, the difference between the calculated and the reported S_1 AEEs probably is the result of the multi-color and -photon excitation of an intermediate state in the ionization process. Noteworthy, the direct transition between the S_1 ($1\ ^1B_{2u}$) and the S_8 state ($2\ ^1B_{2u}$) is symmetry forbidden. Yet, the combined energy of one pump and one probe photon of 7.87 eV exceeds the transition energy to the intermediate state by >0.6 eV, thus a different highly excited state might be excited which deactivates ultrafast into the S_8 state.

The pathway to the second signal α is more ambiguous. It is reasonable to assume that ionization to the D_1 state also involves excitation of the intermediate state S_8, since the electronic configuration of the state corresponds to both the D_0 and the D_1 state (cf. Table 3.6). The broad energy distribution of signal α would consequently indicate a vertical $D_1 \leftarrow S_8$ transition, i.e., the vibrational structure of the D_1 and the S_8 state would show major differences. Fortunately, the optimization of the molecular structure in the D_1 state converged for 1,2,4,5-TFB. Both the calculated molecular structure and vibrational frequencies of the D_1 state are very similar to the structure and frequencies in the D_0 state (cf. Table B.2 in the appendix). Since the $D_0 \leftarrow S_8$ transition is adiabatic and given

Table 3.6. Molecular orbital configuration and their weighted contributions to the S_1, S_2, and S_8 states and the first three ionic states of 1,2,4,5-TFB. Correlations between the neutral and the ionic states according to Koopmans's theorem are given.

neutral state	2 b_{3u} (π)	2 b_{2g} (π)	2 b_{1g} (π)	3 b_{3u} (π^*)	2 a_u (π^*)	10 a_g (σ^*)	11 a_g (σ^*)	weight (%)	corr. ion. state
S_0 ($^1A_1$)	2	2	2						
S_1 ($^1B_{2u}$, $\pi\pi^*$)	2	2	1	1				70	D_0
	2	1	2		1			23	D_1
S_2 ($^1B_{1g}$, $\pi\sigma^*$)	2	2	1			1		57	D_0
	2	2	1				1	15	
S_8 ($^1B_{2u}$, $\pi\pi^*$)	2	1	2		1			69	D_1
	2	2	1	1				21	D_0
ionic state									
D_0 ($^2B_{1g}$, π^{-1})	2	2	1						
D_1 ($^2B_{2g}$, π^{-1})	2	1	2					98	
D_2 ($^2B_{3u}$, π^{-1})	1	2	2					84	

the similarities of the ionic states, a vertical transition to the D_1 state would be rather surprising. Three alternative ionization pathways appear feasible. First of all, the assignment of signal α to the transition to the D_1 state might be wrong and the signal actually originates from the excitation of an unknown high-lying intermediate state within the probe pulse duration, followed by the vertical transition to the D_0 state. Such a state would be located at ≈7 eV based on the AIE to the D_0 state and the band onset at $E_\alpha \approx 0.7$ eV, fitting reasonably well to the transition energy of the S_6 state ($\pi\pi^*$) at 6.85 eV.[38] However, the D_1 state is energetically accessible at the chosen wavelengths and essentially all potential intermediate states electronically correspond to both ionic states D_0 and D_1 (not shown for the sake of brevity). Therefore, total absence of D_1 population is deemed unlikely. Second, a vertical, but direct $D_1 \leftarrow S_1$ transition might be observed. Though the possibility cannot be ruled out, a likewise direct transition to the D_0 state should probably be expected, which should give rise to an additional PE band. Finally, another intermediate state S_x might be excited besides the S_8 state. Based on the band onset at $E_\alpha \approx 0.7$ eV and the adiabatic ionization energy of the D_1 state (10.04 eV)[18], the state would be located at ≈7.6 eV. Neither the calculations herein nor the experimental results in the

literature[36] hint towards a specific electronic state within the myriad of potential intermediate states at transition energies >7.6 eV. Even though it remains elusive why no transition between this merely characterized intermediate state and the D_0 state is observed, the excitation of the state is the most plausible of all presented options. The expected signal corresponding to the $D_1 \leftarrow S_8$ transition probably vanishes within the broad electron distribution of band α. Ultimately, the diffuse nature of band α and lacking further information on the intermediate states prohibit unraveling the exact origin of signal α. Hence, it can also not be resolved if the deactivation of the unknown state leads to the S_8 state and consequently to signal β.

Overall, the initial excitation of the S_1 state is followed by the absorption of a single probe photon within the probe pulse duration, as schematically visualized in Figure 3.16. The introduced excess energy suffices to excite one unknown intermediate state and the S_8 state ($\pi\pi^*$, 2 $^1B_{2u}$). Subsequent absorption of a second probe photon ionizes the molecules and leads to bands α and β via population of the D_1 and the D_0 state.

Single-Color Ionization Pathways

SC two-photon ionization at $\lambda_{pump} = 260$ nm (9.54 eV) yields two signals at $E_\zeta = 0.04$ eV and $E_\eta = 0.13$ eV. The latter is assigned to the adiabatic $D_0 \leftarrow S_0$ ionization, expected to yield PEs with an energy of 0.16 eV. The spacing of 0.09 eV (725 cm^{-1}) between ζ and η fits well to a totally symmetric a_g mode with a frequency of 729 cm^{-1} of the ionic ground state, reported by Sato et al.[41] As an intermediate step, the S_1 state might be excited by absorption of a single pump photon, illustrated in Figure 3.16 (b).

SC ionization at $\lambda_{probe} = 400$ nm by absorption of four photons (12.40 eV) mainly results in a broad PE distribution. Since the electron yield starts to decrease at 2 eV towards higher energies and the adiabatic $D_0 \leftarrow S_0$ transition should yield electrons with 3 eV kinetic energy, the direct ionization pathway seems to be negligible. Although the electron yield is mainly uniform between $E_{el} = 0$–2 eV, two signals, β and a very broad signal γ, are observed. Band β originates from the excitation of the S_8 state (2 $^1B_{2u}$). It is assumed that the S_1 state is excited via absorption of two probe photons. Analogous to the pathway discussed for the multi-color ionization, the subsequent absorption of another probe photon excites the S_8 state, followed by absorption of a fourth photon within the probe pulse duration, leading to the D_0 state. The broad

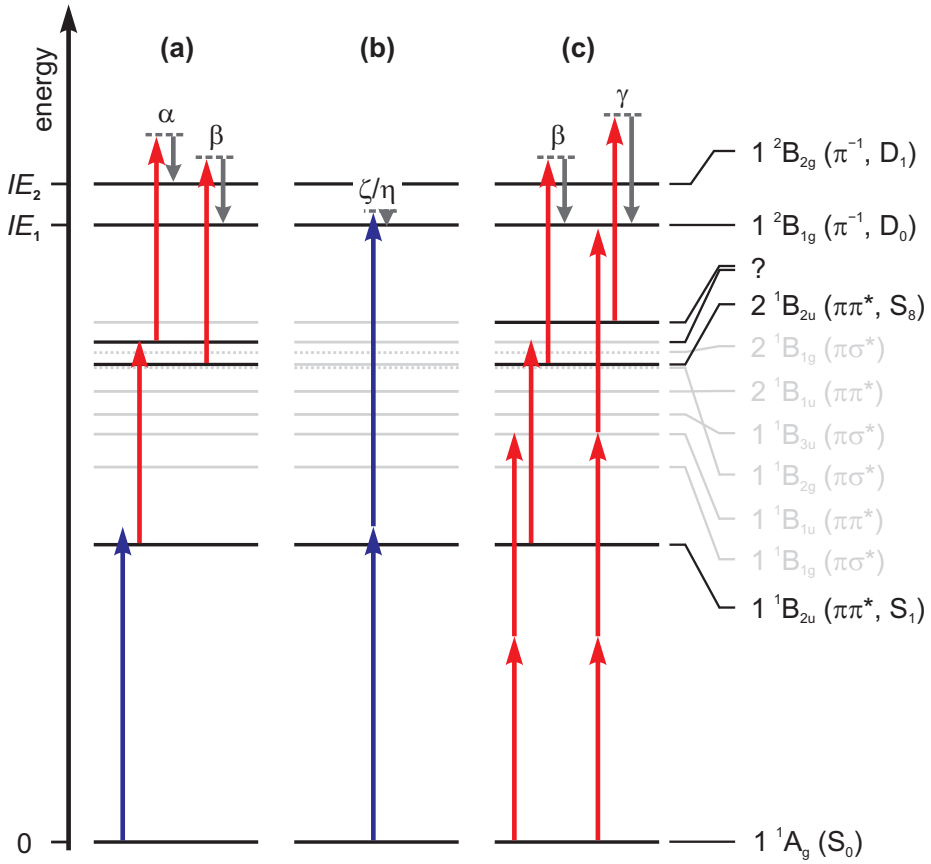

Figure 3.16. Proposed multi-color and single-color ionization schemes for 1,2,4,5-TFB. The energies of the photons at $\lambda_{\text{pump}} = 260$ nm (blue) and $\lambda_{\text{probe}} = 400$ nm (red) and of the photoelectrons (grey) are depicted as vertical arrows. Solid black horizontal lines: experimentally intermediate and final states, solid and dotted (calculated values) grey horizontal lines: non-participating other intermediate states. **(a)** Transient ionization pathways by one-photon absorption to the S_1 state ($1\ ^1B_{2u}$) and subsequent two-photon ionization to the D_0 ($1\ ^2B_{1g}$) and D_1 states ($1\ ^2B_{2g}$) showing the origin of PE peaks α and β. **(b)** Single-color ionization pathways at $\lambda_{\text{pump}} = 260$ nm to the D_0 state showing the origin of PE peaks ζ and η. **(c)** Single-color ionization pathways at $\lambda_{\text{probe}} = 400$ nm to the D_0 state showing the origin of PE peaks β and γ.

band at $E_\gamma = 1.7$ eV probably originates from a three-photon transition to an intermediate state at 7.9 eV. Due to the high density of possible intermediate states,[36,38] assigning a specific one to the signal would be speculative. Noteworthy, the band might also be the result of the direct $D_1 \leftarrow S_0$ transition. Yet, since the direct $D_0 \leftarrow S_0$ is not observed, the excitation of an high-lying intermediate state is considered to be more likely. The proposed SC ionization pathways are displayed in Figure 3.16 (c).

A signal corresponding to the band α in the multi-color PES is not observed in the SC ionization. The absence may indicate that the proposed pathway towards α is prohibited. However, the signal α is very broad and rather indistinct in the multi-color ionization, thus the band probably just vanishes in the background of the SC ionization.

3.3 1,2,3,5-Tetrafluorobenzene

3.3.1 Molecular and Electronic Structure

The gas phase-UV absorption spectrum of 1,2,3,5-TFB is shown in Figure 3.17. A lightly structured absorption band, starting at ≈275 nm (4.51 eV) and peaking at ≈260 nm (4.77 eV), is observed. The first distinct feature of the structure peaks at 264 nm (4.70 eV). A second band arises below 220 nm.

To assign the absorption bands to electronic transitions, the VEE to the first eight electronic states was calculated at RI-SCS-CC2 level of theory. The results are listed in Table 3.7. The first excited state (S_1, $1\ ^1B_2$), with a VEE of 5.08 eV (244 nm), shows $\pi\pi^*$ character. The S_2 state ($1\ ^1B_1$) exhibits $\pi\sigma^*$ character and an VEE of 6.43 eV (193 nm). Nearly isoenergetic at 6.45 eV (192 nm) the S_3 state ($\pi\pi^*$, $2\ ^1A_1$) is found. The S_4 state ($\pi\sigma^*$, $1\ ^1A_2$) is in close vicinity at 6.88 eV (180 nm). The following states show alternating $\pi\pi^*$ and $\pi\sigma^*$ character and are located at VEEs >7 eV in the calculations. The calculated VEEs fit reasonably well to the reported experimental transition energies. In general, the VEEs are overestimated by the CC2 method compared to experimental values. The gap varies between 0.25 eV for the S_3 state and 0.85 eV for the S_2 state. The tendency of RI-SCS-CC2 to overestimate the transition energies of the fluorobenzene was described in the literature[9,10] and discussed in the previous Sections.

Based on the calculations, the absorption band peaking at 260 nm (4.77 eV) is assigned to the S_1 ($\pi\pi^*$) state. The second band probably originates from the absorption of the S_3 state ($\pi\pi^*$).[36,38] In the case of the S_2 state ($\pi\sigma^*$) a VEE of 5.58 eV (222 nm) was reported in the literature,[37] based on an unpublished absorption spectrum. The spectrum herein does not feature a corresponding band.

Optimization of the molecular structures was successful in case of the neutral and ionic ground states and the S_1 state. The ground states are planar, as exemplary illustrated for the S_0 state in Figure 3.18. In contrast, a pronounced deformation is predicted in the molecular structure in the S_1 state. Besides an almost negligible bending of the carbon ring system (±1°), the ring is also slightly twisted in the S_1 state. Thus, no plane is spanned by more than three carbon atoms. To qualify the extent of the deformation of the fluorine atoms, a separate plane is defined for each fluorine atom, spanned by three carbon atoms: the atom directly bonding to the fluorine and its two respective neighboring atoms.

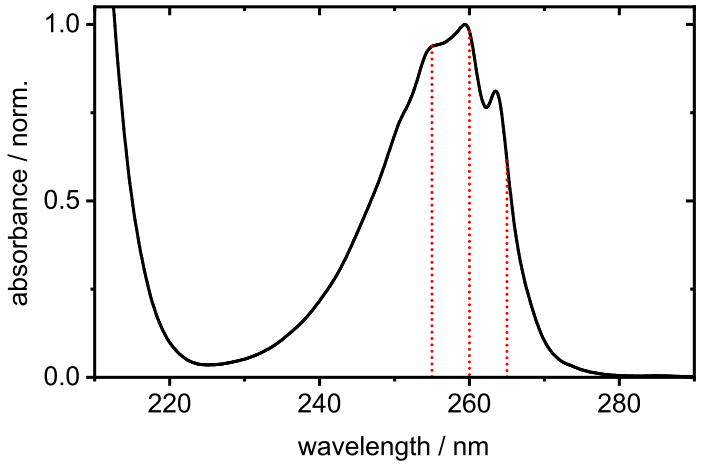

Figure 3.17. Normalized gas-phase UV absorption spectrum of 1,2,3,5-TFB. The dotted red lines indicate the chosen excitation wavelength of $\lambda_{pump} = 265$–255 nm to excite the S_1 state ($\pi\pi^*$).

Table 3.7. Vertical excitation energies (VEE) and oscillator strengths f (in parentheses) of the first eight neutral electronically excited states, the ionic ground state and the first two ionic electronically excited states for 1,2,3,5-TFB, calculated at RI-SCS-CC2 level of theory. Where available, the respective adiabatic energy (AEE) is listed. Experimental energies are given if possible.

	symm.	calc. VEE eV	calc. AEE eV	exp. VEE eV	exp. AEE eV
S_1 ($\pi\pi^*$)	$1\,^1B_2$	5.08 (0.0098)	4.77	4.77[a–c,†]	
S_2 ($\pi\sigma^*$)	$1\,^1B_1$	6.43 (0.0008)		5.58[b]	
S_3 ($\pi\pi^*$)	$2\,^1A_1$	6.45 (0.0000)		6.20[a,c]	
S_4 ($\pi\sigma^*$)	$1\,^1A_2$	6.88 (0.0000)			
S_5 ($\pi\pi^*$)	$3\,^1A_1$	7.31 (0.6445)		6.70[c]	
S_6 ($\pi\sigma^*$)	$2\,^1B_1$	7.39 (0.0114)		6.60[a,c]	
S_7 ($\pi\pi^*$)	$2\,^1B_2$	7.40 (0.6874)		7.08[a,c] / 7.32[†]	
S_8 ($\pi\sigma^*$)	$2\,^1A_2$	7.77 (0.0000)			
D_0 (π^{-1})	$1\,^2B_1$	9.75	9.45		9.53[d–f]
D_1 (π^{-1})	$1\,^2A_2$	10.33			9.93[d]
D_2 (π^{-1})	$2\,^2B_1$	12.81			12.42[d]

[a] Ref. [36] [b] Ref. [37], based on unpublished absorption spectra. [c] Ref. [38]
[d] Ref. [18] [e] Ref. [38] [f] Ref. [39] [†] this work

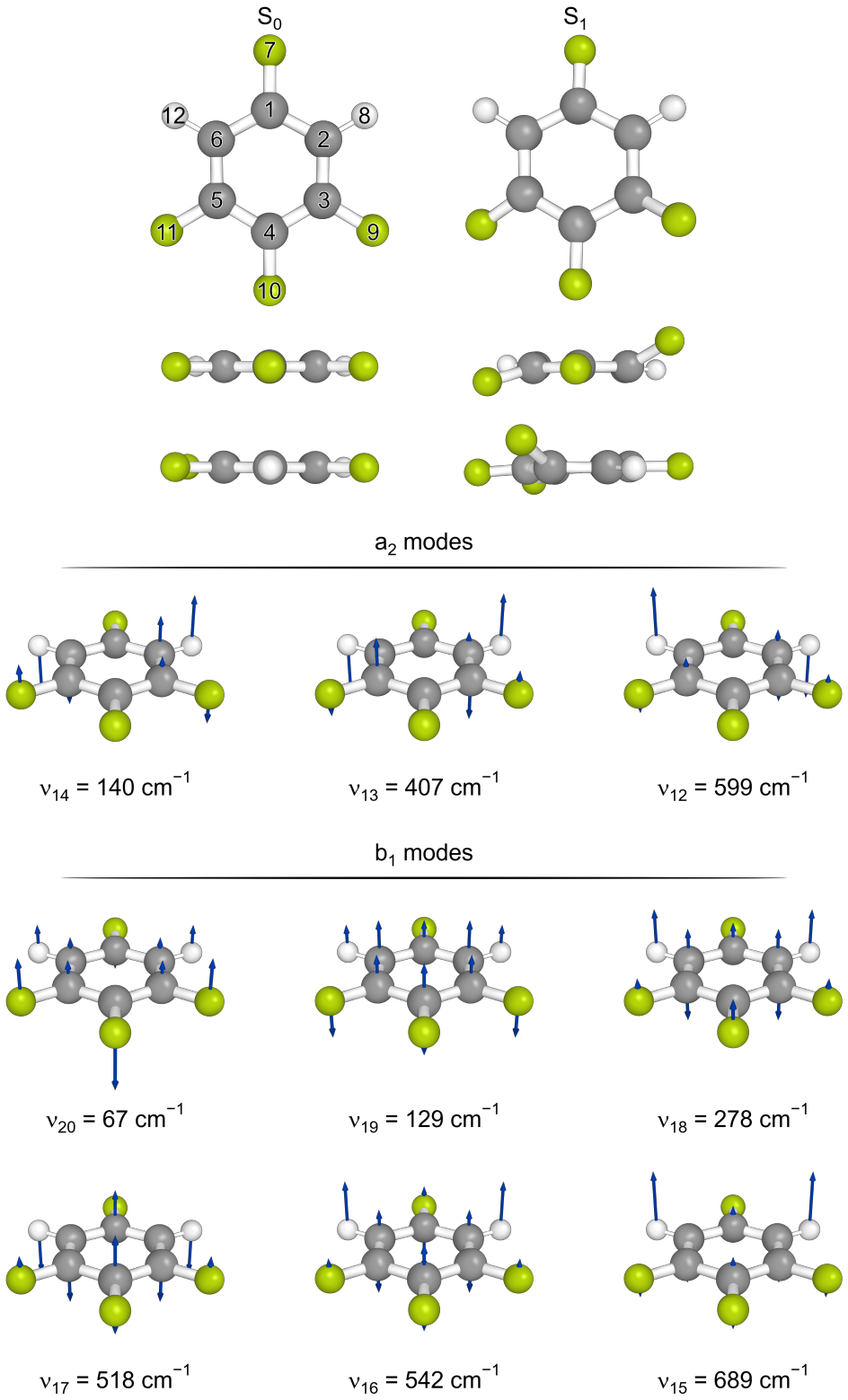

Figure 3.18. Calculated molecular structures of 1,2,3,5-TFB in the S_0 and the S_1 state ($\pi\pi^*$), optimized at the RI-SCS-MP2 and RI-SCS-CC2 levels of theory, respectively. The calculated displacement vectors of the out-of-plane modes are illustrated by blue arrows. Their respective frequencies in the S_1 state are listed.

For example, the "isolated" fluorine atom 7 (numbering according to Figure 3.18) is nearly in-plane (1°) of the plane spanned by the atoms 1–2–6. Fluorine atom 9 is significantly bent out-of-plane by 27°. For atoms 10 and 11 the out-of-plane angles were calculated to be −4° and −14°, respectively. The hydrogen atoms are only marginally bent out-of-plane. Overall, the molecular structure shows essentially a_2 symmetry, though the fluorine atoms 9 and 11 should be distorted to similar extent in the case of pure a_2 symmetry. Moreover, illustrations of the displacement vectors of the out-of-plane vibrational modes and the respective calculated frequencies in the S_1 state are also given Figure 3.18. A comprehensive list of all vibrational frequencies can be found in Table B.3 in the appendix.

Calculation of the S_1 AEE by subtracting the RI-SCS-CC2 single point energy of the optimized structures in the S_0 state from the single point energy in the S_1 state yields 4.77 eV (260 nm). Since this calculated value is identical to the experimental VEE, the actual AEE has to be significantly lower. The same essentially also applies to the first feature of the band structure at 264 nm (4.70 eV). If the peak would correspond to the actual adiabatic transition, the calculations would nearly perfectly predict the AEE, in contrast to the deviation observed for all other molecules in this Thesis (e.g., 1,2,4,5-TFB in the previous Section). Therefore, a more probable initial guess on the AEE is provided by the absorption band onset at ≈275 nm (4.51 eV). High resolution spectroscopy are needed resolve the true AEE.

In addition to the neutral states, the VIEs to the first three ionic states were calculated too. The ionic ground state D_0 ($1\ ^2B_1$) is placed at 9.75 eV. The first excited ionic state D_1 ($1\ ^2A_2$) shows an estimated VIE of 10.33 eV. A gap of ≈2.5 eV separates the D_1 state from the second excited ionic state D_2 ($2\ ^2B_1$) at 12.81 eV. All ionic states exhibit π^{-1} character. Analogous to the AEE, the $D_0 \leftarrow S_0$ AIE was calculated to be 9.45 eV, slightly underestimating the AIE of 9.53 eV.[18,38,39]

3.3.2 Time-Resolved Time-of-Flight Mass Spectra

Three wavelengths were chosen to selectively excite the S_1 state: 265 nm, 260 nm, and 255 nm. The excited molecules were ionized at $\lambda_{probe} = 800$ nm. At $\lambda_{pump} = 260$ nm also the ionization wavelength was varied to $\lambda_{probe} = 400$ nm.

The transient parent ion yields of 1,2,3,5-TFB after excitation at $\lambda_{pump} =$ 260 nm are shown in Figure 3.19. The signals are virtually identical at both

probe wavelengths. Two oscillations with $\nu_{\text{osc1}}^{\text{1,2,3,5-TFB}} = 94\ \text{cm}^{-1}$ and $\nu_{\text{osc2}}^{\text{1,2,3,5-TFB}} = 138\ \text{cm}^{-1}$ dominate the ion yields in the first five picoseconds. The frequencies were determined via Fourier transform of the oscillatory signal component, shown in Figure 3.19 (e). The oscillations decay with

$$\tau_{\text{osc1}}^{\text{1,2,3,5-TFB}} = 1.40\ \text{ps}$$

and

$$\tau_{\text{osc2}}^{\text{1,2,3,5-TFB}} = 1.1\ \text{ps}.$$

Afterwards the signal decays within $\Delta t = 500$ ps, which is well described by three exponential decay functions

$$\begin{aligned}\tau_{2}^{\text{1,2,3,5-TFB}} &= 0.6\text{–}2\ \text{ps},\\ \tau_{3}^{\text{1,2,3,5-TFB}} &= 40\text{–}60\ \text{ps},\\ \tau_{4}^{\text{1,2,3,5-TFB}} &= 250\ \text{ps}.\end{aligned}$$

Changing the excitation wavelength to $\lambda_{\text{pump}} = 265$ nm leads to a slight increase of $\tau_{3}^{\text{1,2,3,5-TFB}}$ to

$$\tau_{3}^{\text{1,2,3,5-TFB}}(265\ \text{nm}) = 59\ \text{ps}.$$

However, the overall lifetime is significantly increased to

$$\tau_{4}^{\text{1,2,3,5-TFB}}(265\ \text{nm}) = 813\ \text{ps},$$

as shown in Figure 3.20. On the contrary, at $\lambda_{\text{pump}} = 255$ nm the decay constants change to

$$\tau_{3}^{\text{1,2,3,5-TFB}}(255\ \text{nm}) = 31.5\ \text{ps},$$

and

$$\tau_{4}^{\text{1,2,3,5-TFB}}(255\ \text{nm}) = 440\ \text{ps}.$$

It should be noted that the error limits of ±180 ps for $\tau_{4}^{\text{1,2,3,5-TFB}}(255\ \text{nm})$ probably result from the substantial decrease of the respective amplitude to less than 5 % at $\lambda_{\text{pump}} = 255$ nm. Furthermore, the initial decay $\tau_{2}^{\text{1,2,3,5-TFB}}$ is virtually unchanged at all excitation wavelengths, as well as no trend regarding the oscillational lifetimes is observed. The fit parameters at all chosen wavelengths are listed in Table 3.8.

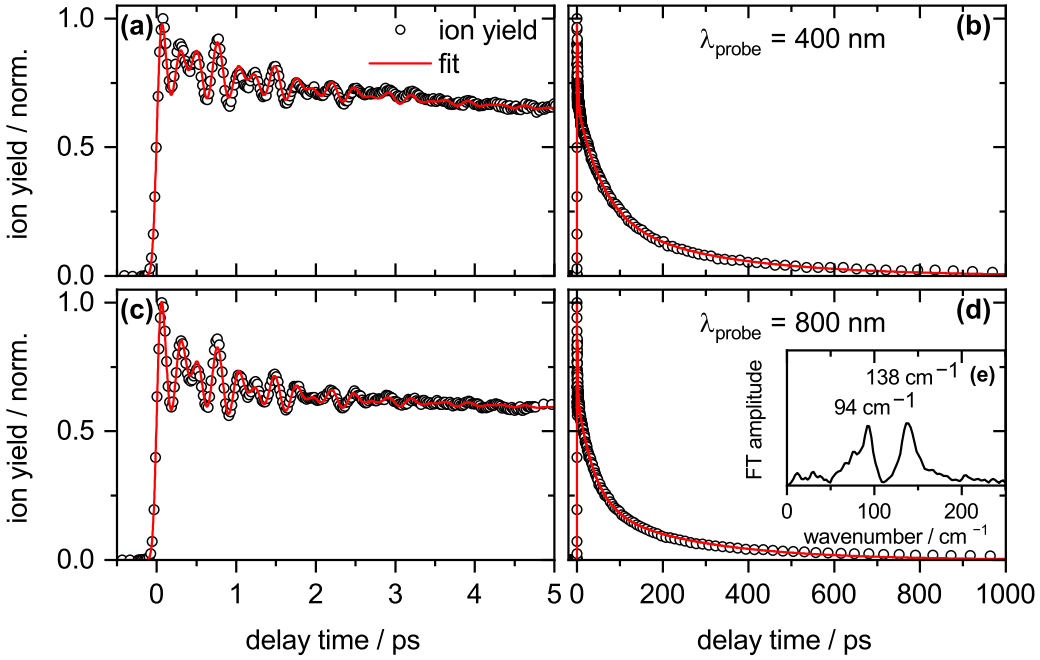

Figure 3.19. Measured transient parent ion yield signals (black circles) and applied fit model functions (red lines) for 1,2,3,5-TFB after excitation at $\lambda_{pump} = 260$ nm and ionization at $\lambda_{probe} = 400$ nm **(a–b)** resp. $\lambda_{probe} = 800$ nm **(c–d)**. The left-hand column shows the data in the first five picoseconds, the right-hand column in the first nanosecond after excitation. The fit parameters are listed in Table 3.8. **(e)** Fourier transform of the oscillatory signal component after subtraction of the exponential decay functions.

Table 3.8. Parameters for the fits of the transient parent ion yields of 1,2,3,5-TFB after excitation at $\lambda_{pump} = 260$ nm and ionization at $\lambda_{probe} = 400$ nm, as well as fit parameters after excitation at $\lambda_{pump} = 265$–255 nm ionization at $\lambda_{probe} = 800$ nm. 2σ fit errors are given in parentheses. If no error is given the value was set fixed.

λ_{pump} nm	σ_{IRF} fs	A_2 %	τ_2 ps	A_3 %	τ_3 ps	A_4 %	τ_4 ps	A_{osc} %	τ_{osc} ps	ν_{osc} cm^{-1}	ϕ_{osc} π
$\lambda_{probe} = 400$ nm											
260	42(2)	15(1)	2.08(14)	37(4)	60.3(68)	20(4)	277(49)	10(1)	1.50(20)	95	−0.36
								18(2)	1.17(13)	138	−0.35
$\lambda_{probe} = 800$ nm											
265	25(1)	18(1)	0.70(5)	11(1)	59(11)	34(1)	813(59)	17(1)	0.68	94	−0.60
								20(1)	0.92(7)	137	−0.57
260	39(2)	15(1)	0.62(5)	34(2)	39.1(28)	18(2)	243(30)	12(1)	1.25(13)	94	−0.25
								21(2)	1.03(8)	138	−0.39
255	40(2)	13(1)	0.58(6)	45(1)	31.5(11)	4(1)	440(180)	13(1)	1.13(12)	96	−0.32
								25(2)	0.96(7)	138	−0.40

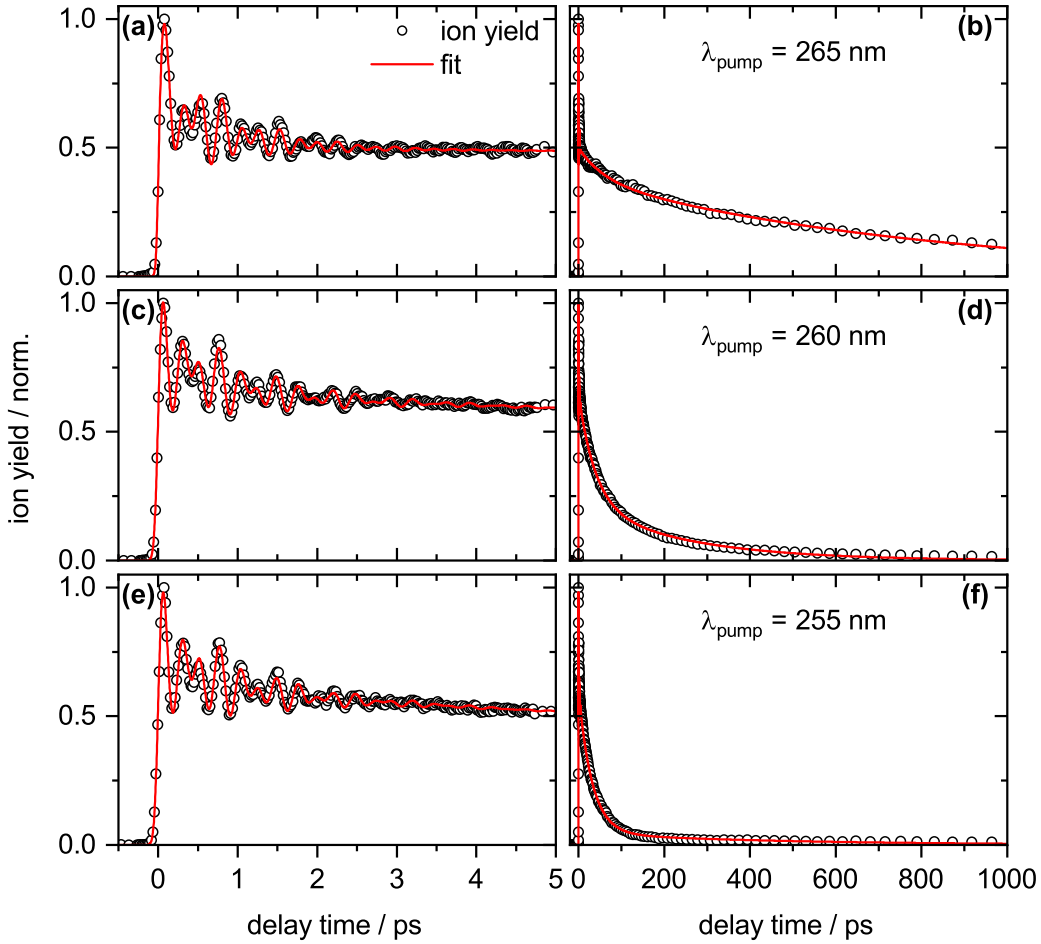

Figure 3.20. Measured transient parent ion yield signals (black circles) and applied fit model functions (red lines) for 1,2,3,5-TFB after excitation at $\lambda_{pump} = 265$ nm **(a–b)**, $\lambda_{pump} = 260$ nm **(c–d)**, and $\lambda_{pump} = 255$ nm **(e–f)** and ionization at $\lambda_{probe} = 800$ nm. The left-hand column shows the data in the first five picoseconds, the right-hand column in the first nanosecond after excitation. The fit parameters are listed in Table 3.8.

Origin of the Oscillation

As discussed in Chapter 1 and extensively in the literature,[5,9,10] the oscillations originate from the vibronic coupling between the initially excited $\pi\pi^*$ state and higher-lying $\pi\sigma^*$ states. 1,2,3,5-TFB highlights vibronic coupling is indeed the reason for the signal oscillations, since the variation of the pump wavelength keeps the oscillation frequencies virtually unaltered, in stark contrast to quantum beatings, for which even slight variations of the pump wavelengths significantly impacts the observed oscillation patterns.[22,24,27,29]

In the case of 1,2,3,5-TFB, the a_2 modes are expected to couple the $\pi\pi^*$ (S_1, $1\ ^1B_2$) and the first $\pi\sigma^*$ state (S_2, $1\ ^1B_1$). The coupling induces a pronounced deformation of the molecular equilibrium structure in the S_1 state. The motif of the deformation essentially shows a_2 symmetry, in good agreement with the expected symmetry of the coupling modes. However, assigning vibrational modes to the oscillations is more challenging. The two lowest-frequency a_2 coupling modes are $\nu_{14} = 140\ \mathrm{cm}^{-1}$ and $\nu_{13} = 407\ \mathrm{cm}^{-1}$ (cf. Figure 3.18). Former fits well to either experimental frequency of $\nu_{\mathrm{osc1}}^{1,2,3,5\text{-TFB}} = 94\ \mathrm{cm}^{-1}$ and $\nu_{\mathrm{osc2}}^{1,2,3,5\text{-TFB}} = 138\ \mathrm{cm}^{-1}$, but unfortunately latter does not. As deviations in the order of $300\ \mathrm{cm}^{-1}$ between the calculated and the real frequencies are not to be expected,[10] at least one oscillational frequency probably originates from the other subset of out-of-plane modes, the b_1 modes. Either of the two lowest-frequency b_1 modes, $\nu_{20} = 67\ \mathrm{cm}^{-1}$ and $\nu_{19} = 129\ \mathrm{cm}^{-1}$, fits well to the observed oscillational frequencies. Therefore, it is assumed that at least one of these b_1 modulates the signal, which might also explain why the calculated molecular structure in the S_1 state does not strictly follow a_2 symmetry. As a consequence, the observable dynamics of 1,2,3,5-TFB seem to be affected by coupling between the S_1 ($\pi\pi^*$, $1\ ^1B_2$) and the S_2 states ($1\ ^1B_1$), as well as between the S_1 and the S_4 state ($1\ ^1A_2$). Such a multi-state coupling will be discussed in greater detail Section 3.10 in light of the results for the other systems.

3.3.3 Time-Resolved Photoelectron Images

The photoelectron images and the corresponding slices of 1,2,3,5-TFB after excitation at $\lambda_{\mathrm{pump}} = 260$ nm and subsequent ionization at $\lambda_{\mathrm{probe}} = 400$ nm are shown in Figure 3.21 at $\Delta t = 0.04$ ps (a), in the first minimum at $\Delta t = 0.13$ ps (b), and the third maximum at $\Delta t = 0.71$ ps (c). In all cases one broad and one narrow signal are observed. In the PES, shown in Figure 3.22 (a), these signals

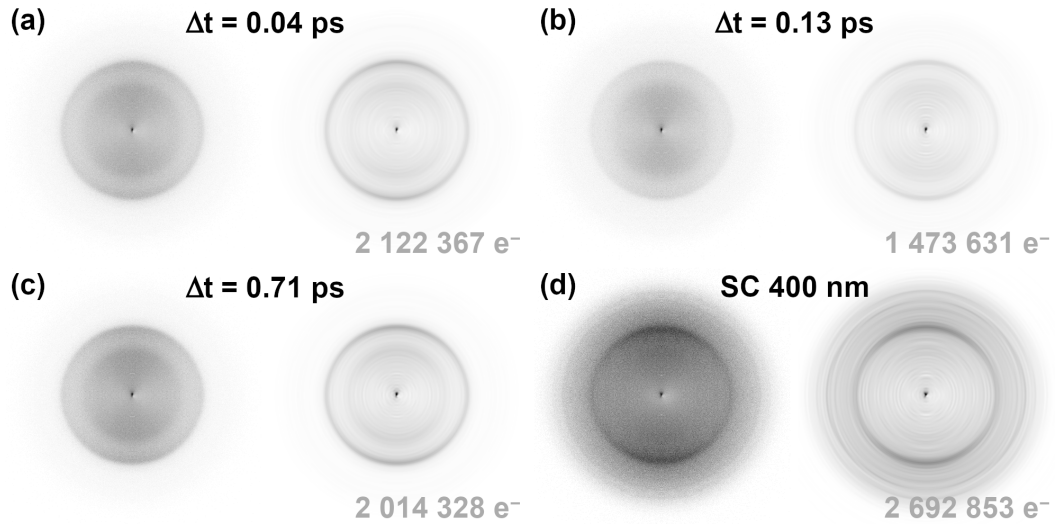

Figure 3.21. Photoelectron images (left) and their corresponding meridional slices through the recovered three-dimensional photoelectron distributions (right) of 1,2,3,5-TFB. **(a)** At $\Delta t = 0.04$ ps after excitation at $\lambda_{\text{pump}} = 260$ nm and subsequent ionization at $\lambda_{\text{probe}} = 400$ nm, **(b)** at $\Delta t = 0.13$ ps (first minimum), and **(c)** at $\Delta t = 0.71$ ps (third maximum). **(d)** High-intensity single-color photoelectron image obtained at 400 nm.

α and β peak at $E_\alpha = 0.4$ eV and $E_\beta = 0.89$ eV, respectively. Both PE signals show a time-dependent oscillating decay and rise in intensity, in agreement with the oscillating parent ion yield.

The photoelectron image and the slice after high-intensity single-color ionization at $\lambda_{\text{probe}} = 400$ nm are depicted in Figure 3.21 (d). The SC ionization mainly yields a broad background. However, one narrow, intense signal is followed by two shallow ones at higher energies. In the PES (Figure 3.22 (b), the latter vanishes in the broad background. The narrow signal is identical to β in the two-color PES.

Ionization Pathways

Likewise to the results on 1,2,3-TriFB, 1,2,4,5-TFB (cf. Sections 3.1 and 3.2, respectively), and PFB,[9] the ionization the excited 1,2,3,5-TFB yields two PE signals. In agreement with previous assignments, the narrow band β is attributed to the transition to the D_0 state and the broad band α to the transition to the D_1 state. The energy difference between $E_\alpha = 0.4$ eV and $E_\beta = 0.89$ eV of >0.4 eV fits well to the energy gap between the ionic states of 0.4 eV (cf. Table 3.7). The absence of additional signals rising in at later delay times indicates that the deactivation of the initially excited S_1 state does not involve conversion to any

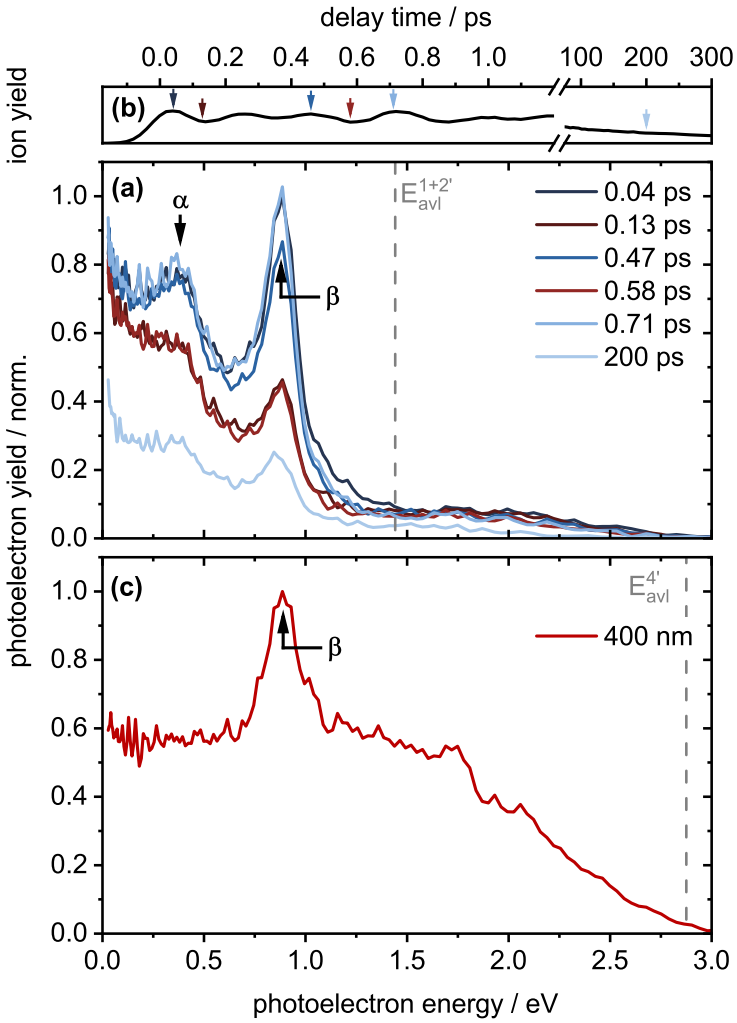

Figure 3.22. **(a)** Transient PE spectra of 1,2,3,5-TFB after excitation at $\lambda_{pump} = 260$ nm and ionization at $\lambda_{probe} = 400$ nm. The two main photoelectron signals labeled α and β are observed at $E_\alpha = 0.4$ eV and $E_\beta = 0.89$ eV. The grey dotted line indicates the maximum available photoelectron energy $E_{avl}^{1+2'}$ associated with the $D_0 \leftarrow S_0$ transition by $1 + 2'$ ionization. **(b)** Corresponding transient parent ion yields adapted from Figure 3.19 (a). Arrows mark the delay time $\Delta t = 0$–200 ps at which the PES were obtained (red at ion yield minima). **(c)** Single-color PE spectrum taken at higher 400 nm probe intensities. The grey dotted line indicates the maximum available photoelectron energies $E_{avl}^{4'}$ generated by four 400 nm photons.

other excited states. Nevertheless, the results of 1,2,3-TriFB and 1,2,4,5-TFB showed that the ionization not necessarily happens to be a direct $D_{0/1} \leftarrow S_1$ transition.

To understand the underlying ionization mechanism, the energy of the state excited prior to ionization can be calculated. Subsequent to the excitation of the S_1 state by the pump pulse, two additional probe photons are needed for the direct ionization. Based on Equation 3.2 in Section 3.1, the sum of the AIE to the D_0 state of 9.53 eV[18,38,39] and the energy of $E_\beta = 0.89$ eV, minus the energy of two probe photons at $\lambda_{\text{probe}} = 400$ nm (2×3.10 eV) yields 4.22 eV (294 nm), which might correspond to the S_1 AEE. However, the absorption band of 1,2,3,5-TFB starts to rise at ≈275 nm (4.51 eV), thus blue-shifted to the calculated value. In combination with the similarities of the PE band patterns compared to 1,2,3-TriFB and 1,2,4,5-TFB, it is deemed more probable that excitation of a high-lying intermediate state within the probe pulse duration alters the PE peak position. The intermediate state has to be excited via absorption of a single probe photon. Just subtracting the energy of one probe photon from the sum of the D_0 AIE and E_β yields 7.32 eV. The energy fits reasonably well to the transition energy of 7.08 eV[36,38] to the $2\ ^1B_2$ state ($\pi\pi^*$, S_7). Therefore, the initial excitation of the S_1 state ($\pi\pi^*$) by the pump pulse probably is followed by the absorption of a single probe photon within the probe pulse duration. The subsequent absorption of a second probe photon ionizes the molecules, populating the D_0 state, as illustrated in Figure 3.23. Since the electronic configuration of the S_7 state corresponds to both accessible ionic states (cf. Table 3.9), it is tentatively assumed that the vertical $D_1 \leftarrow S_7$ transition is the origin of the PE band α.

In the case of the high-intensity single-color ionization at $\lambda_{\text{probe}} = 400$ nm only band β emerges on top of a broad background. The lack of photoelectrons at the maximum available energy for the four-photon transition indicates that the direct $D_0 \leftarrow S_0$ ionization barely occurs. Instead, a vast number of different transitions form the broad and near homogeneous background. The signal β probably originates from the two-photon excitation of the S_1 state, followed by the absorption of another photon to excite the S_7 state. The final absorption of a forth photon ionizes the molecules, as shown in Figure 3.23 (b).

The lack of a band corresponding to signal α is in line with the observations for 1,2,3-TriFB and 1,2,4,5-TFB, for which the SC ionization also did not yield a distinct α band, presumably due to the intense background. However, in contrast to the PE distributions of both aforementioned molecules, the signal α

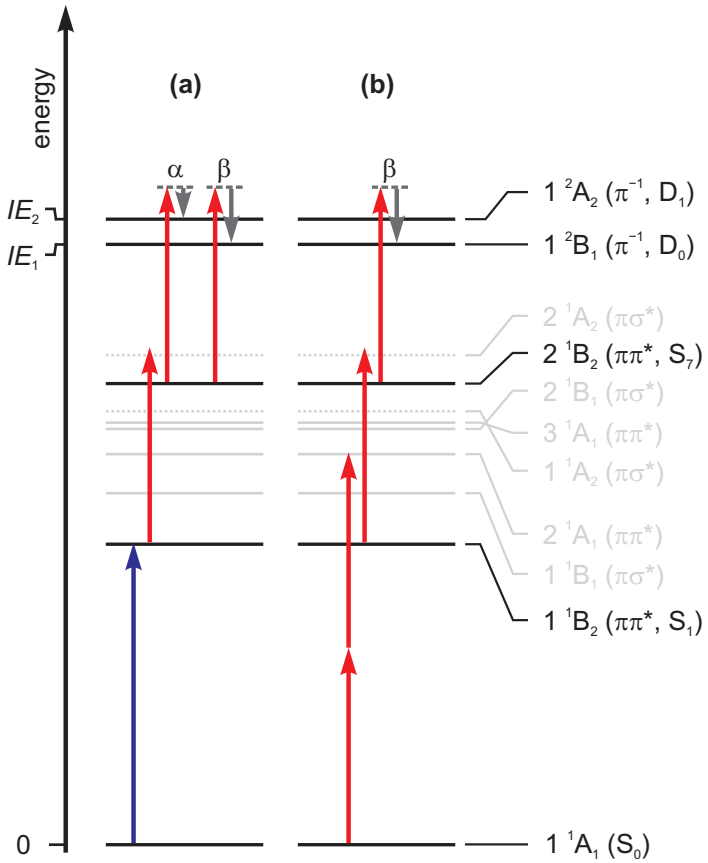

Figure 3.23. Proposed multi-color and single-color ionization schemes for 1,2,3,5-TFB. The energies of the photons at $\lambda_{pump} = 260$ nm (blue) and $\lambda_{probe} = 400$ nm (red) and of the photoelectrons (grey) are depicted as vertical arrows. Solid black horizontal lines: experimentally intermediate and final states, solid and dotted (calculated values) grey horizontal lines: non-participating other intermediate states. **(a)** Transient ionization pathways by one-photon absorption to the S_1 state ($1\ ^1B_2$) and subsequent two-photon ionization to the D_0 ($1\ ^2B_1$) and D_1 states ($1\ ^2A_2$) showing the origin of PE peaks α and β. **(b)** Single-color ionization pathways at $\lambda_{probe} = 400$ nm to the D_0 state showing the origin of PE peak β.

Table 3.9. Molecular orbital configuration and their weighted contributions to the S_1, S_2, and S_7 states and the first three ionic states of 1,2,3,5-TFB. Correlations between the neutral and the ionic states according to Koopmans's theorem are given.

neutral state	4 b_1 (π)	2 a_2 (π)	5 b_1 (π)	3 a_2 (π^*)	6 b_1 (π^*)	19 a_1 (σ^*)	20 a_1 (σ^*)	26 a_1 (σ^*)	weight (%)	corr. ion. state
S_0 ($^1A_1$)	2	2	2							
S_1 ($^1B_2$, $\pi\pi^*$)	2	2	1	1					61	D_0
	2	1	2		1				23	D_1
S_2 ($^1B_1$, $\pi\sigma^*$)	2	2	1			1			43	
	2	2	1					1	20	D_0
	2	2	1				1		18	
S_7 ($^1B_2$, $\pi\pi^*$)	2	1	2		1				51	D_1
	2	2	1	1					33	D_0
ionic state										
D_0 ($^2B_1$, π^{-1})	2	2	1							
D_1 ($^2A_2$, π^{-1})	2	1	2						97	
D_2 ($^2B_1$, π^{-1})	1	2	2						83	

of 1,2,3,5-TFB is rather well defined. Therefore, the total absence of any band corresponding to α may also indicate that the ionization pathways towards α and β are substantially different, and, in fact, do not both involve excitation of the S_7 state. Unfortunately, the limited information available on electronic and molecular structure of the high-lying intermediate and ionic states prohibits gaining further insight into the mechanism.

3.4 1,2,3,4-Tetrafluorobenzene

3.4.1 Molecular and Electronic Structure

The UV absorption spectrum of 1,2,3,4-TFB is shown in Figure 3.24. One structureless absorption band between 275–230 nm is observed. The band peaks at ≈260 nm (4.77 eV). A second band arises at wavelengths <230 nm.

To assign the bands, the VEEs to the first eight neutral excited states were calculated at RI-SCS-CC2 level of theory, listed in Table 3.10. The first excited state S_1 ($2\ ^1A_1$) shows $\pi\pi^*$ character and an estimated VEE of 5.07 eV (245 nm). The optically dark S_2 state ($1\ ^1A_2$) exhibits $\pi\sigma^*$ character and a VEE of 6.33 eV (196 nm). In close vicinity the S_3 state ($\pi\pi^*$, $1\ ^1B_2$) at 6.43 eV (193 nm) is expected, followed by the $\pi\sigma^*$ state S_4 ($2\ ^1B_1$) at 6.57 eV (189 nm). The VEEs to the states S_5–S_8 (two $\pi\pi^*$ and two $\pi\sigma^*$ states) are estimated to exceed 7 eV.

Aided by the calculations, the structureless absorption band peaking at 260 nm is assigned to the S_1 state. As discussed in previous Sections, the calculated VEE overestimates the actual transition energy. The second band originates from the absorption of the S_3 state ($\pi\pi^*$).[36] A VEE of 5.52 eV (225 nm) to the S_2 state ($\pi\sigma^*$) was reported in the literature, based on an unpublished absorption spectrum.[37] The UV spectrum in this work does not show a distinct signal corresponding to the symmetry-forbidden transition.

Optimization of the molecular structure in the neutral ground state S_0 yielded a planar structure, thus 1,2,3,4-TFB belongs to the C_{2v} point group. In the S_1 state the molecules are highly out-of-plane deformed, as shown in Figure 3.25. Especially the fluorine atoms are bent out of the marginally bent and twisted carbon ring. To qualify the extent, a separate plane is defined for each fluorine atom, spanned by three carbon atoms: the atom directly bonding to the fluorine and its two respective neighboring atoms. For example, the fluorine atom 9 (numbering according to Figure 3.25) is nearly in-plane (4°) of the plane spanned by the carbon atoms 2–3–4. Likewise, the fluorine atoms 11 and 12 are nearly in plane, with 8° and 3°, respectively, as are the hydrogen atoms. Contrary, the fluorine atom 10 is significantly bent out-of-plane by −31°. The motif of the deformation cannot be characterized by any irreducible representation of the C_{2v} point group. Moreover, illustrations of the displacement vectors out-of-plane vibrational modes and the respective calculated frequencies in the S_1 state are

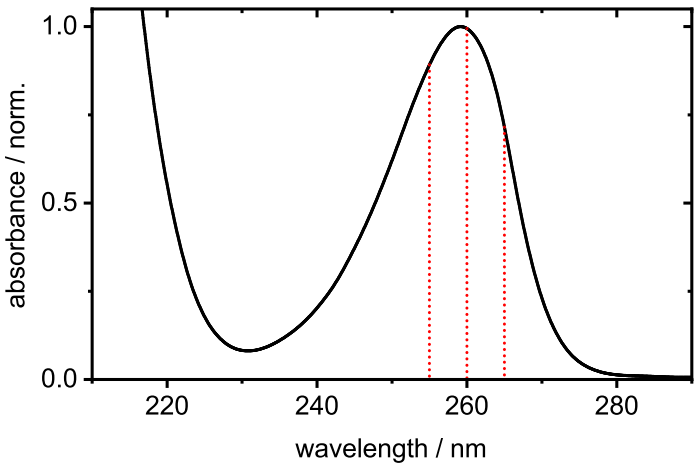

Figure 3.24. Normalized gas-phase UV absorption spectrum of 1,2,3,4-TFB. The dotted red lines indicate the chosen excitation wavelength of $\lambda_{\text{pump}} = 265$–$255$ nm to excite the S_1 state ($\pi\pi^*$).

Table 3.10. Vertical excitation energies (VEE) and oscillator strengths f (in parentheses) of the first eight neutral electronically excited states, the ionic ground state and the first two ionic electronically excited states for 1,2,3,4-TFB, calculated at RI-SCS-CC2 level of theory. Where available, the respective adiabatic energy (AEE) is listed. Experimental energies are given if possible.

	symm.	calc. VEE eV	calc. AEE eV	exp. VEE eV	exp. AEE eV
S_1 ($\pi\pi^*$)	$2\,^1A_1$	5.07 (0.0080)	4.73	4.69[a] / 4.77[†]	
S_2 ($\pi\sigma^*$)	$1\,^1A_2$	6.33 (0.0000)		5.52[a]	
S_3 ($\pi\pi^*$)	$1\,^1B_2$	6.43 (0.0010)		6.43[b]	
S_4 ($\pi\sigma^*$)	$2\,^1B_1$	6.57 (0.0026)			
S_5 ($\pi\sigma^*$)	$2\,^1A_2$	7.21 (0.0000)			
S_6 ($\pi\pi^*$)	$2\,^1B_2$	7.35 (0.6720)		7.21[b] / 7.34[†]	
S_7 ($\pi\pi^*$)	$3\,^1A_1$	7.40 (0.6779)			
S_8 ($\pi\sigma^*$)	$3\,^1B_1$	7.54 (0.0196)			
D_0 (π^{-1})	$1\,^2A_2$	9.72	9.46	9.78[c]	9.53[c–e]
D_1 (π^{-1})	$1\,^2B_1$	10.24			9.88[d]
D_2 (π^{-1})	$2\,^2B_1$	12.79			12.42[d]

[a] Ref. [37], based on unpublished absorption spectra. [b] Ref. [36] [c] Ref. [54]
[d] Ref. [18] [e] Ref. [39] [†] this work

also given Figure 3.25. A comprehensive list of all vibrational frequencies can be found in Table B.4 in the appendix.

The AEE to the S_1 state was calculated to be 4.73 eV (262 nm). Since this value basically places the AEE at the center of the UV absorption band, most certainly the actual AEE is substantially smaller. Though the true AEE needs to be resolved by means of high-resolution spectroscopy, the onset of the absorption band at ≈275 eV (4.51 eV) is a reasonable initial guess.

In addition to the electronic structure of the neutral states, the VIEs to the first three ionic states were calculated, also listed in Table 3.10. The ionic ground state D_0 ($1\ ^2A_2$) is located at 9.72 eV, in near perfect agreement with the experimental transition energy of 9.78 eV.[54] The VIE to the first excited ionic state D_1 ($1\ ^2B_1$) is predicted to be 10.24 eV. The experimentally determined energy gap between the D_0 and the D_1 state of 0.35 eV[18] is in good agreement with the calculated VIE gap of 0.52 eV. Furthermore, the second excited ionic state D_2 ($2\ ^2B_1$) is placed at 12.79 eV. Results of photoelectron spectroscopy confirm the estimated energy difference of more than 2 eV between the D_1 and the D_2 state.[18] All three ionic states show π^{-1} character.

Likewise to the structure in the S_0 state, the molecular structure in the D_0 state also is planar (not shown for the sake of brevity). Calculation of the D_0 AIE yielded 9.46 eV, underestimating the actual AIE of 9.53 eV[18,39,54] only marginally. The D_0 state was the only ionic state for which the structure optimizations converged.

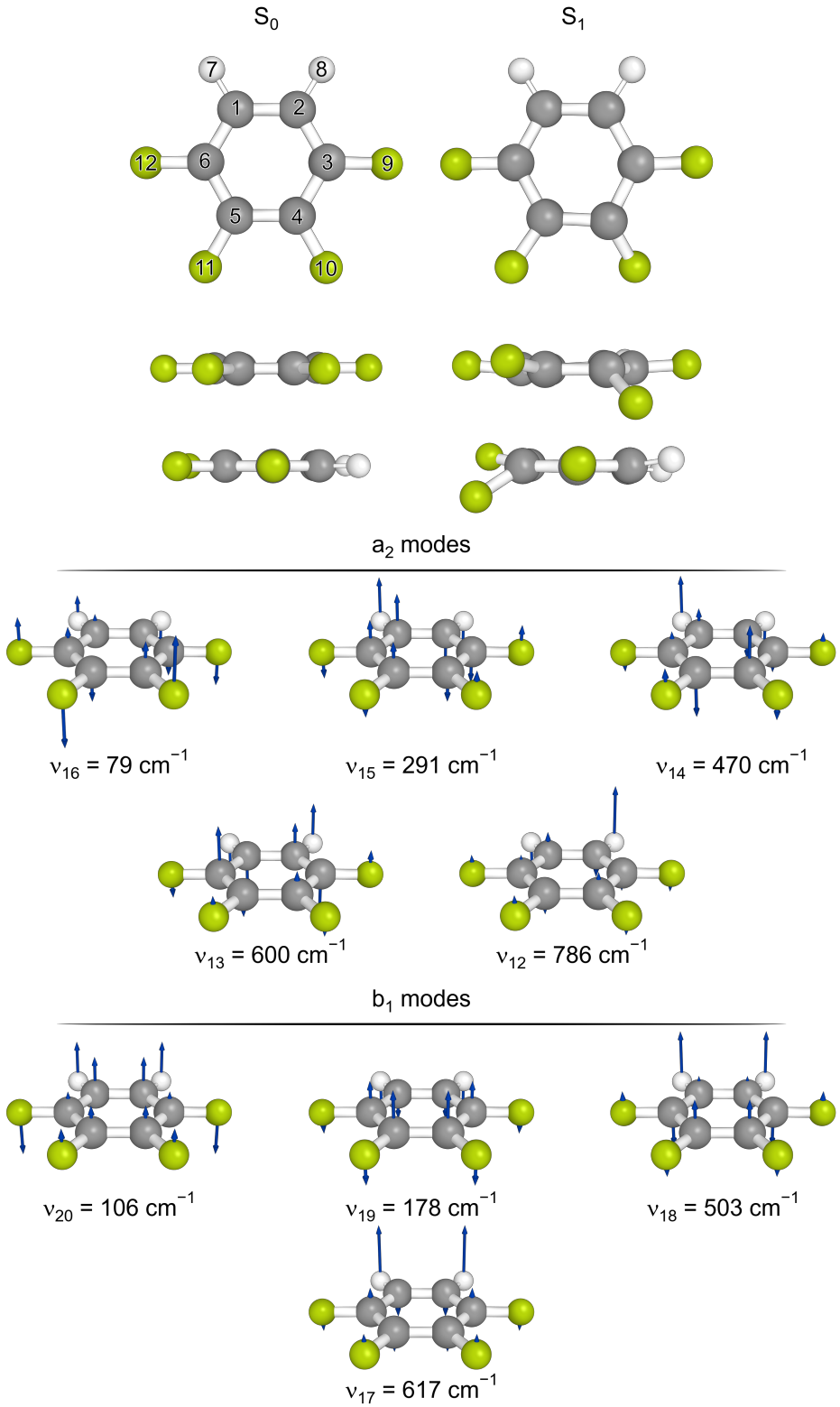

Figure 3.25. Calculated molecular structures of 1,2,3,4-TFB in the S_0 and the S_1 state ($\pi\pi^*$), optimized at the RI-SCS-MP2 and RI-SCS-CC2 levels of theory, respectively. The calculated displacement vectors of the out-of-plane modes are illustrated by blue arrows. Their respective frequencies in the S_1 state are listed.

3.4.2 Time-Resolved Time-of-Flight Mass Spectra

Three excitation wavelengths at $\lambda_{\text{pump}} = 265$ nm, 260 nm and 255 nm were chosen to characterize the dynamics of the S_1 state. The excited molecules were ionized at $\lambda_{\text{probe}} = 800$ nm. At $\lambda_{\text{pump}} = 260$ nm the molecules were additionally probed at $\lambda_{\text{probe}} = 400$ nm.

The transient parent ion yields of 1,2,3,4-TFB after excitation at $\lambda_{\text{pump}} = 260$ nm and ionization at both wavelengths are shown in Figure 3.26. The signal patterns are nearly independent of the probe wavelength. An intense single-frequency oscillation dominates within the first $\Delta t = 20$ ps after excitation. The oscillatory frequency of $\nu_{\text{osc}}^{\text{1,2,3,4-TFB}} = 70$ cm^{-1} was determined by Fourier transform of the oscillatory signal component, depicted in Figure 3.26 (h). The oscillation decays with

$$\tau_{\text{osc}}^{\text{1,2,3,4-TFB}} = 4.3\text{–}4.9 \text{ ps}.$$

Although frequency and lifetime of the oscillation is probe-wavelength independent, the modulation depth at $\lambda_{\text{probe}} = 800$ nm is significantly greater, decreasing the signal nearly to zero at the minima. In contrast, at $\lambda_{\text{probe}} = 400$ nm the parent ion yield decreases only by three quarters of the peak intensity. The underlying exponential decay of the signal is in both cases well described by two decay functions with

$$\tau_{2}^{\text{1,2,3,4-TFB}} = 2.3 \text{ ps}$$

and

$$\tau_{4}^{\text{1,2,3,4-TFB}} = 2300 \text{ ps}.$$

Contrary to the results of 1,2,4,5-TFB (cf. Section 3.2), virtually no change of the dynamics is observed when changing the polarization of the probe pulses from the default parallel to perpendicular polarization with respect to the detector surface, as shown in Figure 3.26 (e–f). Albeit $\tau_{2}^{\text{1,2,3,4-TFB}}(\perp) = 4.45$ ps and $\tau_{\text{osc}}^{\text{1,2,3,4-TFB}}(\perp) = 5.37$ ps being slightly increased compared to their counterparts at parallel polarization, the deviation most likely is due to an overall better data quality at parallel polarization. The fit parameters of the employed model fit functions at all wavelength combinations are listed in Table 3.11.

At $\lambda_{\text{pump}} = 265$ nm neither $\tau_{2}^{\text{1,2,3,4-TFB}}$ nor $\tau_{4}^{\text{1,2,3,4-TFB}}$ change (within the error limits), as shown in Figure 3.27. The oscillation, however, is slightly longer-lived with

$$\tau_{\text{osc}}^{\text{1,2,3,4-TFB}}(265 \text{ nm}) = 5.39 \text{ ps}.$$

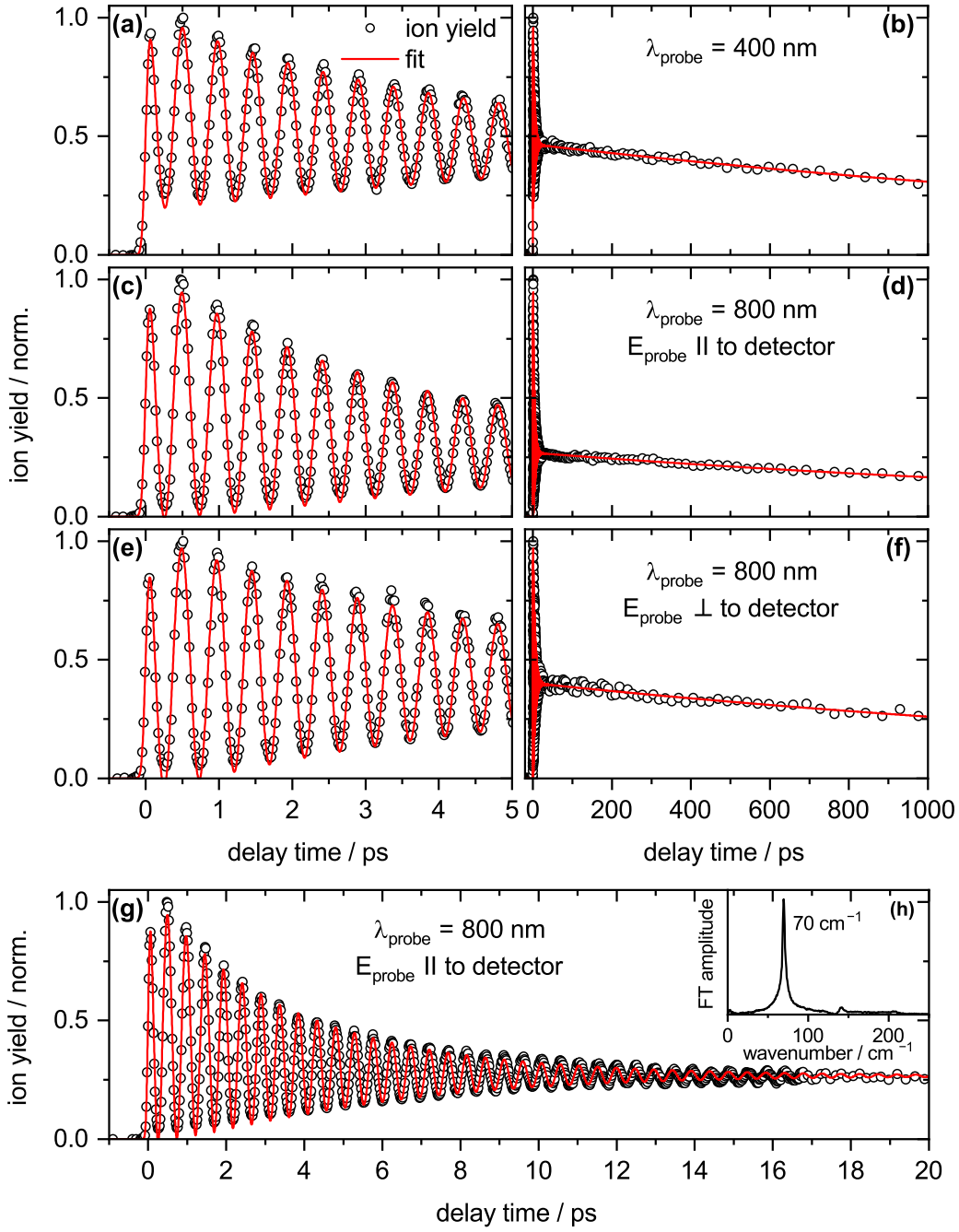

Figure 3.26. Measured transient parent ion yield signals (black circles) and applied fit model functions (red lines) for 1,2,3,4-TFB after excitation at $\lambda_{pump} = 260$ nm and ionization at $\lambda_{probe} = 400$ nm **(a–b)** resp. $\lambda_{probe} = 800$ nm **(c–g)**. The left-hand column shows the data in the first five picoseconds, the right-hand column in the first nanosecond after excitation. The fit parameters are listed in Table 3.11. The probe polarizations at 800 nm were varied from the default ∥ polarization to the detector surface (panels **(c)**, **(d)**, **(g)**) to ⊥ to the detector surface (panels **(e)**, **(f)**). **(g)** Complete decay of the oscillation truncated in **(c)**. **(h)** Fourier transform of the oscillatory signal component after subtraction of the exponential decay functions.

Table 3.11. Parameters for the fits of the transient parent ion yields of 1,2,3,4-TFB after excitation at $\lambda_{pump} = 260$ nm and ionization at $\lambda_{probe} = 400$ nm, as well as fit parameters after excitation at $\lambda_{pump} = 265$–255 nm ionization at $\lambda_{probe} = 800$ nm (polarization $\parallel$ and $\perp$ to detector plane). 2σ fit errors are given in parentheses. If no error is given the value was set fixed.

λ_{pump} nm	pr. pol.	σ_{IRF} fs	A_2 %	τ_2 ps	A_4 %	τ_4 ps	A_{osc} %	τ_{osc} ps	ν_{osc} cm^{-1}	ϕ_{osc} π
$\lambda_{probe} = 400$ nm										
260		39(2)	13(1)	2.33(16)	43(1)	2400(150)	44(1)	4.94(9)	70	−0.10
$\lambda_{probe} = 800$ nm										
265		35(4)	21(1)	2.31(17)	26	1700(230)	53(2)	5.39(13)	70	−0.16
260	$\parallel$	41(2)	22(1)	2.27(10)	24(1)	2100(220)	54(1)	4.26(7)	70	−0.06
	$\perp$	39(3)	7(1)	4.45(76)	37(1)	2300(250)	56(1)	5.37(11)	70	−0.04
255		43(2)	23(1)	1.72(6)	23	1125(65)	54(1)	3.02(5)	69	−0.04

Choosing $\lambda_{pump} = 255$ nm leads to a decrease of the lifetimes to

$$\tau_{osc}^{1,2,3,4\text{-TFB}}(255\text{ nm}) = 3.02\text{ ps}$$
$$\tau_{2}^{1,2,3,4\text{-TFB}}(255\text{ nm}) = 1.72\text{ ps},$$

and

$$\tau_{4}^{1,2,3,4\text{-TFB}}(255\text{ nm}) = 1125\text{ ps}.$$

Especially noteworthy is the substantially shortened overall lifetime at $\lambda_{pump} = 255$ nm. Analogous, near steplike changes of the excited state lifetimes were also observed for 1,2,4,5-TFB (cf. Section 3.2) and 1,2,3,5-TFB (cf. Section 3.3) and are discussed in Section 3.10.

Origin of the Oscillation

As for 1,2,3,5-TFB, varying the pump wavelength does not alter the oscillation frequency, thus essentially ruling out quantum beatings as the underlying mechanism.[22,24,27,29] Since the PE signals (*vide infra*) show no other state than the initially excited S_1 state is populated during the signal decay, the oscillation is attributed to strong vibronic coupling between the initially excited $\pi\pi^*$ state

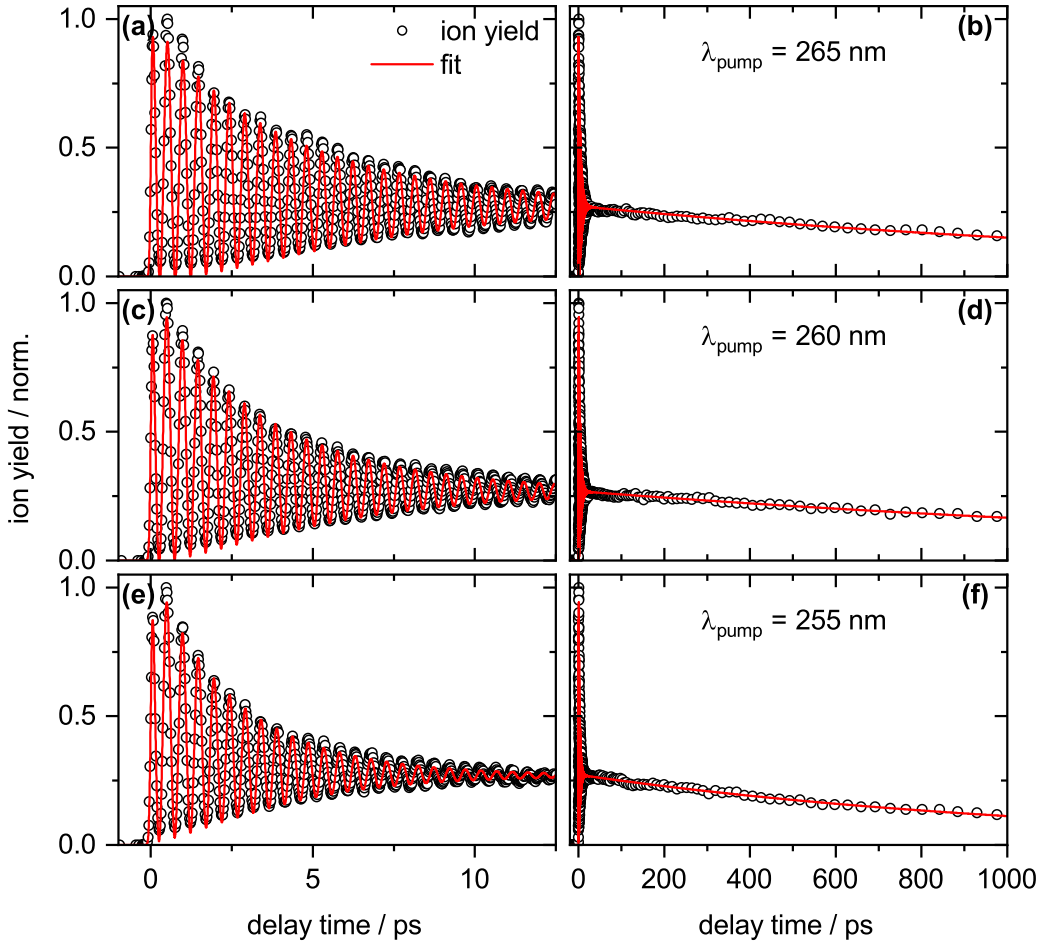

Figure 3.27. Measured transient parent ion yield signals (black circles) and applied fit model functions (red lines) for 1,2,3,4-TFB after excitation at $\lambda_{pump} = 265$ nm **(a–b)**, $\lambda_{pump} = 260$ nm **(c–d)**, and $\lambda_{pump} = 255$ nm **(e–f)** and ionization at $\lambda_{probe} = 800$ nm. The left-hand column shows the data in the first five picoseconds, the right-hand column in the first nanosecond after excitation. The fit parameters are listed in Table 3.11.

(S_1, 2 $^1A_1$) and the S_2 state (1 $^1A_2$), a $\pi\sigma^*$ state. The underlying mechanism is extensively discussed in Chapter 1 and in the literature.[5,9,10]

The coupling is mediated by a coherent wavepacket of vibrational modes. Symmetry suggests the a_2 modes to couple the $\pi\pi^*$ and the $\pi\sigma^*$ state. 1,2,3,4-TFB exhibits five a_2 modes (cf. Figure 3.25). Of these five vibrational modes only $\nu_{16} = 79$ cm^{-1} has a frequency of less than 200 cm^{-1}. As the frequency of ν_{16} fits near perfectly to the oscillational frequency of 70 cm^{-1}, the mode is assigned to be the most dominant mode of the wavepacket. Noteworthy, the optimized molecular structure does not transform according to any irreducible representation of the C_{2v} point group, which indicates the influence of several different vibrational modes, possibly also with different symmetry. If these modes merely stabilize the oscillation between the S_1 and the S_2 state, or enable coupling to higher-lying states needs to be addressed in future high-level calculations.

3.4.3 Time-Resolved Photoelectron Images

In Figure 3.28, the PEI of 1,2,3,4-TFB after excitation at $\lambda_{pump} = 260$ nm and subsequent ionization at $\lambda_{probe} = 400$ nm at $\Delta t = 0.08$ ps (a), in the first minimum at $\Delta t = 0.26$ ps (b), and in the first maximum at $\Delta t = 0.50$ ps (c) are shown. A broad (α) and a narrow signal (β) are observed, which peak at $E_\alpha = 0.2$ eV and $E_\beta = 0.91$ eV, as shown in the PES in Figure 3.29 (a). Both signals oscillate in agreement with the parent ion yield (cf. Figure 3.26). Consequently, at the delay times of the first two maxima following $\Delta t = t_0$ the overall electron yield is higher than at $\Delta t = t_0$, and the electron yield nearly decreases to zero at the minima positions.

Results of the high-intensity single-color ionization at $\lambda_{probe} = 400$ nm are displayed in Figure 3.28 (d). The SC ionization yields the narrow signal β and a broad signal γ, peaking at $E_\gamma = 1.5$ eV, as depicted the PES in Figure 3.29 (c).

Ionization Pathways

The absence of additional signals rising in at any delay time in the time-resolved PES shows that the deactivation of the initially excited S_1 state leads directly to the ground state, without conversion to a different excited state. As a consequence, the signal oscillation is an effect of an altered S_1 potential energy hypersurface, induced by the coupling of the S_1 to the S_2 state. Two signals emerge, since the ionization leads to the ionic ground state D_0 and the first

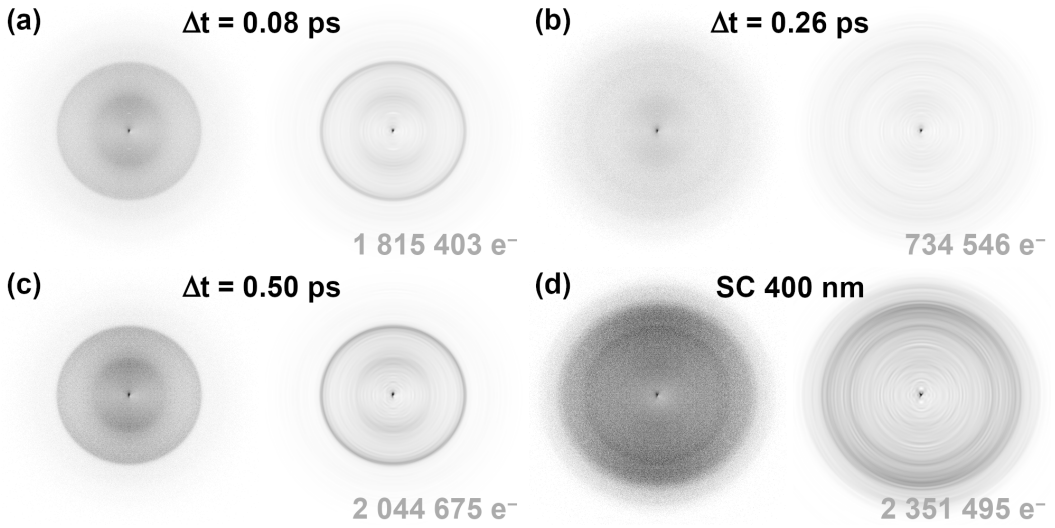

Figure 3.28. Photoelectron images (left) and their corresponding meridional slices through the recovered three-dimensional photoelectron distributions (right) of 1,2,3,4-TFB. **(a)** At $\Delta t = 0.08$ ps after excitation at $\lambda_{\text{pump}} = 260$ nm and ionization at $\lambda_{\text{probe}} = 400$ nm, **(b)** at $\Delta t = 0.26$ ps (first minimum), and **(c)** at $\Delta t = 0.50$ ps (first maximum). **(d)** High-intensity single-color photoelectron images obtained at 400 nm.

excited ionic state D_1. The energy gap between their AIEs of 0.35 eV (cf. Table 3.10) fits to the energy difference of ≈0.7 eV between the peaks of the PES signals α and β, especially considering the broad nature of α. The width of the signals indicates α results from a vertical transition, while in the case of β probably an adiabatic transition is observed.

Assuming an adiabatic transition as the origin of band β, calculation of the excitation energy of the electronic state populated prior to ionization should yield the S_1 AEE. Following Equation 3.2 in Section 3.1, subtracting the energy of the two probe photons at $\lambda_{\text{probe}} = 400$ nm (2×3.10 eV) from the sum of the peak energy $E_\beta = 0.91$ eV and the D_0 AIE of 9.53 eV[18,39,54] yields 4.24 eV. The absorption of the S_1 start to rise at ≈275 eV (4.51 eV). The PE-based and the absorption-based AEE estimates are thus in reasonable agreement, considering the absorption band onset not necessarily reflects the AEE. However, the PE band pattern of 1,2,3,4-TFB is very similar to the ones of 1,2,3-TriFB and 1,2,4,5-TFB (cf. Sections 3.1–3.2), for which excitation of intermediate states in the ionization pathway most likely alters the PE patterns. Analogous excitation may also impact the PE distribution for 1,2,3,4-TFB. Subtracting just the energy of a single probe photon from the sum of the D_0 AIE and E_β yields 7.34 eV, fitting very well to the intense absorption maximum in VUV spectra of the S_6 state ($\pi\pi^*$, $2\ ^1B_2$) at

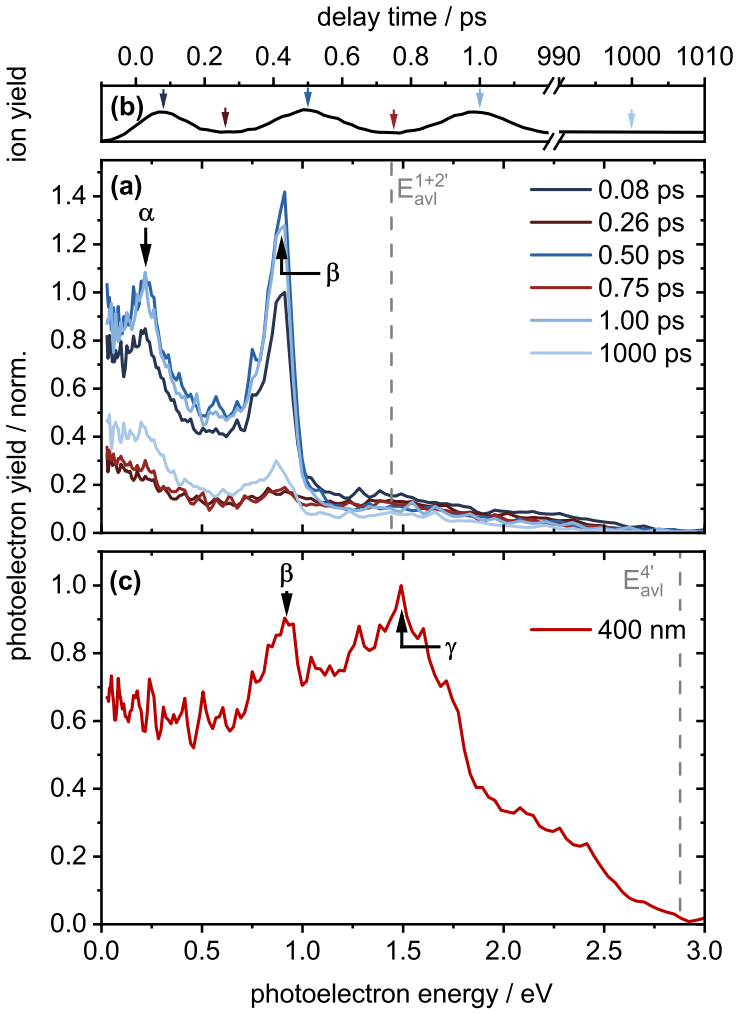

Figure 3.29. **(a)** Transient PE spectra of 1,2,3,4-TFB after excitation at $\lambda_{pump} = 260$ nm and ionization at $\lambda_{probe} = 400$ nm. The two main photoelectron signals labeled α and β are observed at $E_\alpha = 0.2$ eV and $E_\beta = 0.91$ eV. The grey dotted line indicates the maximum available photoelectron energy $E_{avl}^{1+2'}$ associated with the $D_0 \leftarrow S_0$ transition by $1 + 2'$ ionization. **(b)** Corresponding transient parent ion yields adapted from Figure 3.26 (a). Arrows mark the delay time $\Delta t = 0$–1000 ps at which the PES were obtained (red at ion yield minima). **(c)** Single-color PE spectrum taken at higher 400 nm probe intensities. The additional signal γ is located at $E_\gamma = 1.5$ eV. The grey dotted line indicates the maximum available photoelectron energies $E_{avl}^{4'}$ generated by four 400 nm photons.

Table 3.12. Molecular orbital configuration and their weighted contributions to the S_1, S_2, and S_6 states and the first three ionic states of 1,2,3,4-TFB. Correlations between the neutral and the ionic states according to Koopmans's theorem are given.

neutral state	3 b_1 (π)	4 b_1 (π)	3 a_2 (π)	4 a_2 (π^*)	5 b_1 (π^*)	17 a_1 (σ^*)	18 a_1 (σ^*)	24 a_1 (σ^*)	weight (%)	corr. ion. state
S_0 ($^1A_1$)	2	2	2							
S_1 ($^1A_1$, $\pi\pi^*$)	2	2	1	1					60	D_0
	2	1	2		1				32	D_1
S_2 ($^1A_2$, $\pi\sigma^*$)	2	2	1				1		33	
	2	2	1			1			32	D_0
	2	2	1					1	17	
S_6 ($^1B_2$, $\pi\pi^*$)	2	2	1		1				44	D_0
	2	1	2	1					42	D_1
ionic state										
D_0 ($^2A_2$, π^{-1})	2	2	1							
D_1 ($^2B_1$, π^{-1})	2	1	2						97	
D_2 ($^2B_1$, π^{-1})	1	2	2						93	

7.21 eV.[36] Likewise to the S_1 state, the S_6 state also electronically corresponds to the D_0 state, as shown in Table 3.12. Therefore, the initial excitation of the S_1 state might be followed by the absorption of a single probe photon, exciting the S_6 state. Subsequently, the absorption of a second probe photon within the probe pulse duration ionizes the molecules. Nevertheless, the direct ionization cannot be ruled out completely. In combination with the uncertainties regarding the true AEE, both mechanisms seem plausible. Even a third option might be possible. If the S_1 AEE actually is 4.24 eV, the absorption of a single probe photon could resonantly excite the S_6 state. In light of the results for the other TFB isomers and 1,2,3-TriFB, the excitation of an intermediate state is thus deemed very probable.

Since the S_6 state electronically also corresponds to the D_1 state, it is presumed that the broad signal α originates from vertical $D_1 \leftarrow S_6$ transitions. Yet, as no more information than the transition energy to the D_1 state is available, the assignment is rather preliminary. The proposed ionization pathways leading to α and β are depicted in Figure 3.30 (a).

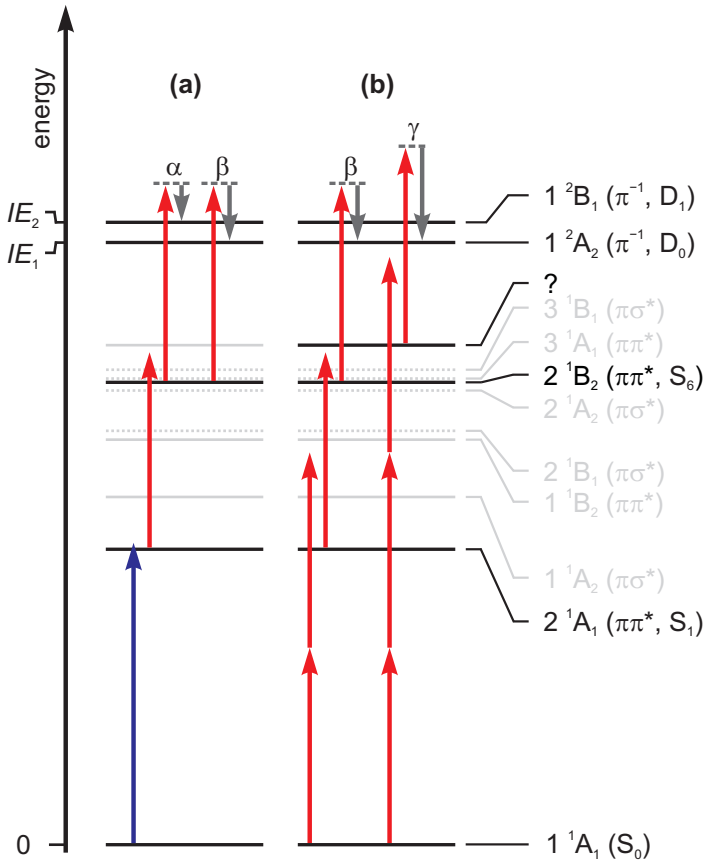

Figure 3.30. Proposed multi-color and single-color ionization schemes for 1,2,3,4-TFB. The energies of the photons at $\lambda_{pump} = 260$ nm (blue) and $\lambda_{probe} = 400$ nm (red) and of the photoelectrons (grey) are depicted as vertical arrows. Solid black horizontal lines: experimentally intermediate and final states, solid and dotted (calculated values) grey horizontal lines: non-participating other intermediate states. **(a)** Transient ionization pathways by one-photon absorption to the S_1 state ($2\ ^1A_1$) and subsequent two-photon ionization to the D_0 ($1\ ^2A_2$) and D_1 states ($1\ ^2B_1$) showing the origin of PE peaks α and β. **(b)** Single-color ionization pathways at $\lambda_{probe} = 400$ nm to the D_0 state showing the origin of PE peaks β and γ.

The SC ionization at $\lambda_{\text{probe}} = 400$ nm yields band β and a second diffuse signal at $E_\gamma = 1.5$ eV, on top of a broad background. The background decreases in intensity towards the maximum available kinetic energy of the four-photon ionization. Hence, the direct $D_0 \leftarrow S_0$ transition only plays a minor role for the signal generation. Absorption of two probe photons probably excites the S_1 state, followed by absorption of another photon to populate the S_6 state. The ionization via absorption of a fourth photon within the probe pulse duration generates signal β, as shown in Figure 3.30 (b). The absence of a band corresponding to signal α of the multi-color case may hint towards differences in the pathways leading to signals α and β. However, the signal may also simply vanish in the broad background. Signal γ most likely is the result of a three-photon transition to an intermediate state at $\approx$7.9 eV. The huge variety of possible states prohibits a more precise determination of the excited state.

3.5 Pentafluoropyridine

This Section is a shortened (omitting the sections abstract, introduction, experimental and computational methods, conclusion, and acknowledgments), but otherwise unaltered version of the publication:

Real-Time Observation of Multi-Mode Vibronic Coherence in Pentafluoropyridine

JONAS ANDREAS KUS, OLE HÜTER, AND FRIEDRICH TEMPS

Institute of Physical Chemistry, Christian-Albrechts-University Kiel, Olshausenstr. 40, D-24098 Kiel, Germany

Reproduced from J. Chem. Phys. **147**, 013938 (2017)*, with the permission of AIP Publishing.*

OWN CONTRIBUTIONS TO THIS MANUSCRIPT:

- Steady-state UV absorption spectroscopy.
- Femtosecond time-resolved time-of-flight mass spectrometry.
- Femtosecond time-resolved photoelectron imaging spectroscopy.
- Analysis of all experimental data.
- Quantum chemical calculations at the RI-SCS-MP2/-CC2 levels of theory.
- Writing of the first draft of the manuscript.

3.5.1 UV Absorption Spectrum and Calculated Electronically Excited States

The gas-phase UV absorption spectrum of PFPy is depicted in Figure 3.31. The spectrum shows a broad band with an absorption maximum at $\lambda = 254$ nm without a resolved vibrational structure. A second absorption band begins to rise at $\lambda < 220$ nm. The respective assignments are found from the quantum chemical calculations. The computed VEEs of the lowest eight electronically excited states are listed in Table 3.13. In the order of increasing energy given by the CC2 method, we have the 1 $^1B_2$ ($\pi\pi^*$), 1 $^1A_2$ ($\pi\sigma^*$), 2 $^1A_1$ ($\pi\pi^*$), 1 $^1B_1$ ($n\pi^*$), 2 $^1B_1$ ($\pi\sigma^*$), 2 $^1A_2$ ($n\pi^*$), 3 $^1A_1$ ($\pi\pi^*$) and 2 $^1B_2$ ($\pi\pi^*$) states. The CC2 and XMCQDPT2 calculations give results in good agreement with each other, although the energetic order differs for a few of the higher-lying states.

The VEE of the 1 $^1B_2$ ($\pi\pi^*$) state is calculated to be 5.10 eV (CC2) or 4.89 eV (XMCQDPT2), in excellent agreement with the experimentally observed absorption maximum at $\lambda = 254$ nm (4.88 eV). In our previous work on PFB,[9] we already observed that the CC2 method places the VEE for this transition slightly too high compared to the experimental result. While the structure optimization in the electronic ground state yields a planar geometry (Figure 3.32(a)), the molecule acquires a strong out-of-plane distortion in the first excited state (Figure 3.32(b)). The N atom is displaced out of the plane defined by the four carbon atoms on the side of the ring by 1.5° and the C and F atoms opposing the N atom by 2.5° and 35°, respectively. The other four F atoms are displaced by about 5° in the opposite direction. This structural deformation corresponds to nuclear motion along normal modes of b_1 symmetry, as will be discussed in Section 3.5.4. (Although the relaxed structures have C_s symmetry, we continue to employ C_{2v} symmetry labels here and in the following as is customary for other C_{2v} molecules with quasi-planar out-of-plane distorted excited electronic state structures.[55])

The adiabatic excitation energy (AEE) of the 1 $^1B_2$ state, which is a good estimate for the excitation energy of the 0–0 transition from the S_0 ground state, amounts to 4.41 eV at the CC2 level of theory. We observed a similarly pronounced energetic stabilization of an out-of-plane deformed structure for the excited state of PFB.[9]

Although we do not expect energetically higher-lying electronic states to be excited by single-photon absorption of our 255 nm pump pulses, their VEEs and

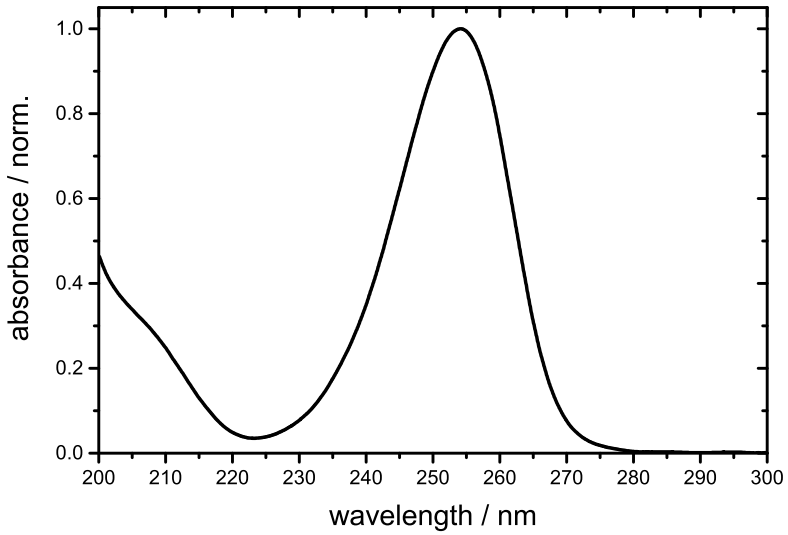

Figure 3.31. Gas phase UV absorption spectrum of PFPy ($p = 0.75$ mbar). The absorption maximum of the 1 $^1B_2$ ($\pi\pi^*$) excited state peaks at $\lambda = 254$ nm. The band at $\lambda < 220$ nm was assigned to the 2 $^1A_1$ ($\pi\pi^*$) state.

Table 3.13. Calculated vertical (VEE) and adiabatic (AEE) transition energies (in eV) from the S_0 (1 $^1A_1$) electronic ground state to the lowest eight valence excited states of the neutral PFPy molecule, to the electronic ground state of the ion, and to the lowest two excited states of the ion. The calculated oscillator strengths are given in parentheses next to the RI-SCS-CC2 energies. Experimental values are given for comparison where available.

State	RI-SCS-CC2 VEE	XMCQDPT2 VEE	RI-SCS-CC2 AEE	Experimental VEE/AEE
1 $^1B_2$ ($\pi\pi^*$)	5.10 (0.056)	4.89	4.41	4.88[a] / 4.60[a]
1 $^1A_2$ ($\pi\sigma^*$)	6.35 (0.000)	6.23	...	...
2 $^1A_1$ ($\pi\pi^*$)	6.64 (0.015)	6.46	...	– / 5.90[a]
1 $^1B_1$ ($n\pi^*$)	6.71 (0.003)	6.35	...	...
2 $^1B_1$ ($\pi\sigma^*$)	7.23 (0.012)	7.22	...	– / 6.12[a]
2 $^1A_2$ ($n\pi^*$)	7.30 (0.000)	6.95	...	...
3 $^1A_1$ ($\pi\pi^*$)	7.59 (0.549)	7.11	...	– / 6.57[a]
2 $^1B_2$ ($\pi\pi^*$)	7.68 (0.487)	7.05	...	
1 $^2A_2$ (π^{-1})	10.28	...	10.00	10.27[b] / 10.08[b]
1 $^2B_1$ (π^{-1})	11.53	...	11.27	11.37[b] / 11.17[b]
1 $^2A_1$ (n^{-1})	12.20	...	...	12.08[b] / 11.84[c]

[a] This work.
[b] Brundle *et al.* (Ref. [56]).
[c] Utsunomiya *et al.* (Ref. [57]).

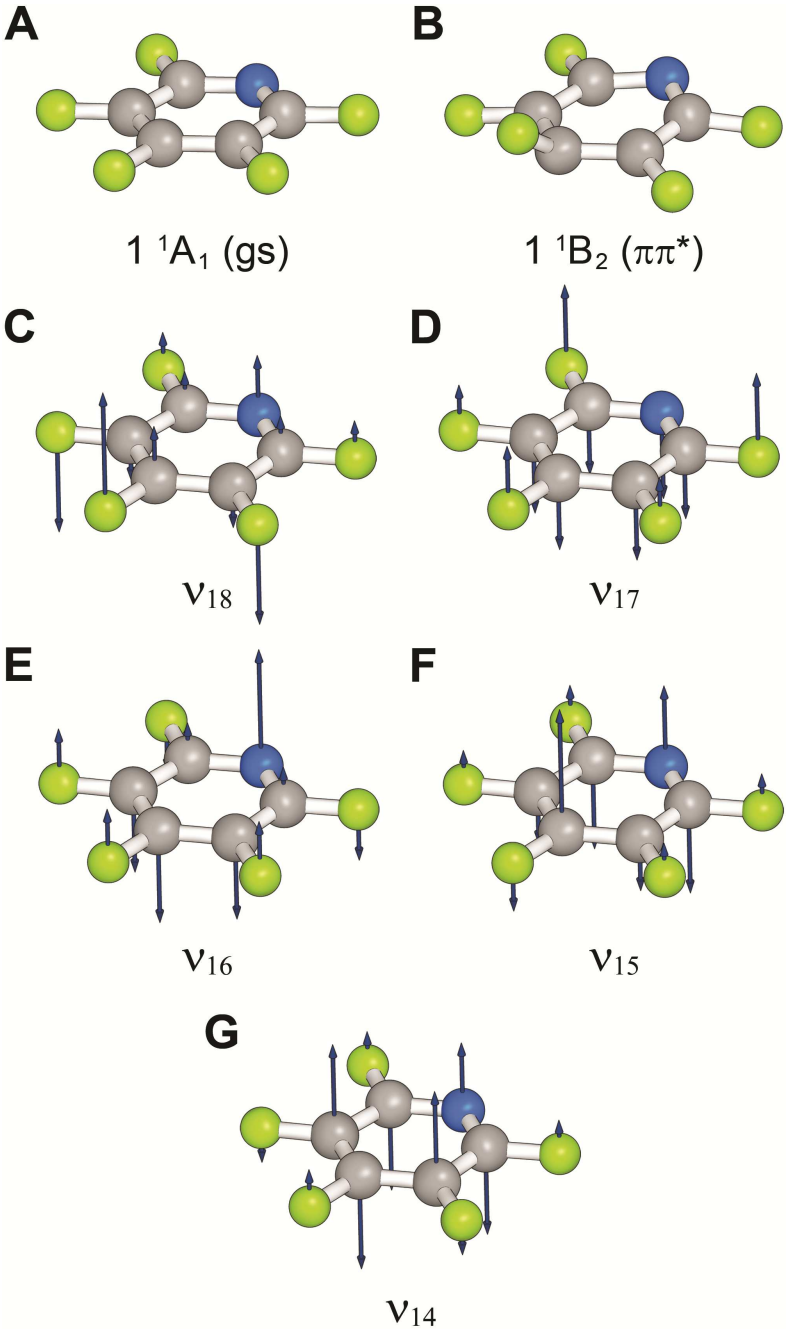

Figure 3.32. RI-SCS-CC2-optimized molecular equilibrium structures (a) in the electronic ground state and (b) in the excited 1 $^1B_2$ ($\pi\pi^*$) state of PFPy. ((c) – (g)) Displacement vectors of the calculated harmonic vibrational normal modes ν_{18} – ν_{14} of b_1 symmetry in order of increasing frequency.

electronic characters were calculated to investigate possible vibronic couplings with the 1 $^1B_2$ ($\pi\pi^*$) state. Moreover, some of those states act as resonant intermediates in the multi-photon probe process. The second $\pi\pi^*$ transition, which leads to the 2 $^1A_1$ state, is computed with a VEE of 6.64 eV (CC2) or 6.46 eV (XMCQDPT2). With an oscillator strength of $f = 0.015$, this transition is likely responsible for the observed UV absorption band at $\lambda < 220$ nm (see Figure 3.31). Higher states of $\pi\pi^*$ character are 3 $^1A_1$ and 2 $^1B_2$ with calculated VEEs of 7.59 eV and 7.68 eV (CC2) or 7.11 eV and 7.05 eV (XMCQDPT2). Both have very large oscillator strengths of $f \sim 0.5$ and are therefore likely to be resonant intermediate states in the multi-photon ionization process.

The symmetry-forbidden transition to the 1 $^1A_2$ ($\pi\sigma^*$) state is calculated to have a VEE of 6.35 eV (CC2) or 6.23 eV (XMCQDPT2). Both calculated values are in good agreement with each other. The computed excitation energies for the 2 $^1B_1$ state reached by the second $\pi\sigma^*$ transition agree with each other as well. As will be discussed in Section 3.5.4, for symmetry reasons only the 1 $^1A_2$ state can vibronically couple to the 1 $^1B_2$ ($\pi\pi^*$) state via b_1 vibrational modes. The VEE for the 1 $^1B_1$ ($n\pi^*$) state is calculated to be at 6.71 eV or 6.35 eV and for the 2 $^1A_2$ ($n\pi^*$) state at 7.30 eV or 6.95 eV, respectively. Here, the computational methods disagree with each other, as the CC2 method systematically places the $n\pi^*$ transitions at higher energies than the XMCQDPT2 method. However, the dynamics in the excited 1 $^1B_2$ ($\pi\pi^*$) state are not expected to be influenced by the 2 $^1A_2$ ($n\pi^*$) state through b_1 modes, although coupling would be allowed by symmetry (see Section 3.5.4).

The electronic structure of the cation was investigated at the CC2 level of theory to aid the assignment of the PE spectra. The vertical and adiabatic ionization energies for the cationic 1 $^2A_2$ (π^{-1}), 1 $^2B_1$ (π^{-1}) and 1 $^2A_1$ (n^{-1}) states are in excellent agreement with the experimental values determined by Brundle *et al.*[56] and Utsunomiya *et al.*[57] (cf. Table 3.13). The third cationic excited state 2 $^2B_1$ (π^{-1}) with an experimentally determined adiabatic IE of 13.46 eV[57] is not reached energetically in our experiment and is therefore not considered any further. The results of the structure optimizations show that the molecule retains a planar geometry in the cationic ground and first excited states with only minor structural differences compared to the neutral ground state.

3.5.2 Time-Resolved Time-of-Flight Mass Spectrometry

The recorded time-resolved parent ion yield signal of PFPy is shown in Figure 3.33(a). The initial spike around $\Delta t = 0$ ps is followed by a pronounced and long-lived periodic modulation of the signal amplitude. The oscillatory behavior can be observed for up to ∼9 ps after the excitation. Subsequently, the ion yield signal decays exponentially within about 200 ps. A zoomed-in plot of the oscillating part is depicted in Figure 3.33(c). The maxima have a temporal spacing of about 0.47 ps, and each of them displays a sub-structure of up to three further local maxima within the first ∼3.5 ps. To ensure that this complex signal modulation is not an effect of experimental noise, the measurements were repeated on several different days. The respective results are shown by the vertically displaced curves in Figure 3.33(c). As can be seen, the modulation pattern of the ion yield signal is reproducible to a remarkable degree. We emphasize that the TOF mass spectrum of PFPy using multiphoton ionization at 402 nm, which is shown in Figure 3.33(b), exhibits no evidence for the dissociation or fragmentation of the excited molecules or ions within our experimental detection sensitivity. Thus, the eventual temporal decay of the PFPy parent ion yield signal in Figure 3.33(a), which is observed on a time scale of ∼40 ps, has to be ascribed to nonadiabatic electronic deactivation from the excited 1 $^1B_2$ ($\pi\pi^*$) state to the S_0 ground state.

The molecular frequencies encoded in the oscillating signal were found by a Fourier transform (FT) analysis. To this end, we first subtracted from the data points the initial spike around time zero and the slowly decaying component of the signal. As shown in Figure 3.34(a), both could be nicely modeled by least-squares fitting using a biexponential decay function convoluted with a Gaussian representing the instrument response function (IRF). The resulting best fit is indicated by the solid red line in Figure 3.34(a). The subtraction of this curve from the experimental ion yield data points gave the oscillatory part of the signal depicted in Figure 3.34(c). The resulting Fourier transform is given in Figure 3.34(b). Four spectral components, corresponding to frequencies of 72 cm^{-1} (I), 144 cm^{-1} (II), 251 cm^{-1} (III), and 281 cm^{-1} (IV), are readily distinguished. The value of frequency II looks like the second harmonic of frequency I. This assumption will be substantiated in Section 3.5.4.

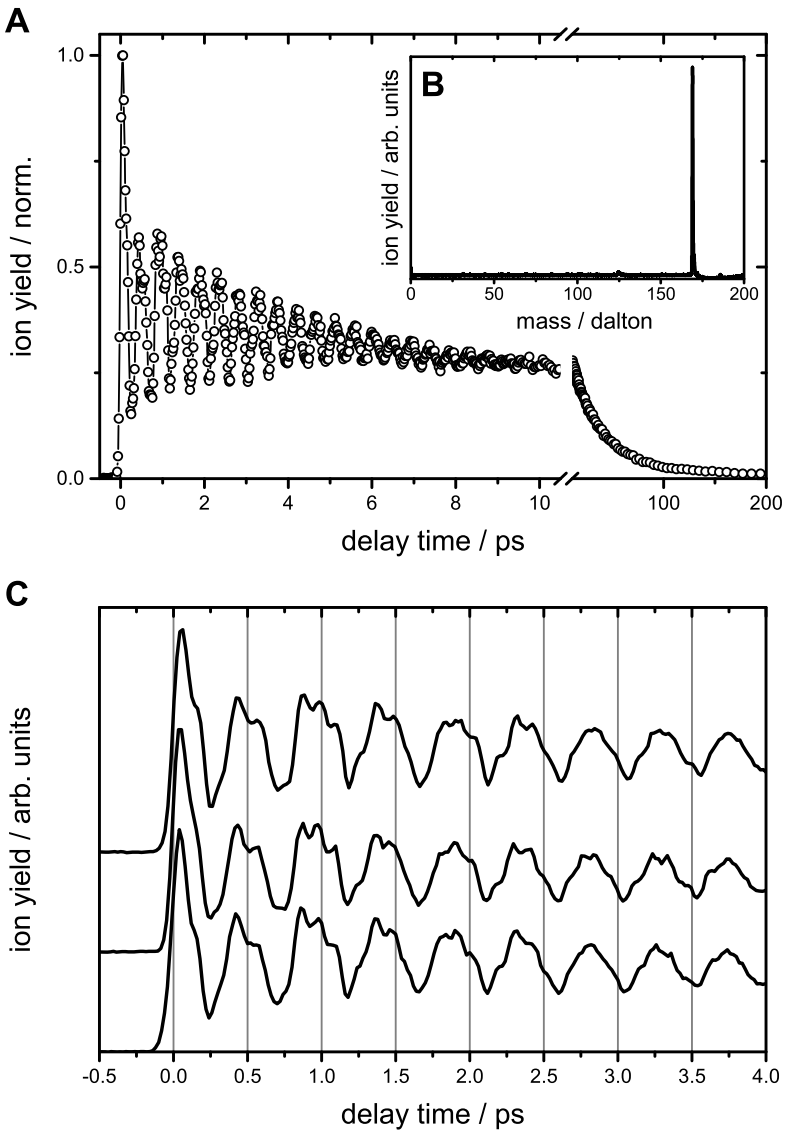

Figure 3.33. (a) Recorded transient PFPy parent ion yield signal as function of pump–probe delay time after excitation at $\lambda_{\text{pump}} = 255$ nm. (b) TOF mass spectrum of PFPy resulting from the multi-photon ionization at $\lambda_{\text{probe}} = 402$ nm. As can be seen, the spectrum shows virtually no fragmentation. (c) Repeated measurements shown on an enlarged time scale up to $\Delta t = 4$ ps. The vertically displaced curves represent separate measurements recorded on different days to highlight the reproducibility of the modulation pattern.

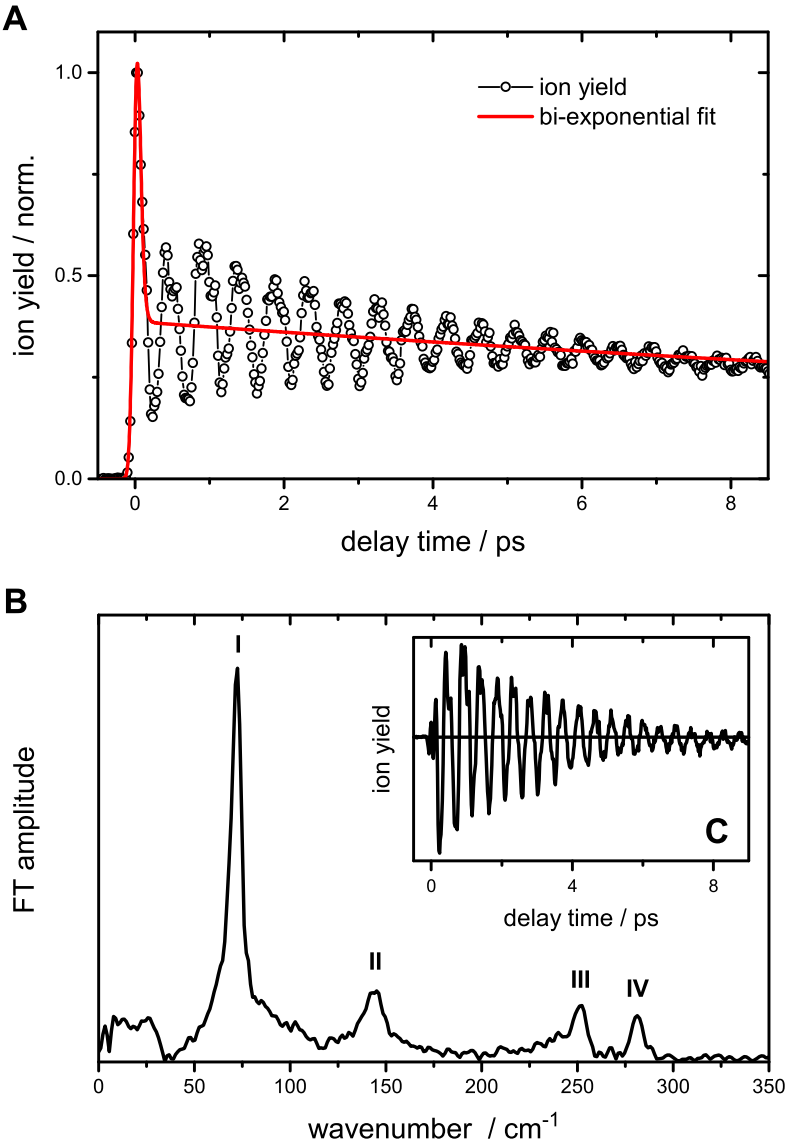

Figure 3.34. (a) Least-squares fit of a biexponentially decaying model function (solid red line) to the transient PFPy ion yield data points (connected circles). (b) Fourier transform of the remaining oscillatory signal shown in the inset (c) after subtraction of the biexponential model decay function. The FT analysis identifies four frequencies at 72 cm^{-1} (I), 144 cm^{-1} (II), 251 cm^{-1} (III), and 281 cm^{-1} (IV).

3.5.3 Time-Resolved Photoelectron Imaging

Time-resolved PE images were recorded using one-photon excitation from the pump pulse and at least two photons from the ionizing probe pulse at temporal delay times corresponding to the first, second, and third maxima of the oscillating ion yield signal, as well as the first and second minima. The resulting raw images together with their Abel-inverted images are shown in Figure 3.35. A probe-only image using four-photon ionization with the 402 nm laser pulses recorded for comparison is reproduced in Figure 3.35(a). Four distinct rings can be identified in the probe-only image, whereas the pump-and-probe time-resolved images at the oscillation maxima (Figures 3.35(b), (d) and (f)) only show three rings. Moreover, the middle ring appears to vanish when going from an oscillation maximum to the minimum (Figures 3.35(c) and (e)).

The photoelectron spectra associated with those images are shown in Figure 3.36 (probe-only) and in Figure 3.37 (pump-and-probe time-resolved). The dashed vertical lines denote the maximal available PE kinetic energy

$$E_{\mathrm{avl}} = \hbar(n \times \omega_{\mathrm{pump}} + m \times \omega_{\mathrm{probe}}) - IE$$

that a photoelectron can gain after an n-photon pump and m-photon probe process with a given adiabatic molecular ionization energy IE. If a higher ionic state with a larger IE is accessed, the available kinetic energy will decrease accordingly. In the probe-only experiment, this energy amounts to $E_{\mathrm{avl}}^{4'} = 2.27$ eV for four-photon ionization, whereas $E_{\mathrm{avl}}^{1+2'} = 0.96$ eV in the time-resolved experiments with the desired $1 + 2'$ (one-photon pump, two-photon probe) process. The probe-only spectrum (Figure 3.36) exhibits four distinct PE bands, which are centered at (a) 0.72 eV, (b) 1.15 eV, (c) 1.60 eV, and (d) 2.00 eV. The PE bands in the pump-and-probe time-resolved PE spectra (Figure 3.37) are centered at virtually identical energies within experimental errors (±0.05 eV) of (a) 0.70 eV, (b) 1.10 eV and (c) 1.60 eV. No peak is observed around 2.00 eV, which is the position of band (d) in Figure 3.36. Band (b) at 1.10 eV corresponds to the middle ring in the PE images that is missing at pump–probe delay times corresponding to oscillation minima.

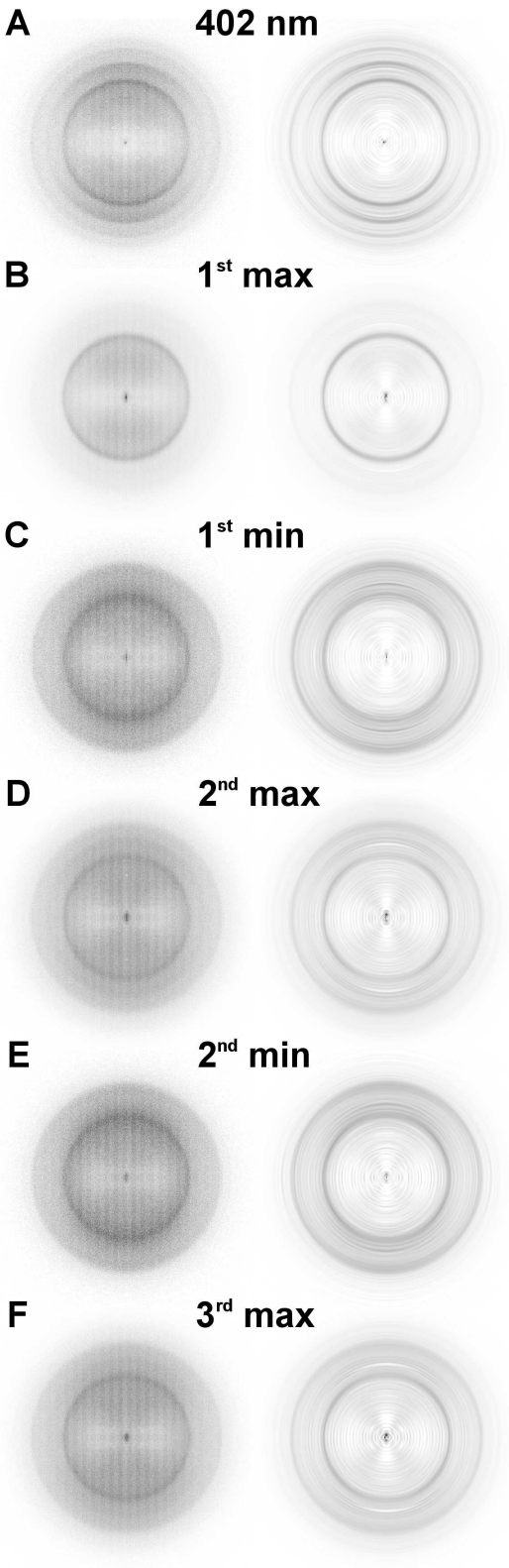

Figure 3.35. Recorded photoelectron images (left) and corresponding meridional slices through the recovered three-dimensional photoelectron distributions (right). (a) PE image by four-photon ionization using the probe laser pulse at $\lambda_{\text{probe}} = 402$ nm only. ((b)–(f)) Transient PE images recorded using both pump and probe laser pulses at delay times corresponding to the first few maxima and minima of the transient ion yield signal.

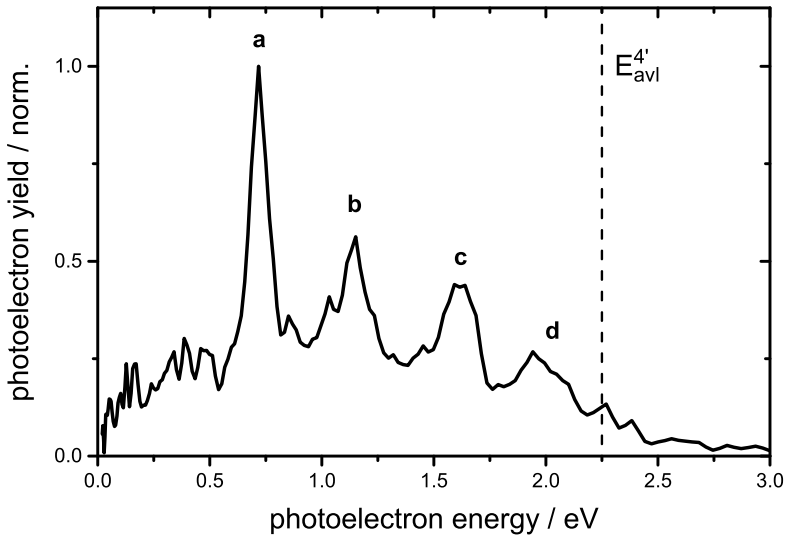

Figure 3.36. Probe-only photoelectron spectrum resulting from four-photon ionization at $\lambda_{probe} = 402$ nm. The maximal available energy in this process is indicated by the dashed vertical line. Four peaking bands can be distinguished, which are centered at (a) 0.72 eV, (b) 1.15 eV, (c) 1.60 eV, and (d) 2.00 eV.

3.5.4 Discussion

Assignment of the Photoelectron Spectra

As found from the excited electronic state calculations (cf. Table 3.13), three energetically close-lying ionic states are accessible from ground-state PFPy by our pump-and-probe scheme: $1\ ^2A_2$ (π^{-1}), $1\ ^2B_1$ (π^{-1}), and $1\ ^2A_1$ (n^{-1}). Several arguments allow us to identify those states in our photoelectron spectra. In particular, the specific ionic state that is reached in a two-color multi-photon ionization process is often determined by a specific molecular orbital that gives the largest contribution to the resonant intermediate excited state accessed by the pump pulse.[16,17] For the assignment of the observed PE bands, it is therefore useful to consider the electron configurations of the involved states in some detail.

Following our CC2 and XMCQDPT2 calculations, the $1\ ^1B_2$ ($\pi\pi^*$), $1\ ^1A_2$ ($\pi\sigma^*$), and $2\ ^1A_1$ ($\pi\pi^*$) excited states all have the largest contribution from the excitation of an electron from the $3a_2$ (π) orbital. The Ionization of the PFPy molecule from either of those excited states will therefore likely lead to the $1\ ^2A_2$ (π^{-1}) ionic state. This is the ground (i.e., D_0) state of the $PFPy^+$ ion. Conversely, the higher-lying $2\ ^1B_1$ ($\pi\sigma^*$), $3\ ^1A_1$ ($\pi\pi^*$), and $2\ ^1B_2$ ($\pi\pi^*$) electronic states have the largest contribution from the excitation of an electron from the $5b_1$ (π)

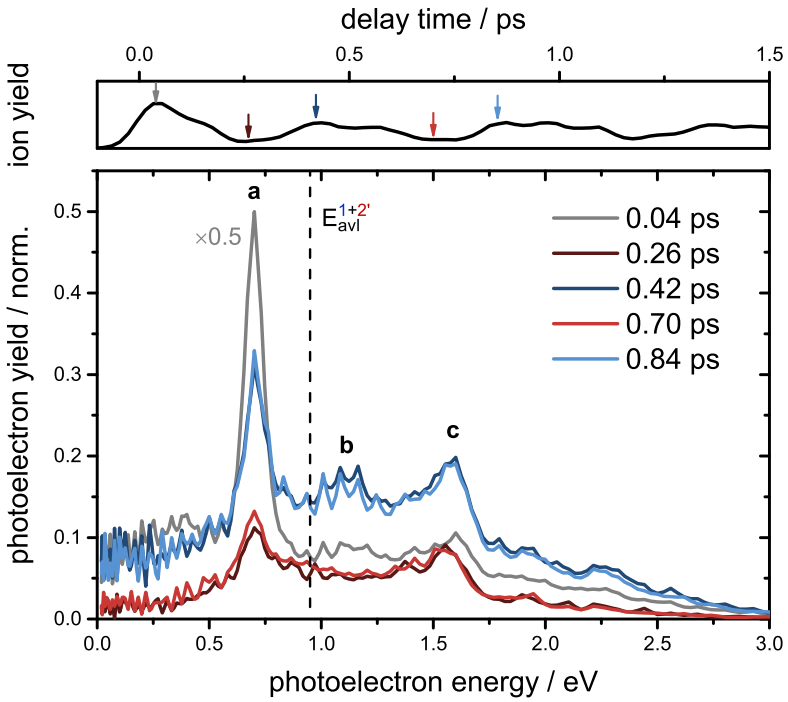

Figure 3.37. Time-resolved photoelectron spectra after excitation at $\lambda_{pump} = 255$ nm and multi-photon ionization at $\lambda_{probe} = 402$ nm. The dashed vertical linemarks the maximal available photoelectron energy $E_{avl}^{1+2'}$ in the $1+2'$ ionization scheme. The spectra were recorded at delay times corresponding to the first, second, and third maxima ($\Delta t = 0.04$, 0.42, and 0.84 ps) and the first and second minima ($\Delta t = 0.26$ and 0.70 ps) of the transient ion yield signal (shown above the spectra for orientation with color-coded arrows indicating the delay times). Note that the spectrum at $\Delta t = 0.04$ ps (gray curve) has been multiplied by a factor of 0.5. At delay times corresponding to the maxima, three distinct bands can be distinguished, which are centered at (a) 0.70 eV, (b) 1.10 eV, and (c) 1.60 eV (see the text). In the oscillation minima, the signal amplitude over the entire spectral range is strongly reduced and band (b) appears to be missing.

orbital. Their ionization is thus expected to reach the first excited 1 $^2B_1$ (π^{-1}) state of $PFPy^+$. By the same token, ionization from one of the 1 $^1B_1$ or 2 $^1A_2$ ($n\pi^*$) excited states should lead to the ion in the 1 $^2A_1$ (n^{-1}) excited state. The electronic excitation and ionization processes that lead to the observed structure of the PE spectra are summarized in the ionization scheme in Figure 3.38 and will be detailed in the following.

Keeping the above-mentioned ionization correlations in mind, PE band (a) in the time-resolved spectra in Figure 3.37 can be unambiguously assigned to ionization from 1 $^1B_2$ ($\pi\pi^*$) to 1 $^2A_2$ (π^{-1}). It is the only signal below $E_{\mathrm{avl}}^{1+2'}$ and has a very large amplitude due to the resonant excitation in the $1+2'$ process (cf. Figure 3.38(a)). From its spectral position, we estimate the AEE of the 1 $^1B_2$ ($\pi\pi^*$) state to be 4.60 eV. As this band (a) is also present in the probe-only PE spectrum (Figure 3.36), the 1 $^1B_2$ ($\pi\pi^*$) state appears to be excited by the probe pulses alone as well. Since the energy of $\hbar\omega = 3.08$ eV of a single probe photon is not sufficient, we propose that a two-photon absorption with a total energy of $\hbar\omega = 6.17$ eV (corresponding to $\lambda = 201$ nm, cf. Figure 3.31) does in fact excite the 2 $^1A_1$ ($\pi\pi^*$) state. To understand how this transition leads to a simultaneous excitation of the 1 $^1B_2$ ($\pi\pi^*$) state, we turn to our computational results and compare those to the structurally related, but highly symmetric, benzene molecule (D_{6h} point group). Both the CC2 and XMCQDPT2 methods reveal that the 2 $^1A_1$ ($\pi\pi^*$) state has major contributions from the $3a_2 \rightarrow 4a_2$ and $5b_1 \rightarrow 6b_1$ electronic transitions, while the 1 $^1B_2$ ($\pi\pi^*$) state is established mostly by the $3a_2 \rightarrow 6b_1$ and $5b_1 \rightarrow 4a_2$ transitions. The occupied $3a_2$ and $5b_1$ π orbitals emerge from the twofold degenerate e_{1g} highest occupied molecular orbital (HOMO) of benzene, while the $4a_2$ and $6b_1$ π^* orbitals correspond to the e_{2u} lowest unoccupied molecular orbital (LUMO). In benzene, transitions between those orbitals are responsible for the 1 $^1B_{2u}$, 1 $^1B_{1u}$, and 1 $^1E_{1u}$ excited states, of which the first two correspond to the 1 $^1B_2$ and 2 $^1A_1$ ($\pi\pi^*$) states of PFPy, where the degeneracy of the MOs is lifted due to the reduction to C_{2v} symmetry. We therefore assume that the excitation of 2 $^1A_1$ can be followed by an ultrafast internal conversion to 1 $^1B_2$. Estimating the AEE of the 2 $^1A_1$ ($\pi\pi^*$) state to be around 5.90 eV, which corresponds to the right shoulder of the absorption band at $\lambda \sim 210$ nm in the UV absorption spectrum (Figure 3.31), a PE band after two-photon ionization to the ionic ground state would be expected at around 2.00 eV (cf. Figure 3.38(a)). This corresponds exactly to the position of PE band (d) in the probe-only PE spectrum in Figure 3.36, thereby suggesting

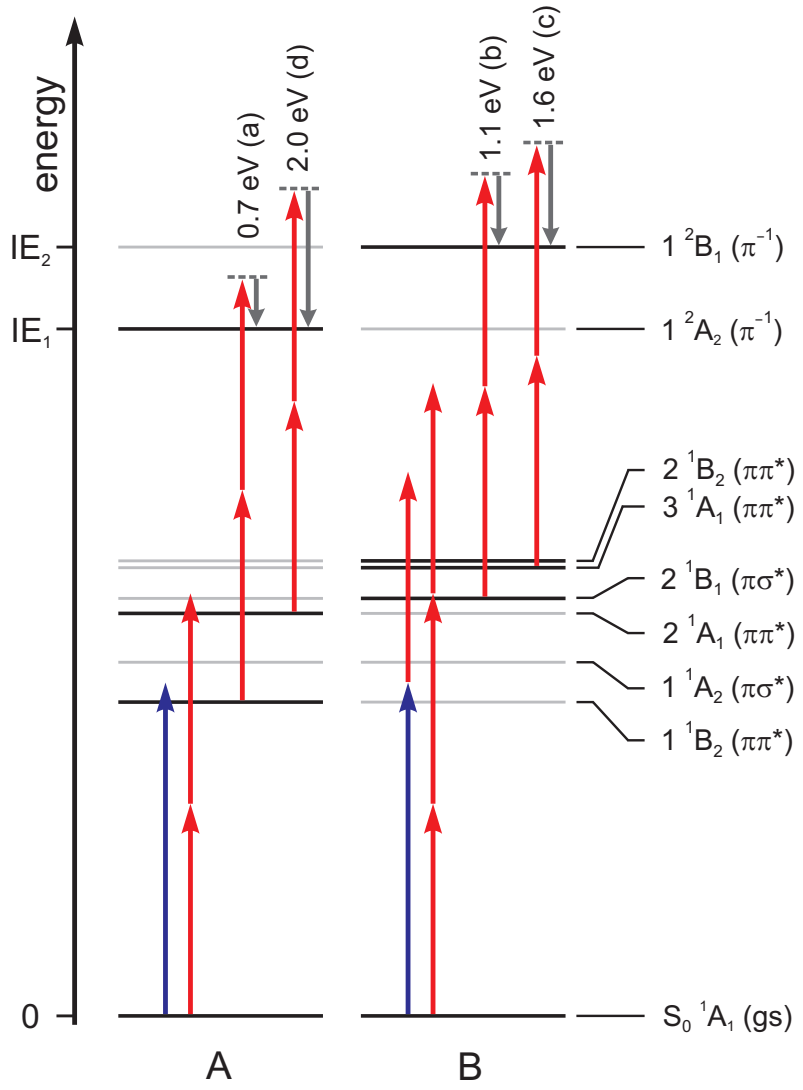

Figure 3.38. Pump–probe scheme in the photoelectron imaging experiment showing the excitation of PFPy with one pump photon at $\lambda_{pump} = 255$ nm (blue arrows) and the multi-photon ionization at $\lambda_{probe} = 402$ nm (red arrows) to different ionic states. (a) Excitation of the two lowest $\pi\pi^*$ states $1\ ^1B_2$ and $2\ ^1A_1$ followed by two-photon ionization to the ionic ground state $1\ ^2A_2$ (π^{-1}), leading to the observed PE bands (a) and (d). (b) Proposed multi-photon excitation of the higher-lying $\pi\pi^*$ states $3\ ^1A_1$ and $2\ ^1B_2$ and of the $2\ ^1B_1$ ($\pi\sigma^*$) state followed by ionization to the first excited $1\ ^2B_1$ (π^{-1}) ionic state, resulting in PE bands (b) and (c). The resulting photoelectron kinetic energies are given vertically above the arrows.

that our above assumptions are correct. Band (d) is missing in the time-resolved PE spectrum in Figure 3.37 because the subsequent absorption of one (time-delayed) probe photon after the absorption of one pump photon excites states of far higher energy than 2 $^1A_1$ ($\pi\pi^*$) (cf. Figure 3.38), giving rise to bands (b) and (c), instead.

PE bands (b) and (c) are present in both the probe-only and the pump-and-probe time-resolved PE spectra and are therefore likely caused by ionization of very high-lying excited electronic states. Those states can be excited by a combination of three probe photons or by one pump plus one probe photon and are subsequently ionized by two additional probe photons (i.e., reached by $3' + 2'$ or $1 + 1' + 2'$ ionization, see Figure 3.38(b)). Their assignment to the emitting electronic states is not straightforward, as the corresponding total photon energies available for the excitation of $\hbar\omega = 9.25$ eV ($3' + 2'$ process) and $\hbar\omega = 7.95$ eV ($1 + 1' + 2'$ process) allow for excitation to all electronic states considered in our quantum chemical calculations (cf. Table 3.13). While PE band (b) has a sharp peak in the probe-only PE spectrum, it displays a partially resolved vibrational structure in the pump-and-probe time-resolved PE spectra. The latter is likely connected to the excitation of a larger number of vibrational modes by the spectrally broad pump pulse. PE band (c), on the other hand, has similar spectral shape in both PE spectra. Moreover, PE band (b) vanishes at delay times corresponding to oscillation minima in the time-resolved PE spectra, while band (c) retains its amplitude in relation to (a). These observations suggest that the electronic characters of the excited states responsible for bands (b) and (c) differ from each other. It seems likely that at least one of the PE bands is due to the excitation of either the 3 $^1A_1$ ($\pi\pi^*$) or the 2 $^1B_2$ ($\pi\pi^*$) state because the corresponding transitions have large calculated oscillator strengths ($f =$ 0.487–0.549). The allowed transition to the 2 $^1B_1$ ($\pi\sigma^*$) state with $f = 0.012$ might also be excited in the multi-photon process. Presuming an ionization of those states to the first excited 1 $^2B_1$ (π^{-1}) ionic state (see the ionization correlations discussed above and Figure 3.38(b)), adiabatic electronic excitation energies of 6.12 eV and 6.57 eV can be calculated from the PE band energies of 1.15 eV (b) and 1.60 eV (c). The excitation energy difference of 0.45 eV is in good agreement with the difference of the calculated CC2 VEEs for the $^1B_1$ ($\pi\sigma^*$) and 3 $^1A_1$ or 2 $^1B_2$ ($\pi\pi^*$) states of 0.36–0.45 eV. The VEEs obtained with the XMCQDPT2 method, on the other hand, predict a smaller energetic difference.

Therefore, the assignments of PE bands (b) and (c) remain somewhat speculative within our present scope.

Periodic Oscillations of the Transient Ion Yield Signal

The periodic modulation of the PFPy ion yield signal (Figure 3.33) is similar in principle to that in our previous work on the PFB molecule.[9] However, the detection of four distinct frequency components in the case of PFPy clearly stands out. The two energetically lowest excited states of both PFPy and PFB are 1 $^1B_2$ ($\pi\pi^*$) and 1 $^1A_2$ ($\pi\sigma^*$) at the Franck-Condon (FC) structure, with a difference in their VEEs of slightly more than 1 eV at the CC2 and XMCQDPT2 levels of theory. Vibronic coupling between those states can be mediated by vibrational modes of b_1 symmetry, which are out-of-plane deformation modes. In our previous study, we calculated the diabatic and adiabatic PECs along the six b_1 normal mode coordinates Q_{20} – Q_{15} of PFB (numbered according to the Mulliken notation) using the XMCQDPT2 method. The results showed that, while the diabatic PECs of the first excited $\pi\pi^*$ state all have their minima at the planar FC structure, the adiabatic PECs exhibit symmetric double wells along the Q_{20}, Q_{18}, Q_{17}, and Q_{16} coordinates with minima at out-of-plane distorted structures. A symmetry-breaking pseudo-Jahn–Teller (PJT) effect[58] is caused by strong vibronic couplings between the 1 $^1B_2$ ($\pi\pi^*$) and 1 $^1A_2$ ($\pi\sigma^*$) states by those b_1 modes. The result is a repulsion between the first and second adiabatic PECs that, for the Q_{20}, Q_{18}, Q_{17}, and Q_{16} coordinates of PFB, is strong enough to stabilize an out-of-plane distorted molecular geometry of the 1 $^1B_2$ ($\pi\pi^*$) state. Subsequent quantum dynamics simulations based on a vibronic coupling model Hamiltonian[59,60] parametrized from the results of the XMCQDPT2 calculations indeed showed that the $\pi\pi^*$ excited PFB molecule performs a long-lived regular periodic motion mainly along Q_{20}, while little oscillatory motion could be observed along other coordinates.[9] The nuclear motion along the b_1 coordinates in the adiabatic picture is associated with a mixing of the $\pi\pi^*$ and $\pi\sigma^*$ electronic characters of the first and second excited states. This mixing is mirrored by the calculated time-dependent diabatic excited-state populations of the $\pi\pi^*$ and $\pi\sigma^*$ states, which accordingly show large amplitude oscillations with opposite phases. The frequency and damping time of the calculated oscillating state populations is in good agreement with the experimentally observed transient ion yield oscillation.[9]

Considering the distinct similarity of the experimental results, the computed electronic excited-state structure, and the molecular equilibrium structure in

the first excited 1 $^1B_2$ ($\pi\pi^*$) state of PFPy in comparison to PFB, the physical mechanisms at the origin of the observed oscillations in the PFPy molecule are assumed to be analogous to those in PFB. As we already noted above, PFPy exhibits an out-of-plane distorted molecular structure in the relaxed first excited state. The distortion corresponds to displacements along normal modes of b_1 symmetry. The respective displacement vectors are visualized in Figures 3.32(c)–(g). Therefore, the adiabatic PECs of PFPy along at least some of the b_1 normal mode coordinates should exhibit similar symmetric double-well shapes induced by 1 $^1B_2$ ($\pi\pi^*$) to 1 $^1A_2$ ($\pi\sigma^*$) vibronic coupling as found in PFB. Notable effects caused by coupling of the 1 $^1B_2$ ($\pi\pi^*$) to the 2 $^1A_2$ ($n\pi^*$) state, which does not exist in PFB, are assumed to be small due to the large energetic distance of more than 2 eV. Furthermore, we do not expect $n\pi^*$ excitation to cause a drastic out-of-plane deformation as calculated for the $\pi\pi^*$ state because the involved MOs are located on the aromatic ring, in contrast to the σ^* MO that is located on the C–F bond.

The calculated harmonic frequencies for the b_1 vibrational modes of PFPy in the ground state and in the first excited state at the CC2 level of theory are compiled in Table 3.14. As can be seen, the frequencies for the ground state are in excellent agreement with experimental values. The frequencies in the first excited state are substantially lower, especially considering the three lowest-frequency modes $\nu_{18} - \nu_{16}$. These frequencies were calculated as finite differences of the first derivatives of the electronic potential energy in the harmonic approximation (cf. Section 2.2). In a highly anharmonic potential, as is the case for the double-well adiabatic PECs, knowledge of the exact curvatures of the potential combined with numerical diagonalization of the corresponding Hamiltonian would be required to gain the physically correct vibrational frequencies. Nonetheless, the low frequency values are fully compatible with the assumed strong vibronic coupling with the 1 $^1A_2$ ($\pi\sigma^*$) excited state.

The FT analysis of the oscillating experimental ion yield signal gave three distinct frequency components of 72 cm^{-1} (I), 251 cm^{-1} (III), and 281 cm^{-1} (IV). Thus, based on the present computational results and the parallels to the results for PFB, we tentatively assign our experimentally observed modulation frequencies to wavepacket motion along the Q_{18}, Q_{17}, and Q_{16} coordinates of PFPy in the first excited state. The 144 cm^{-1} frequency component (II) appears to us to correspond to the second harmonic of frequency I. We note that an appearance of the second harmonic frequency is not unexpected at all, as the

Table 3.14. Calculated harmonic vibrational frequencies of the b_1 normal modes (numbered according to the Mulliken notation) in cm^{-1} in the electronic ground state and the first excited $1\ ^1B_2$ ($\pi\pi^*$) state at the RI-SCS-CC2 level of theory.

No.	$1\ ^1A_1$ (gs) expt.[a]	$1\ ^1A_1$ (gs) calc.[b]	$1\ ^1B_2$ ($\pi\pi^*$) calc.[b]
14	736	746	677
15	620	635	537
16	353	357	264
17	224	219	158
18	174	160	78

[a] Experimental values for the ground state taken from Ref. [63].
[b] This work.

solution of the equation of motion for a vibrational wavepacket in an anharmonic double-well potential is well known to lead to additional oscillatory terms with higher multiples of the fundamental frequency.[61,62] We emphasize, however, that we cannot rule out the alternative of a possible correspondence of the 144 cm^{-1} frequency component to ν_{17}. Clearly, the calculated harmonic vibrational frequencies can only be taken as a zero-order guide for a comparison, so we cannot expect quantitative agreement. Evidently, however, the pump pulse excites a vibrational wavepacket that periodically oscillates in the anharmonic PECs of the b_1 modes. When the wavepacket executes its out-of-plane distortion by moving from the FC region to the outer turning points of the double-well potential curves of the $1\ ^1B_2$ adiabatic state, the electronic wavefunction acquires a pronounced $\pi\sigma^*$ character. The $\pi\pi^*$ character is recovered when the wavepacket returns to the FC structure. This motion is periodically repeated until dephasing of the various components of the wavepacket occurs. The mixing of the $\pi\pi^*$ and $\pi\sigma^*$ characters affects the electronic transition moment for photoionization, as the ionization occurs preferably from the $\pi\pi^*$ electronic configuration. Therefore, the observed experimentally long-lived ion yield oscillations provide a direct mapping of the wavepacket motion in the first excited adiabatic state and of the associated strongly coupled electron-nuclear dynamics.

The appearance of the second harmonic of the 72 cm^{-1} frequency indicates that, similar to PFB, wavepacket motion along the lowest-frequency mode ν_{18} has the largest contribution to the observed behavior. This is also reflected by its amplitude in the Fourier-transformed transient ion yield signal. On the other hand, the simultaneous presence of the higher oscillation frequencies III and IV indicates that, contrary to our results on PFB, regular oscillatory motion takes

place involving higher vibrational modes as well. Moreover, the employed laser pulse parameters are expected to have a pronounced effect on the observable experimental signal. The photon energy and spectral bandwidth of the pump pulses determine the composition of the excited wavepacket from vibrational eigenstates, and the temporal duration of the probe pulses determines whether the induced dynamics can actually be experimentally resolved at all. For a systematic study on the influence of these parameters, improvements of our laser-optical setup are required. Also, detailed calculations of the diabatic and adiabatic PECs along the b_1 coupling modes of PFPy and the frequencies in the double-well PECs are currently underway in our group, and subsequent quantum dynamics simulations to this end are in preparation. However, the complexity of the calculations is raised substantially compared to PFB due to the presence of the energetically close 2 $^1A_2$ ($n\pi^*$) state.

3.6 Pentafluorotoluene

3.6.1 Molecular and Electronic Structure

The gas-phase UV absorption spectrum of PFT is shown in Figure 3.39. In contrast to the UV spectra of 1,2,3-TriFB and the three TFB isomers, two fully resolved structureless bands are observed. The first, less intense peaks at 258 nm (4.80 eV), and the second band peaks at 221 nm (5.61 eV). A third band arises at wavelengths <210 nm (>5.90 eV).

To assign the bands, the VEEs to the first eight neutral excited states were calculated at RI-SCS-CC2 level of theory. The results are listed in Table 3.15. A VEE of 5.08 eV (244 nm) was calculated to the first excited state S_1 ($\pi\pi^*$, 2 ^{1}A′). Two $\pi\sigma^*$ states, S_2 (1 ^{1}A″) and S_3 (2 ^{1}A″), are located at 5.86 eV (212 nm) and 6.03 eV (206 nm), respectively. The fourth excited state S_4 ($\pi\pi^*$, 3 ^{1}A′) has a predicted VEE of 6.45 eV (192 eV). All states beyond the S_4 state exhibit calculated VEEs of >7 eV.

Analogous to the absorption spectra of 1,2,3-TriFB and the three TFB isomers, the first band peaking at 258 nm (4.80 eV) can be assigned to the S_1 state. Assignment of the second band at 258 nm (4.80 eV), however, is not as straightforward. It is tempting to attribute the additional absorption band to the second $\pi\pi^*$ state (S_4). Yet, the calculated VEE of 6.45 eV (192 eV) deviates by ≈0.8 eV from the absorption maxima of the second absorption band, thus fits arguably much better to the absorption bands rising in at wavelengths <210 nm (>5.90 eV). As will be shown in the next Sections, PFT, PFPh, ClPFB, and BrPFB exhibit very similar absorption band patterns. Following the assignment proposed in the literature for PFPh and BrPFB,[66–68] the band peaking at 221 nm (5.61 eV) is attributable to a $\pi\sigma^*$ transition, hence originates either from the transition to the S_2 (212 nm, 5.86 eV) or to the S_3 state (206 nm, 6.03 eV). In contrast to the well-fitting calculated VEEs of both states, the corresponding oscillator strengths provide compelling arguments against a $\pi\sigma^*$ transition. While the $S_3 \leftarrow S_0$ transition supposedly is three times less intense than the one to the S_1 state, the excitation of the S_2 state is even symmetry forbidden. Nevertheless, comparable deviations between prediction and experiments for PFPh were rationalized by pronounced intensity borrowing of the $\pi\sigma^*$ states from the lower-lying $\pi\pi^*$ state.[14,68] The same presumably also applies to the $\pi\sigma^*$ states of PFT and thus the band is indeed assigned to a $\pi\sigma^*$ transition. Since both $\pi\sigma^*$

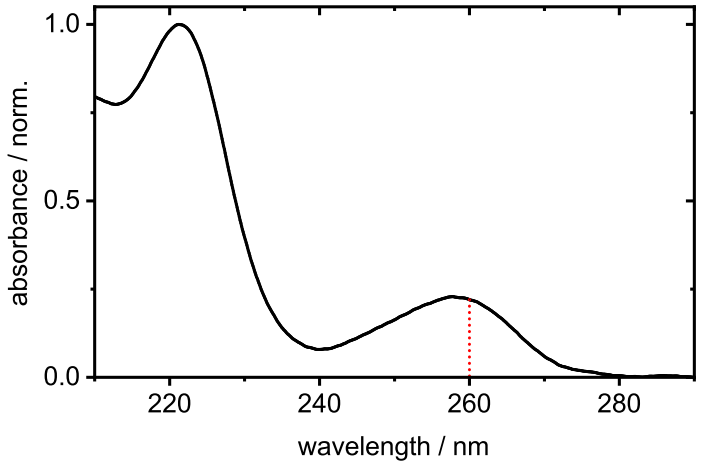

Figure 3.39. Normalized gas-phase UV absorption spectrum of PFT. The dotted red line indicates the chosen excitation wavelength of $\lambda_{\text{pump}} = 260$ nm to excite the S_1 state ($\pi\pi^*$).

Table 3.15. Vertical excitation energies (VEE) and oscillator strengths f (in parentheses) of the first eight neutral electronically excited states, the ionic ground state and the first two ionic electronically excited states for PFT, calculated at RI-SCS-CC2 level of theory. Where available, the respective adiabatic energy (AEE) is listed. Experimental energies are given if possible.

	symm.	calc. VEE eV	calc. AEE eV	exp. VEE eV	exp. AEE eV
S_1 ($\pi\pi^*$)	$2\,^1A'$	5.08 (0.0037)	4.56	4.80[†]	
S_2 ($\pi\sigma^*$)	$1\,^1A''$	5.86 (0.0000)		5.61[†]	
S_3 ($\pi\sigma^*$)	$2\,^1A''$	6.03 (0.0013)			
S_4 ($\pi\pi^*$)	$3\,^1A'$	6.45 (0.0100)			
S_5 ($\pi\pi^*$)	$4\,^1A'$	7.34 (0.6089)		7.2[†]	
S_6 ($\pi\pi^*$)	$5\,^1A'$	7.36 (0.8597)			
S_7 ($\pi\sigma^*$)	$3\,^1A''$	7.50 (0.0107)			
S_8 ($\pi\sigma^*$)	$4\,^1A''$	7.61 (0.0000)			
D_0 (π^{-1})	$1\,^2A''$		9.38	9.63[a–c]	9.4[b,‡]
D_1 (π^{-1})	$2\,^2A''$			9.85[b]	
D_2 (π^{-1})	$3\,^2A''$			12.44[a]	

[a] Ref. [64] [b] Ref. [65] [c] Ref. [39] [†] this work [‡] based on a band onset in the PE spectrum

states are in close vicinity to each other, a clear assignment of the band to either state is prohibited.

Optimization of the molecular structure in the neutral ground state reveals a planar structure for PFT. Excitation to the S_1 state results in a highly out-of-plane deformed structure, as depicted in Figure 3.40. The calculations suggests four carbon atoms are spanning a plane in the S_1 state, namely 2, 3, 5 and 6, though C-1/4 are also nearly in-plane (2°/3°). The methyl group is bent out of the plane by 7°, F-8/12 and F-9/11 by −7° and −9°, respectively. Hence, of the substituents only F-10 (32°) is bent out-of-plane to the same direction as the methyl group. Moreover, the methyl group is rotated by 30° in the excited state. Although PFT belongs to the C_s point group (in the planar ground state), the deformed molecular structure essentially transforms according to the b_1 irreducible representation of the C_{2v} point group. Calculation of the S_1 AEE yields 4.56 eV (272 nm), which fits well to the absorption band onset at ≈280 nm (≈4.43 eV). However, since CC2 tends to overestimate the transition energies,[9,10] the actual AEE might be lower. In addition, the displacement vectors of the out-of-plane modes and their respective calculated frequencies in the S_1 state are illustrated in Figure 3.40, too. A comprehensive list of all modes is given in Table B.6 in the appendix.

In contrast to the VEEs to the neutral states, calculation of the VIEs was unsuccessful. Experimentally determined transition energies show that the D_0 ionic ground state ($1\ ^2A''$) exhibits a VIE of 9.63 eV.[39,64,65] The D_1 state ($2\ ^2A''$) is located at 9.85 eV.[65] Well separated from the two lower-lying ionic states is the D_2 state ($3\ ^2A''$) at 12.44 eV.[64] All states show π^{-1} character. Optimization of the planar molecular structure in the D_0 state ($1\ ^2A''$) converged, yielding an AIE to the D_0 state of 9.38 eV, in near perfect agreement with the reported AIE of 9.4 eV.[65] Unfortunately, the experimental AIE is solely based on an indistinct onset of the PE band of the D_0 state.[65] High-resolution studies are needed to clearly resolve the AIE.

3.6.2 Time-Resolved Time-of-Flight Mass Spectra

The S_1 state was excited at $\lambda_{pump} = 260$ nm and ionized at either $\lambda_{probe} = 400$ nm or 800 nm. The transient parent ion yields of PFT are virtually identical for both probe wavelengths, as shown in Figure 3.41. Intense oscillations with frequencies of $\nu_{osc}^{PFT} = 73\ cm^{-1}$ (cf. results of the Fourier transform in the inset) dominate

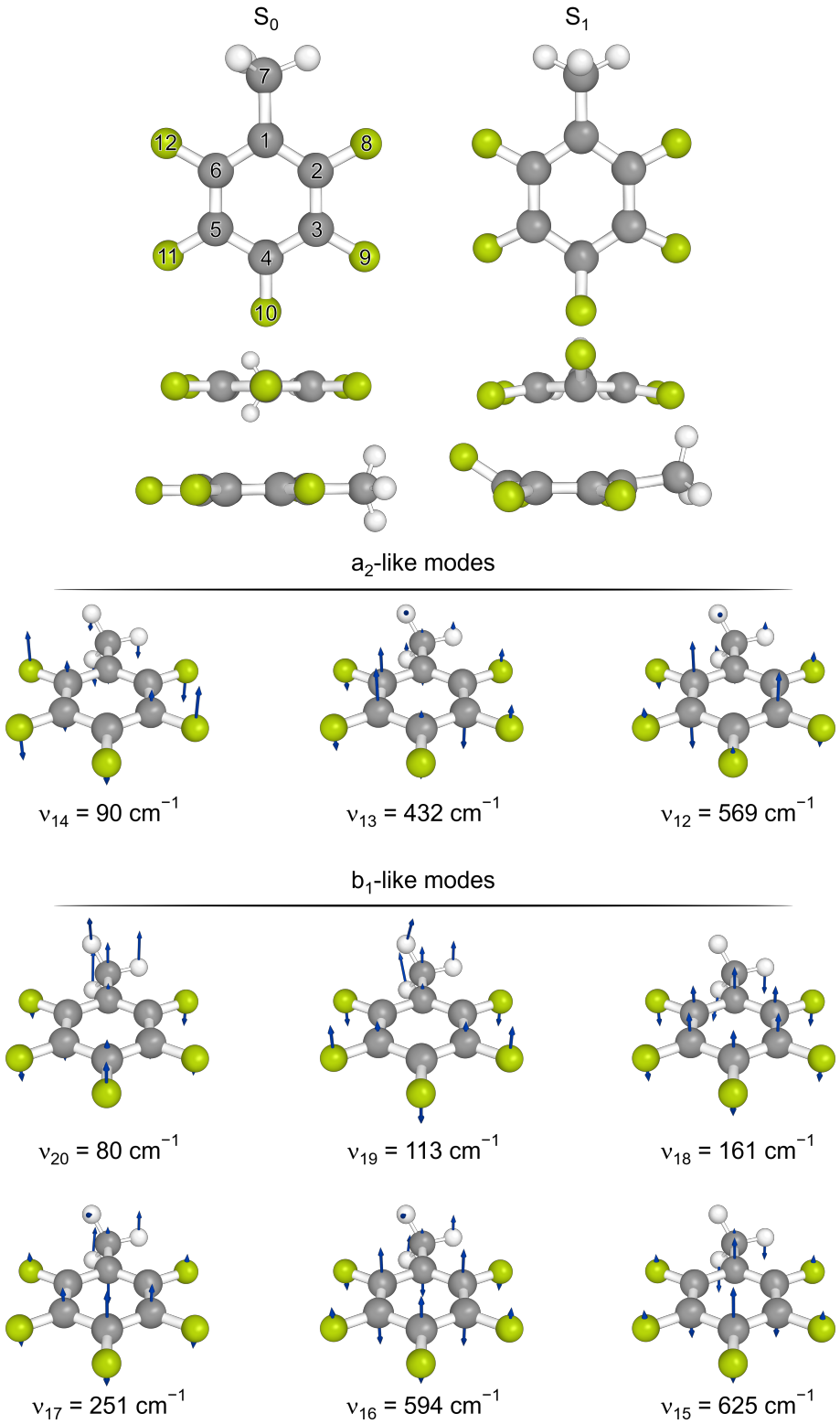

Figure 3.40. Calculated molecular structures of PFT in the S_0 and the S_1 state ($\pi\pi^*$), optimized at the RI-SCS-MP2 and RI-SCS-CC2 levels of theory, respectively. The calculated displacement vectors of the out-of-plane modes are illustrated by blue arrows. Their respective frequencies in the S_1 state are listed.

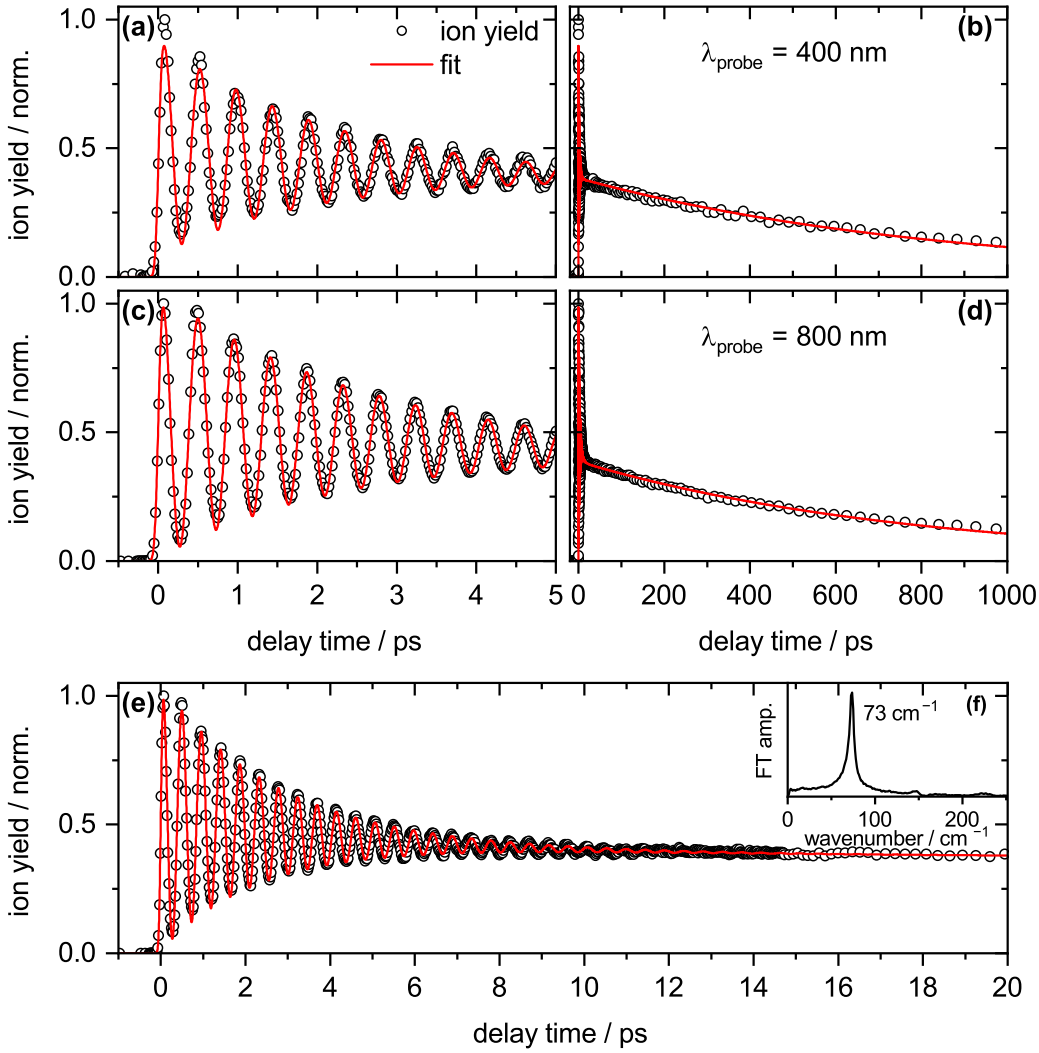

Figure 3.41. Measured transient parent ion yield signals (black circles) and applied fit model functions (red lines) for PFT after excitation at $\lambda_{pump} = 260$ nm and ionization at $\lambda_{probe} = 400$ nm **(a–b)** resp. $\lambda_{probe} = 800$ nm **(c–e)**. The left-hand column shows the data in the first five picoseconds, the right-hand column in the first nanosecond after excitation. The fit parameters are listed in Table 3.16. **(e)** Complete decay of the oscillation truncated in **(c)**. **(f)** Fourier transform of the oscillatory signal component after subtraction of the exponential decay functions.

Table 3.16. Parameters for the fits of the transient parent ion yields of PFT after excitation at $\lambda_{pump} = 260$ nm and ionization at either $\lambda_{probe} = 400$ nm or 800 nm. 2σ fit errors are given in parentheses. If no error is given the value was set fixed.

λ_{probe} nm	σ_{IRF} fs	A_2 %	τ_2 ps	A_4 %	τ_4 ps	A_{osc} %	τ_{osc} ps	ν_{osc} cm^{-1}	ϕ_{osc} π
400	32(3)	12(1)	2.68(22)	40(1)	838(34)	48(1)	2.06(6)	73	−0.31
800	35(2)	13(1)	5.19(34)	35(1)	775(30)	53(1)	2.53(5)	73	−0.20

the signals within the first picoseconds after excitation. As for 1,2,3,4-TFB, the modulation depth is greater at 800 nm. The oscillations decay with

$$\tau_{osc}^{PFT} = 2.1\text{–}2.5 \text{ ps}.$$

The underlying exponential decays are well described by

$$\tau_2^{PFT} = 2.7\text{–}5.2 \text{ ps}$$

and

$$\tau_4^{PFT} = 800 \text{ ps}.$$

The fit parameters are listed in Table 3.16.

Origin of the Oscillation

The PE results (*vide infra*) show that the deactivation of the excited molecules does not involve conversions to different excited states. Thus, modulation of the S_1 potential energy hypersurface has to be the origin for the signal oscillations. As extensively discussed in Chapter 1 and in the literature,[9,10] vibronic coupling between the initially excited S_1 ($\pi\pi^*$) and the higher-lying $\pi\sigma^*$ states, mediated by a wavepacket of out-of-plane modes, induces the pronounced signal oscillations. Since the two lowest-lying $\pi\sigma^*$ states are in close energetic vicinity, it may be possible that the observed oscillation does not originate from the coupling of the S_1 to the S_2 state, but to the S_3 state. Analogous behavior determines the dynamics of 1,2,3-TriFB (cf. Section 3.1), for which comparison of the molecular symmetry in the S_1 state (b_1) with the symmetries of the potential coupling modes hints towards coupling between the S_1 ($^1B_2$) and the S_4 state ($^1A_2$). Although PFT belongs to the C_s point group, the vibrational modes essentially transform according to the irreducible representations of the C_{2v} point group,

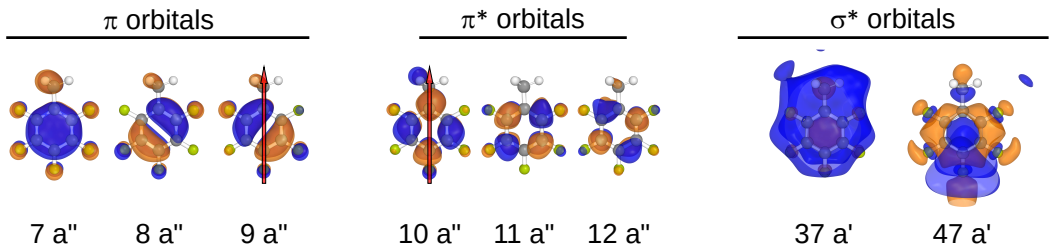

Figure 3.42. Calculated molecular orbitals of the ground state structures for PFT with significant contributions to the electronic configurations of the neutral excited states S_1 ($\pi\pi^*$) and S_2 ($\pi\sigma^*$, cf. Table 3.17). The red arrows indicate a hypothetical axis of symmetry.

if the methyl group is temporarily neglected (cf. Figure 3.40). Therefore, they can be categorized as a_2- and b_1-like modes and their lowest-frequency modes are $\nu_{14}^{\mathrm{PFT}} = 90\ \mathrm{cm}^{-1}$ and $\nu_{20}^{\mathrm{PFT}} = 80\ \mathrm{cm}^{-1}$, respectively. The deformed molecular structure in the S_1 state basically also transforms according to the b_1 irreducible representation. Hence, the coupling mode $\nu_{20}^{\mathrm{PFT}} = 80\ \mathrm{cm}^{-1}$ is assigned to dominate the observed oscillation. The vibrational modes and the molecular structure may lead to the false conclusion that all properties of PFT may be explained by just neglecting the methyl group and assuming PFT to belong to the C_{2v} point group. However, the molecular orbitals do not consistently transform accordingly. As shown in Figure 3.42, depicting the three occupied molecular π orbitals and the unoccupied π^* and σ^* orbitals involved in the transitions leading to the states S_1–S_3 (cf. Table 3.17), some, but not all orbitals are rotated with respect to a hypothetical C_2 symmetry axis, e.g., the π orbital 9 a$''$ and the π^* orbital 10 a$''$. Owing to this inconsistent rotation, the electronic states of PFT cannot be described in terms of irreducible representations of the C_{2v} point group. As a consequence, comparison of the optimized molecular structure with the displacement vectors of the vibrational modes indicates that the b_1-like modes dominate the coupling dynamics but does not enable differentiation between S_1/S_2 and S_1/S_3 coupling. It should be noted that the differentiation between the two possibilities not necessarily holds true or is meaningful, because symmetry-wise the out-of-plane modes may mediate coupling to both states. Such a multi-state coupling is further discussed in Section 3.10.

3.6.3 Time-Resolved Photoelectron Images

The PEI and their corresponding meridional slices of PFT at $\Delta t = 0.03$ ps after excitation at $\lambda_{\mathrm{pump}} = 260$ nm and ionization at $\lambda_{\mathrm{probe}} = 400$ nm (a), in the first

Table 3.17. Molecular orbital configuration and their weighted contributions to the S_1, S_2, S_5, and S_6 states and the first three ionic states of PFT. Correlations between the neutral and the ionic states according to Koopmans's theorem are given.

neutral state	7 a″ (π)	8 a″ (π)	9 a″ (π)	10 a″ (π^*)	11 a″ (π^*)	12 a″ (π^*)	37 a′ (σ^*)	47 a′ (σ^*)	weight (%)	corr. ion. state
S_0 (^{1}A′)	2	2	2							
S_1 (^{1}A′, $\pi\pi^*$)	2	1	2	1					30	D_1
	2	2	1	1					23	D_0
	2	2	1			1			16	
	2	1	2		1				15	D_1
S_2 (^{1}A″, $\pi\sigma^*$)	2	2	1				1		39	D_0
	2	1	2				1		20	D_1
	2	2	1					1	16	D_0
S_5 (^{1}A′, $\pi\pi^*$)	2	1	2		1				31	D_1
	2	2	1	1					30	D_0
	2	1	2			1			18	D_1
S_6 (^{1}A′, $\pi\pi^*$)	2	1	2	1					33	D_1
	2	2	1			1			24	D_0
	2	2	1		1				21	
ionic state										
D_0 (^{2}A″, π^{-1})	2	2	1							
D_1 (^{2}A″, π^{-1})	2	1	2						96	
D_2 (^{2}A″, π^{-1})	1	2	2						79	

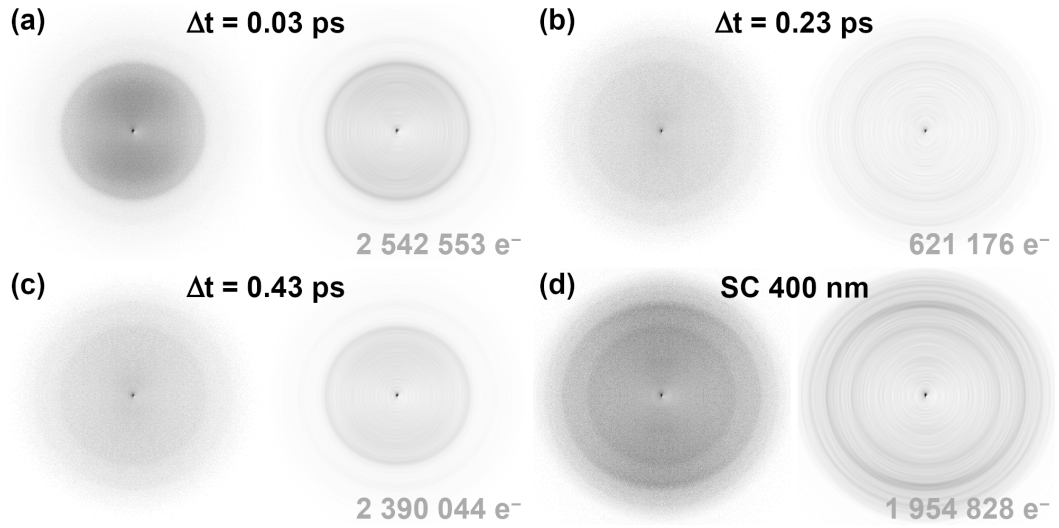

Figure 3.43. Photoelectron images (left) and their corresponding meridional slices through the recovered three-dimensional photoelectron distributions (right) of PFT. **(a)** At $\Delta t = 0.03$ ps after excitation at $\lambda_{\text{pump}} = 260$ nm and ionization at $\lambda_{\text{probe}} = 400$ nm, **(b)** at $\Delta t = 0.23$ ps (first minimum), and **(c)** at $\Delta t = 0.43$ ps (first maximum). **(d)** High-intensity single-color photoelectron images obtained at 400 nm.

minimum of the parent ion yield at $\Delta t = 0.23$ ps (b), and in the first maximum at $\Delta t = 0.43$ ps (c) are shown in Figure 3.43. A broad (α) and a narrow signal (β) are observed, peaking at $E_\alpha = 0.4$ eV and $E_\beta = 0.88$ eV, respectively, as display in the PES Figure 3.44 (a). Both α and β oscillate in intensity likewise to the transient parent ion yield.

The PEI after high-intensity single-color ionization at $\lambda_{\text{probe}} = 400$ nm are depicted in Figure 3.43 (d). Like in the two-color signal, the SC ionization yields β and an additional signal γ peaking at $E_\gamma = 1.7$ eV, as shown in the PES in Figure 3.44 (c).

Ionization Pathways

As discussed in the previous Sections and in the literature,[9] the two signals α and β are the result of the transitions to two ionic states, the D_1 and the D_0 state, respectively. The energy difference of ≈0.5 eV between the band peaks fits reasonably well to the reported vertical ionization energy gap of ≈0.2 eV, especially considering the broad nature of α. Moreover, the significantly different band shapes of α and β indicate the former is a result of a vertical transition, while the latter originates from an adiabatic transition. The absence of additionally emerging bands at any delay time between the pump and the probe pulse

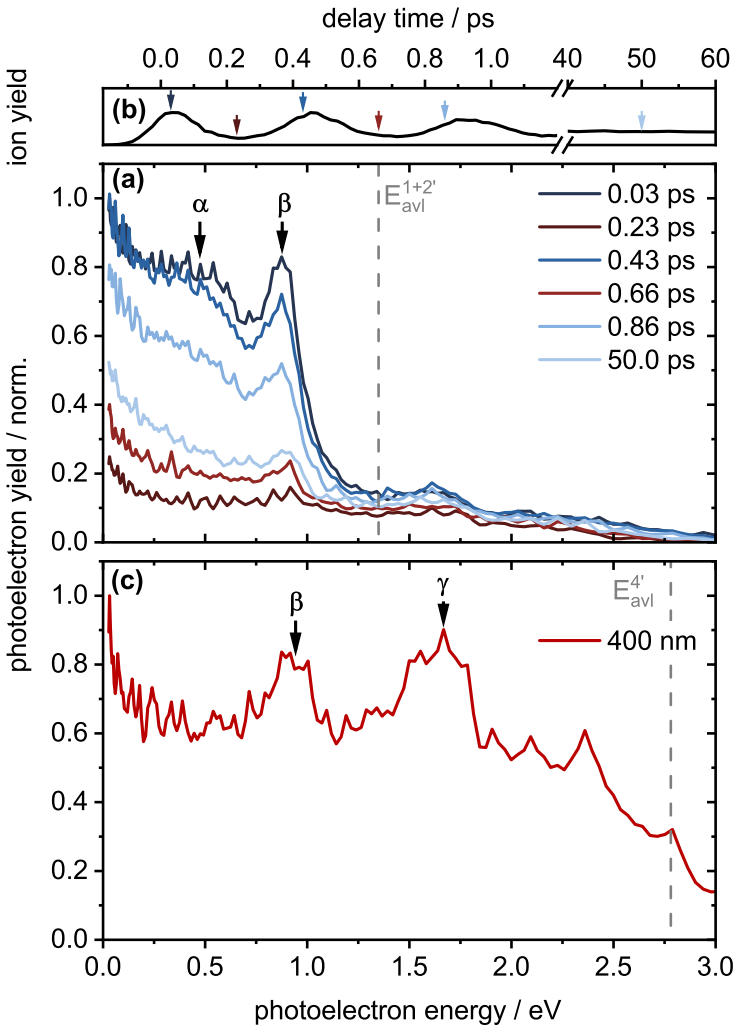

Figure 3.44. **(a)** Transient PE spectra of PFT after excitation at $\lambda_{pump} = 260$ nm and ionization at $\lambda_{probe} = 400$ nm. The two main photoelectron signals labeled α and β are observed at $E_\alpha = 0.4$ eV and $E_\beta = 0.88$ eV. The grey dotted line indicates the maximum available photoelectron energy $E_{avl}^{1+2'}$ associated with the $D_0 \leftarrow S_0$ transition by $1 + 2'$ ionization. **(b)** Corresponding transient parent ion yields adapted from Figure 3.41 (a). Arrows mark the delay time $\Delta t = 0$–50 ps at which the PES were obtained (red at ion yield minima). **(c)** Single-color PE spectrum taken at higher 400 nm probe intensities. The additional signal γ is located at $E_\gamma = 1.7$ eV. The grey dotted line indicates the maximum available photoelectron energies $E_{avl}^{4'}$ generated by four 400 nm photons.

highlights that the mapped dynamics solely happen on the potential energy hypersurface of the initially excited S_1 state.

For PFT, neither vertical nor adiabatic S_1 excitation energies have been reported before. The structureless UV absorption peaks at 4.79 eV (259 nm) provides the VEE, and no absorption is observed below 4.43 eV (280 nm), a first guess on the AEE. In theory, the PES should enable determination of a more precise S_1 AEE, since the narrow peak shape of β indicates an adiabatic $D_0 \leftarrow S_1$ transition. However, calculating the S_1 AEE requires a reliable AIE to the D_0 state, not given for PFT, since the reported D_0 AIE is only based on a rather diffuse photoelectron band onset at 9.4 eV.[65] Calculating the S_1 AEE with $E_\beta = 0.88$ eV and the D_0 AIE of 9.4 eV via Equation 3.2 in Section 3.1 yields 4.1 eV (≈302 nm), which is ≈0.3 eV less than UV absorption band onset in Figure 3.39. The deviation may simply originate from the uncertainties regarding the D_0 AIE. Alternatively, population of an intermediate state by absorption of a single probe photon within the duration of the probe pulse might alter the PE distribution. Such an intermediate state would exhibit a transition energy of 7.2 eV. The calculated VEEs suggest either the S_5 or the S_6 state, located at 7.34 eV and 7.36 eV, respectively, as intermediate state candidates. As the electronic configuration of both $\pi\pi^*$ states corresponds to the D_0 state (cf. Table 3.17), and no experimental studies on the highly excited neutral states were conducted yet, further differentiation is impossible. Considering the ambiguities regarding the AIE of the D_0 state, both the direct $D_0 \leftarrow S_1$ and the excitation of intermediate state(s) present viable ionization pathways. Nevertheless, the PE pattern of PFT is very similar to the one of 1,2,3-TriFB and 1,2,4,5-TFB for which excitation of intermediate states is very likely. Therefore, it is cautiously presumed that indeed either the S_5 or the S_6 state are excited.

The vertical character of the ionization leading to α may originate from differences in the molecular and vibrational structure of the D_1 and the D_0 state, or ionization follows another pathway than towards β. Since essentially all that is known about the D_1 state is the VIE and the electronic configurations of the proposed intermediate states correspond to the D_1 state too, it is for now assumed that excitation of intermediate states plays a major role in the ionization transition to both PE signals, i.e., the ionic states differ in terms of molecular and vibrational structure. The suggested mechanisms resulting in signals α and β are illustrated in Figure 3.45. Notwithstanding of the exact pathway, the excitation of intermediate states only alters the position and shape of the PE bands. The

oscillatory behavior depends on the delay time between the pump and the probe pulse, and thus maps the dynamics of the S_1 state.

The high-intensity SC PES at $\lambda_{\text{probe}} = 400$ nm feature signal β and one distinct band γ at $E_\gamma = 1.7$ eV on top of a broad background. The former probably is the result of the two-photon excitation of the S_1 state, followed by first the one-photon excitation of an intermediate state and subsequently one-photon ionization to the D_0 ground state. The second band γ likely originates from the three-photon transition to an intermediate state at ≈8 eV. As a consequence of the myriad of possible electronic states, no assignment to a specific state is made. Both pathways are depicted in Figure 3.45 (b).

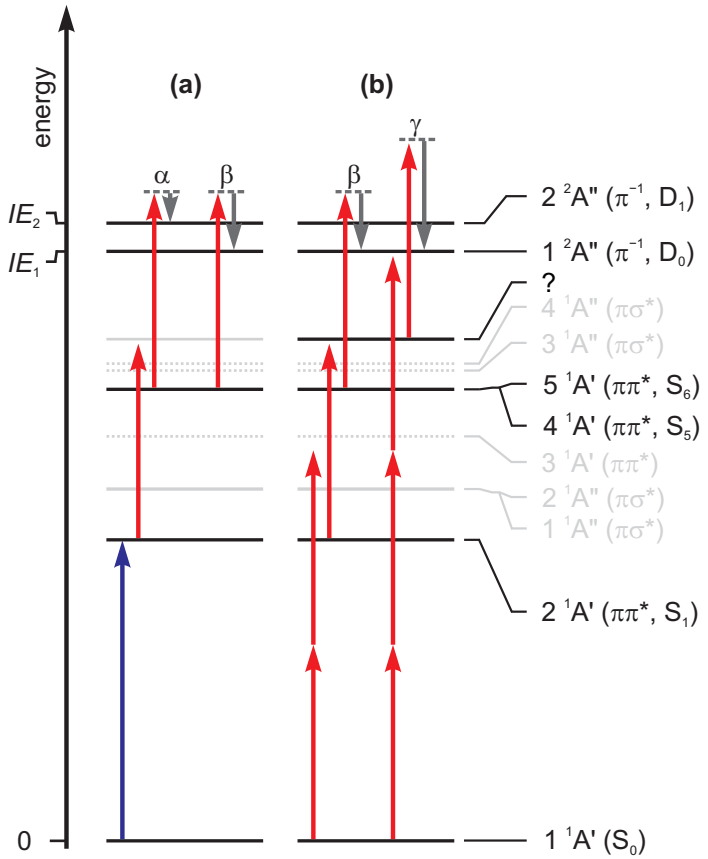

Figure 3.45. Proposed multi-color and single-color ionization schemes for PFT. The energies of the photons at $\lambda_{pump} = 260$ nm (blue) and $\lambda_{probe} = 400$ nm (red) and of the photoelectrons (grey) are depicted as vertical arrows. Solid black horizontal lines: experimentally intermediate and final states, solid and dotted (calculated values) grey horizontal lines: non-participating other intermediate states. **(a)** Transient ionization pathways by one-photon absorption to the S_1 state ($2\ ^1A'$) and subsequent two-photon ionization to the D_0 ($1\ ^2A''$) and the D_1 ($2\ ^2A''$) states showing the origin of PE peaks α and β. **(b)** Single-color ionization pathways at $\lambda_{probe} = 400$ nm to the D_0 state showing the origin of PE peaks β and γ.

3.7 Pentafluorophenol

3.7.1 Molecular and Electronic Structure

The UV absorption spectrum of PFPh is shown in Figure 3.46. Starting at ≈290 nm (≈4.28 eV), three consecutive, structureless absorption bands are observed. The first band peaks at 262 nm (4.73 eV), the second at 232 nm (5.34 eV), and the third at 223 nm (5.56 eV). A fourth band arises at wavelengths <215 nm (>5.77 eV). The intensity of the bands increases with increasing transition energy.

Neutral States

To assign the bands, the first eight excited electronic states were calculated at RI-SCS-CC2 level of theory. The results are listed in Table 3.18. The first excited state S_1 ($\pi\pi^*$) exhibits a VEE of 5.05 eV. The state shows 2 $^1A'$ symmetry, since PFPh belongs to the C_s point group, and is formed by the transition of electrons from occupied π orbitals to unoccupied π^* orbitals, as listed in Table 3.19. These orbitals all show a$''$ symmetry. However, assuming a hypothetical C_2 rotational axis by neglecting the hydroxy group, the molecular orbitals also transform according to the irreducible representations of the C_{2v} point group, as illustrated in Figure 3.47. Two of the three occupied π orbitals exhibit b_1 symmetry, one a_2 symmetry. Of the final π^* orbitals one shows a_2 symmetry and one b_1 symmetry. Thus, the symmetry of the S_1 state corresponds to 1 $^1B_2$ symmetry. The second molecule in this Thesis which belongs to the C_s point group (cf. Section 3.6) is PFT. Albeit the shape of the orbitals are seemingly rather similar to the ones of PFPh, they are inconsistently rotated with respect to an imaginary axis of symmetry, as depicted in Figure 3.47. Thereby, the classification in terms of irreducible representations of the C_{2v} point group is prohibited for PFT.

Following the S_1 state, two $\pi\sigma^*$ states S_2 (1 $^1A''$) and S_3 (2 $^1A''$) are located at 5.32 eV (233 nm) and 5.71 eV (217 nm), respectively. Employing TDDFT calculations a different ordering was proposed earlier, placing the first $\pi\sigma^*$ state below the $\pi\pi^*$ state.[67] Yet, TDDFT also gave the wrong ordering for PFB,[9] and EOM-CCSD calculations of Rajak et al. confirm the electronic structure proposed herein.[68] The $\pi\sigma^*$ states are formed by transitions of electrons from the occupied π orbitals to unoccupied σ^* orbitals. One of the two σ^* orbitals shows pronounced electron density on the fluorine atoms and a node between

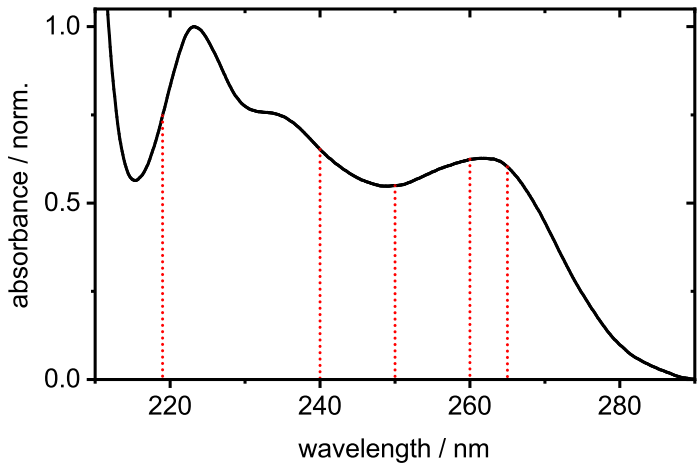

Figure 3.46. Normalized gas-phase UV absorption spectrum of PFPh. The dotted red lines indicate the chosen excitation wavelength of $\lambda_{\text{pump}} = 265$–$219$ nm.

Table 3.18. Vertical excitation energies (VEE) and oscillator strengths f (in parentheses) of the first eight neutral electronically excited states, the ionic ground state and the first two ionic electronically excited states for PFPh, calculated at RI-SCS-CC2 level of theory. Where available, the respective adiabatic energy (AEE) is listed. Experimental energies are given if possible.

	symm.	calc. VEE eV	calc. AEE eV	exp. VEE eV	exp. AEE eV
S_1 ($\pi\pi^*$)	$2\,^1A'$ ($1\,^1B_2$)	5.05 (0.0045)	4.37	4.73[†]	
S_2 ($\pi\sigma^*$)	$1\,^1A''$ ($1\,^1B_1$)	5.32 (0.0003)		5.34[a,†]	
S_3 ($\pi\sigma^*$)	$2\,^1A''$ ($1\,^1A_2$)	5.71 (0.0000)		5.56[a,†]	
S_4 ($\pi\pi^*$)	$3\,^1A'$ ($2\,^1A_1$)	6.35 (0.0388)			
S_5 ($\pi\sigma^*$)	$3\,^1A''$ ($2\,^1B_1$)	6.86 (0.0003)			
S_6 ($\pi\pi^*$)	$4\,^1A'$ ($2\,^1B_2$)	7.27 (0.6134)		7.1[†]	
S_7 ($\pi\pi^*$)	$5\,^1A'$ ($3\,^1A_1$)	7.30 (0.7705)			
S_8 ($\pi\sigma^*$)	$4\,^1A''$ ($2\,^1A_2$)	7.46 (0.0012)			
D_0 (π^{-1})	$1\,^2A''$ ($1\,^2B_1$)	9.55	9.24	9.73[b]	9.3[‡]
D_1 (π^{-1})	$2\,^2A''$ ($1\,^2A_2$)	10.15		9.90[b]	
D_2 (π^{-1})	$3\,^2A''$ ($2\,^2B_1$)	12.46		12.23[b,c]	

[a] Ref. [67] [b] Ref. [69] [c] Ref. [70] [†] this work [‡] re-evaluated in this work, based on Ref. [69]

Table 3.19. Molecular orbital configuration and their weighted contributions to the S_1–S_3, S_6, and S_7 states and the first three ionic states of PFPh. The characters of the orbitals are given with respect to the actual point group C_s and to C_{2v}, valid when neglecting the hydroxy group. Correlations between the neutral and the ionic states according to Koopmans' theorem are given.

neutral state	7 a″ (b_1, π)	8 a″ (a_2, π)	9 a″ (b_1, π)	11 a″ (a_2, π^*)	12 a″ (b_1, π^*)	37 a′† (σ^*)	47 a′ (a_1, σ^*)	wgt. (%)	corr. ion. state
S_0 ($^1A'/^1A_1$)	2	2	2						
S_1	2	2	1	1				47	D_0
($^1A'/^1B_2$, $\pi\pi^*$)	2	1	2		1			36	D_1
S_2	2	2	1			1		58	D_0
($^1A''/^1B_1$, $\pi\sigma^*$)	2	2	1				1	26	
S_3	2	1	2			1		53	D_1
($^1A''/^1A_2$, $\pi\sigma^*$)	2	1	2				1	27	
S_6	2	1	2		1			42	D_1
($^1A'/^1B_2$, $\pi\pi^*$)	2	2	1	1				28	D_0
S_7	2	1	2	1				43	D_1
($^1A'/^1A_1$, $\pi\pi^*$)	2	2	1		1			27	D_0
ionic state									
D_0 ($^2A''/^2B_1$, π^{-1})	2	2	1						
D_1 ($^2A''/^2A_2$, π^{-1})	2	1	2					96	
D_2 ($^2A''/^2B_1$, π^{-1})	1	2	2					79	

† electron density mainly located at the hydroxy group (Rydberg-like character)

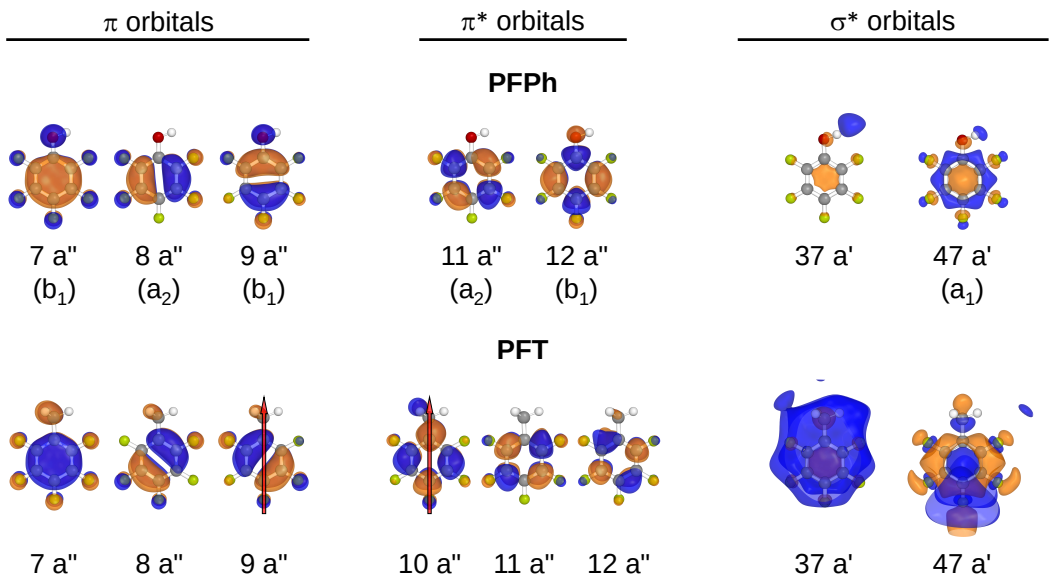

Figure 3.47. Calculated molecular orbitals of the ground state structures for PFPh and PFT with significant contributions to the electronic configurations of the respective neutral excited states S_1–S_3 (see text for details).

the fluorine atoms and the carbon atoms, in agreement with the shape of the σ^* orbitals of the other fluorobenzenes (cf. Section 3.1). However, in contrast to all other molecules herein, PFPh exhibits a hydroxy group. The second populated σ^* orbital (cf. Table 3.19) shows a Rydberg-like density distribution located at the hydrogen atom of the hydroxy group and a node between the hydrogen and the oxygen atom. The distinctly different characteristics of this orbital compared to the first σ^* orbital lowers the $\pi\sigma^*$ transition energies (cf. Section 3.10) and might also enable a dissociation process, as discussed in Subsection 3.7.4. Excluding the σ^* orbital located at the OH group, the S_2 and the S_3 state show 1 $^1B_1$ and 1 $^1A_2$ symmetry, respectively, in terms of irreducible representations of the C_{2v} point group. The VEEs to the S_4 state ($\pi\pi^*$, 3 $^1A'/2\ ^1A_1$) and the S_5 ($\pi\sigma^*$, 3 $^1A''/2\ ^1B_1$) state are calculated to be 6.35 eV (195 nm) and 6.86 eV (181 nm). Further $\pi\pi^*$ and $\pi\sigma^*$ states are located at energies >7 eV

Aided by the calculations, the first absorption band is assigned to the S_1 state. The calculated transition energies to the S_2 (233 nm/5.32 eV) and the S_3 state (217 nm/5.71 eV) fit nearly perfectly to the peak wavelengths of the second (232 nm/5.34 eV) and the third band (223 nm/5.56 eV), respectively. However, the calculated oscillator strengths significantly deviate from the observed band intensities, as the transition to the S_2 state supposedly is a order of magnitude less intense than to the S_1 state. The transition to the S_3 state should even be

optically dark. Nevertheless, high-level calculations suggest that pronounced intensity borrowing from the S_1 drastically alters the absorption strengths of the $\pi\sigma^*$ states, which the calculated oscillator strengths do not account for.[68] Therefore, the two absorption bands are assigned to the S_2 and the S_3 state, in good agreement with the assignments in the literature.[67,68] The band rising at <215 nm probably is the absorption of the S_4 state ($\pi\pi^*$).

Optimization of the molecular structure yields a planar configuration in the S_0 state. In contrast, the molecules are highly out-of-plane distorted in the S_1 state, as shown in Figure 3.48. Since the carbon ring is not just bent, but also twisted in the S_1 state, no more than three atoms span a plane, analogous to structures reported in the literature.[67,68] Although, the atoms deviate only by ±1° from the plane they spanned in the ground state, a separate plane is defined for each substituent, formed by the directly bonding and its two neighboring carbon atoms. O-7 (numbering according to Figure 3.48) is bent out-of-plane by −4° and the dihedral angle of C-2–H-13 is −3°. F-8 is bent out-of-plane by 24°, in the opposed direction compared to O-7. F-9 and F-12 are bent out-of-plane by −11° and F-11 by 18°. In contrast, F-10 is nearly in-plane (−2°). With respect to an imaginary principle axis of symmetry, the deformed molecular structure mainly shows a_2-like symmetry. Yet, the slight out-of-plane bending of O-7 and F-10 indicates the influence of b_1-like modes on the deformation. The displacement vectors of all out-of-plane vibrational modes and their respective frequencies in the S_1 state are depicted in Figure 3.48, too. A list of all vibrational frequencies in the neutral and ionic ground state and the S_1 state is given in Table B.7 in the appendix.

Calculation of the adiabatic excitation energy based on the optimized molecular structures yielded 4.37 eV (284 nm), which fits rather well to the absorption band onset at ≈290 nm (≈4.28 eV), providing an initial guess of the S_1 AEE. Since CC2 tends to overestimate the transition energies,[9,10] the true AEE may be lower.

Ionic States

In addition to the neutral states, the VIEs to the first three ionic states were calculated, all exhibiting π^{-1} character. The ionic ground state D_0 ($1\ ^2A''/1\ ^2B_1$) is placed at 9.55 eV, the first excited ionic state D_1 ($2\ ^2A''/1\ ^2A_2$) at 10.15 eV. Both states are well separated from the second excited state D_2 ($3\ ^2A''/2\ ^2B_1$) at 12.46 eV. Even though the calculated VIEs are in good agreement with the

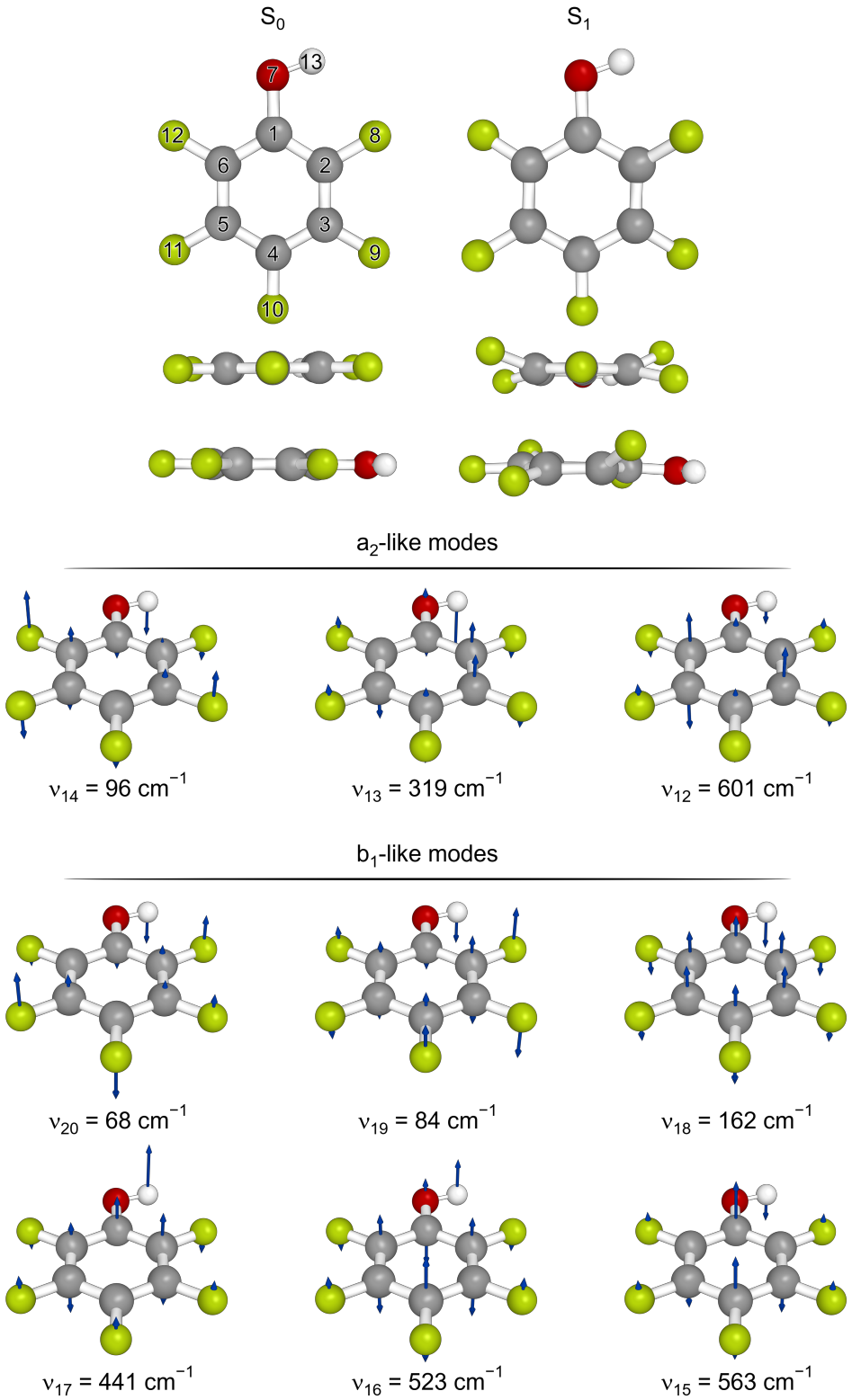

Figure 3.48. Calculated molecular structures of PFPh in the S_0 and the S_1 state ($\pi\pi^*$), optimized at the RI-SCS-MP2 and RI-SCS-CC2 levels of theory, respectively. The calculated displacement vectors of the out-of-plane modes are illustrated by blue arrows. Their respective frequencies in the S_1 state are listed.

experimentally observed ionization energies (cf. Table 3.18), the calculated energy gap between the D_0 and the D_1 state of 0.60 eV is significantly larger than the reported gap of 0.17 eV.[69] However, the individual PES bands of the ionic states that the experimental values are based on are merged. Thus, a clear segregation of the bands is challenging, explaining the deviation between calculation and experiment.

Optimization of the molecular structure reveals that the molecules are planar in the ionic ground state (not shown for the sake of brevity), likewise to the structure in the neutral ground state (cf. Figure 3.48). Calculation of the AIE based on the structures yields 9.24 eV, which is in near perfect agreement with the results of Meier and Turner.[69] In their PES, the D_0 bands starts to rise at 9.20 eV and a first distinct peak is observed at 9.3 eV. Ultimately, the band peaks at 9.90 eV, assigned to the first excited ionic state D_1. It was assumed that the band onset at 9.2 eV corresponds to the adiabatic ionization energy (AIE), instead of the first distinct band feature. Later, Maier et al.[70,71] utilized laser-induced fluorescence to determine the adiabatic energy gap between D_0 and D_2 (2.78 eV). As the energy gap of the states fits well to the energy gap between the first peak of the D_2 PES band (12.07 eV) and the first peak of the D_0 band (9.3 eV), the latter probably is the true AIE. The reassignment is supported by the SC PES at $\lambda_{\mathrm{pump}} = 260$ nm presented herein. Though the experimental AIE is slightly higher than the calculated AIE, the values are still in very good agreement.

3.7.2 Time-Resolved Time-of-Flight Mass Spectra

The transient parent ion yields of PFPh after excitation at $\lambda_{\mathrm{pump}} = 260$ nm and ionization at either $\lambda_{\mathrm{probe}} = 400$ nm or $\lambda_{\mathrm{probe}} = 800$ nm are shown in Figure 3.49. An intense oscillation defines the signal within the first picoseconds. The oscillations exhibit frequencies of $\nu_{\mathrm{osc}}^{\mathrm{PFPh}} = 92\ \mathrm{cm}^{-1}$ (cf. results of the Fourier transform in the inset) and decay with

$$\tau_{\mathrm{ocs}}^{\mathrm{PFPh}} = 1.65\ \mathrm{ps}$$

at both probe wavelengths. The modulation depth is probe-wavelength independent. Subsequently, a rather long-lived signal decay is observed. Three

Table 3.20. Parameters for the fits of the transient parent ion yields of PFPh after excitation at $\lambda_{pump} = 260$ nm and ionization at $\lambda_{probe} = 400$ nm, as well as fit parameters after excitation at $\lambda_{pump} = 265$–219 nm ionization at $\lambda_{probe} = 800$ nm. 2σ fit errors are given in parentheses. If no error is given the value was set fixed.

λ_{pump} nm	σ_{IRF} fs	A_1 %	τ_1 ps	A_3 %	τ_3 ps	A_4 %	τ_4 ps	A_{osc} %	τ_{osc} ps	ν_{osc} cm^{-1}	ϕ_{osc} π
$\lambda_{probe} = 400$ nm											
260	40(2)	22(1)	0.67(6)	33(2)	81.0(75)	10(2)	325	35(2)	1.74(8)	93	−0.09
$\lambda_{probe} = 800$ nm											
265	37(2)	32(2)	0.32(2)	25(1)	57.4(45)	4(1)	300	39(1)	1.53(5)	92	−0.18
260	36(3)	34(2)	0.35(3)	16(1)	59.3(54)	9	260	41(2)	1.59(7)	92	−0.14
250	51(3)	43(3)	0.23(2)	22	22.25(96)			35(2)	1.07(5)	91	−0.22
240	46(2)	45(2)	0.18(1)	19	9.71(35)			36(1)	0.71	92	−0.35
219	110	66(9)	$< \sigma_{IRF}$	12	4.87(12)			22(3)	0.58	93	−0.25

exponential functions are needed to fit the underlying exponential decay. The fitted decay constants were determined to be

$$\tau_1^{PFPh} = 0.35\text{–}0.67 \text{ ps},$$
$$\tau_3^{PFPh} = 60\text{–}80 \text{ ps},$$
$$\tau_4^{PFPh} = 260\text{–}325 \text{ ps}.$$

Note, τ_4^{PFPh} were set fixed. The fit constants for all wavelength combinations are listed in Table 3.20.

In addition, PFPh was also excited at $\lambda_{pump} = 265$ nm, 250 nm, 240 nm, and 219 nm and ionized at $\lambda_{probe} = 800$ nm. The transient parent ion yields at all five excitation wavelengths are depicted in Figure 3.50. The dynamics at $\lambda_{pump} = 265$ nm and 260 nm are virtually identical. In contrast, choosing shorter excitation wavelengths ($\lambda_{pump} \leq 250$ nm) eliminates the long-lived decay component τ_4^{PFPh}, which might hint towards dissociation of the hydroxy group, as discussed in Subsection 3.7.4. Additionally, at $\lambda_{pump} = 250$ nm τ_3^{PFPh} is significantly decreased to

$$\tau_3^{PFPh}(250 \text{ nm}) = 22.25 \text{ ps}.$$

Choosing 240 nm as the excitation wavelength again halves the lifetime to

$$\tau_3^{PFPh}(240 \text{ nm}) = 9.71 \text{ ps}.$$

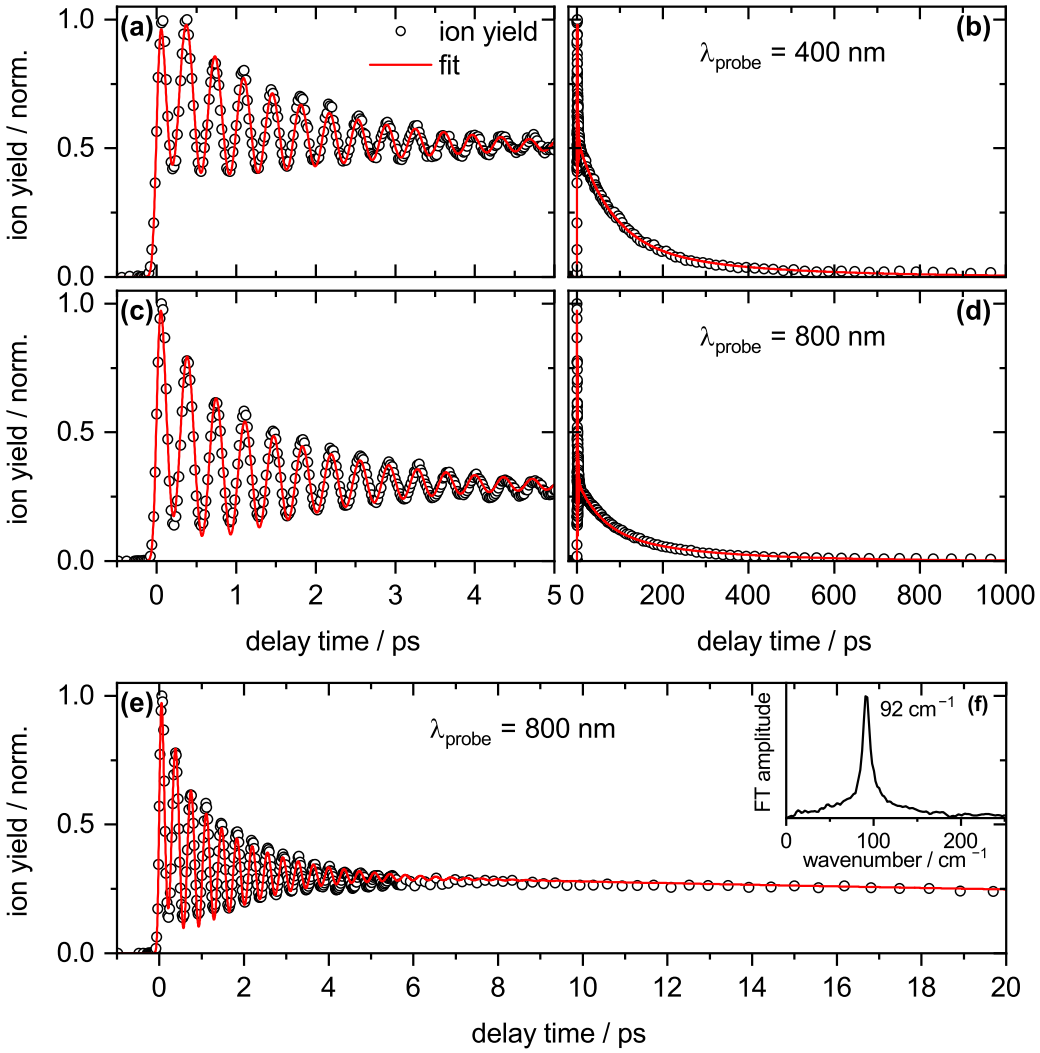

Figure 3.49. Measured transient parent ion yield signals (black circles) and applied fit model functions (red lines) for PFPh after excitation at $\lambda_{pump} = 260$ nm and ionization at $\lambda_{probe} = 400$ nm **(a–b)** resp. $\lambda_{probe} = 800$ nm **(c–e)**. The left-hand column shows the data in the first five picoseconds, the right-hand column in the first nanosecond after excitation. The fit parameters are listed in Table 3.20. **(e)** Complete decay of the oscillation truncated in **(c)**. **(f)** Fourier transform of the oscillatory signal component after subtraction of the exponential decay functions.

A further decrease of τ_3^{PFPh} to

$$\tau_3^{\mathrm{PFPh}}(219\ \mathrm{nm}) = 4.87\ \mathrm{ps}$$

is observed at $\lambda_{\mathrm{pump}} = 219$ nm. Although τ_1^{PFPh} and the lifetime of the oscillation $\tau_{\mathrm{ocs}}^{\mathrm{PFPh}}$ are also decreased at shorter excitation wavelengths, no similar stepwise changes are observed.

Origin of the Oscillation

The oscillations originate from pronounced vibronic coupling between the initially excited S_1 and at least one higher-lying $\pi\sigma^*$ state, either the S_2 or the S_3 state. Owing to the small energy gap of ≈0.2 eV between the states (cf. Table 3.18), coupling to either state seems feasible. Analogous to the coupling dynamics of 1,2,3-TriFB (cf. Section 3.1), the comparison of the molecular structure in the S_1 state with the displacement introduced by the potential coupling modes may shed light on the dynamics. Despite PFPh belonging to the C_s point group, the optimized molecular structure in the S_1 state essentially transforms according to the a_2 irreducible representation of the C_{2v} point group, if the hydrogen atom is neglected. Hence, the most dominant coupling mode probably also shows a_2 symmetry, which leads to the conclusion that the coupling is probably most pronounced between the S_1 ($2\ ^1A'/1\ ^1B_2$) and the S_2 state ($1\ ^1A''/1\ ^1B_1$). Furthermore, the frequency of the lowest-energy a_2-like vibrational mode $\nu_{14}^{\mathrm{PFPh}} = 96\ \mathrm{cm}^{-1}$ (cf. Figure 3.48) fits nearly perfectly to the oscillational frequency of $\nu_{\mathrm{osc}}^{\mathrm{PFPh}} = 93\ \mathrm{cm}^{-1}$, substantiating the proposition. Nevertheless, small deviations from the pure a_2 symmetry of the molecular structure in the S_1 state hint towards influence of the b_1-like modes, thus to coupling to the S_3 state ($2\ ^1A''/1\ ^1A_2$).

Calculations of Rajak et al.[68] revealed that the potential energy curves of the S_1 state show pronounced double-well character along the normal mode coordinates of the lowest-frequency a_2- and b_1-like vibrational modes. Therefore, indeed all out-of-plane modes are involved in the coupling process in case of PFPh. In addition, their calculated interstate coupling parameters and the double-well depths along the normal mode coordinates of both modes indicate the coupling is slightly stronger for the a_2 mode, tough not by a huge margin. In further agreement with the results presented in this Thesis, the coupling parameters also suggest pronounced coupling between the S_1 and S_3 state.[68] The distinctly

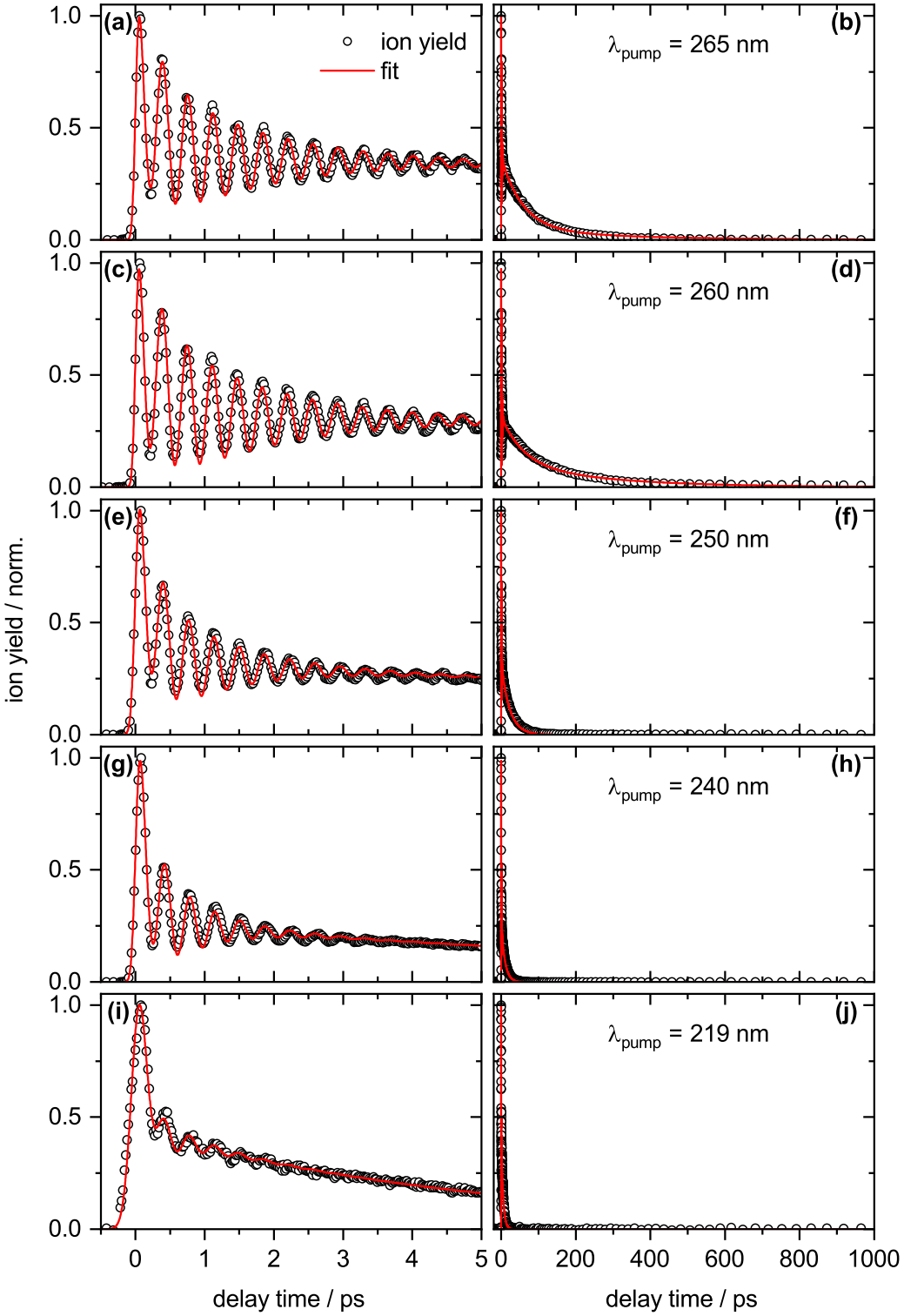

Figure 3.50. Measured transient parent ion yield signals (black circles) and applied fit model functions (red lines) for PFPh after excitation at $\lambda_{pump} = 265$ nm **(a–b)**, $\lambda_{pump} = 260$ nm **(c–d)**, $\lambda_{pump} = 250$ nm **(e–f)**, $\lambda_{pump} = 240$ nm **(g–h)**, and $\lambda_{pump} = 219$ nm **(i–j)** and ionization at $\lambda_{probe} = 800$ nm. The left-hand column shows the data in the first five picoseconds, the right-hand column in the first nanosecond after excitation. The fit parameters are listed in Table 3.20.

distorted potential energy curves of the S_2 state along the out-of-plane normal mode coordinates evident strong vibronic coupling between multiple states is present in PFPh, too.[68] Moreover, the authors simulated the molecular dynamics of the coupling process in the first $\Delta t = 200$ fs after excitation of the S_1 state. The diabatic electronic population analysis showed a somewhat alternating population transfer between the S_1 and the S_2 state, with an oscillational period of 25 fs. Unfortunately, such a fast oscillation is well below the time resolution achieved in this Thesis. Notwithstanding, the chosen simulation timeframe essentially represents the delay time between t_0 and the first minimum of the parent ion yield. Since the minimum corresponds to a vastly increased $\pi\sigma^*$ character of the S_1 state,[9,10] a steep decrease of the $\pi\pi^*$ and an equivalent increase of the $\pi\sigma^*$ state population at $\Delta t = 200$ fs should be observed in the simulations. Yet, except for the fast oscillation, the populations remain essentially constant. Increasing the timeframe of the calculations to one or more full experimentally observed oscillational periods might resolve the discrepancies.

At $\lambda_{\text{pump}} = 219$ nm the molecules are not excited to the S_1 state ($\pi\pi^*$), but to a $\pi\sigma^*$ state, probably the S_3 state. Remarkably, oscillations are still present. The emerging signal oscillations suggest an ultrafast internal conversion from the initially excited $\pi\sigma^*$ state to the S_1 state, presumably within the IRF. Despite the internal conversion, the vibrational wavepacket seems to remain coherent, enabling observation of the coupling. Confirmation of the proposed conversion may be possible via photoelectron spectroscopy. However, a substantially enhanced time resolution compared to $\sigma_{\text{IRF}} = 110$ fs herein will be needed to ensure that all processes within the IRF are actually mapped.

3.7.3 Time-Resolved Photoelectron Images

The time-resolved PEI of PFPh at $\Delta t = 0.03$ ps after excitation at $\lambda_{\text{pump}} = 260$ nm and subsequent ionization at $\lambda_{\text{probe}} = 400$ nm (a) and in the first first minimum of the parent ion yield at $\Delta t = 0.17$ ps (b) are shown in Figure 3.51. The transient images feature a broad (α) and a narrow signal (β). As displayed in the corresponding PES in Figure 3.52 (a), the intensity of α increases towards $E_{\text{el}} = 0$ eV, and thus a clear peaking of α cannot be observed. On the other hand, β is centered at $E_\beta = 0.85$ eV. The electron yields of both signals oscillate according to the transient behavior of ion yield. The PEI resulting from the high-intensity single-color ionization at $\lambda_{\text{pump}} = 260$ nm and $\lambda_{\text{probe}} = 400$ nm

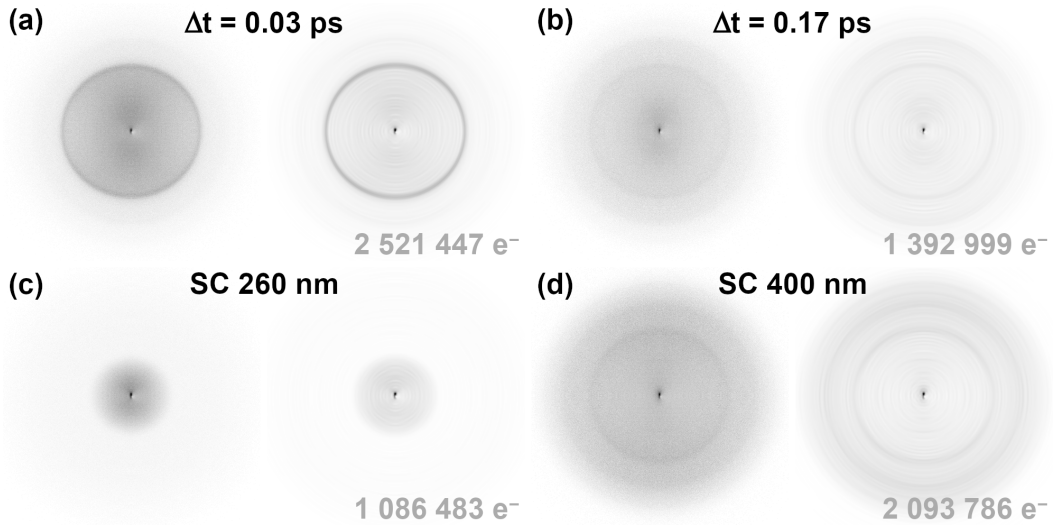

Figure 3.51. Photoelectron images (left) and their corresponding meridional slices through the recovered three-dimensional photoelectron distributions (right) of PFPh. **(a)** At $\Delta t =$ 0.03 ps after excitation at $\lambda_{\text{pump}} = 260$ nm and ionization at $\lambda_{\text{probe}} = 400$ nm and **(b)** at $\Delta t = 0.17$ ps (first minimum). **(c–d)** High-intensity single-color photoelectron images obtained at 260 nm **(c)** and 400 nm **(d)**.

are shown in Figure 3.51 (c) and (d), respectively. The SC ionization at 260 nm results in one signal ζ, which features several peaks with a spacing of ≈0.035 eV (≈280 cm^{-1}). Without applying the Jacobin transform the signal is centered at $E_\zeta = 0.13$ eV, as shown in Figure 3.52 (c). The SC ionization at 400 nm yields the signal β and an additional signal γ at $E_\gamma = 1.7$ eV on top of a broad background.

Ionization Pathways

In accord with the PES of the previously discussed 1,2,3-TriFB, the TFB isomers, and PFT, the two signals in the transient PES are assigned to transitions to the ionic ground state D_0 (β) and the first excited ionic state D_1 (α). Since no additional signals arise at any delay time between the pump and the probe pulses, the oscillation of the signals reflects the time dependent changes of the potential energy hypersurface of the initially excited S_1 state.

The narrow width of β suggests an adiabatic transition to the D_0 state, however, not necessarily reflects a direct $D_0 \leftarrow S_1$ transition, as highlighted in the previous Sections. Based on Equation 3.2 in Section 3.1, the energy of the state populated prior to ionization can be calculated. The sum of the photoelectron energy $E_\beta = 0.85$ eV and the AIE of 9.3 eV, minus the energy of the two photons at

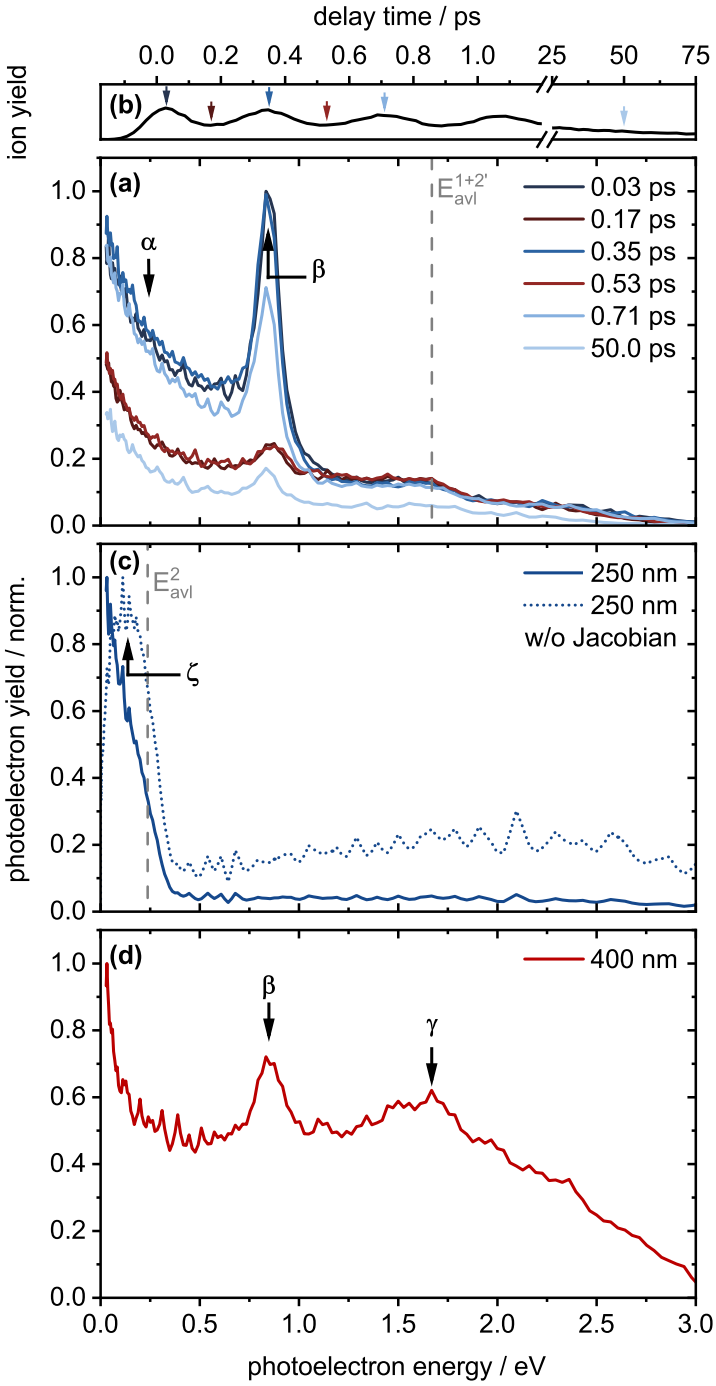

Figure 3.52. **(a)** Transient PE spectra of PFPh after excitation at $\lambda_{pump} = 260$ nm and ionization at $\lambda_{probe} = 400$ nm. Two main photoelectron signals labeled α and β are observed. The intensity of α increases towards $E_{el} = 0$ eV, β peaks at $E_\beta = 0.85$ eV. The grey dotted line indicates the maximum available photoelectron energy $E^{1+2'}_{avl}$ associated with the $D_0 \leftarrow S_0$ transition by $1 + 2'$ ionization. **(b)** Corresponding transient parent ion yields adapted from Figure 3.49 (a). Arrows mark the delay time $\Delta t = 0$–50 ps at which the PES were obtained (red at ion yield minima). **(c–d)** Single-color PE spectra taken at higher 260 nm pump **(c)** and 400 nm probe **(d)** intensities. Solid lines show the PE spectra with Jacobian transformation, dotted lines without. The additional signals γ and ζ are located at $E_\gamma = 1.7$ eV and $E_\zeta = 0.13$ eV. The grey dotted line indicates the maximum available photoelectron energies E_{avl} generated by two 260 nm photons (E^2_{avl}). At 400 nm the max. available energy is 3.1 eV.

$\lambda_{\text{probe}} = 400$ nm (2×3.10 eV) yields 4.0 eV (310 nm), i.e., 0.4 eV less than the calculated S_1 AEE and 0.3 eV lower than the onset of the absorption band at 4.28 eV (290 nm). Therefore, it is assumed that an intermediate state at 7.1 eV is excited in the multi-photon ionization, via absorption of a single probe photon. The ab initio calculations show the state might either be the S_6 ($4\ ^1A'$, $\pi\pi^*$) or the S_7 state ($5\ ^1A'$, $\pi\pi^*$) at 7.27 eV and 7.30 eV, respectively. Both states electronically correspond to the D_0 state, as listed in Table 3.19. In lack of further information on the high-lying states, no differentiation is possible. The two intermediate states also electronically correspond to the D_1 state. As a consequence, the pathways towards α and β are estimated to be very similar, yet in the case of signal α the D_1 state, and not the D_0 state, is populated after ionization. The proposed ionization mechanisms to both PE signals are illustrated in Figure 3.53 (a).

High-intensity SC ionization at $\lambda_{\text{pump}} = 260$ nm yields a signal at $E_\zeta = 0.13$ eV. Thus, 9.41 eV reside in the molecule after ionization by two photons with a total energy of 9.54 eV, fitting reasonably well to the re-evaluated D_0 AIE of 9.3 eV. The small peaks on top of the signal with a spacing of ≈0.035 eV (≈280 cm^{-1}) may show the vibrational progression of the a_1-like mode $\nu_{11}^{\text{PFPh}} = 260$ cm^{-1} or of one of the b_2-like modes $\nu_{30}^{\text{PFPh}} = 283$ cm^{-1} and $\nu_{29}^{\text{PFPh}} = 290$ cm^{-1} (cf. Table B.7).

Analogous high-intensity SC ionization at $\lambda_{\text{probe}} = 400$ nm results in signal β and a second broad band γ peaking at $E_\gamma = 1.7$ eV on top of a broad background. The background is the result of a plethora of transitions. In the case of signal β, probably two-photon excitation of the S_1 state is followed by one-photon excitation of an intermediate state. Absorption of a fourth photon leads to the ionization to the D_0 state. A signal corresponding to α likely vanishes in the background. The second band γ presumably is associated with the excitation of an intermediate state at 7.8 eV. Due to the vast number of possible intermediate states, no specific state is assigned to the signal. The SC ionization pathways are depicted in Figure 3.53 (b) and (c).

3.7.4 Dissociation of PFPh

In the last two decades, the photodissociation dynamics of phenol has received considerable attention of both experimentalists[72–90] and theoreticians[83,91–108] because of its importance as a building block in countless biologically active molecules. Inspired by dissociation of phenol in clusters, Sobolewski and

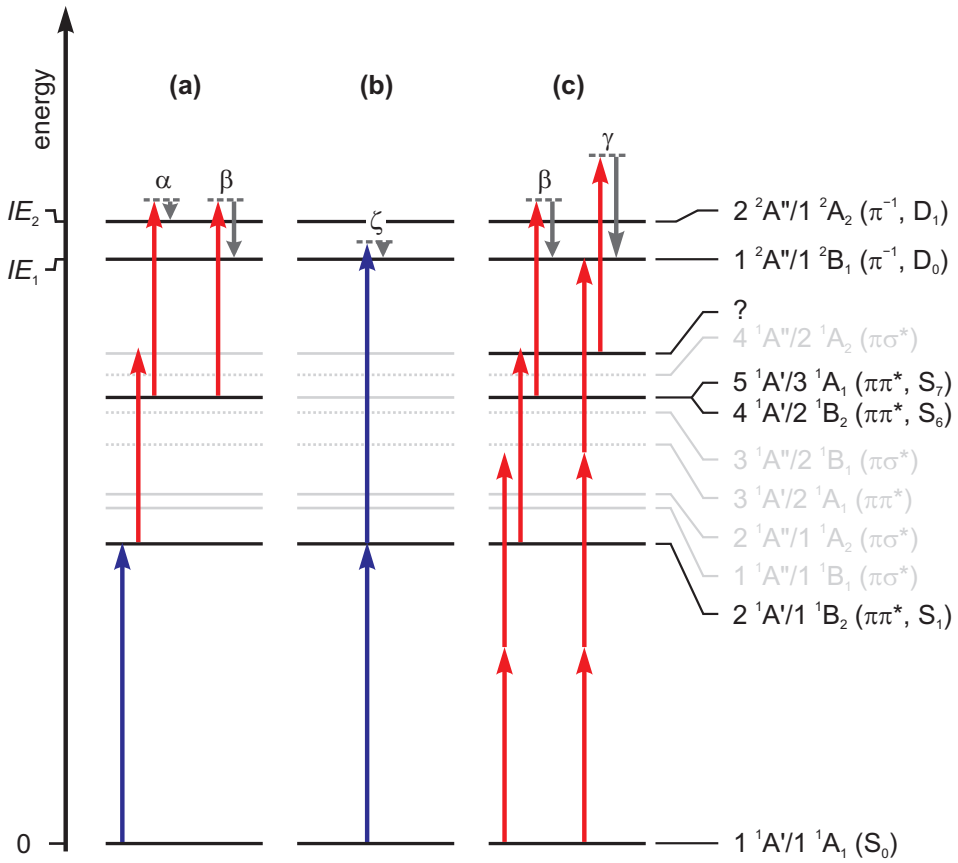

Figure 3.53. Proposed multi-color and single-color ionization schemes for PFPh. The energies of the photons at $\lambda_{\text{pump}} = 260$ nm (blue) and $\lambda_{\text{probe}} = 400$ nm (red) and of the photoelectrons (grey) are depicted as vertical arrows. Solid black horizontal lines: experimentally intermediate and final states, solid and dotted (calculated values) grey horizontal lines: non-participating other intermediate states. **(a)** Transient ionization pathways by one-photon absorption to the S_1 state ($2\,^1A'/1\,^1B_2$) and subsequent two-photon ionization to the D_0 ($1\,^2A''/1\,^2B_1$) and D_1 states ($2\,^2A''/1\,^2A_2$) showing the origin of PE peaks α and β. **(b)** Single-color ionization pathways at $\lambda_{\text{pump}} = 260$ nm to the D_0 state showing the origin of PE peak ζ. **(c)** Single-color ionization pathways at $\lambda_{\text{probe}} = 400$ nm to the D_0 state showing the origin of PE peaks β and γ.

Domcke[91] proposed excitation of the S_1 state, a $\pi\pi^*$ state, might result in the dissociation of the O-H bond. Depending on the excess energy, the population might be transferred from the $\pi\pi^*$ state to the second excited state, a $\pi\sigma^*$ state. The $\pi\sigma^*$ state is characterized by a Rydberg-like electron density located at the O-H group and a node of the density along the O-H bond. Consequently, if the $\pi\sigma^*$ state is populated, the O-H bond breaks. The authors calculated an energy barrier of ≈5 eV for the conical intersection between the $\pi\pi^*$ and the $\pi\sigma^*$ states. Shortly afterwards, Tseng et al. observed the O-H bond dissociation of phenol in the gas phase after excitation at 248 nm (5 eV) via multimass ion imaging,[73] and in the following the barrier of 5 eV was confirmed utilizing high-resolution H-atom Rydberg tagging.[74,75,78] In contrast to the structured distribution of highly energetic protons after excitation at wavelengths <248 nm, an unstructured, broad signal of protons with less energy was observed at wavelengths >248 nm, indicating dissociation is also possible after excitation below the energy barrier. These findings were initially rationalized by a multi-step dissociation. Subsequent to the excitation of the $\pi\pi^*$ an internal conversion to the highly excited ground state (S_0) was assumed, followed by an internal conversion to the $\pi\sigma^*$ state, mediated by out-of-plane modes.[72,75] Later, both theory[83,92,96] and experiments[82–84] confirmed the dissociation is actually enabled via hydrogen atom tunneling through the $\pi\pi^*$–$\pi\sigma^*$ barrier, followed by a conical intersection between the $\pi\sigma^*$ and the ground state.

The timescale of the dissociation also varies strongly depending on the chosen wavelength. While the dissociation after excitation below the barrier generally takes nanoseconds,[72,84,109,110] excitation with more energy, e.g., at $\lambda_{pump} =$ 200 nm, significantly accelerates the process to <150 fs.[79,81] Even small variations of the wavelength can have a huge impact on the dissociation. Earlier it was proposed[75,83,93–95,104,105] that selective excitation of both ring-torsions and the O-H torsional motions greatly promote the dissociation. Recently, Lai et al.[88] seemingly confirmed the proposed pathways, but likewise recent, yet contradicting work by Woo and Kim[90] and Xie et al.[108] indicate the dynamics might be significantly more complex. Thus, despite the comprehensive studies undertaken to understand the dissociation dynamics, the picture can still be considered incomplete.

Ab Initio Calculations for Phenol

The electronic structure of PFPh is comparable to the one of phenol.[67,68] Both exhibit a low-lying $\pi\pi^*$ state (S_1), followed by a $\pi\sigma^*$ state (S_2). For phenol a $\pi\pi^*$–$\pi\sigma^*$ state energy difference of 0.7–1.3 eV was calculated[68,91] and for PFPh a gap of 0.1–0.5 eV (cf. Table 3.18 and Refs. [67, 68]). Thus, it is reasonable to expect photoinduced bond fission of the O-H bond might also occur for PFPh and, consequently, alter the observable time-resolved dynamics. Hitherto, published calculations of the molecular structures and dynamics of PFPh focused on the Franck–Condon region,[67,68] but not on the dissociation dynamics. In order to address the dissociation, the potential energies of the S_0, the S_1, and the S_2 state were calculated with respect to the O-H bond distance for PFPh at RI-SCS-CC2 level of theory. However, to firstly evaluate if the method of choice is suited to describe the dissociation, the dissociation of phenol was calculated at the same level of theory and compared to the results of Sobolewski and Domcke in Figure 3.54. It should be noted that for phenol the $\pi\pi^*$ and the $\pi\sigma^*$ states are explicitly not labeled as S_1 and S_2 in the following, since the order of the states depends on the O-H bond length, as will be shown. A similar, but more intricate dependence of the electronic character is observed for PFPh.

Sobolewski and Domcke optimized the molecular structure of phenol in the $\pi\pi^*$ and $\pi\sigma^*$ states at various different fixed O-H bond lengths at CASSCF level of theory, hence mapping the dissociation pathway. Subsequent to the structure optimization, single point energies for all optimized structures were calculated at CASPT2 level of theory. The energies were referenced to the energy of the ground state, optimized at MP2 level of theory. At increased O-H bond distances the energy of the ground state was calculated based on the structure in the $\pi\sigma^*$ state.[91] Following their example, the optimization of the structures in both low-lying excited states at various different O-H bond lengths at RI-SCS-CC2 level of theory was attempted. Unfortunately, only optimization of the structure in the lowest-lying state converged, thus the presented potential energies at non-equilibrium O-H bond lengths of both the ground state and the higher-lying excited state are based on single point calculations at these structures. In agreement with Sobolewski and Domcke, the molecular structure in the S_0 state, optimized at RI-SCS-MP2 level of theory, was chosen as the energetic zero point too.

Starting at an O-H bond length of ≈0.95 Å, Sobolewski and Domcke reported an AEE to the $\pi\pi^*$ state of 4.24 eV. The $\pi\sigma^*$ is located ≈1.3 eV above the

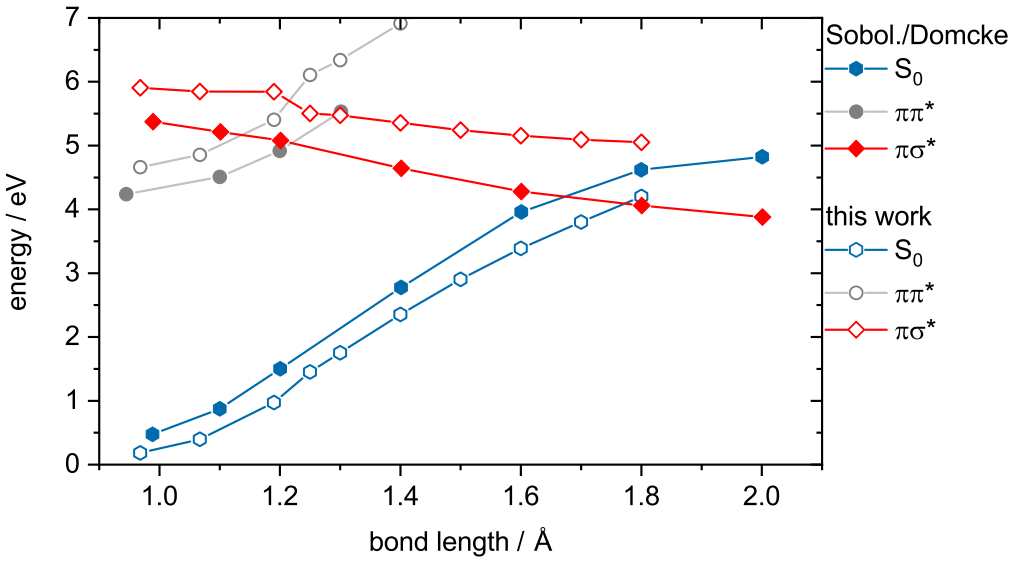

Figure 3.54. Calculated energies of the S_0 state (blue hexagons), the first $\pi\pi^*$ state (grey circles) and the first $\pi\sigma^*$ state (red diamonds) of phenol as a function of the O-H bond distance. Hollow symbols are calculational results of this Thesis, filled symbols are energies adapted from Sobolewski and Domcke.[91]

$\pi\pi^*$ state, though the authors noted that the AEE to the $\pi\pi^*$ state likely is underestimated.[91] Increasing the O-H bond length results in an increase of $\pi\pi^*$ and a decrease of $\pi\sigma^*$ energy. At ≈1.2 Å the states cross at an energy of ≈5 eV (248 nm), thus ≈0.8 eV above the $\pi\pi^*$ minimum. Further increase of the bond length results in a second CI between the $\pi\sigma^*$ and the S_0 state at 1.7 Å, although more recent calculations predict the bond length at the second CI to be 2.1 Å.[83]

In this work, calculations yield a significantly higher $\pi\pi^*$ AEE of 4.66 eV. Nevertheless, the calculated energy gap of ≈1.4 eV to the $\pi\sigma^*$ state (5.91 eV) fits well to result of Sobolewski and Domcke, as does the predicted O-H bond length of ≈0.97 Å in the relaxed $\pi\pi^*$ state. Increasing the O-H bond length increases the $\pi\pi^*$ and decreases the $\pi\sigma^*$ energies. Both states cross at a bond length of ≈1.2 Å, with an energy barrier height of 5.70 eV (≈218 nm). Despite the barrier height being ≈0.70 eV higher than the actual experimental barrier, the calculated O-H bond distance at which the barrier peaks fits surprisingly well to the values reported in the literature. Increasing the bond length up to 1.8 Å increases the S_0 and decreases the $\pi\sigma^*$ state energies, yet the states do not cross. Optimizations at longer bond lengths did not converge. All in all, the calculations overestimate the height of the dissociation barrier and do not yield the second CI between the $\pi\sigma^*$ and the S_0 state, but correctly render the

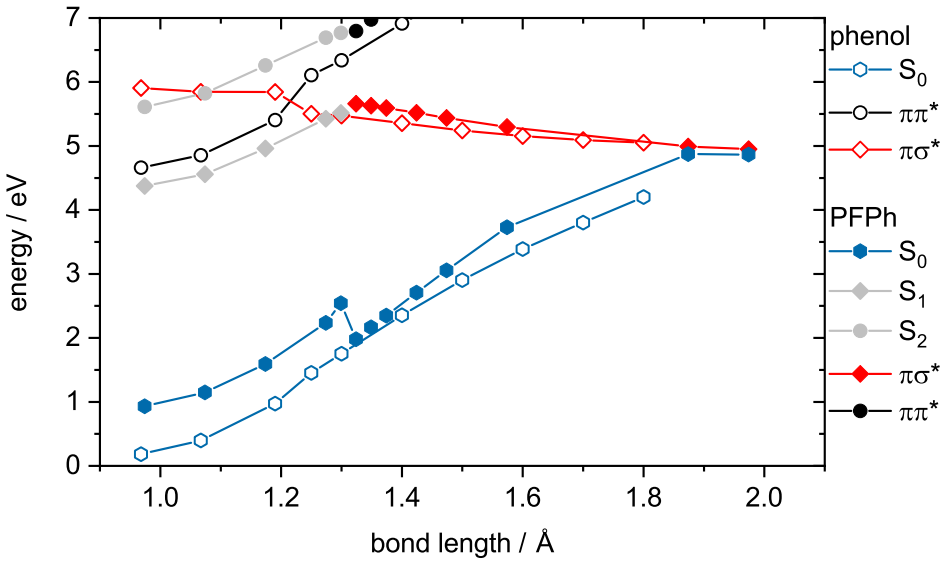

Figure 3.55. Calculated energies of the S_0 state (blue hexagons), the first $\pi\pi^*$ state (black circles) and the first $\pi\sigma^*$ state (red diamonds) as a function of the O-H bond distance of phenol (hollow) and PFPh (filled). In grey are the energies of the S_1 and S_2 state of PFPh for bond lengths shorter than ≈1.3 Å, exhibiting mixed electronic character (see text for details).

crucial energetic trends around the $\pi\pi^*$–$\pi\sigma^*$ CI. Hence, RI-SCS-CC2 is expected to describe the dissociation pathway of PFPh likewise reasonably well.

Comparison of Phenol and PFPh

In Figure 3.55 depicted is the comparison of the phenol and the PFPh calculations. The latter yielded an AEE to the first excited state S_1 of 4.37 eV at an O-H bond length of ≈0.97 Å, and based on the optimized S_1 structure the S_2 state is placed at 5.62 eV. Thus, the states of PFPh are consistently estimated to exhibit lower transition energies than their phenol counterparts. Increasing the O-H bond length in PFPh increases the energies of the S_1 and S_0 states, but simultaneously also increases the S_2 state energy, contrary to the trend of the $\pi\sigma^*$ state in phenol. This increase is observed up to a bond distance of ≈1.3 Å. Within 0.025 Å the S_1 and S_2 states start to diverge as the S_1 state is stabilized. In addition, the potential energy of the S_0 state suddenly decreases, but increases again at longer O-H bond distances. At a bond length of ≈1.8 Å the S_1 and the S_0 states cross.

To understand why the behavior of the S_1 and S_2 states of PFPh and the $\pi\pi^*$ and $\pi\sigma^*$ states of phenol deviates for O-H bond distances of <1.3 Å, a closer look at the states involved is needed. For phenol, the σ^* orbital of the $\pi\sigma^*$ state

is basically a Rydberg orbital located at the hydroxy group, exhibiting a node at the O-H bond (cf. Ref. [91]). In the case of PFPh, the perfluoro effect lowers the σ orbitals located at the C-F bonds in energy. As a consequence, the $\pi\sigma^*$ state is characterized by electron densities partially shifted away from the hydroxy group (cf. Table 3.19 and Figure 3.47). This seemingly negligible difference has severe implications. Excitation of the S_1 state will lead to the already in-depth discussed intense vibronic coupling between the S_1 and the higher-lying S_2 state. The coupling is mediated by out-of-plane vibrational modes. Hence, the coupling is accompanied by a distinct out-of-plane deformation of the formerly planar equilibrium molecular structure (cf. Figure 3.48 and Ref. [67, 68]). Furthermore, the coupling changes the electron densities and characters of the calculated orbitals. As shown in Figure 3.56, the coupling basically merges the π^* and σ^* antibonding orbitals. Thus, for the out-of-plane distorted structures, the S_1 and S_2 states are not formed by transitions from π orbitals to a π^* and a σ^* orbital, respectively, but are characterized by transitions from different π orbitals to a single mixed-character antibonding orbital, which is why the states are neither labeled as $\pi\pi^*$ or $\pi\sigma^*$ states for these deformed structures. Since the antibonding orbital has no Rydberg-like character at the O-H bond anymore, increasing the O-H bond distance increases the energies of both excited states likewise.

This trend is observed up to a bond distance of ≈1.3 Å. Further elongation of the O-H bond by only 0.025 Å results in a sudden structural reorientation from the formerly distorted to a planar molecular structure, as shown in Figure 3.56 (c). Moreover, the previously mixed characters of the orbitals change to pure π^* and σ^* orbitals (cf. Figure 3.56 (b) and (d)). For the latter, the electron density is located mainly at the hydrogen atom and not at the ring anymore. Increasing the O-H bond length further decreases the S_1 state energy, now of pure $\pi\sigma^*$ character, and increases the S_2 energy ($\pi\pi^*$ character).

The RI-SCS-CC2 method obviously fails to describe the change in potential energy for the S_2 state, lacking a CI with the S_1 state. Nevertheless, the trend of the S_1 potential energy closely resembles a prototypical dissociation barrier. Therefore, it is carefully assumed that the S_1 potential energy curve is a valid depiction of the dissociation pathway, indicating an energy barrier of 5.66 eV (219 nm) for the O-H bond fission. As the employed calculations also overestimates the barrier for phenol and yielded a virtually identical peak energy

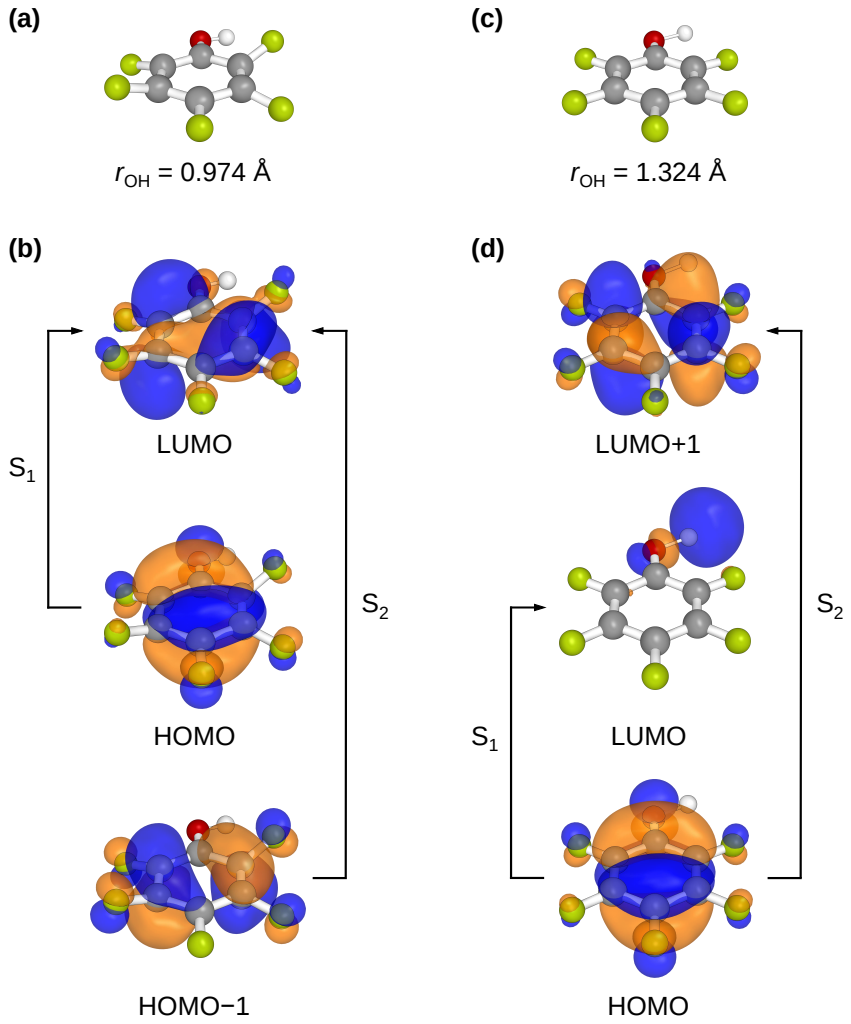

Figure 3.56. **(a)** Out-of-plane distorted equilibrium molecular structure of PFPh in the S_1 state, exhibiting an O-H bond distance of $r_{OH} = 0.974$ Å. **(b)** The S_1 and S_2 states are formed by excitation of an electron from the highest-occupied molecular orbital (HOMO) and the HOMO−1 (both π character) to a mixed-character lowest unoccupied molecular orbital (LUMO). **(c)** At $r_{OH} = 1.324$ Å the molecular structure becomes planar. **(d)** The S_1 and S_2 states are formed by transitions from the HOMO (π) to the LUMO (σ^*) and the LUMO+1 (π^*), respectively.

of 5.70 eV (≈218 nm), the actual barrier height in PFPh likely is lower than 5.66 eV, probably being ≈5 eV (248 nm) too.

Experimental Observation of the Dissociation

Based on the novel calculations in this Thesis, it is reasonable to assume photodissociation might be a possible signal decay channel after excitation of the S_1 state of PFPh as well. Yet, no bond-fission fragments were present in the static TOF-MS at any excitation wavelength, as shown in Figure 3.57. Since Cooper et al.[111] did observe photofragments after excitation of PFPh at $\lambda_{pump} \geq 220$ nm in their high-resolution H Rydberg atom photofragment translational spectra, the TOF-MS herein probably is insensitive for the fragments. However, PFPh dissociates to very little extent compared to other fluorinated phenols.[111] Although the authors argued that the marginal dissociation occurs in the hot ground state, it was noted that only time-resolved measurements will be able to distinguish between dissociation in a hot ground state and in the excited states. The femtosecond time-resolved ion yield measurements for PFPh in this work highlight a noteworthy wavelength dependence of the excited state lifetime. At excitation wavelengths shorter than $\lambda_{pump} = 260$ nm the vanishing of the long-lived decay constant and an overall near step-like reduction of the lifetime is observed. In combination with the calculations, predicting the dissociation will require excitation wavelengths $\lambda_{pump} < 260$ nm, both observations might be connected to an enabled bond dissociation channel in the electronically excited states, as opposed to the proposal of Cooper et al.[111] To ultimately resolve the dissociation mechanism, time-resolved studies targeting the selective detection of the hydrogen fragments via ionization at $\lambda_{probe} = 243.1$ nm would be most valuable.

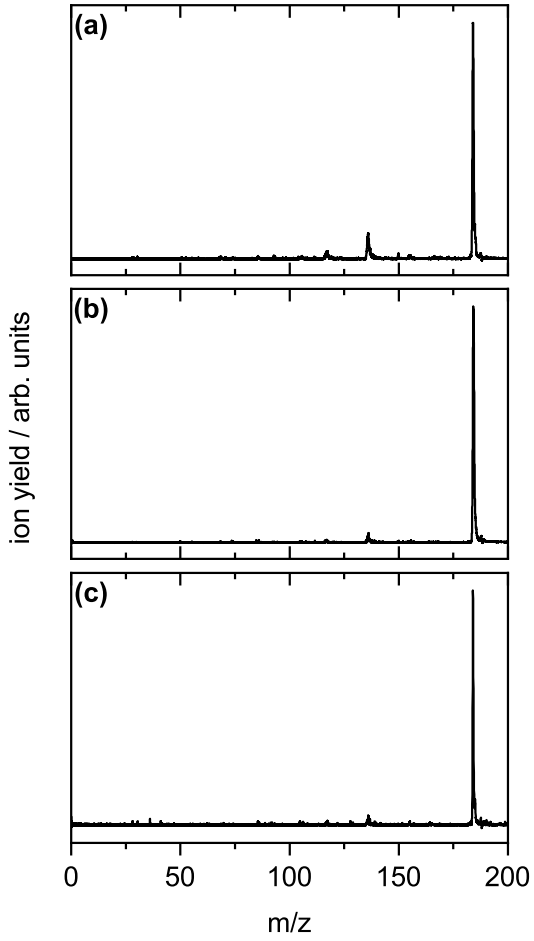

Figure 3.57. TOF mass spectra of PFPh at $\Delta t = t_0$ after excitation at $\lambda_{\text{pump}} = 260$ nm and ionization **(a)** at $\lambda_{\text{probe}} = 400$ nm and **(b)** at $\lambda_{\text{probe}} = 800$ nm. **(c)** TOF mass spectrum of PFPh at $\Delta t = t_0$ after excitation at $\lambda_{\text{pump}} = 219$ nm and ionization at $\lambda_{\text{probe}} = 800$ nm. The intense peaks are the parent ion signals. In **(a)** an additional a carbon ring fragmentation product is observed, basically not present in **(b)** and **(c)**.

3.8 Chloropentafluorobenzene

3.8.1 Molecular and Electronic Structure

The UV absorption spectrum of ClPFB is shown in Figure 3.58. Starting at ≈285 nm (4.35 eV), three structureless bands are observed. The first one peaks at 262 nm (4.73 eV), the second one at 232 nm (5.34 eV). The third band cannot be fully resolved, but rises at wavelengths <215 nm (>5.77 eV).

To unravel the nature of the underlying states, the VEEs to the first eight excited electronic states were calculated at RI-SCS-CC2 level of theory. The results are listed in Table 3.21. A VEE of 5.00 eV (248 nm) is estimated to the first excited state S_1 (1 $^1B_2$), which exhibits $\pi\pi^*$ character. Two nearly isoenergetic $\pi\sigma^*$ states are placed at 5.70 eV and 5.74 eV (≈217 nm), the S_2 (1 $^1B_1$) and the S_3 state (1 $^1A_2$), respectively. The VEE to the S_4 state ($\pi\pi^*$, 2 $^1A_1$) was calculated to be 6.28 eV (197 nm). All other states are located at transition energies >7 eV.

The first absorption band peaking at 262 nm (4.73 eV) is assigned to the S_1 state. The energy difference between the calculated and the experimental VEE of ≈0.3 eV reflects the tendency of the employed RI-SCS-CC2 method to slightly overestimate the transition energies in fluorobenzenes.[9,10] Although it might be tempting to assign the band peaking at 232 nm (5.34 eV) to the second $\pi\pi^*$ state, the energy difference between calculation and experiment would be ≈1 eV. Since a variety of fluorobenzenes exhibits an intense $\pi\pi^*$ absorption band at wavelengths <215 nm,[36,38] the third band rising at <215 nm is assigned to the second $\pi\pi^*$ state, the S_4 state at 6.28 eV (197 nm). Consequently, the second absorption band has to be the result of a $\pi\sigma^*$ transition. However, the calculated oscillator strengths to the S_2 state is only a third of the one predicted for the S_1 state, and the transition to the S_3 state is even optically dark. Yet, as discussed for PFPh (cf. Section 3.7), one of the $\pi\sigma^*$ states probably borrows intensity from the S_1 state, increasing the absorption strength. This intensity borrowing is not reflected in the calculated oscillator strengths. Nevertheless, which $\pi\sigma^*$ transition yields the absorption band remains elusive.

The calculations predict a planar molecular structure in the S_0 state. In contrast, a pronounced out-of-plane deformation is predicted in the S_1 state, as shown in Figure 3.59. The four carbon atoms 2, 3, 5, and 6 span a plane in the S_1 state. The carbon atoms 1 and 4 are slightly bent out of the plane

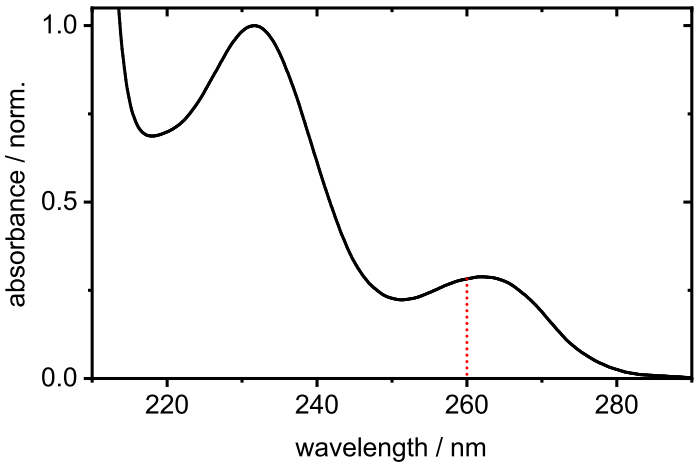

Figure 3.58. Normalized gas-phase UV absorption spectrum of ClPFB. The dotted red line indicates the chosen excitation wavelength of $\lambda_{pump} = 260$ nm to excite the S_1 state ($\pi\pi^*$).

Table 3.21. Vertical excitation energies (VEE) and oscillator strengths f (in parentheses) of the first eight neutral electronically excited states, the ionic ground state and the first two ionic electronically excited states for ClPFB, calculated at RI-SCS-CC2 level of theory. Where available, the respective adiabatic energy (AEE) is listed. Experimental energies are given if possible.

	symm.	calc. VEE eV	calc. AEE eV	exp. VEE eV	exp. AEE eV
S_1 ($\pi\pi^*$)	$1\,^1B_2$	5.00 (0.0039)	4.51	4.73[†]	4.35[†]
S_2 ($\pi\sigma^*$)	$1\,^1B_1$	5.70 (0.0013)		5.34[†]	
S_3 ($\pi\sigma^*$)	$1\,^1A_2$	5.74 (0.0000)			
S_4 ($\pi\pi^*$)	$2\,^1A_1$	6.28 (0.0722)			
S_5 ($\pi\sigma^*$)	$2\,^1B_1$	7.12 (0.0017)			
S_6 ($\pi\pi^*$)	$2\,^1B_2$	7.18 (0.5453)			
S_7 ($\pi\pi^*$)	$3\,^1A_1$	7.20 (0.8436)			
S_8 ($\pi\sigma^*$)	$2\,^1A_2$	7.53 (0.0000)			
D_0 (π^{-1})	$1\,^2B_1$	9.89	9.62		9.72[a]
D_1 (π^{-1})	$1\,^2A_2$	10.14		9.9[b,c]	
D_2 (π^{-1})	$2\,^2B_1$	12.40		12.20[b]	

[a] Ref. [39] [b] Ref. [64] [c] Ref. [112] [†] this work

by 1° and 3°, respectively. The chlorine atom is bent out of the plane by 16° and F-10 by 25°. The remaining fluorine atoms are bent out-of-plane to the opposed direction by −9°. In total, the deformed structure transforms according to the b_1 irreducible representation of the C_{2v} point group. An AEE to the S_1 state of 4.51 eV (275 nm) was calculated based on the optimized structures, in rather good agreement with the band onset at 4.35 eV (285 nm). Moreover, the displacement vectors of all out-of-plane modes and their frequencies are given in Figure 3.59, too. A comprehensive list of all vibrational frequencies can be found in Table B.8 in the appendix.

In addition to the neutral states, the VIEs to the first three ionic states were calculated. The ionic ground state D_0 ($1\ ^2B_1$) is located at 9.89 eV. The first excited ionic state D_1 ($1\ ^2A_2$) exhibits a calculated VIE of 10.14 eV. Both states are well separated from the second excited ionic state D_2 ($2\ ^2B_1$) at 12.40 eV. No experimental VIE was reported for the D_0 state. In contrast, the experimental VIEs to the other two ionic states are in good agreement with the calculated values. Optimization of the molecular structure in the D_0 state yielded a planar structure (not shown for the sake of brevity). The calculated AIE of 9.62 eV underestimates the actual AIE of 9.72 eV.[39]

3.8.2 Time-Resolved Time-of-Flight Mass Spectra

The transient parent ion yields of ClPFB after excitation at $\lambda_{\text{pump}} = 260$ nm and ionization at either $\lambda_{\text{probe}} = 400$ nm or 800 nm are shown in Figure 3.60. After excitation, an ultrafast initial decay within the time-resolution is followed by a signal oscillation. However, at $\lambda_{\text{probe}} = 800$ nm the oscillation is much more pronounced than at $\lambda_{\text{probe}} = 400$ nm. Via Fourier transform of the oscillatory signal component (cf. Figure 3.60 (e)) the oscillatory frequency was determined to be $\nu_{\text{osc}}^{\text{ClPFB}} = 87$–$92\ \text{cm}^{-1}$ and the oscillation decays with

$$\tau_{\text{osc}}^{\text{ClPFB}} = 0.2\text{–}0.7\ \text{ps}.$$

The majority of the signal decays within the following $\Delta t = 100$ ps at both probe wavelengths. The decays can be described by two exponential decay functions

$$\tau_2^{\text{ClPFB}} = 1.5\ \text{ps}$$

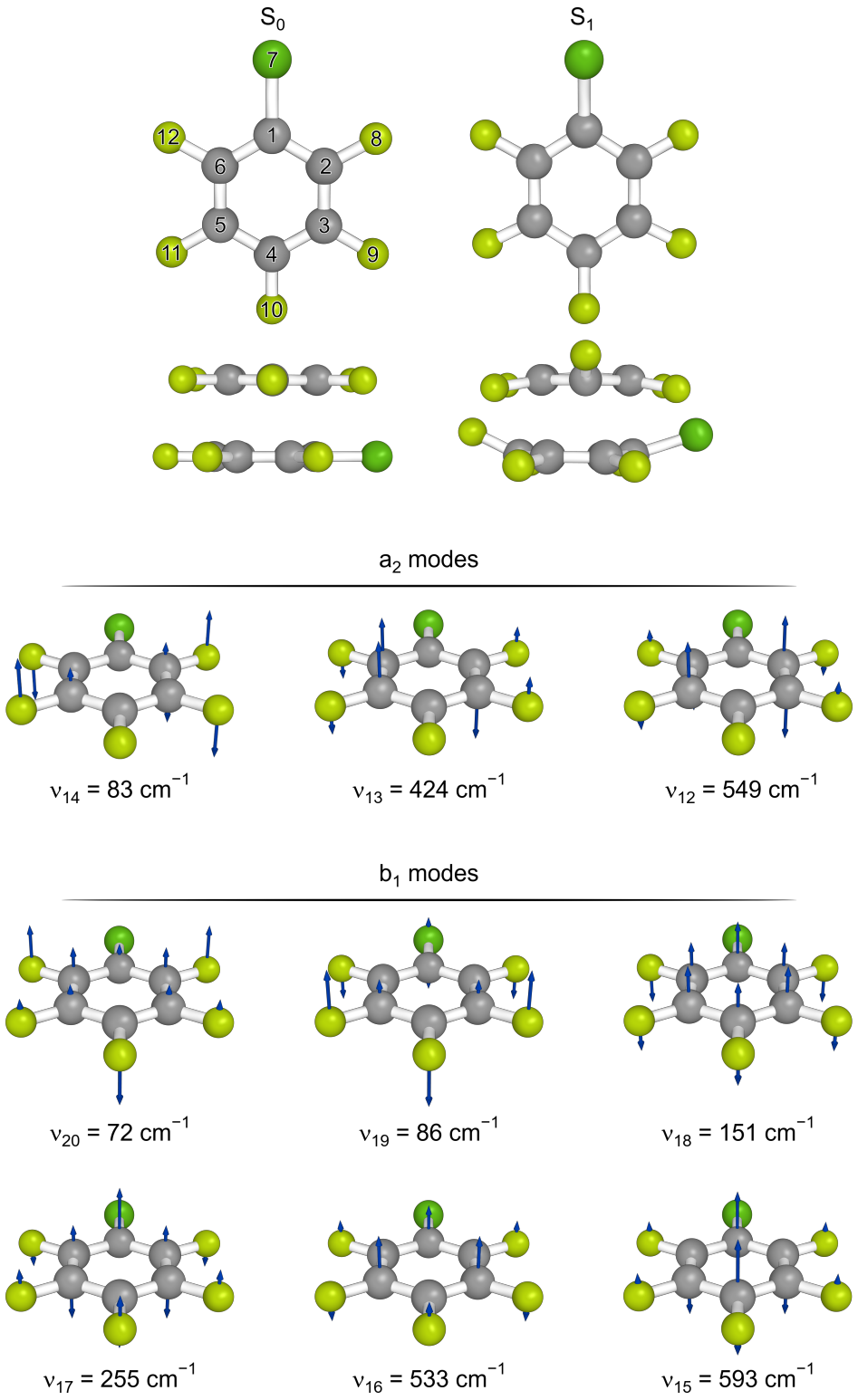

Figure 3.59. Calculated molecular structures of ClPFB in the S_0 and the S_1 state ($\pi\pi^*$), optimized at the RI-SCS-MP2 and RI-SCS-CC2 levels of theory, respectively. The calculated displacement vectors of the out-of-plane modes are illustrated by blue arrows. Their respective frequencies in the S_1 state are listed.

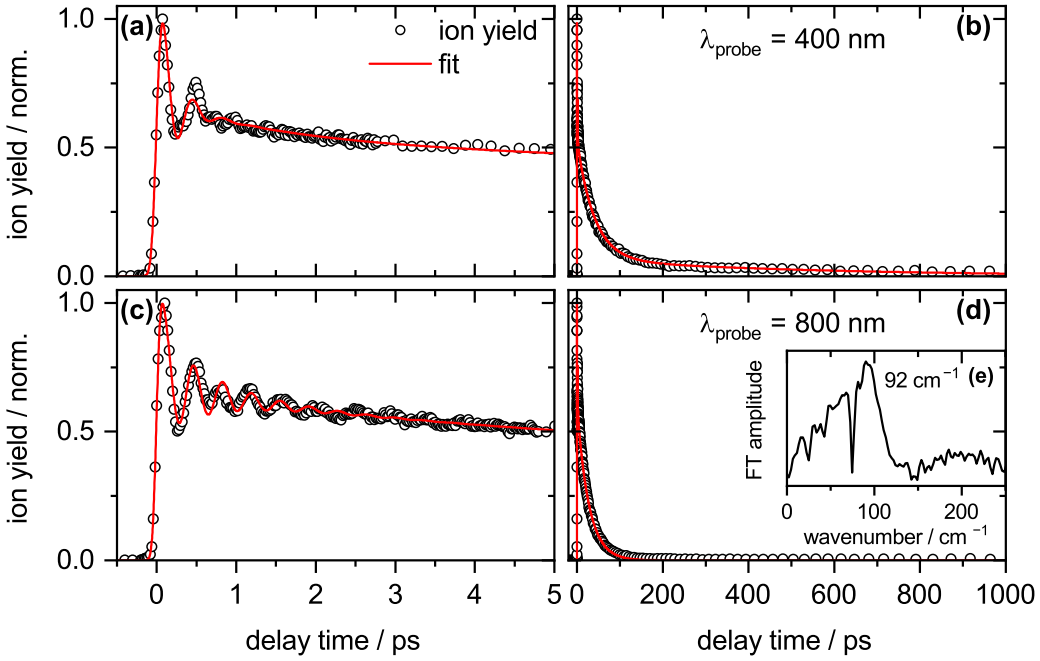

Figure 3.60. Measured transient parent ion yield signals (black circles) and applied fit model functions (red lines) for ClPFB after excitation at $\lambda_{pump} = 260$ nm and ionization at $\lambda_{probe} = 400$ nm **(a–b)** resp. $\lambda_{probe} = 800$ nm **(c–d)**. The left-hand column shows the data in the first five picoseconds, the right-hand column in the first nanosecond after excitation. The fit parameters are listed in Table 3.22. **(e)** Fourier transform of the oscillatory signal component after subtraction of the exponential decay functions.

and

$$\tau_3^{\text{ClPFB}} = 30\text{–}40 \text{ ps}.$$

After ionization at $\lambda_{probe} = 400$ nm a minor long-lived component is observed, described by

$$\tau_4^{\text{ClPFB}}(400 \text{ nm}) = 540 \text{ ps}.$$

Careful inspection of the data at $\lambda_{probe} = 800$ nm reveals that the signal is not decayed to zero at $\Delta t = 300$ ps. Thus, τ_4^{ClPFB} is also observed at 800 nm, but with a negligible amplitude. All fit parameters are listed in Table 3.22.

Origin of the Oscillation

As extensively discussed in Chapter 1 and in the literature,[9,10] the signal oscillations maps the movement of a coherent wavepacket of vibrational modes that mediates coupling between the initially excited S_1 state ($\pi\pi^*$) and a higher-lying $\pi\sigma^*$ state. In the case of ClPFB, the two lowest-lying $\pi\sigma^*$ states exhibit

Table 3.22. Parameters for the fits of the transient parent ion yields of ClPFB after excitation at $\lambda_{pump} = 260$ nm and ionization at either $\lambda_{probe} = 400$ nm or 800 nm. 2σ fit errors are given in parentheses. If no error is given the value was set fixed.

σ_{IRF} fs	A_1 %	τ_1 ps	A_2 %	τ_2 ps	A_3 %	τ_3 ps	A_4 %	τ_4 ps	A_{osc} %	τ_{osc} ps	ν_{osc} cm^{-1}	ϕ_{osc} π
$\lambda_{probe} = 400$ nm												
49(5)	49	$< \sigma_{IRF}$	6(1)	1.45(25)	18(1)	40.3(34)	3(1)	540(250)	24	0.21(2)	87	−0.40
$\lambda_{probe} = 800$ nm												
41(1)	44	$< \sigma_{IRF}$	5(1)	1.56(49)	35(1)	27.24(94)			16(1)	0.66	92	−0.57

nearly identical calculated VEEs, yet different symmetries. While the S_2 state shows $^1B_1$ symmetry, the S_3 state shows $^1A_2$ symmetry. Thus, coupling to the S_1 state ($^1B_2$) is mediated by a_2 and b_1 modes, respectively. Since the deformed molecular structure in the S_1 state transforms according to the b_1 irreducible representation, the coupling between the S_1 and the S_3 state is probably most pronounced. In agreement, the lowest-energy b_1 mode exhibits a frequency of $\nu_{20}^{ClPFB} = 72$ cm^{-1} (cf. Figure 3.59), fitting well to the observed oscillatory frequency of $\nu_{osc}^{ClPFB} = 87$–92 cm^{-1}. Although the lowest-frequency a_2 mode $\nu_{14}^{ClPFB} = 84$ cm^{-1} also fits excellent, the optimized molecular structure shows no influence of a_2 modes. Hence, the coupling to the $^1B_1$ state might be relatively weak. However, influences of the S_2 state on the coupling dynamics are explicitly not ruled out and further high-level calculations might elucidate the role of the S_2 state on the dynamics.

3.8.3 Time-Resolved Photoelectron Images

Shown in Figure 3.61 are the PEI of ClPFB at $\Delta t = 0.02$ ps after excitation at $\lambda_{pump} = 260$ nm and ionization at $\lambda_{probe} = 400$ nm (a), in the first minimum of the parent ion yield at $\Delta t = 0.23$ ps (b), and in the maximum at $\Delta t = 0.44$ ps (c). The respective PES are depicted in Figure 3.62 (a). A broad signal α is followed by a narrow one (β), and the latter peaks at $E_\beta = 0.83$ eV. A distinct center of α cannot be determined. The electron yields of both signals replicate the behavior of the corresponding parent ion yield (cf. Figure 3.62 (b)).

The results of the high-intensity single-color ionization at $\lambda_{probe} = 400$ nm are shown in Figure 3.61 (d) and the corresponding PES in Figure 3.62 (c). In addition to signal β, the PEI exhibits two high-energy signals γ and δ, peaking

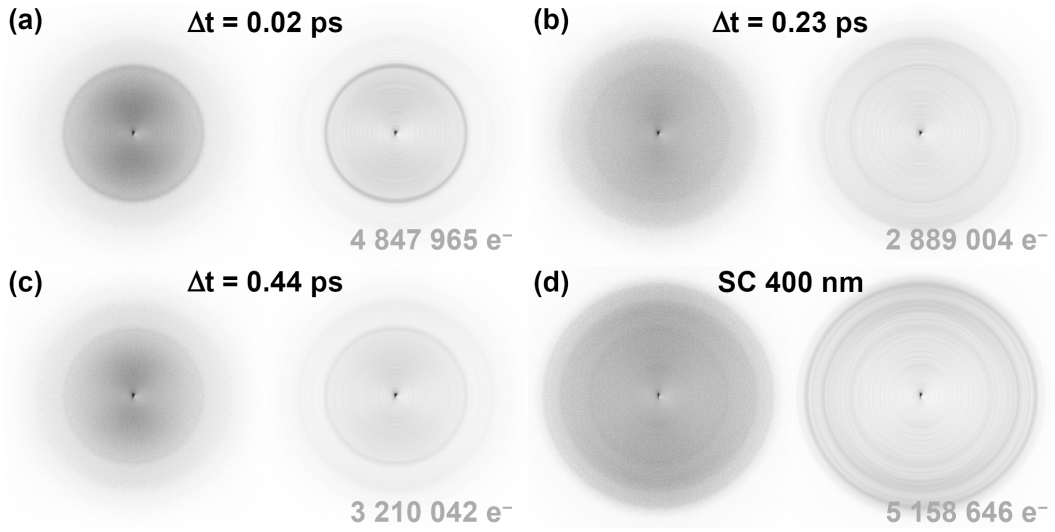

Figure 3.61. Photoelectron images (left) and their corresponding meridional slices through the recovered three-dimensional photoelectron distributions (right) of ClPFB. **(a)** At $\Delta t =$ 0.02 ps after excitation at $\lambda_{\text{pump}} = 260$ nm and ionization at $\lambda_{\text{probe}} = 400$ nm, **(b)** at $\Delta t = 0.23$ ps (minimum of the parent ion yield), and **(c)** at $\Delta t = 0.44$ ps (maximum of the parent ion yield). **(d)** High-intensity single-color photoelectron images obtained at 400 nm.

at $E_\gamma = 1.6$ eV and $E_\delta = 2.2$ eV. Signals γ and δ both feature a broad flank towards lower photoelectron energies.

Ionization Pathways

In agreement with the mechanisms discussed in the previous Sections, the two signals β and α most likely originate from the ionization to the two ionic states D_0 and D_1, respectively. The energy difference of >0.1 eV between the peak energy of β and the onset of α fits well to the energy gap between the D_0 and the D_1 state of ≈0.2 eV (cf. Table 3.21). The absence of additionally arising signals at any delay time indicates that no internal conversion from the initially excited S_1 state to another low-lying excited state takes place.

Based on Equation 3.2 in Section 3.1, the transition energies to the state populated prior to ionization can be calculated, because the narrow width of β suggests an adiabatic transition to the D_0 state and the D_0 AIE is known. The sum of the AIE (9.72 eV[39]) and the peak energy $E_\beta = 0.83$ eV, minus the energy of two probe photons at $\lambda_{\text{probe}} = 400$ nm (2×3.10 eV) yields 4.35 eV (285 nm). As the onset of the S_1 UV absorption band at 4.35 eV (285 nm) and the AEE calculated at CC2 level of theory (4.51 eV) are both in near perfect agreement

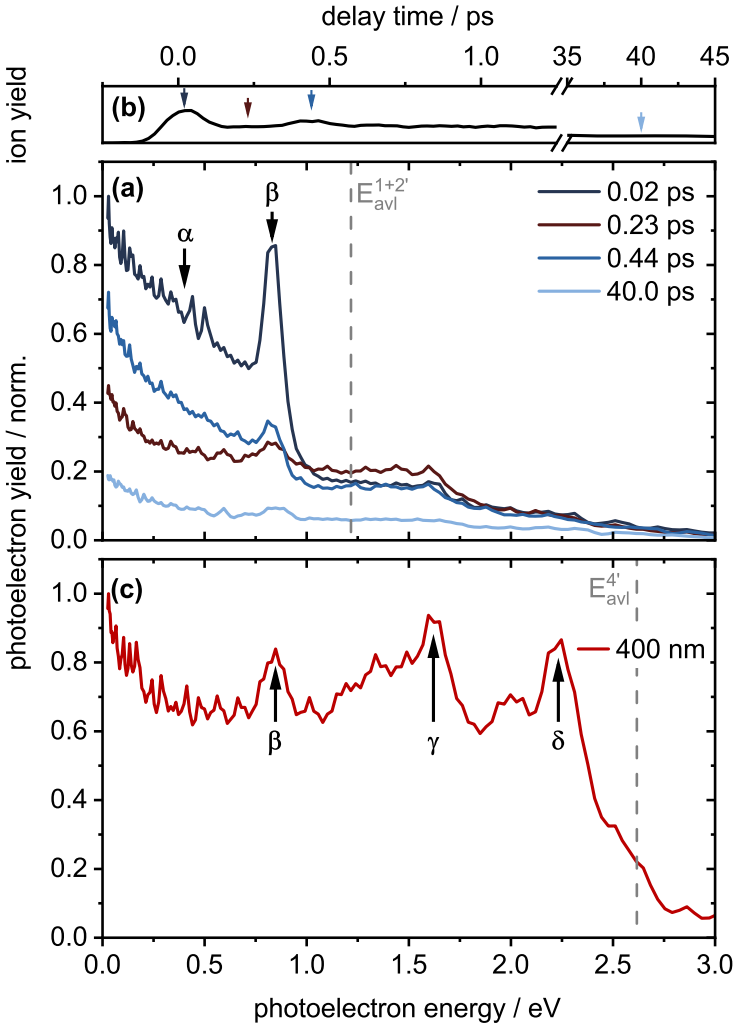

Figure 3.62. **(a)** Transient PE spectra of ClPFB after excitation at $\lambda_{\text{pump}} = 260$ nm and ionization at $\lambda_{\text{probe}} = 400$ nm. The two main photoelectron signals labeled α and β. β peaks at $E_\beta = 0.83$ eV. The grey dotted line indicates the maximum available photoelectron energy $E_{\text{avl}}^{1+2'}$ associated with the $D_0 \leftarrow S_0$ transition by $1+2'$ ionization. **(b)** Corresponding transient parent ion yields adapted from Figure 3.60 (a). Arrows mark the delay time $\Delta t = 0$–40 ps at which the PES were obtained (red at the ion yield minimum). **(c)** Single-color PE spectrum taken at higher 400 nm probe intensities. The additional signals γ and δ are located at $E_\gamma = 1.6$ eV and $E_\delta = 2.2$ eV. The grey dotted line indicates the maximum available photoelectron energies $E_{\text{avl}}^{4'}$ generated by four 400 nm photons.

with the yielded value, the estimated transition energy is probably close to the true S_1 AEE. In contrast to most other molecules in this Thesis, the ionization pathway towards signal β of ClPFB might thus not involve the population of a highly excited intermediate state via absorption of a single probe photon within the probe pulse duration. Nevertheless, the photoelectron distribution of ClPFB is very similar to the PES of the other molecules herein, raising the question if the distributions would be comparable without the population of an intermediate state. If an intermediate state would be excited resonantly, the photoelectron energy might remain largely unaltered, in contrast to the peak width. Such a state would be located at 7.45 eV. According to the conclusions drawn in the previous Sections, the state would likely be a $\pi\pi^*$ state. However, the calculated VEEs of the electronic states up to S_8 do not hint towards a specific state, considering that the excitation energies are rather overestimated than underestimated at the RI-SCS-CC2 level of theory. As the PE band structure is the only evidence pointing towards the excitation of an intermediate state, the direct $D_0 \leftarrow S_1$ transition is preliminarily assumed to be the origin of signal β for now. Yet, it is emphasized that the excitation of an (unknown) intermediate state certainly is a viable option, too. Furthermore, the S_1 state electronically corresponds to both the D_0 and the D_1 state, as shown in Table 3.23. Therefore, band α might be the result of a vertical $D_1 \leftarrow S_1$ transition. The suggested ionization pathways are illustrated in Figure 3.63 (a).

The SC ionization at $\lambda_{\text{probe}} = 400$ nm yields three signals β, γ, and δ, which peak at $E_\beta = 0.83$ eV, $E_\gamma = 1.6$ eV, and $E_\delta = 2.2$ eV, on top of a broad background. Only little photoelectrons with an energy corresponding to the maximum available energy $E_{\text{avl}}^{4'}$ are observed. As a consequence, the direct $D_0 \leftarrow S_0$ transition seems to be a negligible ionization pathway. Band β presumably originates from the two-photon excitation of the S_1 state, followed by ionization to the D_0 state. Signals γ and δ are probably the result of a three-photon excitation of different intermediate states at 8.2 eV and 8.8 eV, respectively, generated by subsequent ionization to the D_0 state. Due to the variety of possible intermediate states, no assignment to any state is made. The broad flank towards lower photoelectron energies of both bands may indicate transitions to the D_1 state, as the reported energy difference between D_0 and D_1 is only of 0.2 eV.[64,112] The proposed SC ionization pathways are shown in Figure 3.63 (b).

Table 3.23. Molecular orbital configuration of ClPFB and their weighted contributions to the first three (electronically excited) neutral and ionic states. Correlations between the neutral and the ionic states according to Koopmans's theorem are given.

neutral state	6 b_1[†] (π)	3 a_2 (π)	7 b_1 (π)	4 a_2 (π^*)	8 b_1 (π^*)	9 b_1 (π^*)	24 a_1 (σ^*)	29 a_1 (σ^*)	30 a_1 (σ^*)	weight (%)	corr. ion. state
S_0 ($^1A_1$)	2	2	2								
S_1 ($^1B_2$, $\pi\pi^*$)	2	2	1	1						41	D_0
	2	1	2		1					38	D_1
	2	1	2			1				18	
S_2 ($^1B_1$, $\pi\sigma^*$)	2	2	1				1			51	
	2	2	1					1		23	D_0
	2	2	1						1	15	
S_3 ($^1A_2$, $\pi\sigma^*$)	2	1	2				1			51	D_1
	2	1	2					1		21	
ionic state											
D_0 ($^2B_1$, π^{-1})	2	2	1								
D_1 ($^2A_2$, π^{-1})	2	1	2							98	
D_2 ($^2B_1$, π^{-1})	1	2	2							86	

[†] HOMO−3

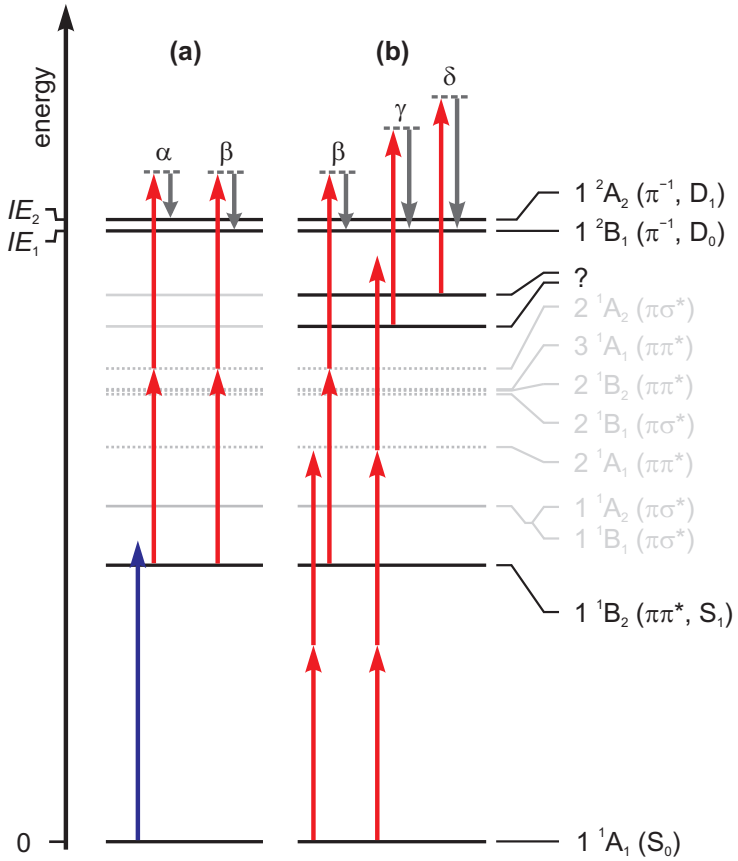

Figure 3.63. Proposed multi-color and single-color ionization schemes for ClPFB. The energies of the photons at $\lambda_{pump} = 260$ nm (blue) and $\lambda_{probe} = 400$ nm (red) and of the photoelectrons (grey) are depicted as vertical arrows. Solid black horizontal lines: experimentally intermediate and final states, solid and dotted (calculated values) grey horizontal lines: non-participating other intermediate states. **(a)** Transient ionization pathways by one-photon absorption to the S_1 state ($1\ ^1B_2$) and subsequent two-photon ionization to the D_0 ($1\ ^2B_1$) and D_1 states ($1\ ^2A_2$) showing the origin of PE peaks α and β. **(b)** Single-color ionization pathways at $\lambda_{probe} = 400$ nm to the D_0 state showing the origin of PE peaks β, γ, and δ.

3.9 Bromopentafluorobenzene

3.9.1 Molecular and Electronic Structure

The gas-phase UV absorption spectrum of BrPFB is shown in Figure 3.64. Three bands are observed. Starting at 290 nm (4.28 eV), the first band peaks at 262 nm (4.73 eV). The band merges with the second band peaking at 241 nm (5.15 eV). A third band rises at wavelengths <220 nm (>5.64 eV).

To assign the bands to electronic transitions, the VEEs to the first eight electronic states were calculated at RI-SCS-CC2 level of theory. The results are listed in Table 3.24. The S_1 state ($\pi\pi^*$, 1 $^1B_2$) exhibits a calculated VEE of 4.99 eV (249 eV). The S_1 state is followed by two $\pi\sigma^*$ states, S_2 (1 $^1B_1$) and S_3 (1 $^1A_2$), at 5.43 eV (228 nm) and 5.66 eV (219 nm), respectively. A VEE of 6.21 eV (200 nm) is estimated to the second $\pi\pi^*$ state S_4 (2 $^1A_1$). All other states exhibit VEEs of more than 6.5 eV.

Based on the calculations, the first band is assigned to the S_1 state. In the literature, the second band was assigned to the S_2 state.[113] Although the calculated oscillator strength of the S_2 state is lower than the one of the S_1 state, the second band is more intense than the S_1 absorption. This discrepancy probably emerges due to intensity borrowing of the S_2 state from the S_1 state, as was discussed for PFPh.[68] Albeit the same may also apply for the S_3 state, no separate absorption band is observed. The third band originates from the absorption of the S_4 state.[113] The calculated VEEs marginally overestimate the experimental VEEs, as is expected, since the CC2 method is known for overestimating the transition energies in fluorobenzenes.[9,10]

Optimization of the molecular structure in the ground state yielded a planar configuration. In contrast, excitation to the S_1 state results in an out-of-plane deformation, as depicted in Figure 3.65. Four carbon atoms 2, 3, 5, and 6 are spanning a plane in the excited state. Br-11 and F-10 are bent out-of-plane by 21° and 23°, respectively. F-8/12 and F-9/11 are bent out-of-plane by −9° and −8°, respectively, in the opposed direction. The structure in the S_1 state therefore exhibits b_1 symmetry. Moreover, illustrations of the displacement vectors out-of-plane vibrational modes and the respective calculated frequencies in the S_1 state are given Figure 3.65, too. A comprehensive list of all vibrational frequencies can be found in Table B.9 in the appendix.

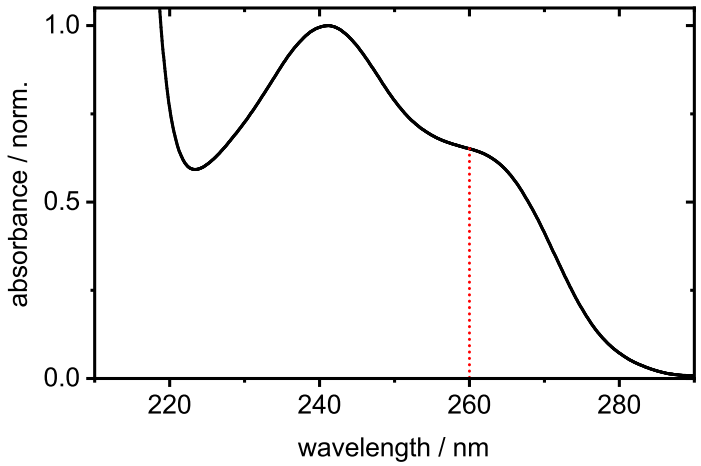

Figure 3.64. Normalized gas-phase UV absorption spectrum of BrFB. The dotted red line indicates the chosen excitation wavelength of $\lambda_{\text{pump}} = 260$ nm to excite the S_1 state ($\pi\pi^*$).

Table 3.24. Vertical excitation energies (VEE) and oscillator strengths f (in parentheses) of the first eight neutral electronically excited states, the ionic ground state and the first two ionic electronically excited states for BrPFB, calculated at RI-SCS-CC2 level of theory. Where available, the respective adiabatic energy (AEE) is listed. Experimental energies are given if possible.

	symm.	calc. VEE eV	calc. AEE eV	exp. VEE eV	exp. AEE eV
S_1 ($\pi\pi^*$)	$1\,^1B_2$	4.99 (0.0050)	4.48	4.73[a,†]	4.37[†]
S_2 ($\pi\sigma^*$)	$1\,^1B_1$	5.43 (0.0014)		5.15[a,†]	
S_3 ($\pi\sigma^*$)	$1\,^1A_2$	5.66 (0.0000)			
S_4 ($\pi\pi^*$)	$2\,^1A_1$	6.21 (0.1221)		6.10[a]	
S_5 ($\pi\sigma^*$)	$2\,^1B_1$	6.57 (0.0024)			
S_6 ($\pi\sigma^*$)	$2\,^1B_2$	6.63 (0.0000)			
S_7 ($\pi\pi^*$)	$3\,^1A_1$	7.09 (0.7834)		6.83[a]	
S_8 ($\pi\pi^*$)	$3\,^1B_2$	7.12 (0.4840)			
D_0 (π^{-1})	$1\,^2B_1$	9.77	9.53		9.68[a]
D_1 (π^{-1})	$1\,^2A_2$	10.09		10.04[a]	
D_2 (n^{-1})	$2\,^2B_2$	11.69		11.49[a]	

[a] Ref. [113] [†] this work

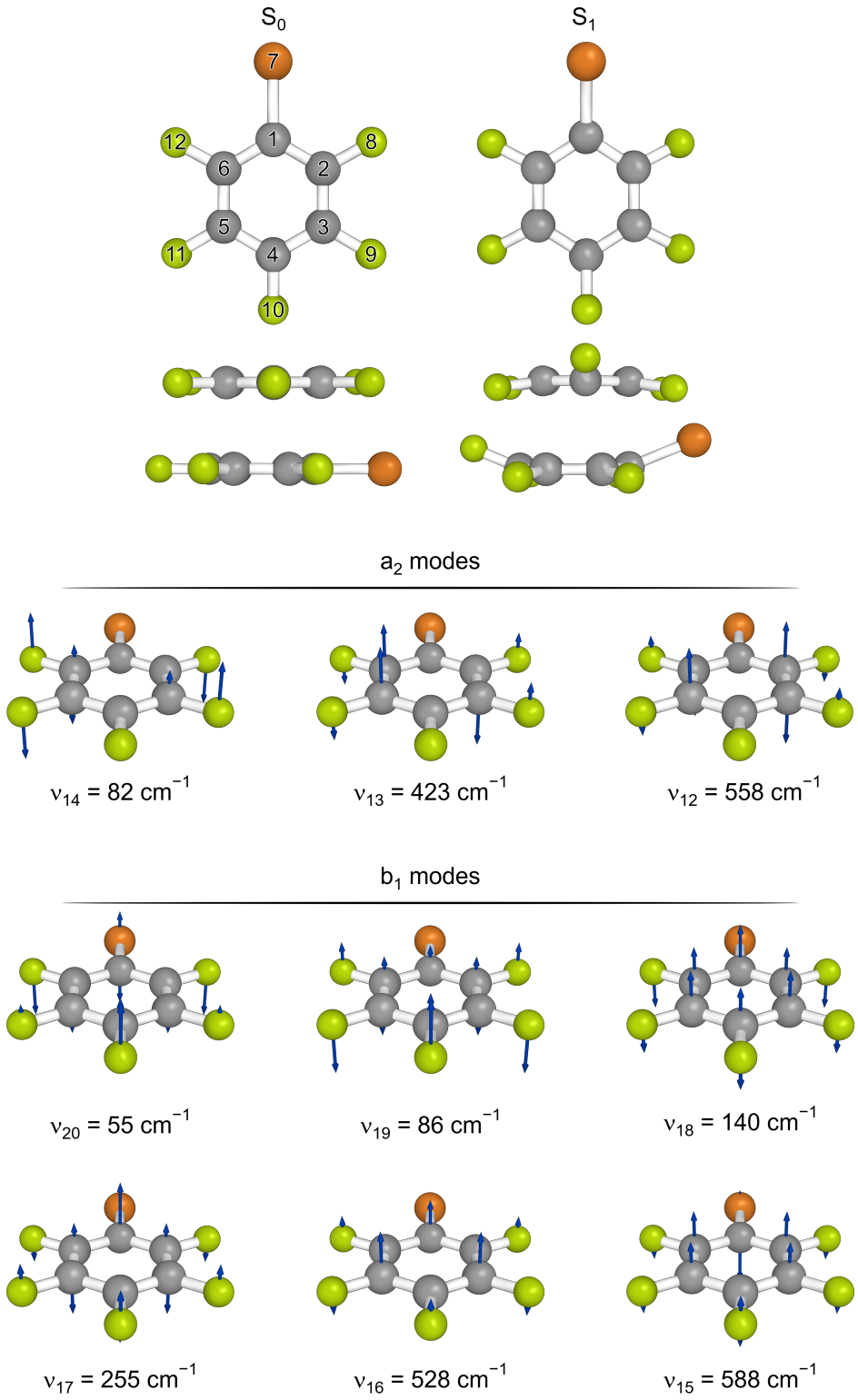

Figure 3.65. Calculated molecular structures of BrPFB in the S_0 and the S_1 state ($\pi\pi^*$), optimized at the RI-SCS-MP2 and RI-SCS-CC2 levels of theory, respectively. The calculated displacement vectors of the out-of-plane modes are illustrated by blue arrows. Their respective frequencies in the S_1 state are listed.

In addition to the neutral states, the VIEs to the first three ionic states were calculated. The ionic ground state D_0 ($1\ ^2B_1$) exhibits a calculated VIE of 9.77 eV. A VIE of 10.09 eV was calculated to the D_1 state ($1\ ^2A_2$). Both states show π^{-1} character, in contrast to the n^{-1} state D_2 ($2\ ^2B_2$), which is located at 11.69 eV. No experimental VIE for the D_0 state was reported, yet the experimental VIEs of the other two ionic states are in near perfect agreement with the calculated values (cf. Table 3.24).

The molecular structure in the D_0 state is planar (not shown for the sake of brevity). The AIE from the neutral to the ionic ground state was calculated to be 9.53 eV, which underestimates the actual AIE of 9.68 eV.[113]

3.9.2 Time-Resolved Time-of-Flight Mass Spectra

As shown in the TOF-MS in Figure 3.66 (a), BrPFB differs from the other fluorobenzenes. While the parent ion still exhibits the highest intensity, dissociation of the C-Br bond forms the $[BrPFB{-}Br]^+$ fragment after excitation at $\lambda_{pump} = 260$ nm and ionization at $\lambda_{pump} = 400$ nm. Further fragmentation is observed, but will not be addressed herein. Time-resolved mapping of the ion yield reveals that the majority of the parent ion decays ultrafast, as shown in Figure 3.66 (b–c). In excellent agreement, Borg et al. previously reported the decay to be faster than $\Delta t = 0.3$ ps.[66] Compared to their work, the time resolution of $\sigma_{IRF} = 50$ fs in this Thesis allows the observation of a shallow shoulder of the signal decay at a delay time of $\Delta t = 0.2$ ps. Although the signal is essentially completely decayed within few hundred femtoseconds, a very low-amplitude signal is observed at later times. The decay was fitted with three exponential decay functions

$$\tau_1^{BrPFB} = 0.05 \text{ ps},$$
$$\tau_2^{BrPFB} = 0.18 \text{ ps}$$

and

$$\tau_3^{BrPFB} = 770 \text{ ps}.$$

The shoulder was accounted for by adding a highly damped oscillation at $\nu_{osc}^{BrPFB} = 111\ cm^{-1}$ with $\tau_{osc}^{BrPFB} = 0.18$ ps. All constants were set fixed and are listed in Table 3.25.

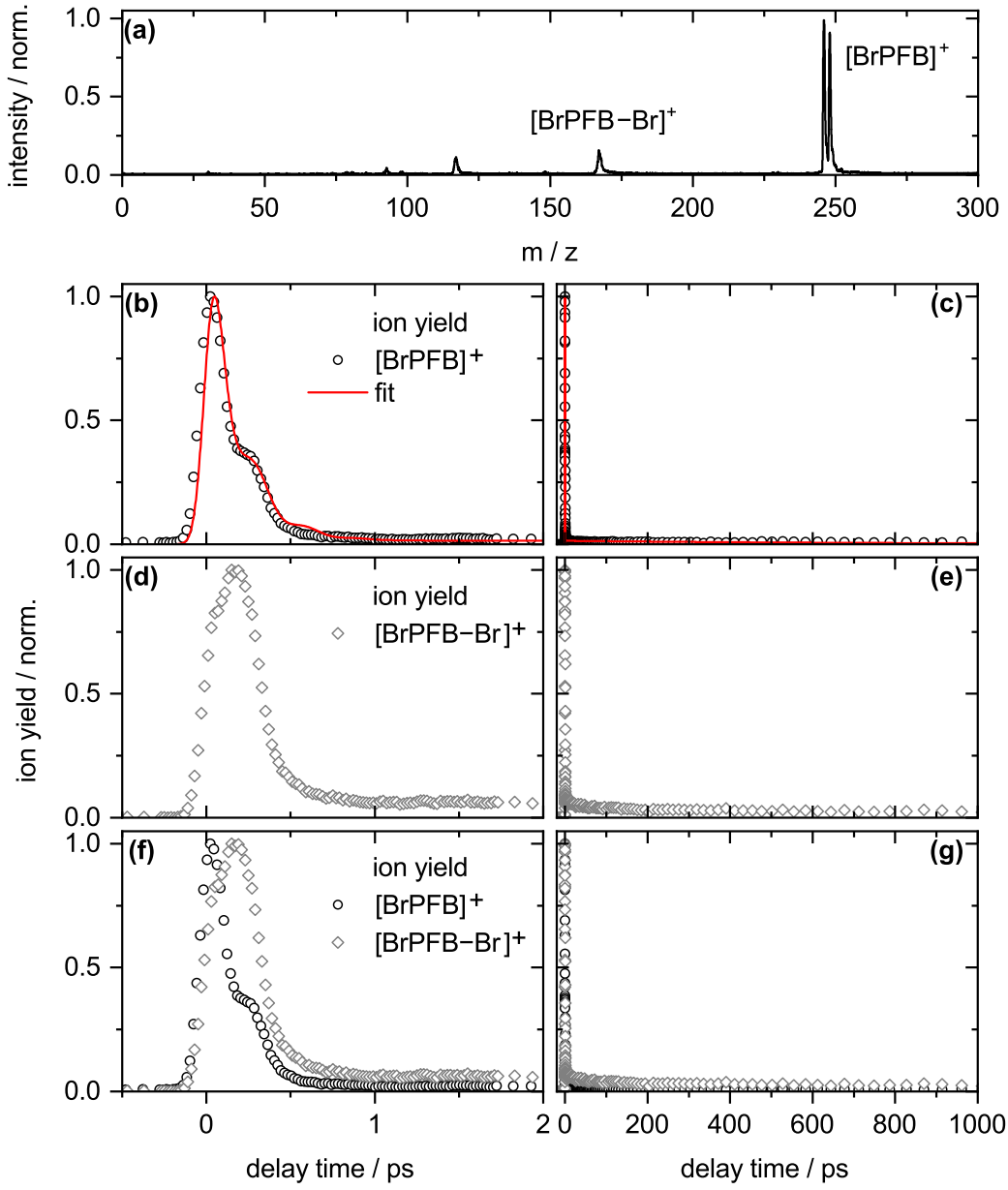

Figure 3.66. **(a)** TOF-MS of BrPFB at $\Delta t = 0$ ps after excitation at $\lambda_{\text{pump}} = 260$ nm and ionization at $\lambda_{\text{pump}} = 400$ nm. **(b–c)** Measured transient parent ion yield signals (black circles) and applied fit model functions (red lines) for the BrPFB parent ion. The left-hand column shows the data in the first two picoseconds, the right-hand column in the first nanosecond after excitation. The fit parameters are listed in Table 3.25. **(d–e)** Measured transient ion yields of the $[\text{BrPFB}{-}\text{Br}]^+$ ion (grey diamonds). **(f–g)** Comparison of the transient ion yields of the BrPFB parent ion (black circles) and the $[\text{BrPFB}{-}\text{Br}]^+$ ions (grey diamonds).

Table 3.25. Parameters for the fits of the transient parent ion yields of BrPFB after excitation at $\lambda_{pump} = 260$ nm and ionization at $\lambda_{probe} = 400$ nm. The values were set fixed.

σ_{IRF} fs	A_1 %	τ_1 ps	A_2 %	τ_2 ps	A_4 %	τ_4 ps	A_{osc} %	τ_{osc} ps	ν_{osc} cm^{-1}	ϕ_{osc} π
50	15	0.05	62	0.18	1	770	22	0.18	111	−0.08

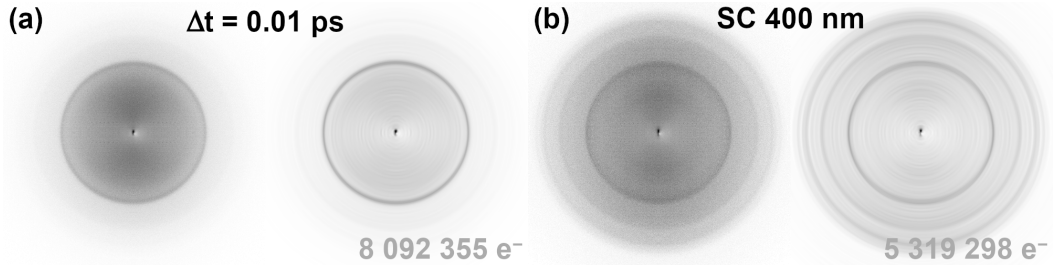

Figure 3.67. Photoelectron images (left) and their corresponding meridional slices through the recovered three-dimensional photoelectron distributions (right) of BrPFB. **(a)** At $\Delta t = 0.01$ ps after excitation at $\lambda_{pump} = 260$ nm and ionization at $\lambda_{probe} = 400$ nm. **(b)** High-intensity single-color photoelectron images obtained at 400 nm.

The ion yield of the $[BrPFB{-}Br]^+$ fragment decays ultrafast too, as shown in Figure 3.66 (d–e). However, the ion yield of the fragment exhibits a delayed rise compared to the parent ion yield, as shown in Figure 3.66 (f–g), and its signal is most intense at the delay time corresponding to the emerging shoulder in the parent ion yield. Afterwards, the fragment ion yield rapidly decays. These decay patterns are discussed in Subsection 3.9.4 in light of the results of the photoelectron imaging.

3.9.3 Time-Resolved Photoelectron Images

The PEI of BrPFB at $\Delta t = 0.01$ ps after excitation at $\lambda_{pump} = 260$ nm and ionization at $\lambda_{probe} = 400$ nm is shown in Figure 3.67 (a). One broad and a narrow signal are observed. No clear center can be determined for the broad signal α, while β peaks at $E_\beta = 0.89$ eV, as shown in the PES in Figure 3.68 (a). The electron yield decreases rapidly, in agreement with the ion yield.

The high-intensity single-color ionization at $\lambda_{probe} = 400$ nm yields three signals in the PEI, displayed in Figure 3.67 (b), one of which is β. The two higher-energy signals γ and δ peak at $E_\gamma = 1.7$ eV and $E_\delta = 2.3$ eV, as depicted in the PES in Figure 3.68 (c).

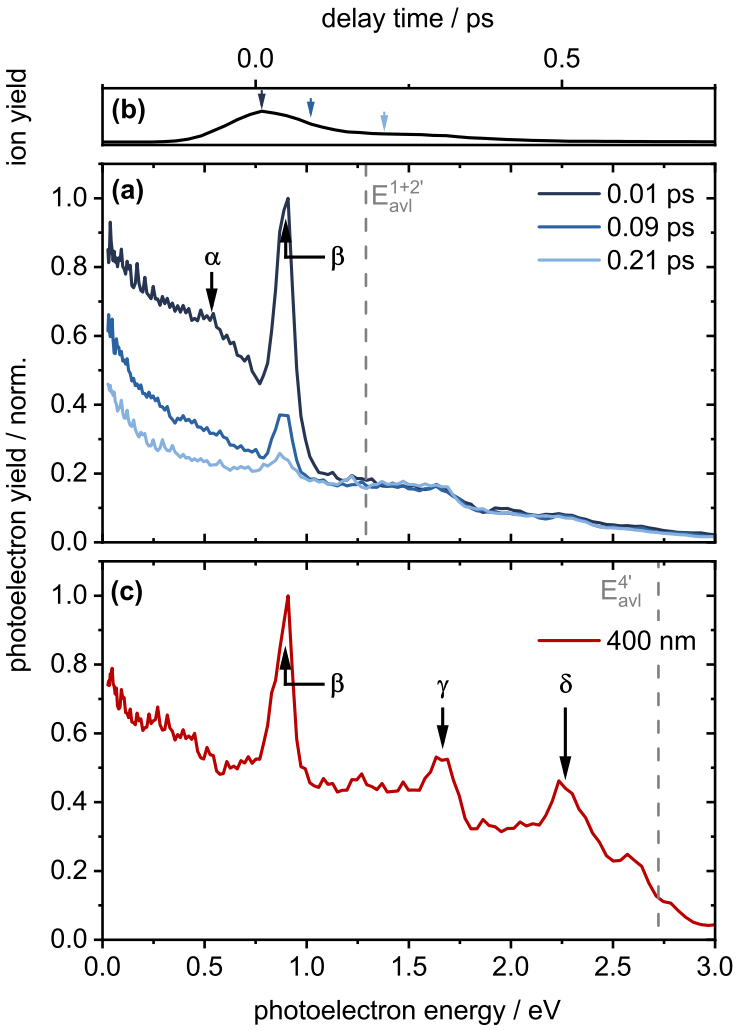

Figure 3.68. **(a)** Transient PE spectra of BrPFB after excitation at $\lambda_{pump} = 260$ nm and ionization at $\lambda_{probe} = 400$ nm. Two main photoelectron signals labeled α and β are observed. Signal β peaks at $E_\beta = 0.89$ eV. The grey dotted line indicates the maximum available photoelectron energy $E_{avl}^{1+2'}$ associated with the $D_0 \leftarrow S_0$ transition by $1 + 2'$ ionization. **(b)** Corresponding transient parent ion yields adapted from Figure 3.66 (a). Arrows mark the delay time $\Delta t = 0$–0.21 ps at which the PES were obtained. **(c)** Single-color PE spectrum taken at higher 400 nm probe intensities. The additional signals γ and δ are located at $E_\gamma = 1.7$ eV and $E_\delta = 2.3$ eV. The grey dotted line indicates the maximum available photoelectron energies $E_{avl}^{4'}$ generated by four 400 nm photons.

Ionization Pathways

The two signals α and β in the time-resolved PES are assigned to transitions to the ionic states D_1 and D_0, respectively. The energy difference of ≈0.2 eV between the peak energy of β and the onset of α fits well to the energy gap of ≈0.3 eV[113] between the two ionic states. Since no additional signals arise at any delay time, no other state than the initially excited S_1 state is populated during the decay process.

The narrow width of β indicates an adiabatic transition to the D_0 state. Therefore, the adiabatic excitation energy of the state populated prior to ionization can be calculated, based on Equation 3.2 in Section 3.1. The sum of the peak energy $E_\beta = 0.89$ eV and the AIE to the D_0 state of 9.68 eV[113] minus the energy of two photons at $\lambda_{\text{probe}} = 400$ nm (2×3.10 eV) yields 4.37 eV (284 nm). The energy fits well with the onset of the S_1 UV absorption band at 4.28 eV (290 nm) and the AEE calculated at RI-SCS-CC2 level of theory of 4.48 eV (277 nm). Therefore, the value probably is close to the true AEE. However, for most other molecules in this work an intermediate state is populated by absorption of a single probe photon within the probe pulse duration. Such an intermediate state would be located at 7.47 eV, fitting well to the so-called "Band I" rising at 7.2 eV observed in photoabsorption experiments by Deprez et al.[113] As a consequence, it should not categorically ruled out that an intermediate state is (resonantly) excited within the probe pulse duration. Although the authors did not address the electronic character of the underlying transition towards "Band I" and the calculations in this work do not hint towards a specific state, the potential intermediate state is probably a $\pi\pi^*$ state, in agreement with the results on other fluorobenzenes.[36,38]

The S_1 state electronically corresponds to both the D_0 and the D_1 state, as shown in Table 3.26. Thus, signal α might be the result of a vertical $D_1 \leftarrow S_1$ transition. Alternatively, the ionization pathway also includes excitation of an intermediate state.

The appearance of band β in the SC ionization at $\lambda_{\text{probe}} = 400$ nm indicates a two-photon transition to the S_1 state, followed by ionization to the D_0 state. A signal corresponding to band α likely vanishes in the broad background. The additional bands γ and δ at $E_\gamma = 1.7$ eV and $E_\delta = 2.3$ eV presumably are the result of a three-photon excitation of two intermediate states. These states would be located at 8.3 eV and 8.8 eV, fitting well to "Band II" (8.1 eV) and "Band IV" (8.8 eV), reported by Deprez et al.[113] The myriad of states with transition energies >7 eV prohibits assignment of any signal to a specific electronic state.

Table 3.26. Molecular orbital configuration of BrPFB and their weighted contributions to the first three (electronically excited) neutral and ionic states. Correlations between the neutral and the ionic states according to Koopmans's theorem are given.

neutral state	18 b_2 (π)	4 a_2 (π)	9 b_1 (π)	10 b_1 (π^*)	11 b_1 (π^*)	5 a_2 (π^*)	28 a_1 (σ^*)	29 a_1 (σ^*)	32 a_1 (σ^*)	weight (%)	corr. ion. state
S_0 ($^1A_1$)	2	2	2								
	2	1	2		1					41	D_1
S_1 ($^1B_2$, $\pi\pi^*$)	2	2	1			1				39	D_0
	2	1	2	1						16	D_1
S_2 ($^1B_1$, $\pi\sigma^*$)	2	2	1				1			37	D_0
	2	2	1						1	34	
	2	1	2				1			37	
S_3 ($^1A_2$, $\pi\sigma^*$)	2	1	2						1	24	D_1
	2	1	2					1		17	
ionic state											
D_0 ($^2B_1$, π^{-1})	2	2	1								
D_1 ($^2A_2$, π^{-1})	2	1	2							97	
D_2 ($^2B_2$, n^{-1})	1	2	2							97	

The subsequent ionization is assumed to lead to the D_0 state. The proposed ionization pathways for both the transient ionization, as for the SC ionization are depicted in Figure 3.69.

3.9.4 Dissociation of BrPFB

BrPFB is the only molecule in this Thesis with a pronounced fragmentation pattern in the TOF-MS. Likewise, BrPFB is also the only molecule herein for which the majority of the ion yield decays within the first $\Delta t = 1$ ps. Therefore, both properties most likely are connected. Indeed, calculation of the potential energy curves with respect to the C-Br bond distance revealed a dissociative pathway in the neutral state.[66] However, the authors attributed the bond fission to an internal conversion to a dissociative $\pi\sigma^*$ state. In the PES no band rises in at any delay time, indicating no direct conversion from the initially excited S_1 to another state takes place. Considering that the authors solely scanned the changes of the potential energy along the C-Br bond length, the vibronic coupling between the S_1 and the higher-lying states is not accounted for. Such a coupling substantially mixes the electronic characters of the states involved. The deformation of the optimized molecular structure in the S_1 strongly hints towards coupling between the S_1 state ($^1B_2$) and the S_3 state ($^1A_2$) via b_1 modes. The shoulder in the parent ion yield decay might even be part of an oscillation pattern, yet the ultrafast signal decay may prevent resolving a complete oscillational period. Thus, the dissociation probably happens on the potential energy hypersurface of a mixed $\pi\pi^*$–$\pi\sigma^*$ state, without the need for a distinct internal conversion. Whether this pathway actually leads to dissociation needs to be verified in additional dynamics simulations.

Although the observed fragments appear to be a direct product of the proposed dissociation, the underlying formation mechanism probably is different. If the fragment ions were generated following dissociation in the neutral state, the corresponding photoelectrons should emerge in the PES as a separate signal. As no additional signal arises at any delay time in the PES, the fragmentation presumably happens in the ionic state. Yet, it is assumed that the evolution on the S_1 potential energy hypersurface facilitates the dissociation in the ionic state. The initial absorption of a pump photon promotes previously planar molecules from the S_0 to the S_1 state. If there is no delay time between the pump and the probe pulses, i.e., $\Delta t = t_0$, the excited quasi-planar molecules are ionized to

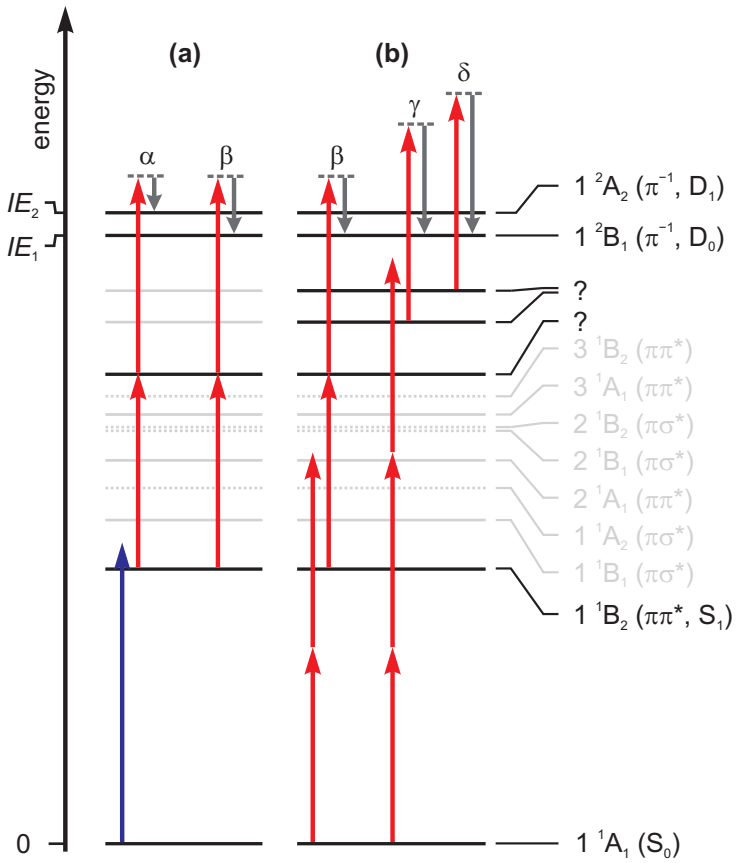

Figure 3.69. Proposed multi-color and single-color ionization schemes for BrPFB. The energies of the photons at $\lambda_{\text{pump}} = 260$ nm (blue) and $\lambda_{\text{probe}} = 400$ nm (red) and of the photoelectrons (grey) are depicted as vertical arrows. Solid black horizontal lines: experimentally intermediate and final states, solid and dotted (calculated values) grey horizontal lines: non-participating other intermediate states. **(a)** Transient ionization pathways by one-photon absorption to the S_1 state (1 $^1B_2$) and subsequent two-photon ionization to the D_0 (1 $^2B_1$) and D_1 states (1 $^2A_2$) showing the origin of PE peaks α and β. **(b)** Single-color ionization pathways at $\lambda_{\text{probe}} = 400$ nm to the D_0 state showing the origin of PE peaks β, γ, and δ.

the ionic states, either directly or via excitation of an intermediate state. Since the fragment ion yield is low at t_0, the fragmentation in the ionic state seems to be unfavorable and mainly parent ions are detected. Shortly after t_0, structural and possibly electronic changes in the S_1 state occur, indicated by the deformed molecular equilibrium structure in the S_1 state (*vide supra*). These changes are transferred to the ionic states which enables very efficient ultrafast dissociation, i.e., the parent ions instantaneously dissociate and the parent ion yield decreases while the fragment ion yield increases. However, ultimately the dynamics in the S_1 state lead to bond breaking in the neutral molecules. The subsequent ionization of the fragments seems to be prohibited at the employed wavelengths. Therefore, both the ion yield of the parent ion and of the fragments rapidly decay. Future studies directly probing, e.g., the bromine atoms[114,115] might allow to gain a deeper insight into these dynamics. As unraveling the dissociation pathway of BrPFB is beyond the scope of this work, it is emphasized that these considerations are very preliminary.

3.10 Comparison of the Calculated Properties and Molecular Dynamics

3.10.1 Molecular and Electronic Structures

An overview of the UV absorption spectra of all nine studied molecules is provided in Figure 3.70. All molecules exhibit a prominent, mostly structureless absorption band centered around 260 nm, though the bands of 1,2,3-TriFB and 1,2,4,5-TFB are slightly shifted towards 250 nm and ≈265 nm, respectively. In addition, the absorption band of 1,2,4,5-TFB is distinctly structured, probably due to the lack of rapid changes of the molecular and electronic structure upon excited state population compared to the other molecules (*vide infra*). The observed peaks correspond to transitions to the fundamental and overtones of the totally symmetric ν_4 mode (cf. Table B.2).[33,35] In the case of the PFB derivatives, the first bands are followed by at least one additional intense absorption band between 250 nm and 210 nm. For all molecules another band arises below 210 nm.

To assign the observed absorption bands, the vertical excitation energies to the excited states were calculated at RI-SCS-CC2 level of theory. Figure 3.71 illustrates the calculated excited state transition energies to the S_1–S_4 states of all addressed molecules (up to the S_5 state for PFPy, owing to the additional $n\pi^*$ state). The first excited state S_1 of any molecule is of $\pi\pi^*$ character and transitions to these states form the first absorption bands. The calculated VEEs are consistently blue-shifted compared to the actual transition energies, in line with the previously reported observation that CC2 tends to overestimate the transition energies in PFB.[9,10] Nevertheless, the calculations correctly predict the $\pi\pi^*$ transition energy for 1,2,4,5-TFB to be the lowest of all molecules and to be the highest for 1,2,3-TriFB. The substitution pattern has essentially no influence on the transition energies to the S_1 states, in excellent agreement with earlier findings.[36,38]

The second excited states are estimate to be, predominantly optically dark, $\pi\sigma^*$ states for every molecule herein, except for 1,2,3-TriFB for which a second $\pi\pi^*$ state is the S_2 state. The more hydrogen atoms are substituted by fluorine atoms, the lower in energy the $\pi\sigma^*$ states become. The reason for this stabilization is the so-called perfluoro effect,[56,116,117] introduced in Chapter 1. In the $\pi\sigma^*$ states, the electron density is mainly located at the fluorine atoms and not in the conjugated π systems any more (cf. Figure 3.4 in Section 3.1). The VEE

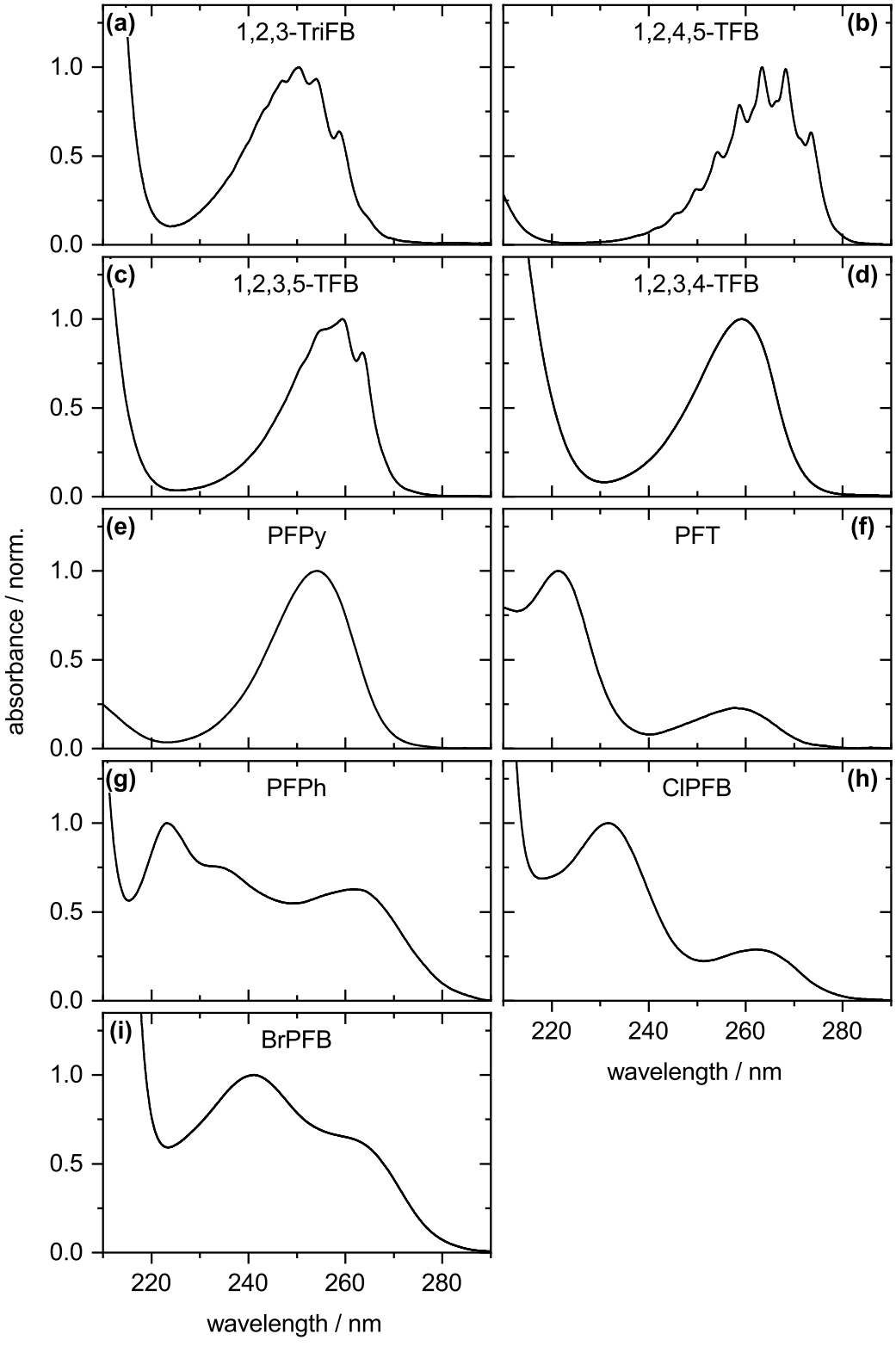

Figure 3.70. Normalized gas-phase UV absorption spectrum of **(a)** 1,2,3-TriFB, **(b)** 1,2,4,5-TFB, **(c)** 1,2,3,5-TFB, **(d)** 1,2,3,4-TFB, **(e)** PFPy, **(f)** PFT, **(g)** PFPh, **(h)** ClPFB, and **(i)** BrPFB.

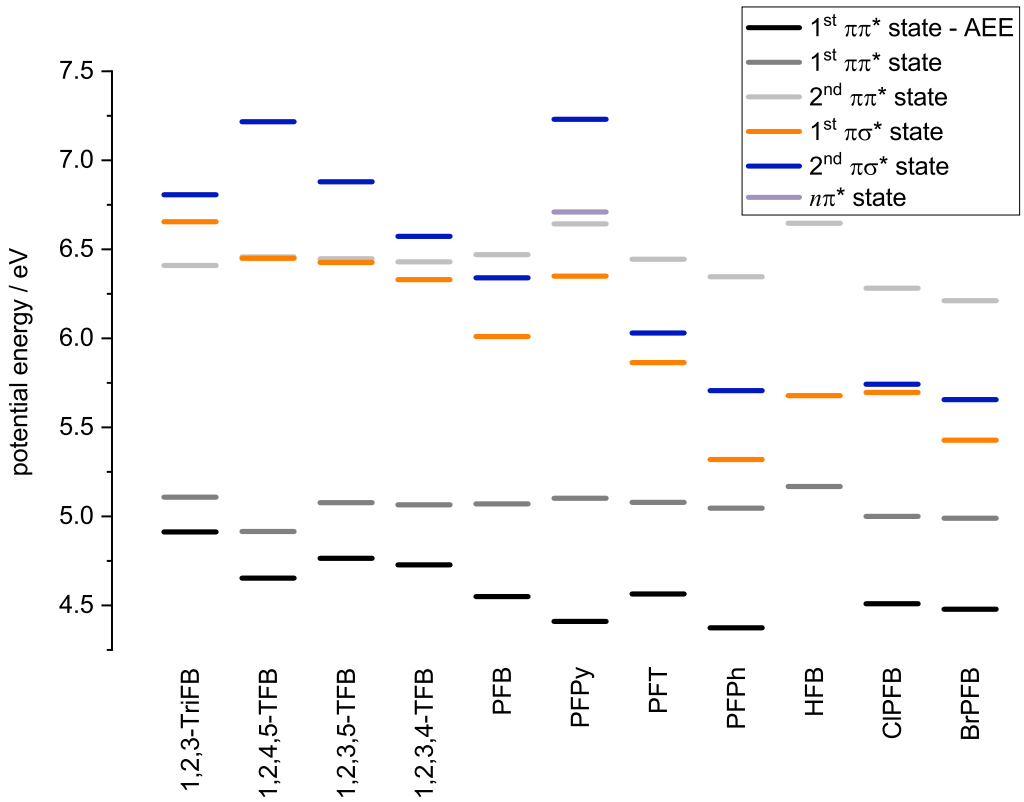

Figure 3.71. Calculated vertical excitation energies to the first (dark grey) and second $\pi\pi^*$ states (light grey), and to the first (orange) and second $\pi\sigma^*$ states (blue), calculated at RI-SCS-CC2 level of theory. In black are the adiabatic excitation energies to the first $\pi\pi^*$ states. PFPy exhibits an additional $n\pi^*$ state (purple). The transition energies for PFB were adapted from earlier work.[9] For HFB the VEEs were calculated by Mondal et al.[14] at EOM-CCSD level of theory. The first two $\pi\sigma^*$ states of HFB are degenerate and no S_1 AEE was reported.

gap between the S_1 ($\pi\pi^*$) and the first $\pi\sigma^*$ state decreases from 1.7 eV for 1,2,3-TriFB to ≈0.9 eV[9] for PFB. Introducing an additional substituent for the sixth hydrogen atom leads to further decrease of the energy differences to, e.g., 0.44 eV for BrPFB. In the case of the $\pi\sigma^*$ states of PFPh, significant portions of the electron density is drawn to the hydroxy group, and the small energy gap of 0.27 eV between the S_1 and the S_2 state is thus attributable to the somewhat altered electronic character compared to the $\pi\sigma^*$ states of the other molecules. The second $\pi\sigma^*$ states experience analogous stabilization, and while the S_1 ($\pi\pi^*$) and the second $\pi\sigma^*$ state of 1,2,4,5-TFB are separated by 2.30 eV, the gap is reduced to 0.67 eV for BrPFB. Although the states are mostly optically dark, pronounced intensity borrowing from the lower-lying $\pi\pi^*$ states enables intense transitions to the $\pi\sigma^*$ states for the PFB derivatives,[14,68] and the additional absorption bands between 250 nm and 210 nm are therefore ascribed to the $\pi\sigma^*$ states. Presumably, the larger energy gaps between the $\pi\pi^*$ and the $\pi\sigma^*$ states hinder likewise processes for the other molecules.

In agreement with the observations for the first $\pi\pi^*$ states, the transition energies to the second $\pi\pi^*$ states are again near constant, and the bands rising in at wavelengths shorter than 210 nm are assigned to these states.

Optimizations of the molecular structures yielded planar configurations in the neutral and ionic ground states and substantial out-of-plane deformations in the S_1 states. The latter are illustrated in Figure 3.72. For most systems at least one of the fluorine atoms is considerably bent out of the carbon ring plane, typically by more than 25°. In contrast, a rather small deformation is predicted for 1,2,4,5-TFB, with the fluorine atoms bent out of the plane by less than 10°. Accurate experimental adiabatic excitation energies are scarce, but were available, the calculated AEEs based on the structures also consistently overestimate the actual AEEs, as for the VEEs.

3.10.2 Time-Resolved Time-of-Flight Mass Spectra

Shortly summarizing the results of the transient parent ion yields, eight different fluorobenzenes and pentafluoropyridine were excited at $\lambda_{pump} = 260$ nm (250 nm for 1,2,3-TriFB and 255 nm for PFPy) and subsequently ionized at either $\lambda_{probe} = 400$ nm or $\lambda_{probe} = 800$ nm (except for PFPy and BrPFB). In addition, the dynamics of the three TFB isomers and PFPh were studied upon excitation at $\lambda_{pump} = 265$–255 nm and $\lambda_{pump} = 265$–219 nm, respectively. An overview of

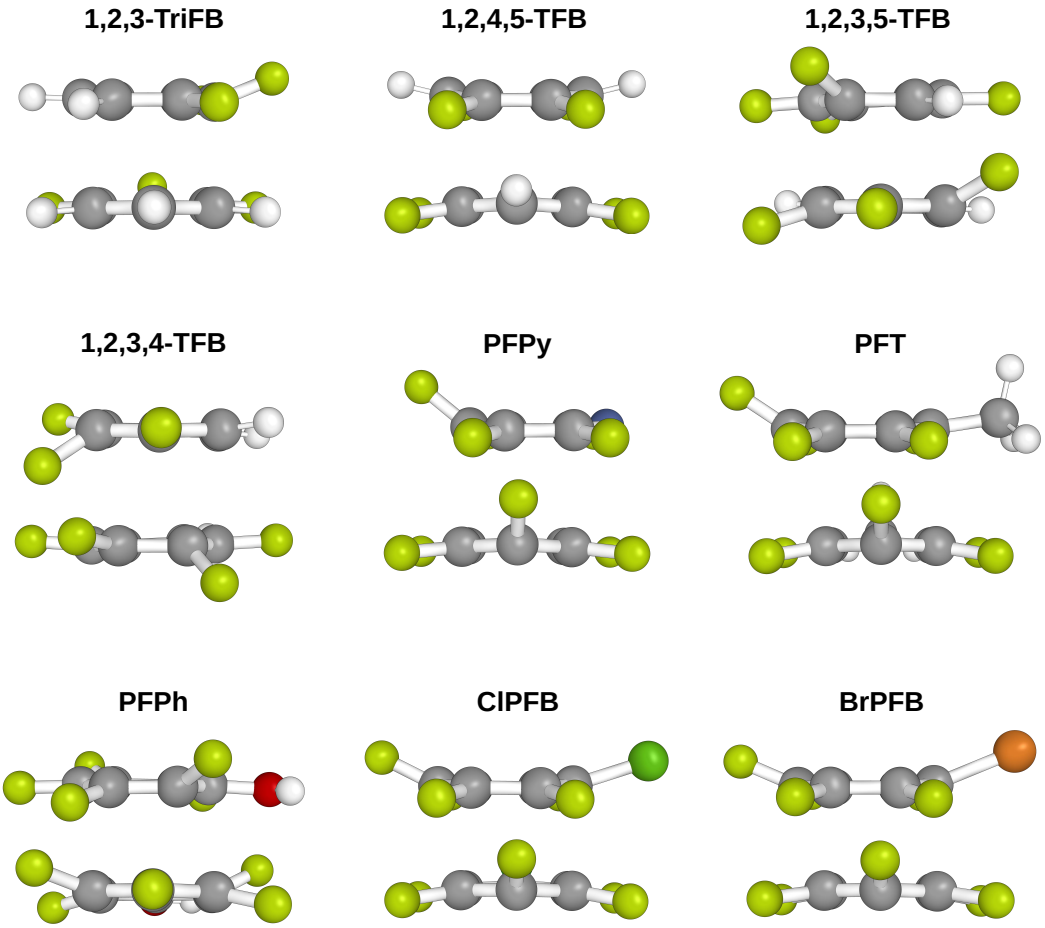

Figure 3.72. Overview of the molecular structures in the S_1 states of the nine molecules studied herein, calculated at RI-SCS-CC2 level of theory.

the observed dynamics is presented in Figures 3.73 and 3.74. The corresponding decay times and oscillation frequencies are given in Table 3.27.

For all molecules but 1,2,4,5-TFB, an oscillation of the parent ion yield within the first picoseconds after excitation is observed. The lifetime of the oscillation ranges between $\tau_{osc} = 0.5$ ps for 1,2,3-TriFB to $\tau_{osc} = 4.27$ ps for 1,2,3,4-TFB, with oscillational frequencies between $\nu_{osc} = 70$ cm^{-1} (1,2,3,4-TFB) and $\nu_{osc} = 281$ cm^{-1} (PFPy). While for most molecules one oscillatory component was determined, the signals of 1,2,3,5-TFB and PFPy are modulated by two and four components, respectively. It should be noted that for PFPy the remarkable multi-component oscillation and instabilities towards long delay times prohibited suitable and reliable fits for the oscillatory and excited state lifetimes. PFPy was actually the first molecule studied and the issues regarding the instabilities were fixed for all other measurements.

In general, the oscillations are more pronounced and well-resolved when choosing $\lambda_{probe} = 800$ nm as the ionization wavelength. This is especially true for 1,2,3-TriFB and ClPFB, for which the oscillation only clearly emerges at $\lambda_{probe} = 800$ nm. Nevertheless, with two exceptions, the lifetime of the signals are virtually identical at both probe wavelengths. The two exceptions are 1,2,3-TriFB and 1,2,4,5-TFB, though not for the same reasons. In the dynamics of 1,2,3-TriFB a fourth, short-lived decay component is revealed at $\lambda_{probe} = 800$ nm, not present at $\lambda_{probe} = 400$ nm. Since this additional decay constant has a low amplitude (<10 %), it is assumed that the slightly better signal to noise ratio at 800 nm favors the detection of the component. For 1,2,4,5-TFB, a delayed signal rise, starting at $\Delta t = 0.5$ ps, is observed at 800 nm, not present at 400 nm. However, the dynamics of 1,2,4,5-TFB are not just wavelength, but also polarization dependent, i.e., the delayed rise is not observed any more when altering the probe pulse polarization. These findings might be correlated to the excitation of an intermediate state in the multi-photon ionization process. At 400 nm the state probably is inaccessible (cf. Section 3.2).

In the following, the oscillatory behavior is compared first, and discussion of the underlying electronic deactivation pathways follows afterwards.

Intensity and Lifetime of the Oscillations

In agreement with the literature,[9,10] the parent ion yield oscillations are attributed to pronounced vibronic coupling between the initially excited S_1 state ($\pi\pi^*$) and higher-lying $\pi\sigma^*$ states, mediated by a coherent wavepacket of out-of-plane

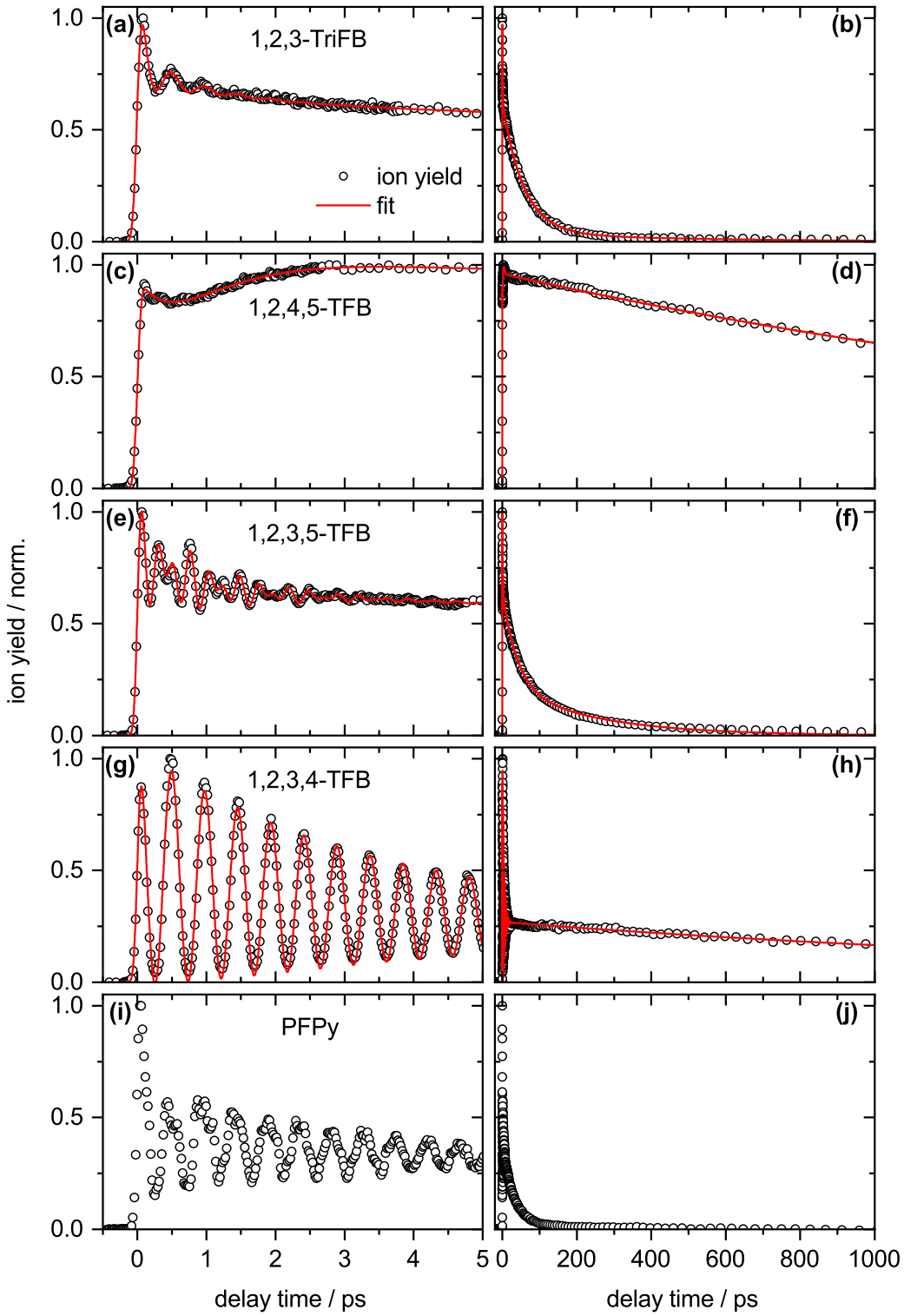

Figure 3.73. Measured transient parent ion yield signals (black circles) and applied fit model functions (red lines) for the parent ions of **(a–b)** 1,2,3-TriFB, **(c–d)** 1,2,4,5-TFB, **(e–f)** 1,2,3,5-TFB, **(g–h)** 1,2,3,4-TFB, and **(i–j)** PFPy[5] after excitation at $\lambda_{pump} = 260$ nm (250 nm and 255 nm for 1,2,3-TriFB and PFPy, respectively) and ionization at $\lambda_{probe} = 800$ nm (402 nm for PFPy). The left-hand column shows the data in the first five picoseconds, the right-hand column in the first nanosecond after excitation.

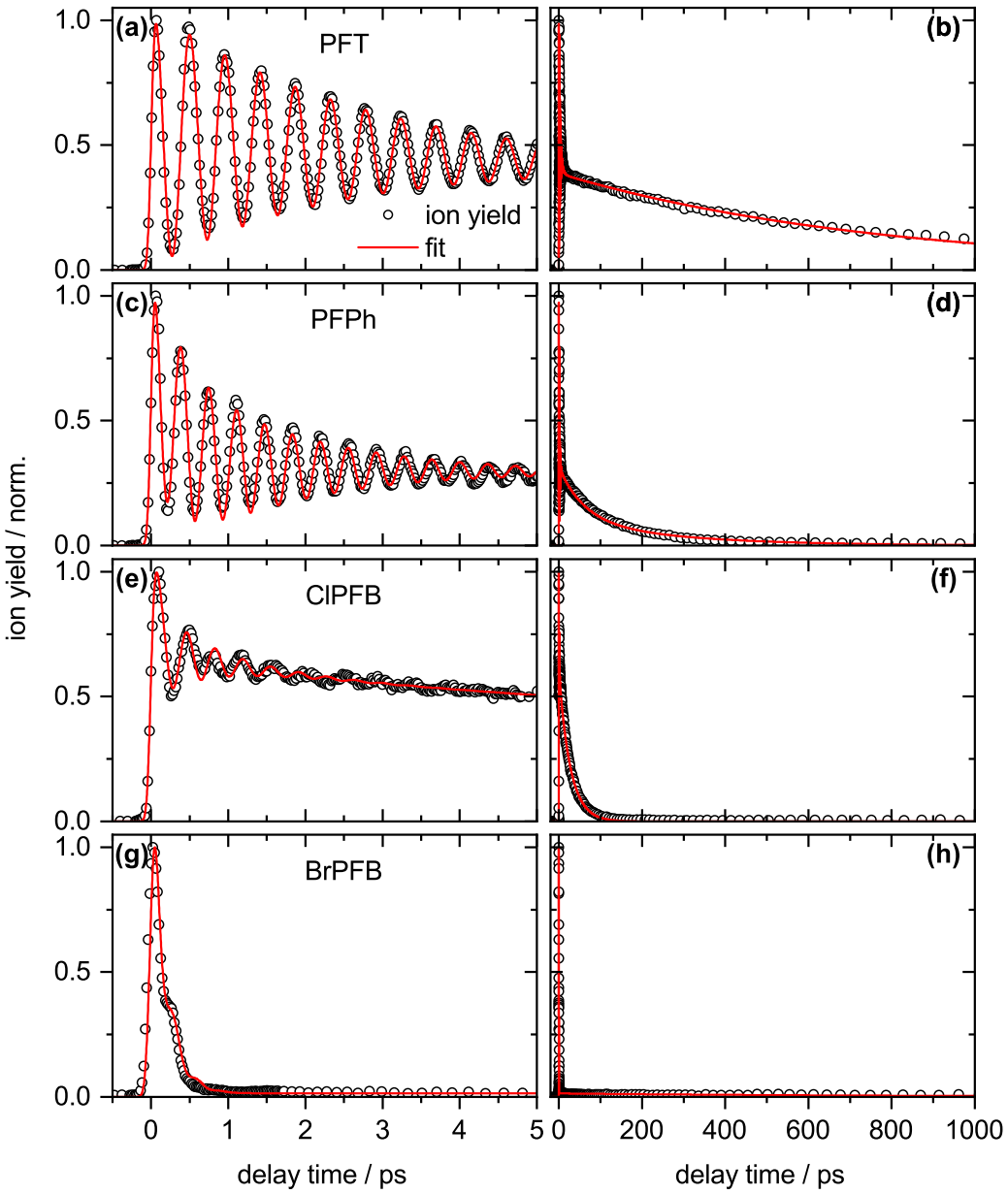

Figure 3.74. Measured transient parent ion yield signals (black circles) and applied fit model functions (red lines) for the parent ions of **(a–b)** PFT, **(c–d)** PFPh, **(e–f)** ClPFB, and **(g–h)** BrPFB after excitation at $\lambda_{pump} = 260$ nm and ionization at $\lambda_{probe} = 800$ nm (400 nm for BrPFB). The left-hand column shows the data in the first five picoseconds, the right-hand column in the first nanosecond after excitation.

Table 3.27. Decay constants and oscillation frequencies of the transient parent ion yields after excitation at $\lambda_{pump} = 260$ nm (†250 nm for 1,2,3-TriFB and 255 nm for PFPy) and ionization at $\lambda_{probe} = 800$ nm (‡402 nm for PFPy and 400 nm for BrPFB). For 1,2,4,5-TFB no oscillation was observed, but a signal rise. 2σ fit errors are given in parentheses. If no error is given, the value was set fixed.

	σ_{IRF} fs	τ_1 ps	τ_2 ps	τ_3 ps	τ_4 ps	τ_{osc} ps	ν_{osc} cm^{-1}
1,2,3-TriFB†	50	$< \sigma_{IRF}$	1.19(14)	56.1(26)	460(260)	0.5	70
1,2,4,5-TFB	45(1)	0.46(19)	2.2(18)		2575(52)	$\tau_{rise} = 1.01(86)$	
1,2,3,5-TFB	39(2)		0.62(5)	39.1(28)	243(30)	1.25(13) 1.03(8)	94 138
1,2,3,4-TFB	41(2)		2.27(10)		2100(220)	4.26(7)	70
PFPy†,‡							72 144 251 281
PFT	35(2)		5.19(34)		775(30)	2.53(5)	73
PFPh	36(3)	0.35(3)		59.3(54)	260	1.59(7)	92
ClPFB	41(1)	$< \sigma_{IRF}$	1.56(49)	27.24(94)	540(250)‡	0.66	92
BrPFB‡	50	0.05	0.18		770	0.18	111

vibrational modes. The coupling alters the potential energy hypersurface of the S_1 state considerably towards double-well potentials along the normal mode coordinates of the coupling modes. The signal oscillations map the movement of the wavepacket on the distorted potential energy hypersurface, and the frequency of the oscillation is mostly determined by a dominant low-frequency mode, exhibiting the highest double-well potential barrier.[9,10] Similar oscillations were observed for PFB[9,11] and HFB.[11,13] As mentioned in the beginning of the Chapter, in HFB the Jahn–Teller effect comes into play, affecting the coupling mechanism. Thus, the dynamics of HFB will not be discussed in depth.

Although the basic mechanism promoting the signal oscillations is identical (except for HFB), still severe substituent-dependent differences become apparent. Interestingly, the oscillatory lifetime, i.e., the dephasing of the wavepacket, increases in the order of

$$\text{1,2,3-TriFB} < \text{1,2,3,5-TFB} < \text{1,2,3,4-TFB} < \text{PFB}$$

but decreases for the PFPy, PFB, and its derivatives following

$$\text{PFB} > \text{PFT} > \text{PFPy} > \text{PFPh} > \text{HFB} > \text{ClPFB}.$$

Basically the same trend is observed for the modulation depths

$$\begin{aligned} \text{1,2,3-TriFB} < \text{1,2,3,5-TFB} \ll \text{1,2,3,4-TFB} \approx \text{PFB}, \\ \text{PFB} > \text{PFT} > \text{PFPh} \geq \text{PFPy} \gg \text{ClPFB} > \text{HFB}. \end{aligned}$$

In the case of BrPFB, the parent ion decays significantly faster than for any other molecule herein. Hence, not even a full oscillational period is mapped. The lifetimes of the two oscillatory components in 1,2,3,5-TFB (≈1.2 ps) are comparable to the lifetime of the oscillation in PFPh (≈1.65 ps), despite latter being much more intense. Otherwise, the similarities of the trends indicates that the reason for the change of both properties is identical.

Overall, more fluorine atoms stabilize the oscillation. Since the energy gap between the coupling states is a major factor determining the coupling strength,[58,59] the discussed lowering of the $\pi\sigma^*$ states in energy most certainly facilitates pronounced coupling and is a viable explanation for the increasingly prominent oscillations going from 1,2,3-TriFB to PFB. Nevertheless, the observed dynamics of the three TFB isomers highlight the coupling is a multi-dimensional problem and cannot simply be attributed to the vertical excitation energy difference between the coupling states at all times. Despite nearly identical $\pi\pi^*$–$\pi\sigma^*$ gaps, ranging from ≈1.5 eV to ≈1.3 eV for 1,2,4,5-TFB and 1,2,3,4-TFB, respectively, the S_1 state dynamics markedly differ. While the transient ion yield of 1,2,4,5-TFB features no oscillatory behavior, pronounced multi-frequency oscillations for 1,2,3,5-TFB and an intense single frequency oscillation for 1,2,3,4-TFB are observed. The oscillation of 1,2,3,4-TFB originates from the coupling of the first $\pi\pi^*$ (S_1, $^1A_1$) to the first $\pi\sigma^*$ state (S_2, $^1A_2$). The coupling is mediated by a_2 vibrational modes. The lowest-frequency a_2 mode ($\nu_{16}^{1,2,3,4\text{-TFB}} = 79$ cm^{-1}) likely dictates the oscillational frequency (cf. Section 3.4). On the other hand, the multi-frequency oscillation of 1,2,3,5-TFB might be the result of two equally dominant modes, forcing the potential energy surface of the S_1 state into a distinct multi-well rather than a double-well potential. However, whereas for 1,2,3,4-TFB and in earlier studies[5,9,10] excellent description of the mechanism was obtained focusing on a single subset of out-of-plane modes, the same does not apply for 1,2,3,5-TFB. In the case of 1,2,3,5-TFB, symmetry suggests the

S_1 ($^1B_2$) and the S_2 state ($^1B_1$) to be coupled by a_2 modes. Yet, vibrational frequency calculations indicate that the signal oscillations partially also originate from coupling mediated by b_1 modes, as discussed in detail in Section 3.3. Hence, it is plausible that simultaneous coupling to the S_2 and additionally to the S_4 state ($\pi\sigma^*$, $^1A_2$) modulates the signal. The lack of multi-frequency oscillations in the signals of, e.g., 1,2,3,4-TFB and PFB seemingly disagrees with the explanation, because for both molecules the second $\pi\sigma^*$ state is energetically even more accessible for the coupling than for 1,2,3,5-TFB (cf. Figure 3.71). Thus, simultaneous coupling to multiple $\pi\sigma^*$ states would be expected to influence the dynamics of these two molecules, too. Notwithstanding, for PFPh calculations of Rajak et al.[68] show that a variety of vibrational modes mediate extensive coupling between the S_1 and two higher-lying $\pi\sigma^*$ states as well (cf. Section 3.7). Since the signal of PFPh is only modulated by a single oscillational frequency, the coupling of multiple states and comparable well depths along the normal mode coordinates of more than one mode seems to not necessarily result in multiple oscillatory components. Therefore, the simultaneous coupling of the S_1 state to the S_2 and the S_4 states are indeed deemed to be the reason for the influences of the a_2 and the b_1 vibrational modes in 1,2,3,5-TFB. On the contrary, the multi-frequency oscillations of PFPy quite clearly can be attributed to coupling between the S_1 and the S_2 state, also via b_1 modes (cf. Section 3.5). The detection of four different oscillational components with frequencies up to $\nu_{osc} = 281$ cm^{-1}, of which at least three originate from different modes, accentuates that even small contributions of a component can be resolved by the experimental setup employed herein. The absence thereof for any other molecule than 1,2,3,5-TFB thereby raises the question how exactly the wavepacket motion has to change the PEHS to enable the observation of more than one mode. In the published calculations for PFB[9,10] and for PFPh[68] the PECs along the normal mode coordinates of multiple modes are, to some extent, rather similar. Still, in the corresponding simulations the dynamics are mainly dominated by a single mode of the wavepacket.[9,10] Performing analogous calculations and simulations for 1,2,3,5-TFB is probably the sensible choice to unravel the exact origin of multi-frequency oscillations in general, given that a low-lying $n\pi^*$ state drastically complicated the calculations in the case of PFPy (cf. Section 3.5). Regardless of the precise mechanism, the experimental results on 1,2,3,5-TFB and PFPy impressively confirm the previously predicted[9,10] impact of different vibrational modes on the observable dynamics.

Pinpointing the decisive differences preventing the oscillations in 1,2,4,5-TFB is expected to be easiest comparing its molecular properties to the ones of 1,2,3,4-TFB and PFB. One might argue that the 0.27 eV larger energy gap between the S_1 and S_2 states in 1,2,4,5-TFB compared to the gap in 1,2,3,4-TFB suffices to prohibit any vibronic coupling. However, earlier resonance-enhanced multiphoton ionization (REMPI) and laser-induced fluorescence (LIF) studies revealed that the lowest-frequency out-of-plane mode also forms a double-well potential for 1,2,4,5-TFB[32–34,41,43] and the authors attributed their findings to vibronic coupling. Consequently, these reports substantiate the question, why no oscillation is observed for 1,2,4,5-TFB. Although the vibronic coupling might be present, the coupling strengths might be significantly lower than in 1,2,3,4-TFB and PFB. A hint that this is indeed the case is provided by the potential energy barriers along the lowest-frequency coupling modes for 1,2,4,5-TFB and PFB. The barrier height of 1,2,4,5-TFB was experimentally determined to be 0.01 eV (80–90 cm^{-1}).[32,33] For PFB the barrier was calculated to be 0.11 eV (890 cm^{-1}).[9] Therefore, the height differs by one order of magnitude and most likely the total deformation of the S_1 PEHS of 1,2,4,5-TFB is rather shallow compared to the one in PFB, further indicated by the small out-of-plane deformation calculated for the S_1 state structure (cf. Figure 3.72). As an implication, the movement of the vibrational wavepacket on the PEHS probably does not alter the ionization probability to the same extend as for PFB, i.e., the ionization probability stays virtually identical, prohibiting experimental mapping of the movement. It should be noted that the oscillation might also be too fast to be observed with a time-resolution $\geq$30 fs.

In combination, the TFB dynamics emphasize one should be careful to readily attribute all observed trends to the simple VEE gaps. The energy difference between the coupling states certainly is an important, but not the sole parameter influencing the coupling mechanism. The out-of-plane motion of just two neighboring fluorine atoms seems to be insufficient to promote oscillations of the time-resolved signal. Including 1,2,3-TriFB in the comparison corroborates the conclusion that also the position of the fluorine atoms plays a major role. As oscillations are observed for 1,2,3-TriFB but not for 1,2,4,5-TFB, at least three fluorine atoms should be in close vicinity to each other to considerably alter the S_1 potential energy hypersurface, though the underlying reasons remain elusive.

Although 1,2,3,4-TFB and PFB show near identical oscillator behavior, the oscillations in PFB are slightly longer lived. Thus, five fluorine atoms appear to

be the "sweet spot" of vibronic coupling. Any other substituent than a hydrogen atom in combination with these five fluorine atoms drastically reduces the modulation depth and the oscillatory lifetime. Noticeable, the damping seems to correlate to the mass of the substituents, the heavier the shorter-lived are the oscillations. Molecular structure optimizations revealed for all derivatives but PFPh that the heavy substituents are moved out of the carbon ring plane, suggesting they are part of the coupling vibration. Potentially, the motion of these heavy substituents facilitates dephasing of the wavepacket. Additional studies on PFB derivatives with longer hydrocarbon chains might confirm this trend. Yet, the substituents also alter the $\pi\pi^*$–$\pi\sigma^*$ energy gaps and especially the gap between the $\pi\pi^*$ and the second $\pi\sigma^*$ state. Compared to PFB, for which the gap was estimated to be ≈1.3 eV, all PFB derivatives consistently exhibit gaps ≤1 eV. In fact, the decrease of the energy gap is accompanied by a decrease of the oscillatory lifetime and modulation depth. As discussed, multi-state coupling does not necessarily result in multiple oscillations. Hence, simultaneous coupling between the $\pi\pi^*$ and multiple $\pi\sigma^*$ states may be enabled, resulting in an overall less regular wavepacket movement and faster dephasing. Based on the optimized molecular structure in the S_1 state, the coupling to the second $\pi\sigma^*$ state is actually rather likely for ClPFB (cf. Section 3.8). Surprisingly, the shallow and short lived oscillations of 1,2,3-TriFB seem to originate from the coupling to the second $\pi\sigma^*$ state too, despite the larger energy difference of 1.7 eV between the coupling states.

The above considerations are mostly based on vertical excitation energy gaps calculated at CC2 level of theory. Owing to the complexity of multi-mode vibronic coupling, the CC2 calculations are only the first step to provide insight into the nuances responsible for the changes of the oscillatory behavior. Solely for the "sweet spot" PFB a combination of ab initio calculations and electronic dynamics simulations reproducing the experimentally observed behavior was reported.[9,10] In the model employed by Sala and coworkers[9,10] the six coupling modes were included, but the totally symmetric modes were preliminarily neglected. These so-called "tuning" modes are known to shift the energy of excited states,[59] so they might eventually change the actual energy gap between the coupling states. Their importance to reproduce the UV spectra of PFB,[12] PFPh,[68] and HFB[14] hints their inclusion in the models might improve the results, as was already implied by Sala and Egorova in their most recent work.[10] Unraveling the observed differences in the vibronic coupling mechanics will ultimately require electronic dynamics

simulations including most vibrational modes. These additional simulations will greatly improve the basis on which to discuss the experimental trends, and might even elucidate why the coupling to the second $\pi\sigma^*$ state seems more pronounced than the coupling to the first $\pi\sigma^*$ in case of 1,2,3-TriFB and why multiple oscillatory frequencies are exclusively observed for 1,2,3,5-TFB and PFPy.

Notwithstanding of the differences, there are also similarities in the damping process. A decrease in oscillational lifetime is observed when choosing shorter excitation wavelengths for the TFB isomers and PFPh, as was already reported for PFB and HFB.[9,13] It is reasonable to assume such a wavelength dependence of the oscillatory lifetime is a universal property that all FBs share. The lifetime at shorter excitation wavelengths probably is reduced as these wavelengths introduce more excess energy in the excited state and thus excite a greater variety of vibrational modes, resulting in different internal vibrational relaxation (IVR) pathways. In the case of PFPh, a higher-lying $\pi\sigma^*$ state was also directly excited at $\lambda_{\text{pump}} = 219$ nm, which presumably deactivates ultrafast into the S_1 state. Despite the significant excess energy, still intense oscillation are observed, leading to the conclusion that the vibronic coupling is so remarkably strong for the fluorobenzenes essentially no amount of excess energy will prohibit the experimentally observable oscillation.

Assignment of the Decay Constants

The time-resolved exponential decays of the parent ion yields represent the deactivation of the S_1 states via different channels. The decay components can be divided into three categories: (ultra)short decays below 10 ps (τ_1/τ_2), intermediate decays between 30–80 ps (τ_3) and long decays >250 ps (τ_4). An overview on the exponential decay parameters is given in Table 3.27. All molecules exhibit at least one (ultra-)short and one long-lived decay component. As the molecular structures in the excited states deviate severely from the neutral and ionic ground state structures, the initial ultrafast decay constants of the molecules showing none or short-lived oscillations are most likely associated with the vibrational wavepacket leaving the FC region, consequently reducing the ionization probability. The same also happens for the other molecules, but the regular wavepacket motion brings them back to the FC region, so the leaving of the FC region is incorporated in the oscillational component. After leaving the FC region, the excess energy of the pump photon is redistributed between

the vibrational modes for all molecules. Presumably, this IVR is responsible for the second short time constants <10 ps, though the transitions between the two processes are probably smooth and not necessarily distinguishable.

Past work revealed an intermediate and a long-lived decay component for PFB, and the intermediate decay was ascribed to IVR, too.[9] However, in this work a strong dependence of the intermediate and the long-lived decay constant are observed. 1,2,3-TriFB, 1,2,3,5-TFB, PFPh, and ClPFB all show an intermediate decay constant and for neither the excited state lifetime exceeds $\tau_4 = 600$ ps, as was essentially also reported for PFB. PFPh even solely shows the intermediate component after excitation at wavelengths shorter than $\lambda_{\text{pump}} = 260$ nm. In contrast, the lifetimes of 1,2,4,5-TFB, 1,2,3,4-TFB, and PFT, lacking this intermediate component, surpass $\tau_4 = 800$ ps. Additional, but very preliminary work on the excited state lifetimes of the TFB isomers in solution via picosecond time-resolved fluorescence substantiates these findings. While one intermediate and one long-lived decay component is observed for 1,2,3,5-TFB, the two other isomers only exhibit one long-lived component, all in the same orders of magnitude as the constants in the transient TOF-MS. Although it should be noted that the fluorescence decay behavior might significantly change after excitation by femtosecond pulses in a molecular beam, it is improbable IVR will alter the signal decays of 1,2,3,5-TFB equally in both fluorescence and transient TOF-MS. In light of the strong dependence of the decay constants and the preliminary results of the time-resolved fluorescence, it is deemed likely that the intermediate time constant may be associated with a second electronic deactivation pathway, and not with IVR, competing with the channel linked to the long decay components. Whether this second channel is not present for 1,2,4,5-TFB, 1,2,3,4-TFB, and PFT in general, or if the chosen wavelengths ($\lambda_{\text{pump}} \geq 255$ nm) simply introduce insufficient excess energy to access the pathway remains elusive.

One possible explanation for the exponential signal decays may be dissociation of the parent ions or excited molecules. Yet, such a dissociation should be accompanied by a rise of fragment ions. Little to none fragments are detected for most of the molecules. Furthermore, breaking of the C-F and C-H bonds requires more than 4.9 eV,[118] not accounting for potential barriers. Hence, the introduced excess energy of 4.77 nm ($\lambda_{\text{pump}} = 260$ nm) is simply insufficient to enable bond fission, essentially ruling out dissociation enhances the signal decay. O-H bond fission, on the other hand, might be a viable deactivation pathway for PFPh. As discussed in depth in Section 3.7 in light of novel calculations,

the dissociation probably requires excitation wavelengths $\lambda_{\text{pump}} < 260$ nm. In the experiments, a distinct reduction of the decay time constants is observed at these pump wavelengths. Simultaneously, the long-lived decay component vanishes. Both observations might be directly linked to the O-H bond fission, and selectively probing the hydrogen fragments may allow further insights into the dissociation dynamics.

In contrast to all other molecules, dissociation is directly observed for BrPFB, with the main fragment being the $[\text{BrPFB}-\text{Br}]^+$ cation. The C-Br bond fission becomes possible, because the bond dissociation energy of 3 eV[118] is exceeded by 1.77 eV at $\lambda_{\text{pump}} = 260$ nm. Though the fragments are presumably generated in the ionic state (cf. Section 3.9), the rapid decay of the parent ion signal is most likely related to the fragmentation of the excited molecules.[66] The almost certain present vibronic coupling to the higher-lying $\pi\sigma^*$ may ease the dissociation.

Overall, bond fissions only play a very minor role as deactivation pathways. Although the scrutiny of the deactivation mechanisms is beyond the scope of this Thesis, the absence of additional signals rising in at later delay times in the PES suggests deactivation directly leads to the S_0 state, without conversion to any intermediate excited electronic state. Moreover, the significant changes of τ_4 within $\Delta\lambda_{\text{pump}} = 5$ nm of excitation energy for the TFB isomers (265–260 nm for 1,2,3,5-TFB and 260–255 nm for the other two), for PFB[9], and for HFB[13] hint to barriers along the pathways associated with the long-lived decay components. In line, most recent theoretical work on HFB suggests that pronounced structural reorganizations on the S_1 potential energy hypersurface may be involved in the deactivation.[119] Unveiling the exact electronic deactivation mechanisms will ultimately require further experimental and theoretical studies, addressing potential conical intersections to the S_0 state and radiative channels.

3.10.3 Time-Resolved Photoelectron Images

The PE results can be summed up as follows: two major signals α and β are observed after excitation by one pump and ionization by two probe photons. The broad signals α are located at PE energies below $E_\alpha = 0.7$ eV, whereas the narrow, well-defined signals β peak at $E_\beta = 0.70$–0.92 eV, as listed in Table 3.28. Evolution of both peaks follows the transient parent ion yield, i.e., if an oscillation of the ion yield is observed both PE signals replicate the behavior. No additional

Table 3.28. Overview of the peak position of the PE signals α and β after excitation at λ_{pump} = 260 nm ([†]250 nm for 1,2,3-TriFB and 255 nm for PFPy) and ionization at λ_{probe} = 400 nm (402 nm for PFPy), and of the SC PE bands γ–η.[‡] If no peak was observed, the band onset is given. All values are in eV.

	multi-color		SC probe			SC pump	
	α	β	γ	δ	ϵ	ζ	η
1,2,3-TriFB[†]	<0.5	0.89	1.5	1.7	2.2	0.14	0.30
1,2,4,5-TFB	0.5	0.92	1.7			0.04	0.13
1,2,3,5-TFB	0.4	0.89					
1,2,3,4-TFB	0.2	0.91	1.5				
PFPy[†]		0.70	1.1	1.6	2.0		
PFT	0.4	0.88	1.7				
PFPh	<0.7	0.85	1.7			0.13	
ClPFB	<0.7	0.83	1.6	2.2			
BrPFB	<0.7	0.89	1.7	2.3			

[‡] Signals β–ϵ of PFPy were labeled (a–d) in Section 3.5, as in the original publication in Ref. [5].

peaks arise at any delay time for any molecule. Thus, no internal conversion to any other neutral excited state is observed.

Signals α are assigned to transitions to the first excited ionic states D_1, while signals β originate from transitions to the ionic ground states D_0. Contrary to the electronic structure of all other molecules, the D_1 state of PFPy was energetically inaccessible at the chosen wavelengths, consequently no signal α emerged. The narrow widths of signals β indicate adiabatic transitions to the D_0 states. Hence, it can readily be estimated how much energy resides in the molecules prior to ionization. These estimations lead to the conclusion that in the cases of 1,2,3-TriFB, the three TFB isomers, PFT, and for PFPh the ionization probably is a stepwise process. The initial excitation of the S_1 state by a pump photon is followed by the absorption of a single probe photon within the probe pulse duration, exciting a high-lying intermediate state. The subsequent absorption of a second photon ionizes the molecules. The excitation of these intermediate states alters the peak positions of the PE signals compared to the expected positions if no intermediate states would be excited. Calculation of their transition energies shows that they are all located at 7.1–7.3 eV, despite the substantial differences of the molecular substitution patterns. Notwithstanding, the states probably also consistently exhibit $\pi\pi^*$ character, for which the perfluoro effect only marginally alters the transition energies.[56,116,117] Accordingly, the near identical estimated transition

energies are actually in excellent agreement with expectations.[36,38] In contrast, the experimental PE signals of PFPy, ClPFB, BrPFB, and the previously reported signals of PFB[9] can be explained assuming a direct $D_0 \leftarrow S_1$ transition. Yet, the similarities of the PE distributions raise the question, if excitation of intermediate states is a pattern generally observed for all studied fluorinated aromatic systems. Recently, Sala and Egorova calculated the PES of PFB after excitation of the S_1 state and subsequent ionization by a single photon at wavelengths $\leq$201 nm.[10] They reported one should expect two PE signals corresponding to the transitions to the D_0 and D_1 states. In further agreement with the observation herein, the two signals are expected to oscillate alike in intensity. The authors also expect additional oscillations in the energy regime. Neither in the current, nor in past work[5,9] such an energy oscillation was observed. Sala and Egorova attributed this major discrepancy between theory and experiment to excitation of intermediate states in the ionization process. Therefore, it is deemed very likely signals β are altered by intermediate states for all FBs and PFPy. More or less resonant excitation of such states is probably the reason why for some molecules the peak positions of β are not affected, yet narrow energy distributions are observed.

The broad energy distributions of signals α are the results of vertical transitions, or to be more precise, a plethora of of transitions to different vibrational states within the final D_1 electronic states. As a consequence, picking an arbitrary electron energy from any of the broad distributions to estimate the energy in the molecule prior to ionization will yield transition energies differing by up to $\approx$1 eV, thus is rather not meaningful. However, the shape of the electron distributions still gives hints regarding the ionization mechanism. The reason why the transitions to the D_1 and the D_0 states yield different energy distributions has to be either substantially differing vibrational and molecular structures in both ionic states, or the two pathways leading to ionization are fundamentally different. Information on the D_1 states is scare. For 1,2,4,5-TFB the optimization of the D_1 molecular structure converged, yielding an essentially identical structure compared to the one in the D_0 state. Hence, the results of 1,2,4,5-TFB indicate that the ionization mechanisms leading to α and β might follow two different routes. Yet, the overall lack of information on the D_1 states and the broad signal widths prohibit detailed insights into whether the transitions to the D_1 states also involve excitation of intermediate states or not.

Only for 1,2,3-TriFB, 1,2,4,5-TFB, and PFPh the ionization energies are sufficiently low to allow for ionization by absorption of two pump photons. The

corresponding signals ζ and η are attributed to the more or less direct $D_0 \leftarrow S_0$ ionization. Although no high-lying states are excited, the respective S_1 states may be involved as intermediate states. In contrast, the high-intensity single-color ionization at $\lambda_{probe} = 400$ nm generally generates only few electrons that can be assigned to the direct $D_0 \leftarrow S_0$ transition. Far more pronounced in these PES are broad, indistinct bands originating from the excitation of high-lying intermediate states within the probe pulse duration. Owing to the estimated transition energies of more than 7.5 eV, these states cannot be further characterized. For all molecules the signals β are also observed in the SC PES at $\lambda_{probe} = 400$ nm. Whether the S_1 states are excited first and afterwards the proposed intermediate states are populated, or if the latter are directly excited by absorption of three probe photons remains elusive.

All in all, the photoelectron distributions of the fluorobenzenes are very similar in shape and position, suggesting likewise similar ionization pathways. Excitation of intermediate states is probably involved in the ionization mechanism. It is, however, worth emphasizing that these intermediate states do not dictate the observed dynamics, since they are solely populated during the probe pulse duration. Therefore, the observed oscillations of the PES and parent ion yields originate from dynamics on the S_1 potential energy hypersurface.

References

[1]H. A. Jahn, E. Teller, and F. G. Donnan, "Stability of polyatomic molecules in degenerate electronic states - I—Orbital degeneracy", Proc. R. Soc. London, A **161**, 220 (1937).

[2]T. J. Sears, T. A. Miller, and V. E. Bondybey, "The Jahn–Teller effect in $C_6F_6^+$", J. Chem. Phys. **74**, 3240 (1981).

[3]K. Raghavachari, R. C. Haddon, T. A. Miller, and V. E. Bondybey, "Theoretical study of Jahn–Teller distortions in $C_6H_6^+$ and $C_6F_6^+$", J. Chem. Phys. **79**, 1387 (1983).

[4]R. S. Mulliken, "Report on notation for the spectra of polyatomic molecules", J. Chem. Phys. **23**, 1997 (1955).

[5]J. A. Kus, O. Hüter, and F. Temps, "Real-time observation of multi-mode vibronic coherence in pentafluoropyridine", J. Chem. Phys. **147**, 013938 (2017).

[6]G. Bieri, L. Åsbrink, and W. von Niessen, "30.4-nm He(II) Photoelectron spectra of organic molecules: Part IV. Fluoro-compounds (C, H, F)", J. Electron Spectrosc. **23**, 281 (1981).

[7]S. Faraji and H. Köppel, "Multi-state vibronic interactions in the 1,2,3-trifluorobenzene radical cation", J. Chem. Phys. **137**, 22A531 (2012).

[8]V. E. Bondybey, J. H. English, T. A. Miller, and R. Shiley, "The laser-induced fluorescence spectrum of the 1,2,3-trifluorobenzene radical cation", J. Mol. Spectrosc. **84**, 124 (1980).

[9]O. Hüter, M. Sala, H. Neumann, S. Zhang, H. Studzinski, D. Egorova, and F. Temps, "Long-lived coherence in pentafluorobenzene as a probe of $\pi\pi^*$ – $\pi\sigma^*$ vibronic coupling", J. Chem. Phys. **145**, 014302 (2016).

[10]M. Sala and D. Egorova, "Imaging large amplitude out-of-plane motion in photoexcited pentafluorobenzene using time-resolved photoelectron spectroscopy: a computational study", Photochem. Photobiol. Sci. **17**, 1036 (2018).

[11]S. A. Kovalenko, A. L. Dobryakov, and V. Farztdinov, "Detecting electronic coherence in excited-state electron transfer in fluorinated benzenes", Phys. Rev. Lett. **96**, 068301 (2006).

[12]T. Mondal and S. Mahapatra, "Photophysics of fluorinated benzene. I. Quantum chemistry", J. Chem. Phys. **133**, 084304 (2010).

[13]H. Studzinski, S. Zhang, Y. Wang, and F. Temps, "Ultrafast nonradiative dynamics in electronically excited hexafluorobenzene by femtosecond time-resolved mass spectrometry", J. Chem. Phys. **128**, 164314 (2008).

[14]T. Mondal, S. R. Reddy, and S. Mahapatra, "Photophysics of fluorinated benzene. III. Hexafluorobenzene", J. Chem. Phys. **137**, 054311 (2012).

[15]T. Koopmans, "Über die Zuordnung von Wellenfunktionen und Eigenwerten zu den einzelnen Elektronen eines Atoms", Physica **1**, 104 (1934).

[16]V. Blanchet, M. Z. Zgierski, and A. Stolow, "Electronic continua in time-resolved photoelectron spectroscopy. I. Complementary ionization correlations", J. Chem. Phys. **114**, 1194 (2001).

[17]M. Schmitt, S. Lochbrunner, J. P. Shaffer, J. J. Larsen, M. Z. Zgierski, and A. Stolow, "Electronic continua in time-resolved photoelectron spectroscopy. II. Corresponding ionization correlations", J. Chem. Phys. **114**, 1206 (2001).

[18]D. G. Streets and G. P. Ceasar, "Inductive and mesomeric effects on the π orbitals of halobenzenes", Mol. Phys. **26**, 1037 (1973).

[19]T. Suzuki, "Nonadiabatic electronic dynamics in isolated molecules and in solution studied by ultrafast time–energy mapping of photoelectron distributions", Bull. Chem. Soc. Jpn. **87**, 341 (2014).

[20]O. Hüter and F. Temps, "Ultrafast α–CC bond cleavage of acetone upon excitation to 3p and 3d Rydberg states by femtosecond time-resolved photoelectron imaging", J. Chem. Phys. **145**, 214312 (2016).

[21]S. Takeuchi and T. Tahara, "Coherent nuclear wavepacket motions in ultrafast excited-state intramolecular proton transfer: Sub-30-fs resolved pump–probe absorption spectroscopy of 10-hydroxybenzo[h]quinoline in solution", J. Phys. Chem. A **109**, 10199 (2005).

[22]J. A. Davies and K. L. Reid, "Elucidating quantum number-dependent coupling matrix elements using picosecond time-resolved photoelectron spectroscopy", Phys. Rev. Lett. **109**, 193004 (2012).

[23]J. D. Young, M. Staniforth, J. C. Dean, G. M. Roberts, F. Mazzoni, T. N. Karsili, M. N. Ashfold, T. S. Zwier, and V. G. Stavros, "Towards understanding photodegradation pathways in lignins: the role of intramolecular hydrogen bonding in excited states", J. Phys. Chem. Lett. **5**, 2138 (2014).

[24]J. Midgley, J. A. Davies, and K. L. Reid, "Complex and sustained quantum beating patterns in a classic IVR system: the $3^1 5^1$ level in S_1 *p*-difluorobenzene", J. Phys. Chem. Lett. **5**, 2484 (2014).

[25]R. Spesyvtsev, T. Horio, Y.-I. Suzuki, and T. Suzuki, "Observation of the wavepacket dynamics on the $^1B_2(^1\Sigma_u^+)$ state of CS_2 by sub-20 fs photoelectron imaging using 159 nm probe pulses", J. Chem. Phys. **142**, 074308 (2015).

[26]J. D. Young, M. Staniforth, M. J. Paterson, and V. G. Stavros, "Torsional motion of the chromophore catechol following the absorption of ultraviolet light", Phys. Rev. Lett. **114**, 233001 (2015).

[27]F. Ling, S. Li, X. Song, Y. Tang, Y. Wang, and B. Zhang, "Visualization of coherent nuclear motion between different geometries in photoexcited 2,4-difluorophenol", Phys. Rev. A **95**, 043421 (2017).

[28]S. Li, J. Long, F. Ling, Y. Wang, X. Song, S. Zhang, and B. Zhang, "Real-time visualization of the vibrational wavepacket dynamics in electronically excited pyrimidine via femtosecond time-resolved photoelectron imaging", J. Chem. Phys. **147**, 044309 (2017).

[29]F. Ling, S. Li, X. Song, Y. Wang, J. Long, and B. Zhang, "Femtosecond time-resolved observation of butterfly vibration in electronically excited *o*-fluorophenol", Sci. Rep. **7**, 15362 (2017).

[30]F. Ling, Y. Wang, S. Li, J. Wei, Y. Tang, and B. Zhang, "Imaging reversible and irreversible structural evolution in photoexcited 2,4-difluoroaniline", J. Phys. Chem. Lett. **9**, 5468 (2018).

[31]F. Ling, S. Li, Y. Wang, P. Wang, and B. Zhang, "Vibrational coherence in the composition-selected wavepacket of photoexcited pyrimidine", J. Chem. Phys. **150**, 044308 (2019).

[32]K. Okuyama, T. Kakinuma, M. Fujii, N. Mikami, and M. Ito, "Electronic spectra of 1,2,4,5-tetrafluorobenzene in a supersonic jet: Butterfly tunneling in the excited state", J. Phys. Chem. **90**, 3948 (1986).

[33]J. M. Hollas and M. Z. Bin Hussein, "The $\widetilde{A}^1B_{2u}$–$\widetilde{X}^1A_g$ electronic absorption spectrum of 1,2,4,5-tetrafluorobenzene: Rotational band contour and vibrational analysis relating to non-planarity in the $\widetilde{A}$ state", Chem. Phys. **124**, 297 (1988).

[34]T. Ridley, D. M. Rogers, and K. P. Lawley, "A combined resonance enhanced multiphoton ionization and ab initio study of the first absorption band of 1,2,4,5-tetrafluorobenzene, pentafluorobenzene, and hexafluorobenzene", J. Chem. Phys. **141**, 154310 (2014).

[35]J. H. S. Green and D. J. Harrison, "Thermodynamic properties of fluorine compounds—XVII. The vibrational spectra and calculated thermodynamic properties of the tetrafluorobenzenes", Spectrochim. Acta A **32A**, 1185 (1976).

[36]R. P. Frueholz, W. M. Flicker, O. A. Mosher, and A. Kuppermann, "Electronic spectroscopy of benzene and the fluorobenzenes by variable angle electron impact", J. Chem. Phys. **70**, 3057 (1979).

[37]D. Phillips, "Substituent effects in the photochemistry of benzene vapour", J. Photochem. **1**, 97 (1972).

[38]J. Philis, A. Bolovinos, G. Andritsopoulos, E. Pantos, and P. Tsekeris, "A comparison of the absorption spectra of the fluorobenzenes and benzene in the region 4.5-9.5 eV", J. Phys. B: At. Mol. Phys. **14**, 3621 (1981).

[39]S. G. Lias, J. E. Bartmess, J. F. Liebman, J. L. Holmes, R. D. Levin, and W. G. Mallard, "Gas-phase ion and neutral thermochemistry", J. Phys. Chem. Ref. Data **17, Sup. 1**, 861 (1988).

[40]H. Y. So and R. C. Dunbar, "Photodissociation of gas-phase halogenated benzene radical cations", J. Chem. Phys. **90**, 2192 (1989).

[41]S. Sato, K. Ikeda, and K. Kimura, "ZEKE photoelectron spectroscopy and ab initio force-field calculation of 1,2,4,5-tetrafluorobenzene", J. Electron Spectrosc. **88-91**, 137 (1998).

[42]K. Takazawa and M. Fujii, "Butterfly vibration of the tetrafluorobenzene cation studied by pulsed field ionization-zero kinetic energy photoelectron spectroscopy", J. Electron Spectrosc. **112**, 241 (2000).

[43]G. Orlandi and F. Zerbetto, "Vibronic coupling in 1,2,4,5-tetrafluorobenzene: The double-minimum potential of the butterfly motion (Q_{11}) in the state S_1", J. Phys. Chem. **91**, 4238 (1987).

[44]S. T. Pratt, "Excited-state molecular photoionization dynamics", Rep. Prog. Phys. **58**, 821 (1995).

[45]K. Kimura, "Development of laser photoelectron spectroscopy based on resonantly enhanced multiphoton ionization", J. Electron Spectrosc. **100**, 273 (1999).

[46]F. Gunzer, S. Krüger, and J. Grotemeyer, "Photoionization and photofragmentation in mass spectrometry with visible and UV lasers", Mass Spectrom. Rev. **38**, 202 (2019).

[47]T. Suzuki and B. J. Whitaker, "Non-adiabatic effects in chemistry revealed by time-resolved charged-particle imaging", Int. Rev. Phys. Chem. **20**, 313 (2001).

[48]D. W. Chandler, A. I. Chichinin, T. S. Einfeld, A. T. J. B. Eppink, K.-H. Gericke, O. Heber, H. Helm, P. L. Houston, T. N. Kitsopoulos, K. T. Lorenz, C. Maul, U. Müller, D. H. Parker, T. P. Rakitzis, J. L. Springfield, D. Strasser, T. Suzuki, E. A. Wade, B. J. Whitaker, S.-M. Wu, and D. Zajfman, *Imaging in Molecular Dynamics: Technology and Applications*, edited by B. J. Whitaker (Cambridge University Press, Cambridge, 2003).

[49]T. Suzuki, "Femtosecond time-resolved photoelectron imaging", Annu. Rev. Phys. Chem. **57**, 555 (2006).

[50]H. Stapelfeldt and T. Seideman, "Colloquium: aligning molecules with strong laser pulses", Rev. Mod. Phys. **75**, 543 (2003).

[51]V. Kumarappan, S. S. Viftrup, L. Holmegaard, C. Z. Bisgaard, and H. Stapelfeldt, "Aligning molecules with long or short laser pulses", Phys. Scr. **76**, C63 (2007).

[52]R. C. Estler and R. N. Zare, "Laser-induced chemiluminescence: variation of reaction rates with reagent approach geometry", J. Am. Chem. Soc. **100**, 1323 (1978).

[53]M. J. Weida and C. S. Parmenter, "Aligning symmetric and asymmetric top molecules via single photon excitation", J. Chem. Phys. **107**, 7138 (1997).

[54]J. A. Sell, D. M. Mintz, and A. Kuppermann, "Photoelectron angular distributions of carbon—carbon PI electroncs in ethylene, benzene, and their fluorinated derivatives", Chem. Phys. Lett. **58**, 601 (1978).

[55]D. J. Clouthier and D. A. Ramsay, "The spectroscopy of formaldehyde and thioformaldehyde", Annu. Rev. Phys. Chem. **34**, 31 (1983).

[56]C. R. Brundle, M. B. Robin, and N. A. Kuebler, "Perfluoro effect in photoelectron spectroscopy. II. Aromatic molecules", J. Am. Chem. Soc. **94**, 1466 (1972).

[57]C. Utsunomiya, T. Kobayashi, and S. Nagakura, "Photoelectron angular distribution measurements for some pyridines", Bull. Chem. Soc. Jpn. **51**, 3482 (1978).

[58]I. B. Bersuker, "Pseudo-Jahn–Teller effect—A two-state paradigm in formation, deformation, and transformation of molecular systems and solids", Chem. Rev. **113**, 1351 (2013).

[59]H. Köppel, W. Domcke, and L. S. Cederbaum, "Multimode molecular dynamics beyond the Born-Oppenheimer approximation", in *Adv. Chem. Phys.* Edited by I. Prigogine and S. A. Rice, 57th ed. (John Wiley & Sons, Inc., New York), pp. 59–246.

[60]G. A. Worth, H.-D. Meyer, H. Köppel, L. S. Cederbaum, and I. Burghardt, "Using the MCTDH wavepacket propagation method to describe multimode non-adiabatic dynamics", Int. Rev. Phys. Chem. **27**, 569 (2008).

[61]B. M. Garraway and K.-A. Suominen, "Wave packet dynamics in molecules", Contemp. Phys. **43**, 97 (2002).

[62]L. D. Landau and E. M. Lifshitz, *Mechanics*, 3rd ed. (Butterworth-Heinemann, Oxford, 1976).

[63]D. A. Long and R. T. Bailey, "Spectroscopic and thermodynamics studies of pyridine. Part 3.—Pentafluoropyridine", Trans. Faraday Soc. **59**, 599 (1963).

[64]B. C. Trudell and S. J. W. Price, "The ultraviolet photoelectron spectra of C_6F_5X compounds, X = (F, Cl, Br, I, H, CH_3)", Can. J. Chem. **57**, 2256 (1979).

[65]J. P. Maier, O. Marthaler, and M. Mohraz, "Decay of some substituted benzene cations in the $\widetilde{B}$ states in the gaseous phase", J. Chim. Phys. **77**, 661 (1980).

[66]O. A. Borg, Y.-J. Liu, P. Persson, S. Lunell, D. Karlsson, M. Kadi, and J. Davidsson, "Photochemistry of bromofluorobenzenes", J. Phys. Chem. A **110**, 7045 (2006).

[67]S. Karmakar, D. P. Mukhopadhyay, and T. Chakraborty, "Electronic spectra and excited state dynamics of pentafluorophenol: Effects of low-lying $\pi\sigma^*$ states", J. Chem. Phys. **142**, 184303 (2015).

[68]K. Rajak, A. Ghosh, and S. Mahapatra, "Photophysics of phenol and pentafluorophenol: The role of nonadiabaticity in the optical transition to the lowest bright $^1\pi\pi^*$ state", J. Chem. Phys. **148**, 054301 (2018).

[69]J. P. Maier and D. W. Turner, "Steric inhibition of resonance studied by molecular photoelectron spectroscopy. Part 3.—Anilines, phenols and related compounds", J. Chem. Soc., Faraday Trans. 2 **69**, 521 (1973).

[70]J. P. Maier, L. Misev, and R. H. Shiley, "Laser induced excitation spectra of the cations of some fluoro-substituted phenols ($\widetilde{B}^2A'' \leftrightarrow \widetilde{X}^2A''$) in the gaseous phase", Helv. Chim. Acta **63**, 1920 (1980).

[71]J. P. Maier, O. Marthaler, M. Mohraz, and R. H. Shiley, "Emission spectra of the cations of some fluoro-substituted phenols in the gaseous phase", J. Electron Spectrosc. **19**, 11 (1980).

[72]A. Sur and P. M. Johnson, "Radiationless transitions in gas phase phenol and the effects of hydrogen bonding", J. Chem. Phys. **84**, 1206 (1986).

[73]C.-M. Tseng, Y. T. Lee, and C.-K. Ni, "H atom elimination from the $\pi\sigma^*$ state in the photodissociation of phenol", J. Chem. Phys. **121**, 2459 (2004).

[74]M. N. R. Ashfold, B. Cronin, A. L. Devine, R. N. Dixon, and M. G. D. Nix, "The role of $\pi\sigma^*$ excited states in the photodissociation of heteroaromatic molecules", Science **312**, 1637 (2006).

[75]M. G. D. Nix, A. L. Devine, B. Cronin, R. N. Dixon, and M. N. R. Ashfold, "High resolution photofragment translational spectroscopy studies of the near ultraviolet photolysis of phenol", J. Chem. Phys. **125**, 133318 (2006).

[76]C.-M. Tseng, Y. T. Lee, M.-F. Lin, C.-K. Ni, S.-Y. Liu, Y.-P. Lee, Z. F. Xu, and M. C. Lin, "Photodissociation dynamics of phenol", J. Phys. Chem. A **111**, 9463 (2007).

[77]M. L. Hause, Y. Heidi Yoon, A. S. Case, and F. Fleming Crim, "Dynamics at conical intersections: The influence of O-H stretching vibrations on the photodissociation of phenol", J. Chem. Phys. **128**, 104307 (2008).

[78]M. N. R. Ashfold, A. L. Devine, R. N. Dixon, G. A. King, M. G. D. Nix, and T. A. A. Oliver, "Exploring nuclear motion through conical intersections in the UV photodissociation of phenols and thiophenol", Proc. Natl. Acad. Sci. U.S.A. **105**, 12701 (2008).

[79]A. Iqbal, L.-J. Pegg, and V. G. Stavros, "Direct versus indirect H atom elimination from photoexcited phenol molecules", J. Phys. Chem. A **112**, 9531 (2008).

[80]G. A. King, T. A. A. Oliver, M. G. D. Nix, and M. N. R. Ashfold, "High resolution photofragment translational spectroscopy studies of the ultraviolet photolysis of phenol-d_5", J. Phys. Chem. A **113**, 7984 (2009).

[81]A. Iqbal, M. S. Y. Cheung, M. G. D. Nix, and V. G. Stavros, "Exploring the time-scales of H-atom detachment from photoexcited phenol-h_6 and phenol-d_5: Statistical vs nonstatistical decay", J. Phys. Chem. A **113**, 8157 (2009).

[82]G. A. Pino, A. N. Oldani, E. Marceca, M. Fujii, S.-I. Ishiuchi, M. Miyazaki, M. Broquier, C. Dedonder, and C. Jouvet, "Excited state hydrogen transfer dynamics in substituted phenols and their complexes with ammonia: $\pi\pi^*$-$\pi\sigma^*$ energy gap propensity and ortho-substitution effect", J. Chem. Phys. **133**, 124313 (2010).

[83]R. N. Dixon, T. A. A. Oliver, and M. N. R. Ashfold, "Tunnelling under a conical intersection: Application to the product vibrational state distributions in the UV photodissociation of phenols", J. Chem. Phys. **134**, 194303 (2011).

[84]G. M. Roberts, A. S. Chatterley, J. D. Young, and V. G. Stavros, "Direct observation of hydrogen tunneling dynamics in photoexcited phenol", J. Phys. Chem. Lett. **3**, 348 (2012).

[85]Y. Zhang, T. A. A. Oliver, M. N. R. Ashfold, and S. E. Bradforth, "Contrasting the excited state reaction pathways of phenol and *para*-methylthiophenol in the gas and liquid phases", Faraday Discuss. **157**, 141 (2012).

[86]R. A. Livingstone, J. O. F. Thompson, M. Iljina, R. J. Donaldson, B. J. Sussman, M. J. Paterson, and D. Townsend, "Time-resolved photoelectron imaging of excited state relaxation dynamics in phenol, catechol, resorcinol, and hydroquinone", J. Chem. Phys. **137**, 184304 (2012).

[87]Y.-C. Lin, C. Lee, S.-H. Lee, Y.-Y. Lee, Y. T. Lee, C.-M. Tseng, and C.-K. Ni, "Excited-state dissociation dynamics of phenol studied by a new time-resolved technique", J. Chem. Phys. **148**, 074306 (2018).

[88]H. Y. Lai, W. R. Jhang, and C.-M. Tseng, "Communication: Mode-dependent excited-state lifetime of phenol under the S_1/S_2 conical intersection", J. Chem. Phys. **149**, 031104 (2018).

[89]K. I. Hilsabeck, J. L. Meiser, M. Sneha, J. A. Harrison, and R. N. Zare, "Non-resonant photons catalyze photodissociation of phenol", J. Am. Chem. Soc. **141**, 1067 (2019).

[90]K. C. Woo and S. K. Kim, "Multidimensional H atom tunneling dynamics of phenol: Interplay between vibrations and tunneling", J. Phys. Chem. A **123**, 1529 (2019).

[91]A. L. Sobolewski and W. Domcke, "Photoinduced electron and proton transfer in phenol and its clusters with water and ammonia", J. Phys. Chem. A **105**, 9275 (2001).

[92]A. L. Sobolewski, W. Domcke, C. Dedonder-Lardeux, and C. Jouvet, "Excited-state hydrogen detachment and hydrogen transfer driven by repulsive $^1\pi\sigma^*$ states: A new paradigm for nonradiative decay in aromatic biomolecules", Phys. Chem. Chem. Phys. **4**, 1093 (2002).

[93]Z. Lan, W. Domcke, V. Vallet, A. L. Sobolewski, and S. Mahapatra, "Time-dependent quantum wave-packet description of the $^1\pi\sigma^*$ photochemistry of phenol", J. Chem. Phys. **122**, 224315 (2005).

[94]M. G. Nix, A. L. Devine, R. N. Dixon, and M. N. Ashfold, "Observation of geometric phase effect induced photodissociation dynamics in phenol", Chem. Phys. Lett. **463**, 305 (2008).

[95]O. P. J. Vieuxmaire, Z. Lan, A. L. Sobolewski, and W. Domcke, "*Ab initio* characterization of the conical intersections involved in the photochemistry of phenol", J. Chem. Phys. **129**, 224307 (2008).

[96]H. An and K. K. Baeck, "Quantum wave packet propagation study of the photochemistry of phenol: isotope effects (Ph-OD) and the direct excitation to the $^1\pi\sigma^*$ state", J. Phys. Chem. A **115**, 13309 (2011).

[97]S. G. Ramesh and W. Domcke, "A multi-sheeted three-dimensional potential-energy surface for the H-atom photodissociation of phenol", Faraday Discuss. **163**, 73 (2013).

[98]X. Xu, K. R. Yang, and D. G. Truhlar, "Diabatic molecular orbitals, potential energies, and potential energy surface couplings by the 4-fold way for photodissociation of phenol", J. Chem. Theory Comput. **9**, 3612 (2013).

[99]X. Zhu and D. R. Yarkony, "Fitting coupled potential energy surfaces for large systems: Method and construction of a 3-state representation for phenol photodissociation in the full 33 internal degrees of freedom using multireference configuration interaction determined data", J. Chem. Phys. **140**, 024112 (2014).

[100]D. B. Jones, G. B. da Silva, R. F. C. Neves, H. V. Duque, L. Chiari, E. M. de Oliveira, M. C. Lopes, R. F. da Costa, M. T. do N. Varella, M. H. F. Bettega, M. A. P. Lima, and M. J. Brunger, "An experimental and theoretical investigation into the excited electronic states of phenol", J. Chem. Phys. **141**, 074314 (2014).

[101]X. Xu, J. Zheng, K. R. Yang, and D. G. Truhlar, "Photodissociation dynamics of phenol: Multistate trajectory simulations including tunneling", J. Am. Chem. Soc. **136**, 16378 (2014).

[102]K. R. Yang, X. Xu, J. Zheng, and D. G. Truhlar, "Full-dimensional potentials and state couplings and multidimensional tunneling calculations for the photodissociation of phenol", Chem. Sci. **5**, 4661 (2014).

[103]X. Zhu, C. L. Malbon, and D. R. Yarkony, "An improved quasi-diabatic representation of the 1, 2, 3^1A coupled adiabatic potential energy surfaces of phenol in the full 33 internal coordinates", J. Chem. Phys. **144**, 124312 (2016).

[104]C. Xie, J. Ma, X. Zhu, D. R. Yarkony, D. Xie, and H. Guo, "Nonadiabatic tunneling in photodissociation of phenol", J. Am. Chem. Soc. **138**, 7828 (2016).

[105]H. Guo and D. R. Yarkony, "Accurate nonadiabatic dynamics", Phys. Chem. Chem. Phys. **18**, 26335 (2016).

[106]C. Xie and H. Guo, "Photodissociation of phenol via nonadiabatic tunneling: Comparison of two ab initio based potential energy surfaces", Chem. Phys. Lett. **683**, 222 (2017).

[107]Y. He, H. Zhao, and W. Wang, "Photodissociation of phenol in the adiabatic representation: Tunneling, motions of phenyl ring, and kinetic isotope effects", Int. J. Quantum Chem. **118**, e25786 (2018).

[108]C. Xie, B. Zhao, C. L. Malbon, D. R. Yarkony, D. Xie, and H. Guo, "Insights into the mechanism of nonadiabatic photodissociation from product vibrational distributions. The remarkable case of phenol", J. Phys. Chem. Lett. **11**, 191 (2020).

[109]R. J. Lipert, G. Bermudez, and S. D. Colson, "Pathways of S_1 decay in phenol, indoles, and water complexes of phenol and indole in a free jet expansion", J. Phys. Chem. **92**, 3801 (1988).

[110]C. Ratzer, J. Küpper, D. Spangenberg, and M. Schmitt, "The structure of phenol in the S_1 state determined by high resolution UV-spectroscopy", Chem. Phys. **283**, 153 (2002).

[111]G. A. Cooper, M. R. Cobbin, and M. N. R. Ashfold, "Effects of ring fluorination on the ultraviolet photodissociation dynamics of phenol", J. Phys. Chem. A **124**, 9698 (2020).

[112]M. Mohraz, J. P. Maier, E. Heilbronner, G. Bieri, and R. H. Shiley, "He(Iα) and He(IIα) photoelectron spectra of fluorinated chloro- and bromo-benzenes", J. Electron Spectrosc. **19**, 429 (1980).

[113]N. Deprez, S. Eden, S. V. Hoffmann, N. J. Mason, J. Delwiche, and M.-J. Hubin-Franskin, "Electronic spectroscopy of bromopentafluorobenzene by high-resolution vacuum ultraviolet photoabsorption, electron impact, and photoelectron spectroscopies", Int. J. Mass Spectrom. **277**, 35 (2008).

[114]S. Arepalli, N. Presser, D. Robie, and R. J. Gordon, "The detection of bromine atoms by resonant multiphoton ionization", Chem. Phys. Lett. **117**, 64 (1985).

[115]J. B. Simeonsson and R. C. Sausa, "Trace detection of ambient brominated compounds by laser-induced photofragmentation/fragment detection spectrometry", Spectrochim. Acta B **49**, 1545 (1994).

[116]C. R. Brundle, M. B. Robin, N. A. Kuebler, and H. Basch, "Perfluoro effect in photoelectron spectroscopy. I. Nonaromatic molecules", J. Am. Chem. Soc. **94**, 1451 (1972).

[117]A. P. Hitchcock, P. Fischer, A. Gedanken, and M. B. Robin, "Antibonding σ^* valence MOs in the inner-shell and outer-shell spectra of the fluorobenzenes", J. Phys. Chem., 531.

[118]Y.-R. Luo, *Handbook of Bond Dissociation Energies in Organic Compounds* (CRC Press LLC, Boca Raton, 2003).

[119]J. M. Cox, M. Bain, M. Kellogg, S. E. Bradforth, and S. A. Lopez, "Role of the perfluoro effect in the selective photochemical isomerization of hexafluorobenzene", J. Am. Chem. Soc. **143**, 7002 (2021).

Summary and Outlook

4

This Thesis aimed to unveil how different substituents influence the dynamics of the first excited singlet state S_1 ($\pi\pi^*$ character) in highly fluorinated aromatic compounds. To gain a deeper insight, the number and position of the fluorine atoms attached to the benzene core were systematically varied, additional non-fluorine substituents were introduced, and the aromatic backbone was changed. Overall, nine different molecules were subject of femtosecond time-resolved time-of-flight mass spectrometry and the corresponding photoelectron imaging spectroscopy. Namely, 1,2,3-trifluorobenzene (1,2,3-TriFB), 1,2,4,5-tetrafluorobenzene (1,2,4,5-TFB), 1,2,3,5-TFB, 1,2,3,4-TFB, pentafluorotoluene (PFT), pentafluorophenol (PFPh), chloropentafluorobenzene (ClPFB), bromopentafluorobenzene (BrPFB), and pentafluoropyridine (PFPy) were chosen. Furthermore, the experiments were supported by ab initio calculations at the RI-SCS-MP2 and RI-SCS-CC2 levels of theory.

The excitation wavelengths were carefully selected to exclusively excite the lowest-lying $\pi\pi^*$ states. Thus, 1,2,3-TriFB and PFPy were excited at $\lambda_{\text{pump}} =$ 250 nm and 255 nm, respectively, while $\lambda_{\text{pump}} = 260$ nm was chosen as the excitation wavelength for all other molecules. Subsequent to excitation, the molecules were ionized at either $\lambda_{\text{probe}} = 400$ nm or 800 nm, though the dynamics turned out to be virtually probe-wavelength independent. As exceptions, PFPy and BrPFB were solely ionized at $\lambda_{\text{probe}} = 402$ nm and 400 nm, respectively.

Electronic Deactivation

The electronic deactivation after excitation of the $\pi\pi^*$ states was mapped as the decay of the parent ion yields. Following the leaving of the Franck–Condon (FC) region and internal vibrational redistribution (τ_1/τ_2), two different deactivation patterns were observed. Either the transient behavior was characterized by one long-lived exponential decay ($\tau_4 \geq 800$ ps, 1,2,4,5-TFB, 1,2,3,4-TFB, and PFT), or by a combination of an intermediate ($\tau_3 = 30$–80 ps) and a long-lived exponential decay, substantially shortened to $\tau_4 < 800$ ps (1,2,3-TriFB, 1,2,3,5-

TFB, PFPh, and ClPFB). In the latter case, the intermediate and long-lived decay constants were assigned to two different deactivation channels.

To elucidate the nature of these pathways, the excitation wavelength was altered for selected molecules. Varying the excitation wavelengths for the TFBs by just 5 nm (from $\lambda_{\text{pump}} = 265$ nm to 260 nm for 1,2,3,5-TFB and from $\lambda_{\text{pump}} = 260$ nm to 255 nm for the other two isomers) resulted in considerably reduced overall lifetimes, revealing a barrier along the pathway associated with the long-lived decay constant τ_4. For PFPh, the constant even completely vanished after excitation at wavelengths $\lambda_{\text{pump}} \leq 250$ nm. Ab initio calculations indicated that the energy at these wavelengths might be sufficient to enable O-H bond breaking. Thus, the significantly changed excited state lifetimes were preliminaryly attributed to potentially emerging O-H bond fission. Unfortunately, no fragments were observed, even though they were detected in high-resolution spectroscopy.[1] Employing $\lambda_{\text{pump}} = 243.1$ nm in future experiments as the ionization wavelength may reveal atomic hydrogen and shed light on the presumed OH dissociation channel. In contrast, photodissociation of the C-Br bond was observed for BrPFB. The fragments were presumably generated in the ionic state, but the ultrafast decay of a majority of the parent ion signal lead to the conclusion that dissociation is the all-dominating pathway in the neutral state, too. For all other molecules, dissociation was ruled out confidently as a major decay pathway, as the chosen wavelengths did not introduce sufficient energy to allow bond fission and virtually no fragments were present in the mass spectra.

To unravel the relaxation pathways further, time-resolved photoelectron spectroscopy was employed. For nearly all molecules two distinct photoelectron signals were observed right after excitation. A broad band α comprised photoelectrons with less than 0.7 eV kinetic energy. The second, narrow band β was sharply centered at 0.70–0.92 eV (PFPy and 1,2,4,5-TFB, respectively). The two bands evolved identically in time, and thus were both attributed to originate from the initially excited S_1 state. No further bands emerged at any later delay time for any molecule. The narrow band was assigned to the transition to the ionic ground state (D_0) and the broad one to the transition to the first excited ionic state (D_1). The photoelectron spectrum of PFPy exhibited only the narrow band β, supporting the assignment, because the D_1 state was energetically inaccessible at the chosen wavelengths, prohibiting the rise of the broad band α. Discrepancies between the expected and actual kinetic energies of photoelectrons in the transition to the D_0 states unveiled that intermediate

electronic states are excited by the absorption of a single probe photon in the multi-photon ionization process for essentially all molecules. Whether excitation of these intermediate $\pi\pi^*$ states is also part of the ionization pathway leading to the D_1 state remained largely elusive. However, the results on 1,2,4,5-TFB hint towards differences in the mechanisms.

Even though the studies performed in the scope of this Thesis provide a comprehensive set of data, there are still open questions regarding the S_1 deactivation pathways. As for benzene, most certainly fluorescence will be part of the relaxation process. If radiative or nonradiative channels play a more prominent role for the deactivation needs to be addressed in upcoming investigations. Since no additional PE signals emerged at any delay time in the experiments herein, presumably neither the internal conversion (IC) to different excited singlet states nor intersystem crossing (ISC) to triplet states are involved in the decay. Therefore, the most probable nonradiative pathway is the direct IC to the ground state. Additional calculations and experiments, utilizing different methods like time-resolved infrared absorption, may elucidate if severe structural deformations ease the IC, as reported for benzene. Ultimately, these investigations might also unravel why some of the molecules feature two channels, while others exhibit only one major decay pathway. Overall, however, the work herein gives unprecedented systematic insight into the deactivation dynamics of fluorinated aromatic molecules and lays the foundation for these future investigations.

Manifestation of Vibronic Coupling

Beyond the deactivation dynamics and the ionization pathways, the first picoseconds after excitation turned out to be the most fascinating aspect of the excited-state dynamics of fluorinated aromatic systems. Within this time frame, extensive signal oscillations of both the ion and the electron yield were observed for all molecules, but 1,2,4,5-TFB. The oscillational frequencies mostly ranged between 70–90 cm^{-1}, yet also frequencies up to 281 cm^{-1} (PFPy) were detected. As changing the excitation wavelength did not have any impact on the oscillational frequencies, quantum beating could be ruled out safely as the underlying mechanism. Taking also into account that the photoelectron spectroscopy results established no IC to different excited states took place, these oscillations must originate from cyclic motions on highly distorted S_1 potential energy hypersurfaces (PEHS).

Guided by previous work on pentafluorobenzene (PFB),[2] the oscillations were attributed to vibronic coupling between the $\pi\pi^*$ and higher-lying $\pi\sigma^*$ states, latter lowered in energy compared to benzene owing to the fluorine atoms. In general, the coupling is mediated by out-of-plane vibrational modes. The broadband femtosecond laser pulses excite a wavepacket of these modes in the S_1 state. Motion along the normal mode coordinates of the coupling modes deforms the molecular structures and mixes the electronic characters of the coupling states, stabilizing the lower-lying S_1 state and destabilizing the higher-lying state. More precisely, for PFB the potential energy curves showed pronounced double-well character along the normal mode coordinates of the coupling modes, with a barrier at the quasi-planar Franck–Condon region. In the well minima the ionization probability is reduced. The highly regular movement of the wavepacket on the PEHS between the well minima and the FC region now periodically alters the ionization probability, leading to oscillations of the observables.

The magnitude, i.e., modulation depth, of the oscillation depends on the severity of the induced electronic and molecular changes and its lifetime on the dephasing of the wavepacket. Significant substituent-dependent differences of these two key properties were observed. Introducing more fluorine atoms stabilized the wavepacket and the oscillatory lifetime increased from

$$\tau_{\text{osc}}^{\text{1,2,3-TriFB}} = 0.5 \text{ ps}$$

for 1,2,3-TriFB to

$$\tau_{\text{osc}}^{\text{1,2,3,4-TFB}} = 4.26 \text{ ps}$$

for 1,2,3,4-TFB, even surpassed by PFB[2]

$$\tau_{\text{osc}}^{\text{PFB}} = 6.5 \text{ ps}.$$

Alike, the modulation depth increased in the order of

$$\text{1,2,3-TriFB} < \text{1,2,3,5-TFB} \ll \text{1,2,3,4-TFB} \approx \text{PFB}$$

Ab initio calculations unveiled that the stabilization likely is promoted by a reduction of the $\pi\pi^*$–$\pi\sigma^*$ energy gap, i.e., stronger coupling, since the gap decreases from 1.7 eV for 1,2,3-TriFB to ≈0.9 eV[2] for PFB.

Substituting the hydrogen atom in PFB by a different halogen or functional group, or introducing a heteroatom in the aromatic system, also closes the energy gap (e.g., to 0.3 eV in case of PFPh). Although these reductions lead to expectations of even more pronounced coupling effects, neither an increase in oscillatory lifetime nor in modulation depth were observed. On the contrary, the lifetime decreased in the order of

$$\text{PFB} > \text{PFT} > \text{PFPy} > \text{PFPh} > \text{ClPFB}.$$

and ranged between $\tau_{osc} = 0.66$–2.53 ps for ClPFB and PFT, respectively. The modulation depth basically changed in the same way:

$$\text{PFB} > \text{PFT} > \text{PFPh} \geq \text{PFPy} \gg \text{ClPFB}.$$

Two probable reasons for the destabilization of the wavepacket were determined. First of all, the faster damping of the oscillation may be attributable to the increased mass of the substituents, since ab initio calculations showed strong out-of-plane displacement of these substituents is part of the coupling motion. Moreover, the calculations revealed for ClPFB the coupling between the $\pi\pi^*$ and the second $\pi\sigma^*$ states might be actually more decisive for the dynamics than the coupling to the first $\pi\sigma^*$ state. In contrast to the lesser-fluorinated molecules, the second $\pi\sigma^*$ states are consistently lower in energy for the PFB derivatives, possibly enabling strong, simultaneous coupling between the $\pi\pi^*$ and both $\pi\sigma^*$ states, presumably having overall adverse effects on the regular wavepacket motion. Yet, the coupling to the second $\pi\sigma^*$ state seems to be stronger than to the lower-lying one for 1,2,3-TriFB, too, indicating the coupling strength to different states is most definitely not solely dependent on the simple $\pi\pi^*$–$\pi\sigma^*$ energy gaps.

Multi-Mode Oscillations

Drastic changes of the oscillatory behavior occurred upon introducing a nitrogen atom to the aromatic ring. Albeit not exhibiting the most pronounced or longest-

lived oscillation, the most complex ion yield pattern was observed for PFPy. Four frequencies

$$\nu_{\text{osc1}}^{\text{PFPy}} = 72 \text{ cm}^{-1}$$
$$\nu_{\text{osc2}}^{\text{PFPy}} = 144 \text{ cm}^{-1}$$
$$\nu_{\text{osc3}}^{\text{PFPy}} = 251 \text{ cm}^{-1}$$
$$\nu_{\text{osc4}}^{\text{PFPy}} = 281 \text{ cm}^{-1}$$

modulated the signal. At least three of the frequencies were attributed to genuinely different vibrational modes. In the case of $\nu_{\text{osc2}}^{\text{PFPy}}$ it could not be ruled out that the frequency is an overtone of $\nu_{\text{osc1}}^{\text{PFPy}}$. The underlying vibrational modes most likely all exhibit b_1 symmetry, therefore coupling the $\pi\pi^*$ and the first $\pi\sigma^*$ state. The positions of the main minima and maxima of the signal are dominated by $\nu_{\text{osc1}}^{\text{PFPy}}$. All other frequencies merely alter the peak shape at the maxima. The complex modulation pattern prohibited fitting and consequently determination of the damping times. Nevertheless, the dynamics of PFPy impressively show a basic concept of vibronic coupling, previously only ascertained in simulations. The dynamics simulations clearly predicted that the oscillation will not be stable and observable if the $\pi\pi^*$ and the $\pi\sigma^*$ states are just coupled by one mode. Actually only the movement of a coherent wavepacket of modes induces strong oscillations.[2] Yet, the observed signals were only modulated by a single, dominant mode. The observed oscillation pattern of PFPy, however, now prove the motion of more than one mode can be mapped experimentally in real time.

A similarly unique behavior was detected for the parent ion yield of 1,2,3,5-TFB, featuring two different oscillational frequencies:

$$\nu_{\text{osc1}}^{\text{1,2,3,5-TFB}} = 94 \text{ cm}^{-1}$$
$$\nu_{\text{osc2}}^{\text{1,2,3,5-TFB}} = 138 \text{ cm}^{-1}.$$

Notwithstanding of their considerably different periods, the oscillations were equally long-lived with

$$\tau_{\text{osc1}}^{\text{1,2,3,5-TFB}} = 1.25 \text{ ps}$$
$$\tau_{\text{osc2}}^{\text{1,2,3,5-TFB}} = 1.03 \text{ ps}.$$

Contrary to PFPy, both oscillatory components were also equally intense. The frequencies were assigned to two different types of out-of-plane modes, the a_2

and the b_1 modes, mediating the coupling of the $\pi\pi^*$ state to two different $\pi\sigma^*$ states.

1,2,3,5-TFB belongs to the arguably most astonishing set of molecules within this work: the tetrafluorobenzenes. Despite identical number of fluorines and near identical electronic structure, these three molecules exhibit completely different coupling dynamics. While the ion yield of 1,2,3,5-TFB oscillates with two frequencies, only a single frequency was detected for 1,2,3,4-TFB. Yet, latter oscillation was far more pronounced compared to the oscillations observed for 1,2,3,5-TFB. Furthermore, no oscillation at all was observed for 1,2,4,5-TFB. The lack thereof is in contrast to previously published high-resolution studies on 1,2,4,5-TFB,[3] reporting a distinct double-well potential along the normal mode coordinate of the lowest-frequency coupling mode. However, the deformation of the PEHS of 1,2,4,5-TFB by vibronic coupling was estimated to be too shallow to alter ionization probability in broadband femtosecond experiments. The true reason why the coupling seems to be less strong in 1,2,4,5-TFB and why multi-mode oscillations are solely observed for 1,2,3,5-TFB, and also for PFPy, was not resolved by the supporting ab initio calculations and thus remained elusive.

Outlook

Especially the behavior of the TFB isomers highlights the limitation of the ab initio methods RI-SCS-MP2 and RI-SCS-CC2 employed herein. The methods are well-suited to predict trends like the equilibrium molecular structures in excited states or the magnitude of the vibrational frequencies, but fail in accounting for the fine details of vibronic coupling. To elucidate the origins of the signal variations for the isomers, as well as of the trends in lifetime and modulation depth for the other molecules herein, high-level ab initio calculations in combination with quantum dynamics simulations are needed, as were already conducted for PFB.[2] This very much non-trivial task becomes even more challenging when not merely including the coupling modes, but also the totally-symmetric tuning modes, altering the potential energy difference of the coupled states. Their inclusion might eventually be necessary for the simulations to fit to the experiments and may explain, why for some molecules the coupling to the second $\pi\sigma^*$ state appears to be stronger than to the lower-lying one. Similar calculations are also needed to unravel how the fluorine atoms alter the O-H bond fission in PFPh, as the preliminary calculations in this work are just the first step to do so.

Besides theoretical studies, several questions may be answered by additional experimental investigations. Firstly, high-resolution transition energies to the (excited) neutral and ionic states may further substantiate the proposed ionization mechanisms. Moreover, in the past it was suggested the photoelectrons should oscillate in both intensity and energy regime, but the excitation of intermediate states prohibited their detection. Shortening the ionization wavelength to $\lambda_{\text{probe}} = 200$ nm and enabling single-photon ionization may reveal these energy oscillations. Since in this work a consistent decrease in modulation depth was observed when choosing $\lambda_{\text{probe}} = 400$ nm over $\lambda_{\text{probe}} = 800$ nm as the probe wavelength, the modulation depth might turn out to be even worse at $\lambda_{\text{probe}} = 200$ nm. In addition, the latter also allows for two-photon single-color ionization of molecules in the ground state, increasing the background signal. Nevertheless, switching to a highly energetic probe wavelength will be the only option to prohibit extensive excitation of intermediate states. Though largely irrelevant for the other molecules, probing at $\lambda_{\text{probe}} = 243.1$ nm would be key to shed light on the presumed O-H bond dissociation of PFPh by ionizing atomic hydrogen. If fragments are detected, the actual dissociation barrier can be determined by tuning the pump wavelength, too. Finally, the electronic deactivation of the S_1 state is for the most part not yet understood. As a first step, the lifetimes in the gas phase and in solution should be compared, because if the decay mechanisms in both phases are identical a broad variety of experimental techniques becomes available to ultimately elucidate the mechanism.

Notwithstanding of the challenges ahead, this Thesis provides a solid experimental foundation for future studies. The diverse dynamics of all nine molecules allow to propose some rules of thumb which should be fulfilled to enable observation of vibronic coupling.

1. The higher the number of fluorine atoms and the closer these are, the more likely oscillations will occur.
2. At least three fluorine atoms should be in close vicinity to each other.
3. Additional substituents tend to damp the oscillation.
4. Less calculated energy between the $\pi\pi^*$ and the $\pi\sigma^*$ states does not necessarily equals stronger oscillations.

These rules may be utilized by experimentalists to design new types of systems exhibiting vibronic coupling. Especially interesting will be if rule no. 3

also holds true for extended aromatic systems with multiple rings (e.g., trans-2, 3, 4, 5, 6, 2′, 3′, 4′, 5′, 6′-decafluorostilbene). For theoreticians, in particular the observations for the TFB isomers may be fruitful. In contrast to most other molecules, the electronic structure of these three isomers is nearly equal and rather simple. No distortion by *n* orbitals (PFPy), or bond fission (PFPh) are to be expected. Yet, their dynamics are distinctly different. Therefore, the TFB isomers are a promising set of molecules to benchmark novel multi-mode vibronic coupling models, and to explore how the potential energy hypersurface has to be shaped to enable observation of (multi-frequency) oscillations in the first place.

References

[1]G. A. Cooper, M. R. Cobbin, and M. N. R. Ashfold, "Effects of ring fluorination on the ultraviolet photodissociation dynamics of phenol", J. Phys. Chem. A **124**, 9698 (2020).

[2]O. Hüter, M. Sala, H. Neumann, S. Zhang, H. Studzinski, D. Egorova, and F. Temps, "Long-lived coherence in pentafluorobenzene as a probe of $\pi\pi^*$ – $\pi\sigma^*$ vibronic coupling", J. Chem. Phys. **145**, 014302 (2016).

[3]K. Okuyama, T. Kakinuma, M. Fujii, N. Mikami, and M. Ito, "Electronic spectra of 1,2,4,5-tetrafluorobenzene in a supersonic jet: Butterfly tunneling in the excited state", J. Phys. Chem. **90**, 3948 (1986).

Danksagung

Zuallererst möchte ich mich bei meinem Betreuer Prof. Friedrich Temps für die Möglichkeit bedanken in seinem Arbeitskreis an einem hochaktuellen und spannenden Themenfeld arbeiten zu können. Außerdem danke ich Ihnen ausdrücklich für die wissenschaftlichen Freiheiten die Sie mir ermöglicht haben, sodass ich mich als Wissenschaftler entscheidend weiterentwickeln konnte!

Sonja Ehmke und Tanja Stojšić gebührt mein Dank für ihre unermüdliche Hilfe bei allen Verwaltungs- und Organisationsfragen und dass ihr immer Euer Möglichstes getan habt schnell und unbürokratisch Lösungen zu finden.

Dem gesamten technischen Personal, Haxhi Dragusha, Uwe Eggers, Timo Görgens, Finn-Ole Grünau, Frank Herzog, Michael Karstens, Frank Laasch, Mark Pohl, Andreas Sievers, Klaus Warns und Klaus-Dieter Will danke ich herzlich für Eure immer wieder hervorragenden Ideen und Umsetzungen allerlei mehr oder weniger sinnigen Aufbauten! Zusätzlich danke ich insbesondere Timo, Frank und Andreas für eure Geduld mir ständig wieder euer Handwerk zu erklären und über alles Mögliche zu diskutieren. Das wird mir fehlen.

Die Vakuumtechnik, das Gasphasen UV und diverse andere Spielereien wären sicherlich nicht so reibungsfrei gelaufen ohne Joachim Gripp. Dafür danke ich dir sehr!

Auch wenn das Endergebnis jetzt deutlich anders aussieht, danke ich Falk Renth für seine zahlreichen Korrekturanmerkungen, die mir in einigen Bereichen doch nochmal eine neue Sicht auf meine Arbeit ermöglicht haben.

Riesen Dank gebührt unbestreitbar allen aktuellen und ehemaligen Mitgliedern des AK Temps, Julia Bahrenburg, Dennis Bank, Birthe Behr, Mats Bohnsack, Hendrik Böhnke, Swantje Caliebe, Mahmoud M. Elshanawany, Simone Gorski-Bilke, Rebecca Holtmann, Ole Hüter, Anja Köhntopp, Vivian Lukaszczuk, Rebecca Marschan, Sebastian Megow, Amke Nimmrich, Pascal Pessier, Hendrik Rapp, Tim Raeker, Katharina Röttger, Matthieu Sala, Sebastian Schatz, Uta C. Stange, Alexander Thrun, Shuangqing Wang und Malte Wellmann (ich hoffe, ich habe niemanden vergessen). Eure Hilfe und der meist gesittete Meinungsaustausch zu Experimentaufbauten, Messdaten und deren Interpretation, generell dummen Ideen und gesellschaftlichen sowie politische Fragestellungen (wo wir dann ins

ungesittete abdriften..) werde ich nie vergessen! Die Hilfsbereitschaft die ich von euch erfahren habe sucht seinesgleichen! Ich bin froh in meiner Zeit viele besondere Menschen kennengelernt zu haben, die ich jetzt auch meine Freunde nennen darf. Ich danke euch auch dafür, dass ihr sehr tolerant bezüglich der Musikwahl im Keller wart.

Ole Hüter danke ich zunächst einmal für den Aufbau des Experiments, sodass diese Arbeit überhaupt möglich war. Viel wichtiger jedoch, du hast dich, obwohl Du selbst in der stressigen Endphase deiner Doktorarbeit warst, meiner angenommen und mich detailliert in das Experiment eingearbeitet. Auch die zahlreichen Diskussionen zu Weiterentwicklungen der Methoden und Messdaten waren für mich von unschätzbarem Wert!

Meinem Nachfolger, Pascal Pessier, wünsche ich alles erdenklich Gute und massiven Erfolg für seine Arbeit. Ich bin überzeugt, dass du den haben wirst! Ich habe mein Möglichstes getan dich gut einzuarbeiten und hoffe, das ist mir gelungen. Im Gegenzug hast du mir durch Diskussion über meine Daten und Korrekturlesen auch äußerst weitergeholfen!

Meinem Büro, Birthe, Sebastian und Hendrik danke ich für die tolle Arbeitsatmosphäre, die von totaler, konzentrierter Stille bis zu Meine-Ohren-bluten-von-Weihnachtsmusik alles beinhaltete!

Außeruniversitär (ab hier dann ohne Nachnamen, Datenschutz und so) danke ich Dennis, Lea, Rebecca, Jan, Pascal, Sebastian und Carina für die Donnerstagabende. Auch wenn trash-TV nicht zu meiner Dauerunterhaltung wird, waren und (hoffentlich bald wieder) sind die Abende doch immer wieder ein highlight meiner Woche.

Hendrik und Hinnerk danke ich besonders für die Zeit am Wasser, die mich doch immer wieder auf den Boden der Tatsachen geholt und zu meiner Entspannung maßgeblich beigetragen hat. Ich sollte zwar wahrscheinlich aufgeben die Heringskrone erringen zu wollen und gemessen an meiner Erfolgsquote die Angel ganz einmotten, aber ich freue mich dennoch auf den nächsten Tag/Abend mit euch! Weiterhin danke ich euch, dass ihr immer ein offenes Ohr habt.

Es gibt sicherlich nicht viele Wegbegleiter, abgesehen von meiner Familie, die mich so lange schon unterstützen wie Leon und Esther, sowie Keven und Michi. Danke, dass ich mich bisher immer auf euch verlassen konnte (und mir auch sicher sein kann, dass es so bleibt) und für die zahllosen gemeinsamen Abende, sei es an einem Ort oder nur ein virtuelles Zusammenkommen.

Flo, Markus, Jasmin und Michi danke ich herzlich für die vielen Stunden, meist digitaler Unterhaltung, die zum Abschalten Gold wert waren. Obwohl ich mich auch wieder darauf freue, hoffe ich auch, dass wir uns bald auf einem analogen Spieleabend o. Ä. treffen werden!

Der größte Dank von allen geht aber ganz klar an meine Familie(n). Kein einziger Datenpunkt der Originaldaten, geschweige denn ein Wort in dieser Arbeit, wäre zustande gekommen, wenn ihr nicht als Fels in der Brandung und Unterstützung in allen Lebenslagen da gewesen wärt. Ihr habt euch über jeden Erfolg genauso gefreut wie ich und habt mit mir bei jedem Misserfolg und Rückschlag gelitten, mich aber auch wieder aufgebaut. Diese Arbeit ist ebenso eure wie es meine ist. Ich bin unendlich froh jeden Einzelnen von euch zu haben.

Lina und Benjamin, ihr seid das Licht meines Lebens.

Calculated Cartesian Coordinates

A

Table A.1. Calculated cartesian coordinates in the S_0 state ($1\ ^1A_1$) of 1,2,3-TriFB in Å, optimized at RI-SCS-MP2 level of theory.

C	1.212 549 3	0.000 000 0	−0.747 363 0
C	1.197 679 1	0.000 000 0	0.639 399 7
C	0.000 000 0	0.000 000 0	1.347 138 0
C	−1.197 679 1	0.000 000 0	0.639 399 7
C	−1.212 549 3	0.000 000 0	−0.747 363 0
C	0.000 000 0	0.000 000 0	−1.435 599 3
H	2.162 128 5	0.000 000 0	−1.262 201 5
F	2.344 817 4	0.000 000 0	1.331 956 7
F	0.000 000 0	0.000 000 0	2.681 028 2
F	−2.344 817 4	0.000 000 0	1.331 956 7
H	−2.162 128 5	0.000 000 0	−1.262 201 5
H	0.000 000 0	0.000 000 0	−2.516 121 9

Table A.2. Calculated cartesian coordinates in the S_1 state ($1\ ^1B_2$) of 1,2,3-TriFB in Å, optimized at RI-SCS-CC2 level of theory.

C	1.222 535 2	−0.029 310 3	−0.761 216 7
C	1.205 399 3	0.061 109 8	0.660 563 5
C	0.001 397 7	0.172 702 8	1.423 936 2
C	−1.204 107 7	0.059 769 2	0.663 128 0
C	−1.224 083 9	−0.030 630 1	−0.758 630 2
C	−0.001 499 3	−0.100 503 0	−1.484 369 9
H	2.178 923 3	0.014 229 9	−1.263 628 5
F	2.373 313 1	0.145 316 1	1.311 336 2
F	0.003 005 2	−0.251 531 4	2.710 431 2
F	−2.370 738 3	0.142 793 6	1.316 315 1
H	−2.181 547 4	0.011 877 4	−1.259 092 9
H	−0.002 597 3	−0.195 824 1	−2.558 772 1

Table A.3. Calculated cartesian coordinates in the D_0 state ($1\ ^2B_1$) of 1,2,3-TriFB in Å, optimized at RI-SCS-MP2 level of theory.

C	1.253 413 7	−0.000 045 3	−0.738 347 6
C	1.238 953 5	−0.000 047 5	0.621 060 7
C	−0.005 667 5	0.000 003 4	1.337 938 7
C	−1.250 422 3	0.000 040 1	0.634 189 7
C	−1.253 493 3	0.000 042 1	−0.727 248 7
C	0.012 401 3	0.000 001 1	−1.396 465 7
H	2.184 498 4	−0.000 066 5	−1.285 349 7
F	2.323 767 4	−0.000 086 6	1.337 823 2
F	0.009 096 5	0.000 016 8	2.629 815 8
F	−2.342 868 6	0.000 072 3	1.352 220 1
H	−2.177 713 4	0.000 070 4	−1.286 072 0
H	0.008 034 4	−0.000 000 4	−2.479 535 7

Table A.4. Calculated cartesian coordinates in the S_0 state ($1\ ^1A_g$) of 1,2,4,5-TFB in Å, optimized at RI-SCS-MP2 level of theory.

C	0.695 169 8	1.194 601 3	0.000 000 0
C	1.400 765 7	0.000 000 0	0.000 000 0
C	0.695 169 8	−1.194 601 3	0.000 000 0
C	−0.695 169 8	−1.194 601 3	0.000 000 0
C	−1.400 765 7	0.000 000 0	0.000 000 0
C	−0.695 169 8	1.194 601 3	0.000 000 0
F	−1.354 665 1	2.359 784 5	0.000 000 0
F	1.354 665 1	2.359 784 5	0.000 000 0
H	2.480 595 6	0.000 000 0	0.000 000 0
F	1.354 665 1	−2.359 784 5	0.000 000 0
F	−1.354 665 1	−2.359 784 5	0.000 000 0
H	−2.480 595 6	0.000 000 0	0.000 000 0

Table A.5. Calculated cartesian coordinates in the S_1 state ($1\ ^1B_{2u}$) of 1,2,4,5-TFB in Å, optimized at RI-SCS-CC2 level of theory.

C	0.712 715 5	1.183 738 1	0.132 392 5
C	1.492 237 6	−0.000 013 7	0.209 269 3
C	0.712 690 2	−1.183 752 2	0.132 442 6
C	−0.712 716 7	−1.183 737 9	0.132 459 3
C	−1.492 231 4	0.000 018 9	0.209 342 9
C	−0.712 691 3	1.183 762 3	0.132 506 3
F	−1.324 090 7	2.359 812 5	−0.040 157 8
F	1.324 116 5	2.359 748 4	−0.040 528 5
H	2.541 470 5	−0.000 019 3	0.460 558 1
F	1.324 073 4	−2.359 801 0	−0.040 282 1
F	−1.324 133 9	−2.359 750 1	−0.040 397 5
H	−2.541 467 3	0.000 024 9	0.460 457 5

Table A.6. Calculated cartesian coordinates in the D_0 state ($1\ ^2B_{1g}$) of 1,2,4,5-TFB in Å, optimized at RI-SCS-MP2 level of theory.

C	0.725 245 4	1.172 240 8	0.000 000 0
C	1.449 292 8	0.000 000 0	0.000 000 0
C	0.725 245 4	−1.172 240 8	0.000 000 0
C	−0.725 245 4	−1.172 240 8	0.000 000 0
C	−1.449 292 8	0.000 000 0	0.000 000 0
C	−0.725 245 4	1.172 240 8	0.000 000 0
F	−1.309 455 9	2.329 268 8	0.000 000 0
F	1.309 455 9	2.329 268 8	0.000 000 0
H	2.530 016 4	0.000 000 0	0.000 000 0
F	1.309 455 9	−2.329 268 8	0.000 000 0
F	−1.309 455 9	−2.329 268 8	0.000 000 0
H	−2.530 016 4	0.000 000 0	0.000 000 0

Table A.7. Calculated cartesian coordinates in the D_1 state ($1\ ^2B_{2g}$) of 1,2,4,5-TFB in Å, optimized at RI-SCS-CC2 level of theory.

C	0.687 042 3	1.238 042 8	−0.000 002 7
C	1.378 346 0	−0.000 101 5	−0.000 005 9
C	0.686 859 3	−1.238 143 6	0.000 002 5
C	−0.687 042 4	−1.238 043 1	0.000 000 4
C	−1.378 346 3	0.000 101 4	−0.000 006 2
C	−0.686 859 1	1.238 143 5	0.000 005 5
F	−1.383 166 9	2.351 125 6	0.000 027 0
F	1.383 512 8	2.350 922 3	−0.000 004 8
H	2.463 707 0	−0.000 184 9	−0.000 016 2
F	1.383 166 8	−2.351 125 8	0.000 011 9
F	−1.383 512 2	−2.350 922 9	0.000 010 2
H	−2.463 707 3	0.000 186 1	−0.000 021 6

Table A.8. Calculated cartesian coordinates in the D_2 state ($1\ ^2B_{3u}$) of 1,2,4,5-TFB in Å, optimized at RI-SCS-CC2 level of theory.

C	0.712 979 1	1.214 869 2	0.000 006 7
C	1.440 908 0	−0.000 106 9	0.000 012 8
C	0.712 800 1	−1.214 974 6	−0.000 000 4
C	−0.712 979 2	−1.214 869 4	−0.000 002 0
C	−1.440 908 0	0.000 106 7	−0.000 007 5
C	−0.712 800 0	1.214 974 4	−0.000 009 0
F	−1.351 663 4	2.357 182 4	−0.000 025 2
F	1.352 011 5	2.356 982 3	0.000 015 6
H	2.523 282 3	−0.000 186 3	0.000 025 6
F	1.351 663 1	−2.357 182 7	−0.000 013 6
F	−1.352 011 2	−2.356 982 6	0.000 004 1
H	−2.523 282 3	0.000 187 4	−0.000 007 1

Table A.9. Calculated cartesian coordinates in the S_0 state ($1\ ^1A_1$) of 1,2,3,5-TFB in Å, optimized at RI-SCS-MP2 level of theory.

C	1.218 783 6	0.000 000 0	0.725 461 8
C	0.000 000 0	0.000 000 0	1.387 925 6
C	−1.218 783 6	0.000 000 0	0.725 461 8
C	−1.195 789 8	0.000 000 0	−0.661 846 8
C	0.000 000 0	0.000 000 0	−1.372 112 6
C	1.195 789 8	0.000 000 0	−0.661 846 8
F	2.344 194 2	0.000 000 0	−1.347 229 2
H	2.154 822 1	0.000 000 0	1.262 401 7
F	−2.344 194 2	0.000 000 0	−1.347 229 2
F	0.000 000 0	0.000 000 0	−2.705 869 7
F	0.000 000 0	0.000 000 0	2.732 480 1
H	−2.154 822 1	0.000 000 0	1.262 401 7

Table A.10. Calculated cartesian coordinates in the S_1 state ($1\ ^1B_2$) of 1,2,3,5-TFB in Å, optimized at RI-SCS-CC2 level of theory.

C	1.194 852 7	0.255 635 3	1.065 381 6
C	−0.063 171 3	0.026 145 1	1.688 447 2
C	−1.286 457 5	−0.198 247 7	1.021 215 2
C	−1.218 931 4	−0.124 738 8	−0.386 783 7
C	0.022 179 2	0.052 320 4	−1.063 330 1
C	1.255 653 4	0.241 303 2	−0.353 902 6
F	2.389 952 7	−0.217 890 8	−0.956 717 9
H	2.070 256 9	0.442 120 9	1.670 286 8
F	−2.343 442 3	0.058 466 4	−1.095 386 1
F	0.017 545 3	0.123 227 6	−2.390 403 4
F	−0.083 790 5	0.040 011 4	3.025 008 0
H	−2.203 247 9	−0.398 369 6	1.551 323 6

Table A.11. Calculated cartesian coordinates in the D_0 state ($1\ ^2B_1$) of 1,2,3,5-TFB in Å, optimized at RI-SCS-MP2 level of theory.

C	1.249 358 0	−0.000 011 7	0.716 614 1
C	0.000 020 4	0.000 004 5	1.365 857 3
C	−1.249 325 1	−0.000 005 6	0.716 713 1
C	−1.249 336 8	−0.000 006 4	−0.647 930 2
C	−0.000 030 0	0.000 008 0	−1.361 782 2
C	1.249 309 0	−0.000 015 1	−0.648 032 2
F	2.334 556 6	−0.000 028 2	−1.371 195 3
H	2.170 501 8	−0.000 014 4	1.282 364 0
F	−2.334 604 4	−0.000 005 6	−1.371 027 9
F	−0.000 091 7	0.000 044 4	−2.635 853 7
F	0.000 082 5	0.000 033 0	2.671 765 9
H	−2.170 440 2	−0.000 002 8	1.282 505 4

Table A.12. Calculated cartesian coordinates in the S_0 state ($1\ ^1A_1$) of 1,2,3,4-TFB in Å, optimized at RI-SCS-MP2 level of theory.

C	0.695 425 0	0.000 000 0	−1.165 889 4
C	1.381 299 8	0.000 000 0	0.045 400 5
C	0.697 645 9	0.000 000 0	1.250 023 0
C	−0.697 645 9	0.000 000 0	1.250 023 0
C	−1.381 299 8	0.000 000 0	0.045 400 5
C	−0.695 425 0	0.000 000 0	−1.165 889 4
F	−1.357 148 5	0.000 000 0	−2.322 133 8
F	1.357 148 5	0.000 000 0	−2.322 133 8
H	−1.258 024 8	0.000 000 0	2.173 105 5
F	−2.720 708 4	0.000 000 0	0.019 494 2
F	2.720 708 4	0.000 000 0	0.019 494 2
H	1.258 024 8	0.000 000 0	2.173 105 5

Table A.13. Calculated cartesian coordinates in the S_1 state ($2\ ^1A_1$) of 1,2,3,4-TFB in Å, optimized at RI-SCS-CC2 level of theory.

C	0.742 154 2	−0.104 308 7	−1.266 013 1
C	1.370 994 9	−0.069 184 2	0.017 388 4
C	0.686 844 2	−0.013 608 5	1.262 321 2
C	−0.717 264 7	0.102 663 9	1.300 424 9
C	−1.368 230 5	0.026 781 9	0.050 780 0
C	−0.675 842 0	−0.064 028 0	−1.199 991 2
F	−1.406 512 4	−0.300 275 6	−2.297 118 1
F	1.370 138 6	0.530 301 7	−2.306 482 7
H	−1.278 663 9	0.240 666 9	2.210 264 0
F	−2.696 719 3	−0.029 973 9	0.006 997 5
F	2.704 025 6	−0.179 540 2	0.055 651 6
H	1.269 075 3	−0.139 495 5	2.165 777 7

Table A.14. Calculated cartesian coordinates in the D_0 state ($1\ ^2A_2$) of 1,2,3,4-TFB in Å, optimized at RI-SCS-MP2 level of theory.

C	0.686 612 6	0.000 000 0	−1.215 761 7
C	1.365 279 4	0.000 000 0	0.038 981 0
C	0.683 804 7	0.000 000 0	1.285 261 6
C	−0.683 804 7	0.000 000 0	1.285 261 6
C	−1.365 279 4	0.000 000 0	0.038 981 0
C	−0.686 612 6	0.000 000 0	−1.215 761 7
F	−1.382 036 2	0.000 000 0	−2.319 385 6
F	1.382 036 2	0.000 000 0	−2.319 385 6
H	−1.267 893 6	0.000 000 0	2.194 786 6
F	−2.654 063 0	0.000 000 0	0.016 072 4
F	2.654 063 0	0.000 000 0	0.016 072 4
H	1.267 893 6	0.000 000 0	2.194 786 6

Table A.15. Calculated cartesian coordinates in the S_0 state ($1\ ^1A_1$) of PFPy in Å, optimized at RI-SCS-MP2 level of theory.

N	0.000 000 0	0.000 000 0	−1.607 713 2
C	1.128 581 1	0.000 000 0	−0.934 180 9
C	1.200 908 6	0.000 000 0	0.452 889 7
C	−1.128 581 1	0.000 000 0	−0.934 180 9
C	−1.200 908 6	0.000 000 0	0.452 889 7
C	0.000 000 0	0.000 000 0	1.155 042 5
F	−2.258 710 7	0.000 000 0	−1.631 299 4
F	−2.361 500 2	0.000 000 0	1.099 176 7
F	2.361 500 2	0.000 000 0	1.099 176 7
F	0.000 000 0	0.000 000 0	2.479 512 2
F	2.258 710 7	0.000 000 0	−1.631 299 4

Table A.16. Calculated cartesian coordinates in the S_1 state ($1\ ^1B_2$) of PFPy in Å, optimized at RI-SCS-CC2 level of theory.

N	−0.000 053 6	0.224 785 8	−1.679 860 5
C	1.100 055 1	0.068 822 6	−0.936 764 7
C	1.167 248 6	−0.109 288 1	0.475 071 1
C	−1.100 132 1	0.069 190 8	−0.936 644 8
C	−1.167 234 3	−0.108 911 2	0.475 194 7
C	0.000 042 9	−0.148 383 6	1.296 472 3
F	−2.242 262 1	0.014 255 3	−1.594 263 0
F	−2.368 595 7	−0.302 094 5	1.016 220 5
F	2.368 598 5	−0.302 852 2	1.015 974 3
F	0.000 239 2	0.581 016 0	2.463 105 3
F	2.242 093 5	0.013 459 1	−1.594 505 3

Table A.17. Calculated cartesian coordinates in the D_0 state ($1\ ^2A_2$) of PFPy in Å, optimized at RI-SCS-MP2 level of theory.

N	0.000 000 0	0.000 000 0	−1.658 594 3
C	1.111 993 0	0.000 000 0	−0.968 792 2
C	1.174 596 3	0.000 000 0	0.479 276 3
C	−1.111 993 0	0.000 000 0	−0.968 792 2
C	−1.174 596 3	0.000 000 0	0.479 276 3
C	0.000 000 0	0.000 000 0	1.199 998 6
F	−2.239 192 4	0.000 000 0	−1.590 902 0
F	−2.321 832 4	0.000 000 0	1.058 642 8
F	2.321 832 4	0.000 000 0	1.058 642 8
F	0.000 000 0	0.000 000 0	2.502 145 7
F	2.239 192 4	0.000 000 0	−1.590 902 0

Table A.18. Calculated cartesian coordinates in the S_0 state ($1\ ^1A'$) of PFT in Å, optimized at RI-SCS-MP2 level of theory.

C	0.017 713 3	1.174 071 0	0.000 000 0
C	1.405 864 8	1.153 430 4	0.000 000 0
C	2.067 283 2	−0.070 510 4	0.000 000 0
C	1.333 917 3	−1.250 345 3	0.000 000 0
C	−0.056 354 8	−1.193 076 7	0.000 000 0
C	−0.751 484 5	0.012 444 6	0.000 000 0
C	−2.254 858 4	0.084 635 0	0.000 000 0
F	−0.600 148 9	2.364 068 1	0.000 000 0
F	2.106 154 4	2.288 211 8	0.000 000 0
F	3.398 391 6	−0.110 033 5	0.000 000 0
F	1.964 660 0	−2.425 414 4	0.000 000 0
F	−0.727 577 9	−2.353 872 9	0.000 000 0
H	−2.683 594 5	−0.913 078 0	0.000 000 0
H	−2.609 982 9	0.619 735 2	−0.879 831 1
H	−2.609 982 9	0.619 735 2	0.879 831 1

Table A.19. Calculated cartesian coordinates in the S_1 state ($2\ ^1A'$) of PFT in Å, optimized at RI-SCS-CC2 level of theory.

C	0.021 703 9	1.159 728 5	0.163 209 9
C	1.451 085 9	1.129 509 6	0.129 627 6
C	2.194 908 0	−0.070 126 1	−0.001 248 8
C	1.375 720 3	−1.227 020 1	0.005 805 4
C	−0.052 787 6	−1.169 435 0	0.040 831 1
C	−0.802 658 8	0.022 699 1	0.056 758 2
C	−2.290 141 9	0.080 386 8	−0.136 285 0
F	−0.540 315 5	2.345 344 5	0.411 423 3
F	2.086 297 9	2.280 220 0	0.376 616 6
F	3.326 588 9	−0.065 072 9	−0.786 224 5
F	1.935 478 1	−2.435 393 6	0.128 829 8
F	−0.690 052 9	−2.336 279 1	0.165 429 7
H	−2.760 433 6	−0.810 912 7	0.274 691 2
H	−2.551 412 5	0.144 038 1	−1.196 139 2
H	−2.703 980 2	0.952 312 8	0.366 674 7

Table A.20. Calculated cartesian coordinates in the D_0 state ($1\ ^2A''$) of PFT in Å, optimized at RI-SCS-MP2 level of theory.

C	0.028 868 1	1.150 230 0	−0.000 047 5
C	1.447 178 1	1.162 067 9	0.000 092 4
C	2.110 068 1	−0.034 316 0	−0.000 040 9
C	1.332 429 3	−1.235 451 7	0.000 029 2
C	−0.098 154 8	−1.210 885 3	−0.000 114 6
C	−0.779 799 0	−0.022 354 7	0.000 007 3
C	−2.274 481 7	0.085 117 7	0.000 020 4
F	−0.567 316 5	2.305 254 1	−0.000 092 4
F	2.085 476 1	2.304 128 0	0.000 149 1
F	3.408 446 4	−0.133 906 8	−0.000 041 6
F	1.944 440 7	−2.358 123 4	0.000 119 7
F	−0.698 539 9	−2.378 771 7	−0.000 155 9
H	−2.727 191 8	−0.901 392 2	0.000 048 6
H	−2.605 723 1	0.634 184 1	−0.881 300 7
H	−2.605 700 0	0.634 220 2	0.881 327 0

Table A.21. Calculated cartesian coordinates in the S_0 state ($1\ ^1A'$) of PFPh in Å, optimized at RI-SCS-MP2 level of theory.

C	−0.413 492 7	1.276 144 9	0.000 000 0
C	0.975 886 0	1.230 938 6	0.000 000 0
C	1.639 939 1	0.008 232 7	0.000 000 0
C	0.905 126 5	−1.171 264 3	0.000 000 0
C	−0.481 885 3	−1.110 933 7	0.000 000 0
C	−1.165 817 0	0.102 130 5	0.000 000 0
O	−2.519 551 5	0.182 580 1	0.000 000 0
F	−1.032 025 9	2.457 262 6	0.000 000 0
F	1.676 778 7	2.364 300 7	0.000 000 0
F	2.972 209 3	−0.031 097 0	0.000 000 0
F	1.525 595 0	−2.350 827 1	0.000 000 0
F	−1.204 274 3	−2.245 168 6	0.000 000 0
H	−2.878 487 9	−0.712 299 4	0.000 000 0

Table A.22. Calculated cartesian coordinates in the S_1 state ($2\ ^1A'$) of PFPh in Å, optimized at RI-SCS-CC2 level of theory.

C	−3.970 276 0	0.381 152 9	0.010 950 0
C	−2.561 233 1	0.361 290 4	0.004 227 6
C	−1.939 697 9	−0.902 264 0	0.027 813 3
C	−2.674 875 7	−2.120 320 6	0.042 535 3
C	−4.072 523 9	−2.101 460 2	0.017 453 2
C	−4.719 099 4	−0.826 209 6	−0.000 793 4
O	−6.053 119 2	−0.732 989 1	0.076 225 9
F	−4.611 566 7	1.526 579 9	0.278 544 6
F	−1.870 349 2	1.442 200 4	−0.425 393 1
F	−0.612 106 6	−0.967 118 3	0.079 924 2
F	−2.014 966 1	−3.256 212 8	0.328 379 1
F	−4.774 480 1	−3.151 745 9	−0.534 555 5
H	−6.414 016 0	−1.637 073 2	0.094 688 8

Table A.23. Calculated cartesian coordinates in the D_0 state ($1\ ^2A''$) of PFPh in Å, optimized at RI-SCS-MP2 level of theory.

C	−0.380 516 7	1.279 391 2	0.000 000 0
C	0.983 237 5	1.271 719 6	0.000 000 0
C	1.619 003 1	0.042 992 7	0.000 000 0
C	0.881 070 1	−1.208 168 8	0.000 000 0
C	−0.488 907 9	−1.173 367 0	0.000 000 0
C	−1.150 278 2	0.066 515 3	0.000 000 0
O	−2.461 610 7	0.209 988 6	0.000 000 0
F	−1.026 579 9	2.398 197 1	0.000 000 0
F	1.685 150 3	2.380 581 6	0.000 000 0
F	2.897 042 4	−0.028 582 2	0.000 000 0
F	1.571 027 2	−2.313 051 3	0.000 000 0
F	−1.214 872 0	−2.276 072 8	0.000 000 0
H	−2.913 765 1	−0.650 144 1	0.000 000 0

Table A.24. Calculated cartesian coordinates in the S_0 state ($1\ ^1A_1$) of ClPFB in Å, optimized at RI-SCS-MP2 level of theory.

C	1.199 778 4	0.000 000 0	−0.664 104 3
C	1.203 861 9	0.000 000 0	0.725 896 2
C	0.000 000 0	0.000 000 0	1.421 880 2
C	−1.203 861 9	0.000 000 0	0.725 896 2
C	−1.199 778 4	0.000 000 0	−0.664 104 3
C	0.000 000 0	0.000 000 0	−1.374 661 6
Cl	0.000 000 0	0.000 000 0	−3.087 883 2
F	2.363 546 7	0.000 000 0	−1.310 073 5
F	2.355 911 6	0.000 000 0	1.392 703 5
F	0.000 000 0	0.000 000 0	2.751 816 3
F	−2.355 911 6	0.000 000 0	1.392 703 5
F	−2.363 546 7	0.000 000 0	−1.310 073 5

Table A.25. Calculated cartesian coordinates in the S_1 state ($1\ ^1B_2$) of ClPFB in Å, optimized at RI-SCS-CC2 level of theory.

C	1.187 620 2	0.047 891 4	−0.677 519 8
C	1.191 721 4	0.040 729 3	0.748 494 6
C	−0.000 076 3	0.005 403 7	1.511 170 5
C	−1.191 869 6	0.038 924 2	0.748 423 1
C	−1.187 623 1	0.045 960 9	−0.677 585 1
C	0.000 088 9	−0.014 530 1	−1.440 944 8
Cl	0.000 582 3	−0.537 187 5	−3.085 226 3
F	2.349 992 2	0.254 089 2	−1.289 767 7
F	2.359 155 7	0.237 247 9	1.362 065 0
F	0.000 303 9	−0.602 563 4	2.728 947 9
F	−2.359 607 5	0.233 686 8	1.361 915 8
F	−2.350 288 2	0.250 347 7	−1.289 977 7

Table A.26. Calculated cartesian coordinates in the D_0 state ($1\ ^2B_1$) of ClPFB in Å, optimized at RI-SCS-MP2 level of theory.

C	1.239 446 1	0.000 003 4	−0.654 715 7
C	1.248 352 1	−0.000 016 4	0.715 911 7
C	−0.000 002 7	0.000 005 9	1.401 315 6
C	−1.248 354 6	0.000 019 0	0.715 916 4
C	−1.239 444 3	−0.000 026 0	−0.654 711 5
C	0.000 003 2	0.000 004 5	−1.367 434 3
Cl	−0.000 001 4	0.000 044 1	−3.024 539 1
F	2.359 460 7	0.000 015 3	−1.326 306 7
F	2.349 197 6	−0.000 037 5	1.420 193 3
F	0.000 002 1	0.000 012 8	2.680 476 0
F	−2.349 204 2	0.000 043 7	1.420 195 2
F	−2.359 454 7	−0.000 068 9	−1.326 305 3

Table A.27. Calculated cartesian coordinates in the S_0 state ($1\ ^1A_1$) of BrPFB in Å, optimized at RI-SCS-MP2 level of theory.

C	0.000 000 0	0.000 000 0	−1.362 273 0
C	1.199 031 5	0.000 000 0	−0.651 748 7
C	1.203 891 2	0.000 000 0	0.738 484 9
C	−1.199 031 5	0.000 000 0	−0.651 748 7
C	−1.203 891 2	0.000 000 0	0.738 484 9
C	0.000 000 0	0.000 000 0	1.434 372 1
F	−2.366 553 0	0.000 000 0	−1.292 232 0
F	−2.355 560 8	0.000 000 0	1.406 134 4
F	2.355 560 8	0.000 000 0	1.406 134 4
F	0.000 000 0	0.000 000 0	2.764 189 6
Br	0.000 000 0	0.000 000 0	−3.237 565 8
F	2.366 553 0	0.000 000 0	−1.292 232 0

Table A.28. Calculated cartesian coordinates in the S_1 state ($1\ ^1B_2$) of BrPFB in Å, optimized at RI-SCS-CC2 level of theory.

C	0.000 132 0	−0.037 459 7	−1.436 912 6
C	1.185 116 7	−0.077 070 2	−0.668 385 4
C	1.192 320 2	−0.029 942 5	0.756 786 5
C	−1.184 985 6	−0.077 226 2	−0.668 601 3
C	−1.192 452 1	−0.030 127 5	0.756 569 0
C	−0.000 139 6	0.015 877 3	1.514 012 3
F	−2.351 399 5	−0.305 105 4	−1.268 072 0
F	−2.358 183 7	−0.189 488 1	1.380 310 3
F	2.357 962 8	−0.189 103 8	1.380 740 1
F	−0.000 292 4	0.594 184 3	2.740 896 8
Br	0.000 254 5	0.630 262 1	−3.219 699 8
F	2.351 666 8	−0.304 800 2	−1.267 643 9

Table A.29. Calculated cartesian coordinates in the D_0 state ($1\ ^2B_1$) of BrPFB in Å, optimized at RI-SCS-MP2 level of theory.

C	0.000 031 8	−0.000 008 0	−1.357 171 8
C	1.235 444 9	0.000 002 4	−0.642 689 3
C	1.246 270 3	−0.000 002 9	0.727 873 1
C	−1.235 430 3	−0.000 004 9	−0.642 649 5
C	−1.246 293 1	0.000 005 1	0.727 916 9
C	−0.000 026 0	0.000 011 5	1.412 775 8
F	−2.362 437 4	0.000 020 6	−1.305 874 6
F	−2.348 951 6	−0.000 023 9	1.432 264 5
F	2.348 889 5	−0.000 036 5	1.432 254 5
F	0.000 025 2	0.000 023 4	2.692 074 1
Br	−0.000 017 9	−0.000 020 3	−3.170 891 4
F	2.362 494 6	0.000 033 6	−1.305 882 2

Vibrational Frequencies

B

Table B.1. Calculated harmonic vibrational frequencies in the S_0, S_1, and D_0 state of 1,2,3-TriFB. All values are given in cm^{-1}.

	no.	S_0 ($1\ ^1A_1$)	S_1 ($1\ ^1B_2$)	D_0 ($1\ ^2B_1$)
a_1	1	3254	3258	3264
	2	3232	3229	3247
	3	1667	1552	1801
	4	1562	1423	1411
	5	1337	1286	1365
	6	1255	1180	1358
	7	1082	1009	1034
	8	838	807	818
	9	699	662	735
	10	482	395	477
	11	305	264	304
a_2[†]	12	890	705	919
	13	579	397	576
	14	252	153	219
b_1[†,‡]	15	958	739	1024
	16	773	584	857
	17	593	511	640
	18	498	338	374
	19	307	171	295
	20	147	70	115
b_2	21	3248	3232	3276
	22	1662	1877	2797
	23	1521	1535	1671
	24	1359	1405	1543
	25	1277	1216	1311
	26	1179	1152	1195
	27	1037	963	1117
	28	579	531	616
	29	504	455	527
	30	278	245	292

[†] out-of-plane modes [‡] coupling modes

Table B.2. Calculated vibrational frequencies of 1,2,4,5-TFB in the S_0, the S_1, and the D_0–D_2 states based on the respective calculated molecular structures. The frequencies in the S_0 state are compared with experimental gas phase values, where available. All values are given in cm^{-1}.

	no.	expt. S_0[a]	S_0 ($1\,^1A_g$)	S_1 ($1\,^1B_{2u}$)	D_0 ($^2B_{1g}$)	D_1 ($1\,^2B_{2g}$)	D_2 ($1\,^2B_{3u}$)
a_g	1	3104	3257	3249	3258	3216	3241
	2	1644	1679	1583	1611	1699	1569
	3	1378	1414	1352	1527	1423	1416
	4	746	758	719	747	748	733
	5	486	491	418	491	482	475
	6	275[b]	275	267	289	268	272
b_{1g}[†]	7	411	423	350	474	400	359
b_{2g}[†]	8	865[b]	808	424	880	871	749
	9	669[c]	545	487	637	544	518
	10	290	275	168	207	214	242
b_{3g}	11	1644	1679	1527	1491	1681	1418
	12	1197[c]	1221	1173	1249	1259	1199
	13	1130	1150	1113	1166	1203	1031
	14	636	640	610	650	652	628
	15	411	419	371	335	433	341
a_u[†]	16	665[b]	673	531	735	662	621
	17	140[b]	127	100	106	110	111
b_{1u}	18	3093	3256	3251	3257	3215	3240
	19	1440	1466	1370	1566	1425	1561
	20	1228	1232	1168	1354	1329	1334
	21	702	708	679	754	741	761
	22	344	346	335	387	353	360
b_{2u}	23	1542	1577	1420	1517	1592	1597
	24	1269	1341	1862	1470	1468	1391
	25	1166	1194	1166	1245	1230	1221
	26	854	874	811	892	892	876
	27	297	297	298	313	291	296
b_{3u}[†,‡]	28	867	886	515	935	945	741
	29	457	467	362	456	393	441
	30	193	199	82	187	195	178

[a] Ref. [1] [b] inferred value [c] liquid phase [†] out-of-plane modes [‡] coupling modes

Table B.3. Calculated harmonic vibrational frequencies in the S_0, S_1, and D_0 state of 1,2,3,5-TFB, and experimentally determined vibrational frequencies in the S_0 states. All values are given in cm^{-1}.

	no.	expt. S_0[a]	S_0 ($1\ ^1A_1$)	S_1 ($1\ ^1B_2$)	D_0 ($1\ ^2B_1$)
a_1	1	3108	3263	3271	3269
	2	1642	1682	1562	1854
	3	1533	1570	1405	1657
	4	1388	1416	1316	1543
	5	1247	1259	1218	1393
	6	1130	1154	1120	1228
	7	1000	1016	951	1049
	8	789	796	757	761
	9	577	581	561	590
	10	442	445	393	442
	11	303	306	294	302
a_2[†,‡]	12	843	855	599	981
	13	564[b]	578	407	573
	14	254	257	140	226
b_1[†]	15	843	838	689	915
	16	707	646	542	651
	17	609	553	518	485
	18	364	371	278	251
	19[‡]	207	205	129	184
	20[‡]	140	138	67	108
b_2	21	3086	3264	3240	3263
	22	1632	1675	1865	2881
	23	1461	1494	1515	1604
	24	1274	1351	1381	1444
	25	1176	1207	1177	1250
	26	1056	1072	982	1099
	27	639	644	617	636
	28	507	509	404	549
	29	331	333	332	348
	30	279	276	239	296

[a] Ref. [1] [b] liquid phase [†] out-of-plane modes [‡] coupling modes

Table B.4. Calculated harmonic vibrational frequencies in the S_0, S_1, and D_0 state of 1,2,3,4-TFB, and experimentally determined vibrational frequencies in the S_0 states. All values are given in cm^{-1}.

	no.	expt. S_0[a]	S_0 ($1\,^1A_1$)	S_1 ($2\,^1A_1$)	D_0 ($1\,^2A_2$)
a_1	1	3100	3258	3266	3263
	2	1636	1674	1860	1816
	3	1523	1555	1550	1657
	4	1331	1357	1373	1543
	5	1261	1347	1294	1462
	6	1165	1188	1129	1274
	7	1052	1067	1001	1134
	8	683	691	676	666
	9	457	457	410	461
	10	324	324	326	306
	11	289[b]	276	244	267
a_2[†,‡]	12	926[b]	923	786	984
	13	722[b]	573	600	577
	14	535	487	470	383
	15	372	365	291	253
	16	155	144	79	103
b_1[†]	17	803	816	617	910
	18	596	606	503	639
	19	281	295	178	341
	20	154	156	106	133
b_2	21	3082	3244	3219	3714
	22	1605	1673	1504	3282
	23	1523	1555	1416	2512
	24	1278	1284	1243	1398
	25	1241	1263	1166	1316
	26	993	999	926	978
	27	748	754	729	747
	28	604	610	580	696
	29	485	487	400	473
	30	281	282	266	313

[a] Ref. [1] [b] inferred value [†] out-of-plane modes [‡] coupling modes

Table B.5. Calculated harmonic vibrational frequencies in the S_0, S_1, and D_0 state of PFPy, and experimentally determined vibrational frequencies in the S_0 states. All values are given in cm^{-1}.

	no.	expt. S_0[a]	S_0 ($1\ ^1A_1$)	S_1 ($1\ ^1B_2$)	D_0 ($1\ ^2A_2$)
a_1	1	1650	1681	1538	1716
	2	1529	1568	1365	1596
	3	1420	1456	1419	1556
	4	1285	1310	1192	1384
	5	1077	1093	968	1149
	6	694	707	694	714
	7	593	597	631	602
	8	476	480	434	479
	9	310	347	356	372
	10	273	273	292	284
a_2[†]	11	570	703	634	761
	12	428	441	397	473
	13	174	122	87	99
b_1[†,‡]	14	736	746	677	818
	15	620	635	537	647
	16	353	357	264	336
	17	224	219	158	214
	18	174	160	78	145
b_2	19	1650	1681	1466	1533
	20	1492	1532	1349	1406
	21	1285	1335	1930	1357
	22	1172	1190	1149	1240
	23	983	997	941	1038
	24	706	744	715	755
	25	457	460	397	389
	26	310	319	316	323
	27	224	272	237	264

[a] Ref. [2] [†] out-of-plane modes [‡] coupling modes

Table B.6. Calculated harmonic vibrational frequencies in the S_0, S_1, and D_0 state of PFT, and experimentally determined vibrational frequencies in the S_0 states. All values are given in cm^{-1}.

	no.	exp. S_0[a]	S_0 ($1\,^1A'$)	S_1 ($2\,^1A'$)	D_0 ($1\,^2A''$)
a_1 / a'	1	1659	1693	1566	3327
	2	1520	1559	1421	1659
	3	1440	1478	1350	1554
	4	1307	1324	1248	1399
	5	1126	1147	1045	1179
	6	960	979	912	1008
	7	597	605	570	652
	8	552	561	509	558
	9	442	446	397	502
	10	313	332	332	343
	11	269	276	276	277
a_2 / a''[†]	12		667	569	711
	13	389	398	432	440
	14	146	134	90	113
b_1 / a''[†,‡]	15	728	633	625	632
	16	614	466	594	519
	17	358	360	251	362
	18	269	212	161	215
	19	218	152	113	118
	20	146	131	80	83
b_2 / a'	21	1659	1675	1851	2193
	22	1500	1550	1472	1818
	23	1264	1342	1348	1460
	24	1147	1166	1128	1252
	25	1044	1099	1074	1140
	26	714	748	717	756
	27	442	449	377	443
	28	332	310	309	313
	29	288	283	253	295
	30	190	263	238	261
			methyl group vibrations		
a_1 / a'	31	2943	3086	3052	3071
	32	1373	1436	1440	1438
a_2 / a''	33		28	50	99
b_1 / a''	34	2957	3156	3171	3160
	35	1455	1514	1507	1501
	36	1079	1068	1055	1059
b_2 / a'	37	2978	3195	3133	3190
	38	1455	1502	1522	1501
	39	1044	954	903	977

[a] Ref. [3] [†] out-of-plane modes [‡] coupling modes

Table B.7. Calculated harmonic vibrational frequencies in the S_0, S_1, and D_0 state of PFPh, and experimentally determined vibrational frequencies in the S_0 states. All values are given in cm^{-1}.

	no.	exp. S_0[a]	S_0 ($1\ ^1A'$)	S_1 ($2\ ^1A'$)	D_0 ($1\ ^2A''$)
a_1 / a'	1	1667	1699	1579	1626
	2	1540	1575	1435	1589
	3	1483	1525	1378	1421
	4	1313	1335	1227	1337
	5	1151	1174	1122	1236
	6	1005	1022	973	1075
	7	607	608	574	632
	8	569	565	506	574
	9	444	450	404	419
	10	322	321	280	321
	11	245	272	260	260
a_2 / a''[†,‡]	12	643	651	601	726
	13	372	387	319	403
	14	136	135	96	130
b_1 / a''[†]	15	715	665	563	754
	16	636	453	523	566
	17	369	367	441	457
	18	296	216	162	226
	19	208	145	84	122
	20	136	139	68	112
b_2 / a'	21	1660	1692	1821	2493
	22	1520	1555	1513	1756
	23	1358	1369	1401	1453
	24	1138	1159	1056	1171
	25	977	992	903	1036
	26	782	783	750	802
	27	430	447	361	456
	28	292	315	311	337
	29	268	283	255	290
	30	199	269	232	283
hydroxy group vibrations					
	31	3629	3819	3667	3754
	32	1225	1278	1266	1290
	33	334	361	544	547

[a] Ref. [4] [†] out-of-plane modes [‡] coupling modes

Table B.8. Calculated harmonic vibrational frequencies in the S_0, S_1, and D_0 state of ClPFB, and experimentally determined vibrational frequencies in the S_0 states. All values are given in cm^{-1}.

	no.	exp. S_0 [a–c]	S_0 ($1\,^1A_1$)	S_1 ($1\,^1B_2$)	D_0 ($1\,^2B_1$)
a_1	1	1644	1677	1554	2491
	2	1513	1551	1396	1807
	3	1439	1471	1375	1503
	4	1296	1310	1220	1373
	5	1103	1117	1023	1220
	6	886	896	833	967
	7	587	590	582	658
	8	613	520	467	527
	9	393	396	374	416
	10	307	309	303	316
	11	278	275	266	274
a_2 [†]	12	650	665	549	662
	13	375	388	424	382
	14	140	134	83	121
b_1 [†,‡]	15	721	644	593	701
	16	628	522	533	572
	17	353	363	255	435
	18	206	212	151	214
	19	172	154	86	114
	20	104	108	72	86
b_2	21	1644	1670	1860	4234
	22	1515	1545	1479	1692
	23	1274	1329	1348	1500
	24	1157	1174	1115	1226
	25	998	1007	953	1089
	26	757	767	738	695
	27	441	445	367	541
	28	310	309	304	321
	29	245	276	242	286
	30	201	202	180	205

[a] Ref. [5] [b] Ref. [6] [c] Ref. [7] [†] out-of-plane modes [‡] coupling modes

Table B.9. Calculated harmonic vibrational frequencies in the S_0, S_1, and D_0 state of BrPFB, and experimentally determined vibrational frequencies in the S_0 states. All values are given in cm^{-1}.

	no.	exp. S_0[a–c]	S_0 ($1\ ^1A_1$)	S_1 ($1\ ^1B_2$)	D_0 ($1\ ^2B_1$)
a_1	1	1638	1673	1551	2532
	2	1519	1549	1410	1773
	3	1428	1459	1356	1480
	4	1290	1306	1219	1348
	5	1097	1108	1018	1200
	6	840	849	770	918
	7	584	588	574	661
	8	495	503	443	512
	9	362	365	359	378
	10	282	283	276	287
	11	240	245	231	258
a_2[†]	12	652	668	558	670
	13	378	390	423	386
	14	140	133	82	121
b_1[†,‡]	15	719	636	588	705
	16	620	559	528	596
	17	348	357	255	423
	18	207	211	140	211
	19	175	158	86	124
	20	89	91	55	76
b_2	21	1638	1668	1844	4233
	22	1513	1540	1471	1691
	23	1273	1332	1345	1498
	24	1159	1172	1116	1222
	25	995	1003	951	1092
	26	737	760	731	715
	27	440	444	367	538
	28	309	310	305	324
	29	240	276	244	286
	30	155	155	135	141

[a] Ref. [5] [b] Ref. [6] [c] Ref. [7] [†] out-of-plane modes [‡] coupling modes

References

[1]J. H. S. Green and D. J. Harrison, "Thermodynamic properties of fluorine compounds—XVII. The vibrational spectra and calculated thermodynamic properties of the tetrafluorobenzenes", Spectrochim. Acta A **32A**, 1185 (1976).

[2]D. A. Long and R. T. Bailey, "Spectroscopic and thermodynamics studies of pyridine. Part 3.—Pentafluoropyridine", Trans. Faraday Soc. **59**, 599 (1963).

[3]R. T. Bailey and S. G. Hasson, "The vibrational spectra of pentafluorotoluene", Spectrochim. Acta A **25**, 467 (1969).

[4]J. H. S. Green and D. J. Harrison, "Thermodynamic properties of fluorine compounds 19. Hexafluorobenzene, pentafluorophenol, 1,3,5-trichlorotrifluorobenzene, and pentafluorobenzaldehyde: vibrational assignments and chemical thermodynamic properties", J. Chem. Thermodyn. **8**, 529 (1976).

[5]D. A. Long and D. Steele, "The vibrational spectra and assignments for C_6F_5Cl, C_6F_5Br and C_6F_5I", Spectrochim. Acta **19**, 1955 (1963).

[6]I. J. Hyams, E. R. Lippincott, and R. T. Bailey, "The Raman and low frequency infrared spectra of C_6F_5Cl, C_6F_6Br and C_6F_5I", Spectrochim. Acta **22**, 695 (1966).

[7]S. G. Frankiss and D. J. Harrison, "Thermodynamic properties of fluorine compounds—XVI. The vibrational spectra and thermodynamic functions of pentafluorobenzene, chloropentafluorobenzene, bromopentafluorobenzene and methylpenta-fluorobenzene", Spectrochim. Acta A **31A**, 1839 (1975).

Photoelectron Images

C

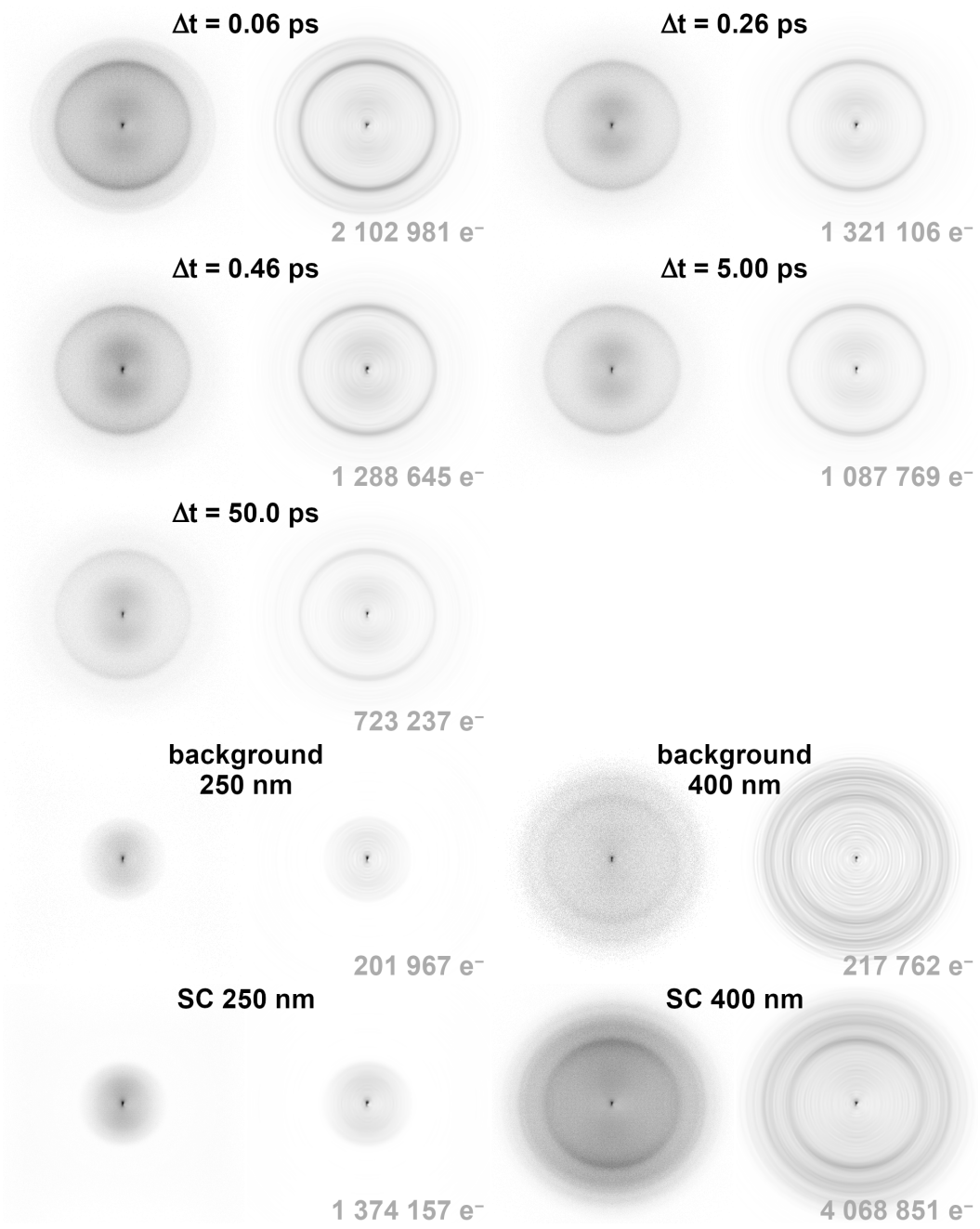

Figure C.1. Photoelectron images (left) and their corresponding meridional slices through the recovered three-dimensional photoelectron distributions (right) of 1,2,3-TriFB after excitation at $\lambda_{\text{pump}} = 250$ nm and ionization at $\lambda_{\text{probe}} = 400$ nm, as well as SC images.

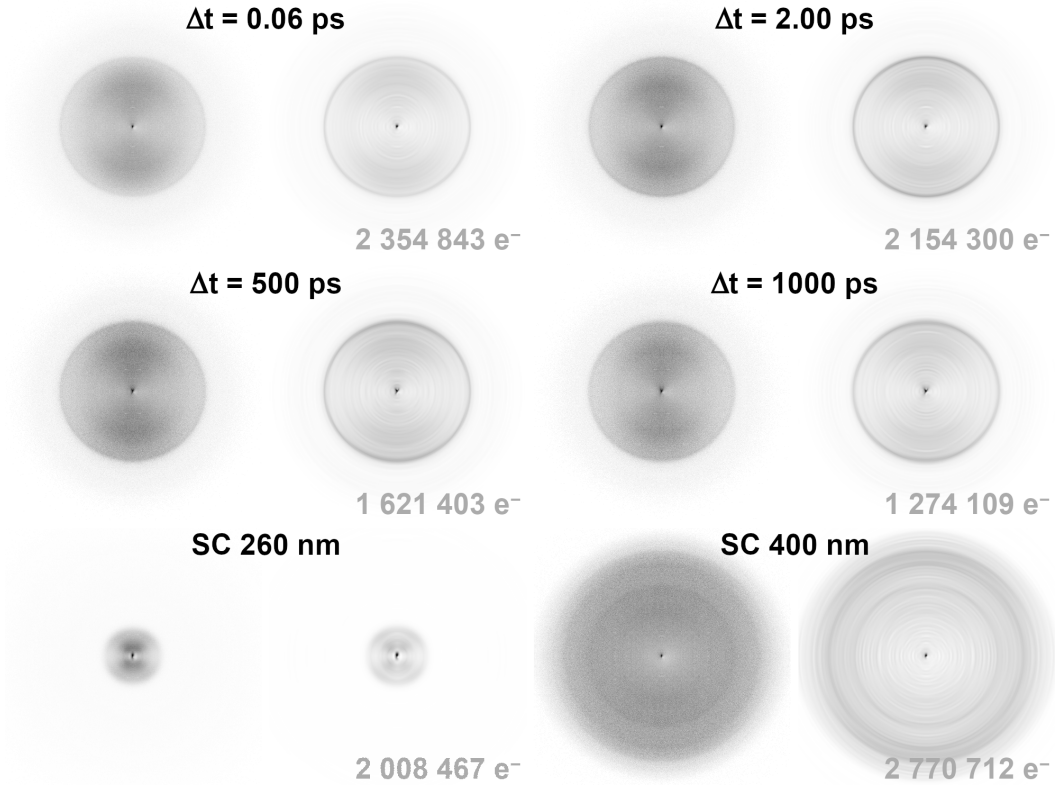

Figure C.2. Photoelectron images (left) and their corresponding meridional slices through the recovered three-dimensional photoelectron distributions (right) of 1,2,4,5-TFB after excitation at $\lambda_{\text{pump}} = 260$ nm and ionization at $\lambda_{\text{probe}} = 400$ nm, as well as SC images.

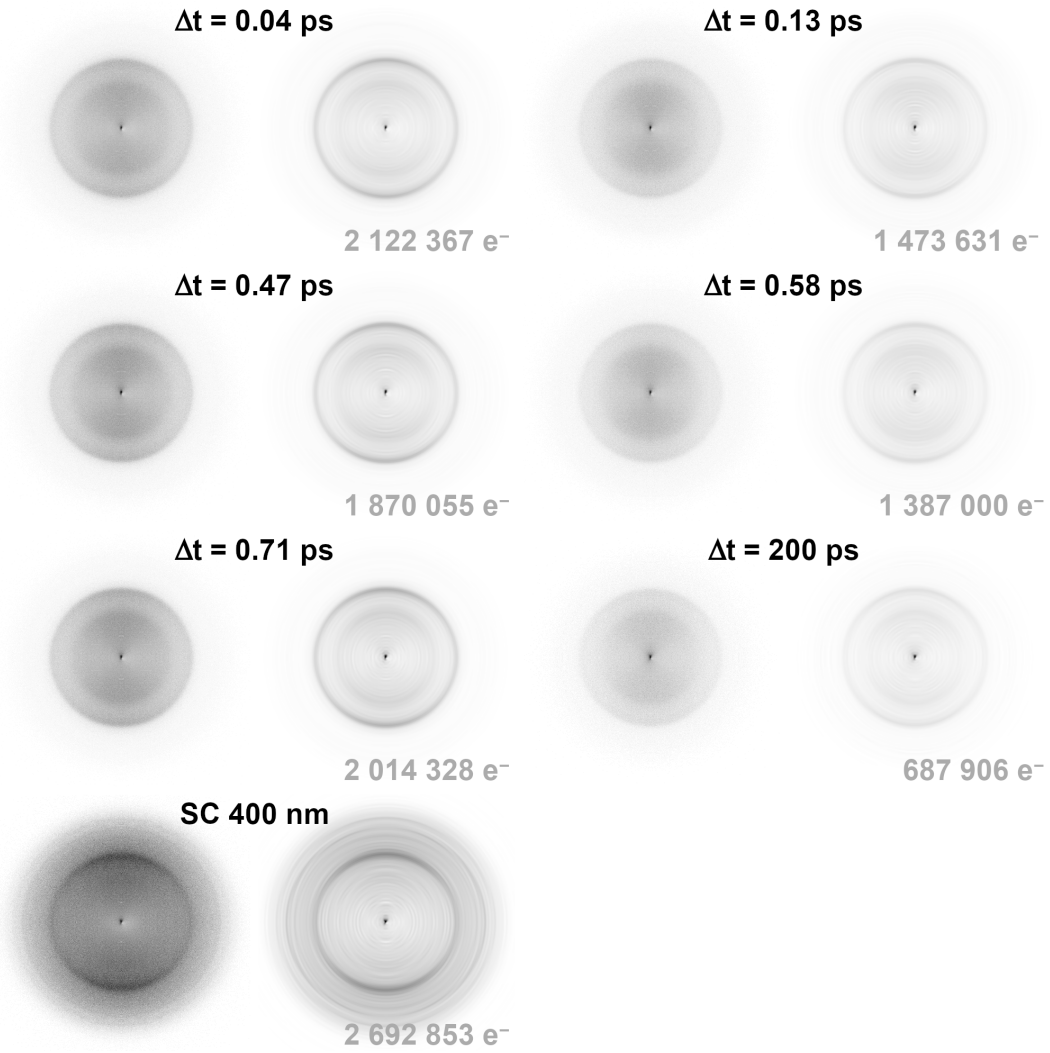

Figure C.3. Photoelectron images (left) and their corresponding meridional slices through the recovered three-dimensional photoelectron distributions (right) of 1,2,3,5-TFB after excitation at $\lambda_{pump} = 260$ nm and ionization at $\lambda_{probe} = 400$ nm, as well as SC image at $\lambda_{probe} = 400$ nm.

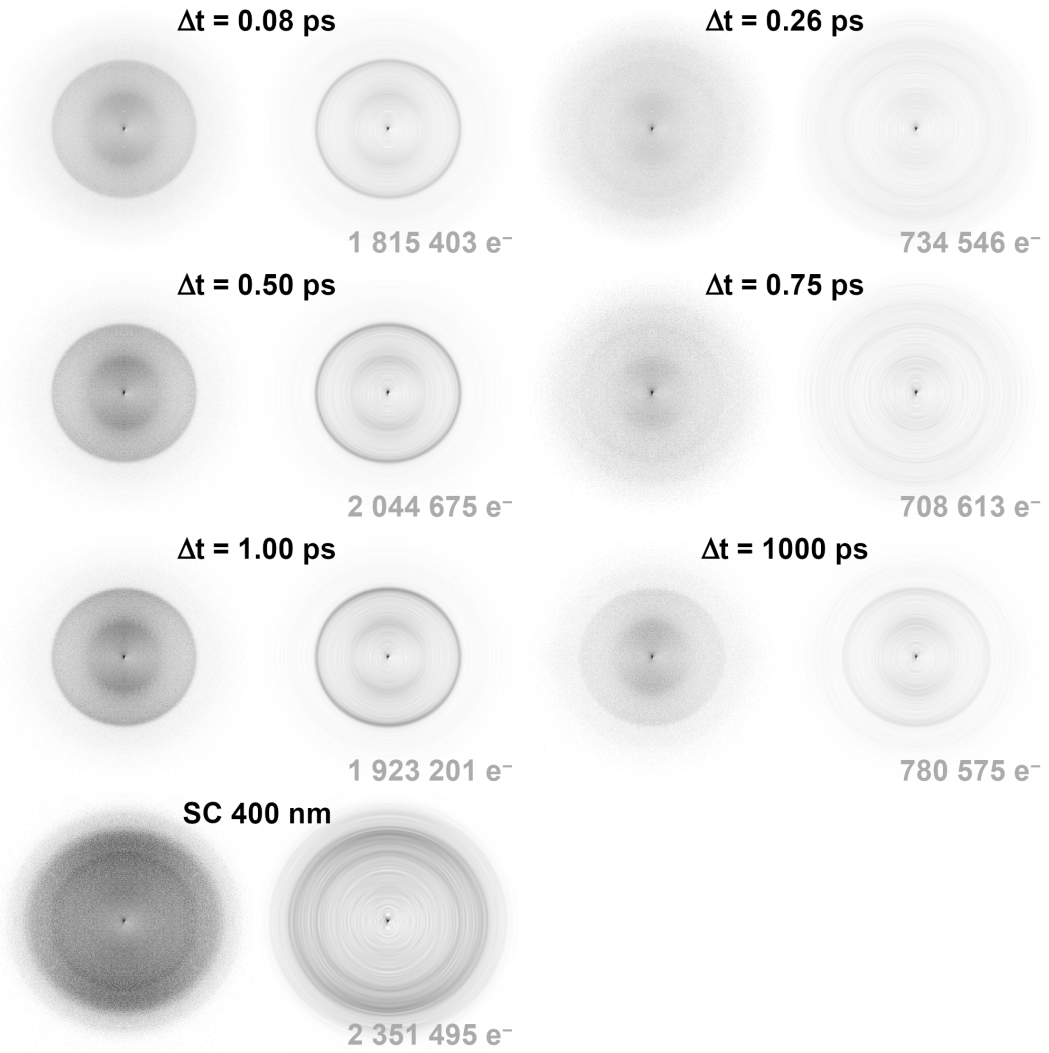

Figure C.4. Photoelectron images (left) and their corresponding meridional slices through the recovered three-dimensional photoelectron distributions (right) of 1,2,3,4-TFB after excitation at $\lambda_{\text{pump}} = 260$ nm and ionization at $\lambda_{\text{probe}} = 400$ nm, as well as SC image at $\lambda_{\text{probe}} = 400$ nm.

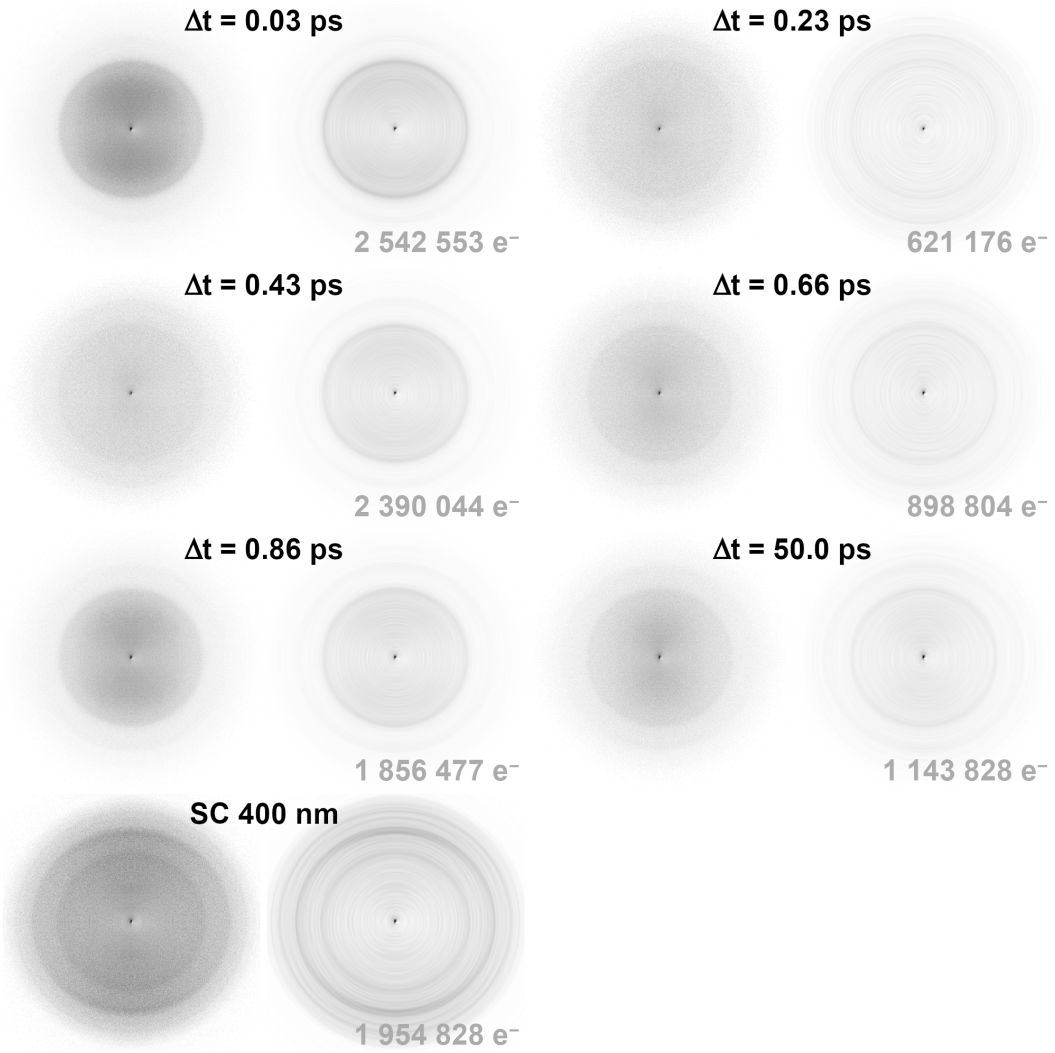

Figure C.5. Photoelectron images (left) and their corresponding meridional slices through the recovered three-dimensional photoelectron distributions (right) of PFT after excitation at $\lambda_{\text{pump}} = 260$ nm and ionization at $\lambda_{\text{probe}} = 400$ nm, as well as SC image at $\lambda_{\text{probe}} = 400$ nm.

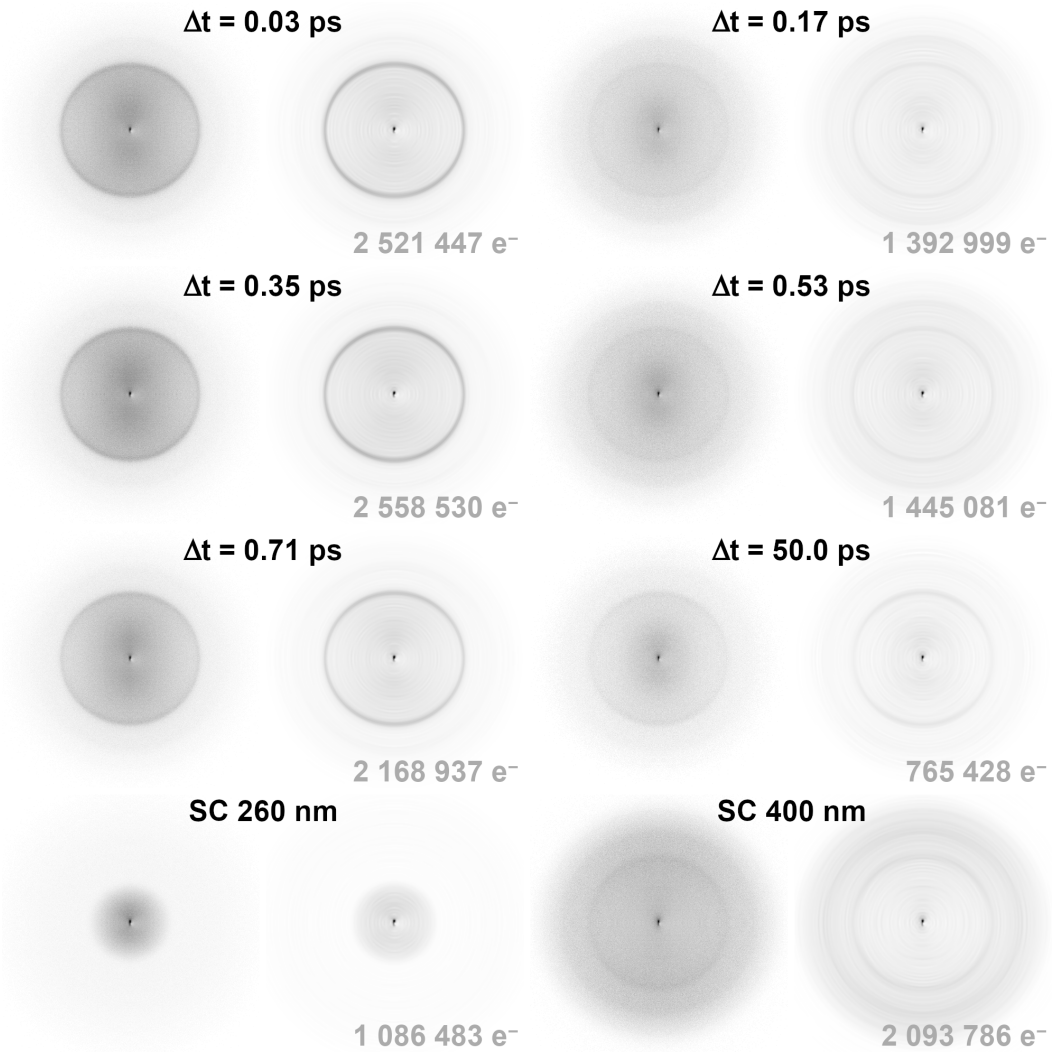

Figure C.6. Photoelectron images (left) and their corresponding meridional slices through the recovered three-dimensional photoelectron distributions (right) of PFPh after excitation at $\lambda_{\text{pump}} = 260$ nm and ionization at $\lambda_{\text{probe}} = 400$ nm, as well as SC images.

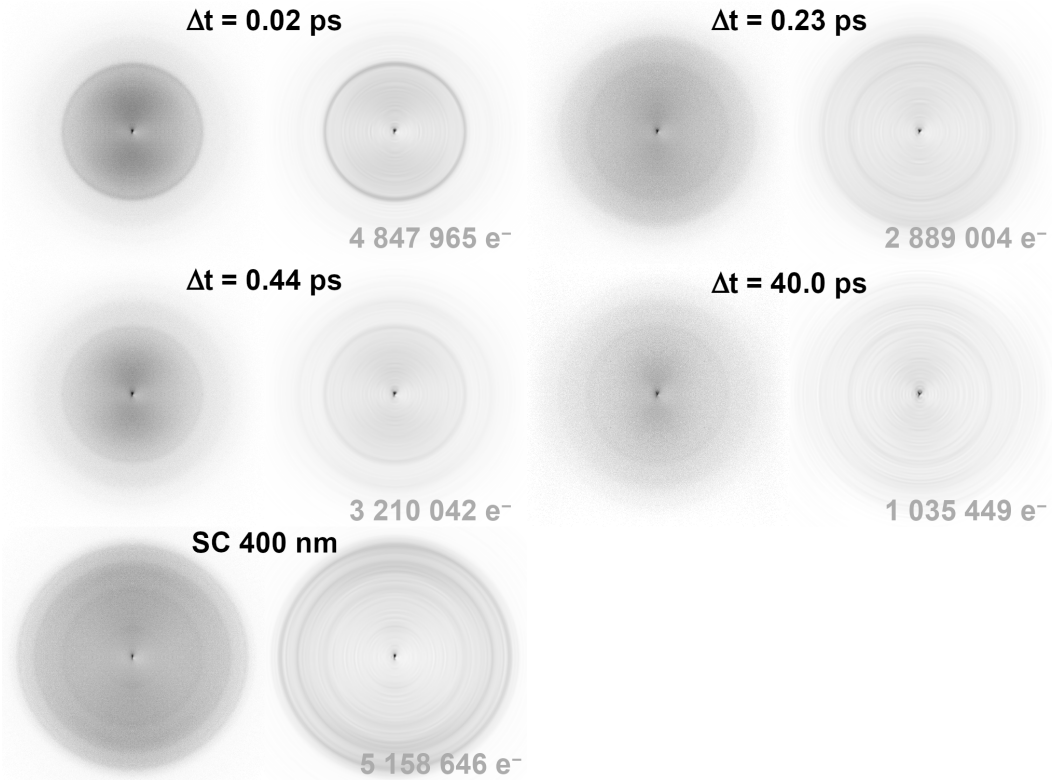

Figure C.7. Photoelectron images (left) and their corresponding meridional slices through the recovered three-dimensional photoelectron distributions (right) of ClPFB after excitation at $\lambda_{\text{pump}} = 260$ nm and ionization at $\lambda_{\text{probe}} = 400$ nm, as well as SC image at $\lambda_{\text{probe}} = 400$ nm.

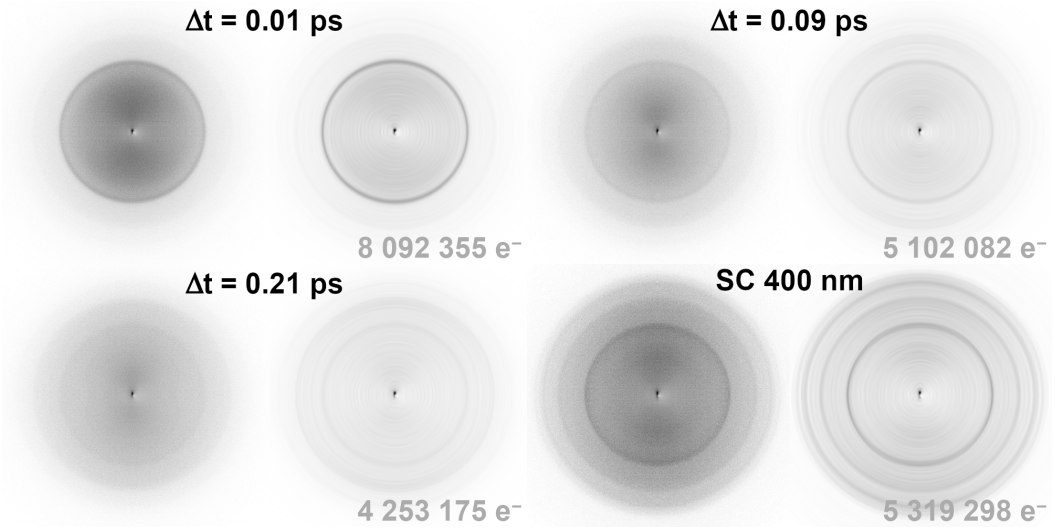

Figure C.8. Photoelectron images (left) and their corresponding meridional slices through the recovered three-dimensional photoelectron distributions (right) of BrPFB after excitation at $\lambda_{\text{pump}} = 260$ nm and ionization at $\lambda_{\text{probe}} = 400$ nm, as well as SC image at $\lambda_{\text{probe}} = 400$ nm.

List of Figures

List of Tables